

**Measurement of Neutrino Oscillation Parameters
with Precise Calculation of Reactor Neutrino Spectrum
at KamLAND**

Kyo Nakajima
Graduate School of Science, Tohoku University
Sendai 980-8578, Japan

February 2005

Abstract

The primary purpose of the KamLAND (Kamioka Liquid scintillator Anti-Neutrino Detector) experiment is the measurement of neutrino oscillations using reactor $\bar{\nu}_e$'s with long baselines. In a 766 ton-year exposure of KamLAND between March 9, 2002 and January 11, 2004, 258 $\bar{\nu}_e$ candidate events with $\bar{\nu}_e$ energies above 3.4 MeV are observed, which include 17.8 expected background events. The precise calculation of reactor $\bar{\nu}_e$ spectrum is important and essential to find evidence of reactor $\bar{\nu}_e$ oscillation and precise oscillation parameter measurements. By tracing the thermal output data of 52 reactors in Japan, expected time-dependent reactor $\bar{\nu}_e$ events at KamLAND are calculated. The expected number of $\bar{\nu}_e$ events is $365.2 \pm 23.7(\text{syst})$ with $\bar{\nu}_e$ energies above 3.4 MeV assuming no anti-neutrino oscillation.

The ratio of the number of observed events to the expected number of events assuming no oscillation is $0.658 \pm 0.044(\text{stat}) \pm 0.047(\text{syst})$. This deficit confirms $\bar{\nu}_e$ disappearance at 99.998% significance level. The observed energy spectrum disagrees with the expected spectral shape in the absence of neutrino oscillation at 99.6% significance and prefers the distortion expected from $\bar{\nu}_e$ oscillation effects. A two-neutrino oscillation analysis of the KamLAND data gives a mass-squared difference $\Delta m^2 = 7.9_{-0.5}^{+0.6} \times 10^{-5} \text{eV}^2$ and a mixing angle $\tan^2\theta = 0.46$. These values are in excellent agreement with the "Large Mixing Angle" solution to the solar neutrino problem. Assuming CPT invariance, a combined analysis of data from KamLAND and solar neutrino experiments yields $\Delta m^2 = 7.9_{-0.5}^{+0.6} \times 10^{-5} \text{eV}^2$ and $\tan^2\theta = 0.40_{-0.07}^{+0.10}$, the most precise determination to date.

Acknowledgements

First of all, I have to express my great appreciation to Professor Atsuto Suzuki, the spokesperson of KamLAND. He gave me with the opportunity to take part in this experiment.

I would like to be thankful to Associate Professor Fumihiko Suekane, my advisor. He gave me many guidance and suggestions during graduate studies.

I would like to thank Professor Kunio Inoue, Associate Professor Junpei Shirai and Associate Professor Masayuki Koga of Tohoku University. I also thank Dr. Yasuhiro Kishimoto, Dr. Tadao Mitsui, Dr. Koichiro Furuno, Dr. Masakazu Motoki, Dr. Jean-Stephane Ricol, Dr. Yoshihito Gando, Kyoko Tamae, Sanshiro Enomoto, Hideki Watanabe, Haruo Ikeda, Itaru Shimizu, Yotaro Koseki, Kentaro Owada, Kiyoshi Ikeda, Takayuki Araki, Koichi Ichimura, Yusuke Tsuda, Momoyo Ogawa and Shin Takeuchi as KamLAND collaborators at Tohoku; Dr. Kenji Ishihara, Dr. Toshiyuki Iwamoto, Dr. Hiroshi Ogawa and Dr. Osamu Tajima as past KamLAND collaborators; and Professor Akira Yamaguchi, Professor Hitoshi Yamamoto, Associate Professor Tomoki Hayashino, Dr. Tadashi Nagamine, Dr. Takuya Hasegawa, Tomoaki Takayama, Hiromitsu Hanada and Takashi Nakajima, Fujio Miura, Yuri Endo and Akemi Ohtsuka as members at Tohoku. And thank to KamLAND collaborators from all other institutes.

I gratefully acknowledge the cooperation from many companies. The monthly reactor data have been provided by courtesy of the following electric associations in Japan: Hokkaido, Tohoku, Tokyo, Hokuriku, Chubu, Kansai, Chugoku, Shikoku and Kyushu Electric Power Companies, Japan Atomic Power Co. and Japan Nuclear Cycle Development Institute. TEPCO Systems Co. provided information about reactor core analysis. The Kamioka Mining and Smelting Company has provided a lot of service. KamLAND is supported by the Center of Excellence program of the Japanese Ministry of Education, Culture, Sports, Science, and Technology under grant 09CE2003, and by the United States Department of Energy under grant DEFG03-00ER41138.

Finally I would like to thank my parents, Ryo and Nobuko Nakajima.

Contents

1	Introduction	1
1.1	The neutrino	2
1.2	Neutrino oscillation	3
1.2.1	Two flavour neutrino oscillations in vacuum [13]	3
1.2.2	Three flavour neutrino oscillations in vacuum [77]	4
1.2.3	Two flavour neutrino oscillations in matter (MSW effect) [13]	5
1.3	Neutrino oscillation experiments	6
1.3.1	Solar neutrino experiments	8
1.3.2	Atmospheric neutrino experiments	11
1.3.3	Accelerator neutrino experiments	12
1.3.4	Reactor $\bar{\nu}_e$ experiments	14
1.4	KamLAND experiment	16
2	KamLAND experiment	19
2.1	Anti-neutrino detection method	19
2.1.1	Delayed coincidence technique	19
2.1.2	Positron energy and cross section of the inverse β -decay reaction [42]	20
2.1.3	Observed energy spectrum	22
2.2	Location of KamLAND	23
2.2.1	Coordinates of KamLAND	25
2.3	Detector design	25
2.3.1	Liquid scintillator and buffer oil	25
2.3.2	PMTs	28
2.3.3	Front-End Electronics(FEE)	32
2.3.4	Trigger system	34
2.3.5	Plastic balloon and balloon strap	35
2.3.6	Veto detector	35
2.3.7	Purification system	37
2.3.8	Water purification system	37
2.3.9	Nitrogen supply system	38
3	Event reconstruction and detector calibration	39
3.1	Waveform analysis	39
3.2	Gain calibration	41
3.3	Bad channel selection	43
3.4	Timing calibration	43
3.5	Vertex reconstruction and fiducial volume	45
3.5.1	Vertex reconstruction	45

3.5.2	Deviation of the reconstructed vertex	47
3.5.3	Systematic uncertainty on the fiducial volume	47
3.6	Energy reconstruction	50
3.6.1	Visible energy calculation	50
3.6.2	Systematic uncertainty of the visible energy calculation	53
3.7	Muon track reconstruction	58
3.7.1	Selection criteria	58
3.7.2	Muon track reconstruction	58
3.7.3	Residual charge	59
3.8	Noise event selection (Noise cut)	62
3.9	Flasher event selection (Flasher cut)	63
4	Background estimation	64
4.1	Single event distribution	64
4.2	Background for reactor $\bar{\nu}_e$ selection	67
4.2.1	Accidental background	67
4.2.2	^9Li and ^8He spallation products	67
4.2.3	Fast neutron	71
4.2.4	$^{13}\text{C}(\alpha, n)^{16}\text{O}$	71
5	Event selection	77
5.1	Data collection	77
5.2	Livetime calculation	77
5.2.1	Deadtime	79
5.2.2	Vetotime	80
5.2.3	Livetime	80
5.3	Detection efficiency	82
5.3.1	Space correlation	82
5.3.2	Time correlation	83
5.3.3	Delayed energy	84
5.4	Reactor $\bar{\nu}_e$ event selection	84
5.4.1	Event selection criteria	84
5.4.2	Event reduction	85
6	Fission rate calculation	90
6.1	Reactor neutrino	91
6.1.1	Fission elements in reactor cores	91
6.1.2	Neutrino energy spectrum of each fission element	91
6.1.3	Energy released per fission reaction	94
6.1.4	Core thermal output	95
6.2	Time evolution of the fission rate	96
6.2.1	Burnup	96
6.2.2	Burnup equation	96
6.3	Fission rate calculation using the reactor core analysis method [63, 64]	99
6.3.1	Reactor core analysis method	99
6.3.2	Burnup dependence at typical reactors	99
6.4	Fission rate calculation using simplified method [63, 64]	100
6.4.1	Reactor operation data for simplified method [63, 64]	102

6.4.2	Burnup dependence in reference cores	103
6.4.3	Correction for variation of new fuel enrichment	107
6.4.4	Correction for exchanged fuel volume ratio	109
6.4.5	Correction for absolute burnup at the beginning of the cycle	109
6.5	Systematic error of the simple method	110
7	Expected reactor anti-neutrino event estimation	112
7.1	Japanese commercial reactors	112
7.1.1	Basic parameters	112
7.1.2	Operation data of each reactor	116
7.1.3	Comparisons between the thermal output and the electric output	121
7.1.4	Fission rate of each reactor	123
7.2	Korean commercial reactors	125
7.2.1	Korean power reactors	125
7.2.2	Operation data of each reactor	125
7.2.3	Fission rate of each reactor	125
7.3	World reactors	128
7.4	Contribution from long lived nuclides	130
7.5	Anti neutrino flux at KamLAND	134
7.6	Reactor $\bar{\nu}_e$ events at KamLAND assuming no anti-neutrino oscillation	134
8	Analysis	141
8.1	Event ratio and significance of reactor $\bar{\nu}_e$ disappearance	142
8.2	Correlation between observed event rate and reactor $\bar{\nu}_e$ flux	142
8.2.1	Expected event rate bin case	143
8.2.2	Livetime bin case	145
8.3	Oscillation Analysis	147
8.3.1	Rate-and-shape analysis	147
8.3.2	Scaled no-oscillation spectrum	149
8.3.3	L/E analysis	149
8.3.4	Combined analysis	150
9	Conclusion	153
A	Japanese research reactors and world reactors	154
B	Operation data of Japanese reactors	156
C	Operation data of Korean reactors	159
	Bibliography	161

List of Figures

1.1	Survival probability for $P(\bar{\nu}_e \rightarrow P(\bar{\nu}_e))$	5
1.2	Matter effect in KamLAND reactor $\bar{\nu}_e$ analysis [53]	6
1.3	The regions of neutrino parameter space favored or excluded by various neutrino oscillation experiments [29]	7
1.4	Solar neutrino generation in the pp chains	8
1.5	Solar neutrino flux predicted by the SSM	9
1.6	Fluxes of ^8B solar neutrinos	11
1.7	Solar neutrino global analysis [57]	13
1.8	Zenith angle distributions of μ -like and e-like events for sub-GeV and multi-GeV data sets [9]	13
1.9	Allowed oscillation parameter regions for 2-flavor $\nu_\mu \leftrightarrow \nu_\tau$ oscillations [86]	14
1.10	Map of Nuclear power reactors in Japan [69]	17
1.11	The reactor distance distribution for the thermal output flux at KamLAND . . .	18
1.12	Sensitivity of KamLAND	18
1.13	Statistical significance for the reactor neutrino disappearance as a function of the uncertainty of the expected reactor $\bar{\nu}_e$ events	18
2.1	Delayed coincidence technique	19
2.2	Observed spectrum	22
2.3	Observed spectrum per fission reaction of each isotope	22
2.4	Expected reactor $\bar{\nu}_e$ energy spectrum with contributions of geo-neutrinos [30] . .	23
2.5	KamLAND Detector	24
2.6	Sideview of KamLAND detector	26
2.7	R3250 20-inch PMT from Hamamatsu	29
2.8	R7250 17-inch PMT from Hamamatsu	29
2.9	Circuit diagram of the voltage divider in the 17-inch PMT	29
2.10	Oil-proof housing of 17inch PMT	30
2.11	Quantum efficiency of 17inch PMTs	31
2.12	Schematic diagram of the front-end electronics	32
2.13	Transparency of balloon film	36
2.14	Veto counter	36
2.15	Purification system	37
2.16	Water purification system	37
2.17	Nitrogen gas purification system	38
3.1	Example of waveforms of input pulses	40
3.2	KamLAND event display	41
3.3	Time variation of the mean single photo-electron charge	42

3.4	Time variation of the number of bad channels	44
3.5	Schematic diagram of the timing calibration	44
3.6	Correlation between time and charge at a 17inch PMT	45
3.7	Correlation between time and charge at a 20inch PMT	45
3.8	Timing distribution of 1 p.e. events	46
3.9	Measured speed of light for calibration sources at z positions	46
3.10	Z-deviations with source calibrations	48
3.11	Systematic uncertainty on the fiducial volume	48
3.12	$^{12}\text{B}/^{12}\text{N}$ events following muons	49
3.13	Energy distribution of $^{12}\text{B}/^{12}\text{N}$ events following muons	49
3.14	Vertex distribution of $^{12}\text{B}/^{12}\text{N}$ events	50
3.15	Timing distribution of detected signals after the correction for time of flight	51
3.16	Time dependence of the visible energy of the neutron capture gamma event	54
3.17	Position dependence of the visible energy of the neutron capture gamma event	55
3.18	Energy non-linearity from characteristics between the 17inch PMT and the 20 inch PMT	56
3.19	Non-linearity of the visible energy to the real energy	57
3.20	Time and charge distribution of the muon events	59
3.21	Muon track reconstruction	60
3.22	Correlations between the total charge in the inner detector and the muon track length, in the liquid scintillator (upper) and in the buffer oil (lower)	60
3.23	Normalized charge by reconstructed muon track length	61
3.24	Event displayies of a typical noise event and a typical flasher event	63
4.1	Vertex distribution of each energy range in the whole volume	65
4.2	Energy spectra of single events with fiducial radius	66
4.3	Accidental time and energy spectrum for 5.5 m fiducial volume	68
4.4	Prompt energy spectrum of $^9\text{Li}/^8\text{He}$ events	69
4.5	Time and distance distributions of muon events	70
4.6	Fast neutron candidates	72
4.7	Total cross sections of (α, n) reactions for nuclei	73
4.8	$^{13}\text{C}(\alpha, n)^{16}\text{O}$ correlated background	74
4.9	Energy spectra for $^{13}\text{C}(\alpha, n)^{16}\text{O}$ background	75
5.1	History of the operation at KamLAND	78
5.2	Ratio of unknown deadtime in percentage	80
5.3	Ratio of livetime/runtime for each run	81
5.4	Space correlation between prompt and delayed events	82
5.5	Time difference from muons to spallation neutron capture candidates	83
5.6	Prompt energy and delayed energy distribution	86
5.7	Vertex distribution of the delayed coincidence events	87
5.8	Profiles of $\bar{\nu}_e$ candidates	88
5.9	Profiles of $\bar{\nu}_e$ candidates	89
6.1	Fission rates at a unit of the Palo Verde reactor [40]	92
6.2	Fission product yield curve [41]	93
6.3	Reactor neutrino energy spectrum	93
6.4	Heat balance at BWR and PWR cores	95
6.5	Time evolution of the number densities	98

6.6	Time evolution of the fission reaction rates	98
6.7	Relative fission yields for typical reactor cores by the detailed calculation	101
6.8	Flow chart of the simple method of the fission rate calculation	102
6.9	Burnup effect at the number of expected events	104
6.10	Burnup dependence of the expected energy spectra	105
6.11	Burnup at EOC	108
6.12	Fuel volume correction model	109
6.13	Comparison between fission rate calculated by detailed method and simple method	110
6.14	Comparison between fission rate calculated by detailed method and simple method	111
6.15	Comparison between energy spectrum of anti-neutrino calculated by detailed method and simple method	111
7.1	History of a total thermal power of electric-power producing reactors in Japan	113
7.2	Nuclear power plants in Japan	114
7.3	Rated thermal efficiencies of Japanese power reactors	116
7.4	Contribution of rated thermal output flux at KamLAND	117
7.5	Reactor operation status	118
7.6	Cycle number distribution of reactor cores	119
7.7	Example of the thermal output at the start-up	120
7.8	Example of the thermal output at the shutdown	121
7.9	Example of the thermal power data of a typical BWR	122
7.10	Comparisons between the electricity generation using KamLAND data and JAIF data	123
7.11	Electricity generation comparisons between the KamLAND data and the JAIF data	124
7.12	Example of the fission rate of each element at a typical reactor	125
7.13	Relative fission reaction rate flux at KamLAND from all Japanese power reactors	126
7.14	Nuclear power stations in South Korea [69]	126
7.15	The time variation of the electricity generation at the Korean nuclear power stations	127
7.16	Map of nuclear power reactors in the world [69]	129
7.17	Contribution from reactors out of japan to thermal output flux	129
7.18	$\bar{\nu}_e$ energy spectra from long lived nuclides	131
7.19	Contribution from long lived nuclides	133
7.20	Contributions from long lived nuclides at KamLAND	134
7.21	The thermal power flux from reactors at KamLAND	135
7.22	The reactor neutrino flux at KamLAND	135
7.23	Time variation of the mean of distance	136
7.24	Expected reactor $\bar{\nu}_e$ energy spectrum	136
7.25	Expected reactor $\bar{\nu}_e$ energy spectrum	137
7.26	Expected reactor $\bar{\nu}_e$ energy spectrum for the long lived nuclides	138
7.27	Time and distance variation of the expected reactor $\bar{\nu}_e$ events at KamLAND	140
8.1	Reactor $\bar{\nu}_e$ flux dependence of the event rate	143
8.2	Observed $\bar{\nu}_e$ event rate versus no-oscillation $\bar{\nu}_e$ event rate	144
8.3	Time dependence of $\bar{\nu}_e$ events	145
8.4	Observed $\bar{\nu}_e$ event rate versus no-oscillation $\bar{\nu}_e$ event rate	146
8.5	Prompt event energy spectrum of $\bar{\nu}_e$ candidate events with associated background spectra	147

8.6	Allowed region of the neutrino oscillation parameter from KamLAND data . . .	148
8.7	Best fit of the scaled no-oscillation spectrum	149
8.8	Ratio of the observed $\bar{\nu}_e$ spectrum to the expectation for no-oscillation versus L_0/E	150
8.9	Combined two-neutrino oscillation analysis of KamLAND and observed solar neutrino fluxes	151

List of Tables

1.1	History of the neutrino physics before KamLAND	2
1.2	Solar neutrino energy in the pp cycle	9
1.3	Recent results from the seven solar-neutrino experiments and a comparison with standard solar-model predictions [29]	12
1.4	Events(Observed/Expected) from reactor $\bar{\nu}_e$ experiments	15
2.1	Ratio of the number of the expected $\bar{\nu}_e$ events for each isotope	23
2.2	Coordinates of KamLAND detector	25
2.3	Element of liquid scintillator for KamLAND [53]	27
2.4	Liquid scintillator and Buffer oil for KamLAND [53]	27
2.5	Neutron capture nuclei	28
2.6	Voltage divider circuit of the 17-inch PMT	30
2.7	Summary of the 17-inch PMT characteristics	30
2.8	Properties of ATWD	33
2.9	Content of radioactive impurities in the balloon structure [51].	35
3.1	Parameters and values for calculation of position dependent visible energy	51
3.2	Correlation of calibration source energy with visible energy E_{vis}	53
3.3	Systematic uncertainty in the energy scale at $E_{\text{prompt}} = 2.6\text{MeV}$	57
4.1	Summary of background estimation	64
4.2	Nuclei emit neutron after β -decays which mimic delayed coincidence signal	68
4.3	Target nuclei of (α, n) reaction [58, 59]	73
4.4	Summary of the $^{13}\text{C}(\alpha, n)^{16}\text{O}$ backgrounds	76
5.1	Summary of measurement periods for the reactor neutrino analysis	78
5.2	Detection efficiency above 2.6 MeV prompt energy threshold	82
5.3	$\bar{\nu}_e$ event reduction	85
6.1	Main components of the U-Pu chain in nuclear fuel	91
6.2	The released energy and available energy per fission with a thermal neutron in ^{235}U [65]	94
6.3	Parameters of BWR and PWR	94
6.4	Constants of the isotopes	97
6.5	Available energy per fission reaction	98
6.6	Typical reactor cores used for the detailed calculation	100
6.7	Reactor data for neutrino flux calculation	100
6.8	Constants of the reference reactor cores for the detailed calculation and the simplified calculation	104

6.9	Correction factors for the absolute burnup at BOC	110
7.1	Handling of each reactor in the fission rate calculation at KamLAND	113
7.2	Power reactors in Japan	115
7.3	Time dependence of the operation data parameters	117
7.4	Operation status of power reactors	119
7.5	Time interval of the operation data	120
7.6	Korean commercial reactors	128
7.7	Fission rate flux at KamLAND from reactors outside of Japan and South Korea.	130
7.8	Long lived nuclides in fission products	131
7.9	Reference of the electricity generation at Japanese power reactors	131
7.10	Yields of fission fragments (in %)[50]	132
7.11	Number of expected events in the absence of anti-neutrino disappearance	137
7.12	Ratio of number of expected events for the long live nuclides	139
7.13	Systematic uncertainties relate to reactors	139
8.1	Systematic uncertainties for $\bar{\nu}_e$ detection above 2.6 MeV prompt energy threshold	141
8.2	Number of $\bar{\nu}_e$ events above $E_{\text{prompt}} = 2.6\text{MeV}$	142
8.3	Fit parameters for the $\bar{\nu}_e$ flux dependence	144
8.4	Fit parameters for the $\bar{\nu}_e$ flux dependence	146
A.1	Japanese research reactors	154
A.2	World reactors	154
A.2	World reactors	155
B.1	Average output of Japanese power reactors	157
B.1	Average output of Japanese power reactors	158
C.1	Converted thermal output of Korean commercial reactors	160

Chapter 1

Introduction

The Kamioka Liquid scintillator Anti-Neutrino Detector (KamLAND) [1] is a low energy $\bar{\nu}_e$ and ν_e detector using ultra-pure liquid scintillator and large photo-cathode photomultiplier tubes. The current main subject of the KamLAND experiment is measurement of neutrino oscillations using reactor $\bar{\nu}_e$'s. By using a long baseline of $\sim 180\text{km}$ and low energy neutrinos, the sensitivity of neutrino mass differences is $\sim 10^{-5}\text{eV}^2$, which includes the LMA solution for the solar neutrino problem. The data taking started on January 22, 2002. By now, KamLAND reported evidence for reactor $\bar{\nu}_e$ disappearance [2] in 2002, and evidence of spectral distortion as $\bar{\nu}_e$ oscillation effects [3] in 2004. In this thesis, neutrino oscillation parameters are determined based on a 766 ton-year exposure of KamLAND between March 9, 2002 and January 11, 2004. The reactor $\bar{\nu}_e$ energy spectrum and expected reactor $\bar{\nu}_e$ events at KamLAND are calculated by tracing time-dependent thermal output data of all Japanese power reactors.

Structure of this thesis is as follows.

- Chapter 1:
Neutrino oscillations and neutrino experiments are reviewed.
- Chapter 2:
The KamLAND experiment is reviewed.
- Chapter 3:
Event reconstruction at KamLAND detector is described.
- Chapter 4:
Background estimation for reactor $\bar{\nu}_e$ search is described.
- Chapter 5:
Selection of reactor $\bar{\nu}_e$ candidates is shown.
- Chapter 6:
Reactors as sources of $\bar{\nu}_e$ are described. Calculation method of the fission rate of each element at Japanese commercial reactors are described.
- Chapter 7:
Expected reactor $\bar{\nu}_e$ events in the analysis period are obtained using the previous method and actual operation data. Contribution from reactors outside of Japan is also investigated.
- Chapter 8:
The expected $\bar{\nu}_e$ events in the absence of oscillations are compared with the observed

events and significance of the $\bar{\nu}_e$ disappearance is obtained. Correlation between the no-oscillation expected event rate and the observed event rate is studied. The best fit values for two flavor neutrino oscillations are determined.

1.1 The neutrino

Neutrinos are neutral elementary particles with a spin of $1/2$. Its existence was predicted by W. Pauli in 1930 [4]. Table 1.1 summarizes history of the neutrino before KamLAND. Anti-neutrinos from reactors were discovered [5] by F. Reines and C. Cowan in 1956 based on the reaction $\bar{\nu}_e + p \rightarrow e^+ + n$. The positron and electron annihilate, giving two simultaneous photons. The neutron is thermalized until it is eventually captured by a Cadmium nucleus, emitting photons some 15μ seconds after the positron signal. These delayed coincidence signals were detected and the existence of the neutrino was confirmed. The neutrinos produced in association with muons were observed [7] at the Brookhaven National Laboratory in 1962 and were found to be different from those produced in association with electrons. This was the discovery of the second type of neutrino, ν_μ . The precise measurement of the decay width of the Z boson in e^+e^- collider at LEP constrains the number of light neutrino families to three [10]. The neutrinos produced in association with tau particles were discovered [11] by DONUT Collaboration in 2000. By now, three flavors of neutrino were observed by experiments and the phenomenon of neutrino oscillations was studied experimentally and theoretically.

1930	W.Pauli made a prediction of neutrino [4].
1956	F.Reines and C.Cowan detected electron antineutrinos from nuclear reactors [5].
1958	The idea of neutrino oscillations was introduced by Pontecorvo [6].
1962	The second type of neutrinos, ν_μ , were observed using an accelerator [7].
1962	The lepton mixing matrix was introduced by Maki, Nakagawa, and Sakata [8].
1987	The neutrino burst from the supernova 1987A was observed at Kamiokande [35].
1991	The number of neutrino flavor is limited to three by LEP [10].
1998	The neutrino oscillations in atmospheric neutrinos were observed at SK [9].
2000	The third type of neutrinos, ν_τ , were observed [11].
2001	The flavor conversion of solar neutrinos were observed at SNO with SK data [12].

Table 1.1: History of the neutrino physics before KamLAND.

In the Standard Model, 6 quarks and 6 leptons, are the constituents of matter. All of these have been discovered experimentally. Each charged lepton (electron, muon, tau) is associated with a neutral lepton or neutrino (ν_e, ν_μ, ν_τ). The quarks are grouped by pairs according to the same rule and so the three generations of leptons and can be written as

$$\begin{pmatrix} \nu_e \\ e \end{pmatrix} \quad \begin{pmatrix} \nu_\mu \\ \mu \end{pmatrix} \quad \begin{pmatrix} \nu_\tau \\ \tau \end{pmatrix} \quad \text{leptons}$$

$$\begin{pmatrix} u \\ d \end{pmatrix} \quad \begin{pmatrix} c \\ s \end{pmatrix} \quad \begin{pmatrix} t \\ b \end{pmatrix} \quad \text{quarks}$$

In the standard model, the neutrino has a zero mass, a zero charge and a spin $1/2$. Because neutrinos are electrically neutral, they are not affected by the electro-magnetic interactions which act on electrons and other charged particles. They are affected only by a weak interaction of much shorter range than electromagnetism, and are therefore able to travel great distances in

matter without interacting. There is no compelling reason why neutrinos should have zero mass (like the photon), and many experiments have tried to find the finite neutrino mass directly by measuring the energy spectrum of tritium β -decays. These experiment could not find finite mass, and the current upper limit for the $\bar{\nu}_e$ mass is 3 eV at 95% C.L. [14]. So, the neutrino mass is lighter than that of the electron by more than five orders of magnitude. This large mass difference between electron and ν_e can not be explained naturally by the standard model, and may imply a new physics.

1.2 Neutrino oscillation

1.2.1 Two flavour neutrino oscillations in vacuum [13]

Generally, the flavor eigenstates $|\nu_\alpha\rangle$ and mass eigenstates $|\nu_i\rangle$ are related by 3×3 unitary matrix U which is called the lepton mixing matrix, or Maki-Nakagawa-Sakata (MNS) matrix as follows

$$|\nu_\alpha\rangle = \sum_i U_{\alpha i} |\nu_i\rangle. \quad (1.1)$$

Assuming initial state at $t = 0$ is $|\nu(t=0)\rangle = |\nu_\alpha\rangle = U_{\alpha j} |\nu_j\rangle$, time evolution of the neutrino state at time t becomes

$$|\nu(t)\rangle = \sum_j U_{\alpha j} e^{-iE_j t} |\nu_j\rangle. \quad (1.2)$$

The matrix amplitude of finding the neutrino in a flavor state $|\nu_\beta\rangle$ at the time t is

$$A(\nu_\alpha \rightarrow \nu_\beta; t) = \langle \nu_\beta | \nu(t) \rangle \quad (1.3)$$

$$= \sum_j U_{\alpha j} e^{-iE_j t} \langle \nu_\beta | \nu_j \rangle = \sum_{i,j} U_{i\beta}^* U_{\alpha j} e^{-iE_j t} \langle \nu_i | \nu_j \rangle = \sum_j U_{j\beta}^* e^{-iE_j t} U_{\alpha j}. \quad (1.4)$$

So that the probability of the transformation of a flavor eigenstate neutrino ν_α into another flavor eigenstate ν_β after time t is given by

$$P(\nu_\alpha \rightarrow \nu_\beta; t) = |A(\nu_\alpha \rightarrow \nu_\beta; t)|^2 = \left| \sum_j U_{j\beta}^* e^{-iE_j t} U_{\alpha j} \right|^2. \quad (1.5)$$

This phenomenon is called ‘‘neutrino oscillation’’ in vacuum.

Let us consider the 2 generation case for simply, ν_α ($\alpha = e, \mu$) and ν_j ($j = 1, 2$). In this case, the lepton mixing matrix U can be expressed by 2×2 matrix as

$$U = \begin{pmatrix} \cos\theta & \sin\theta \\ -\sin\theta & \cos\theta \end{pmatrix} \quad (1.6)$$

where θ is the mixing angle.

Assuming two neutrinos have same momentum p , because neutrino mass m_j is very small compared with its energy, the energy E_j can be expressed as

$$E_j = \sqrt{p^2 + m_j^2} \sim p + \frac{m_j^2}{2p} \sim p + \frac{m_j^2}{2E} \quad (1.7)$$

where, p is the momentum of relativistic neutrinos.

The $\nu_e \rightarrow \nu_e$ survival probability is given as

$$P(\nu_e \rightarrow \nu_e; t) = 1 - P(\nu_e \rightarrow \nu_\mu; t) \quad (1.8)$$

$$= 1 - \sin^2 2\theta \sin^2 \left(\frac{\Delta m^2}{4E} t \right) = 1 - \sin^2 2\theta \sin^2 \left(1.27 \frac{\Delta m^2 (\text{eV}^2) L(\text{m})}{E(\text{MeV})} \right). \quad (1.9)$$

Here, $\Delta m^2 = m_2^2 - m_1^2$.

The first oscillation maximum occurs at

$$l_{\text{osc}}(\text{m}) = \frac{1.24E(\text{MeV})}{\Delta m^2(\text{eV}^2)}. \quad (1.10)$$

1.2.2 Three flavour neutrino oscillations in vacuum [77]

The flavor eigenstates $\nu_\alpha(t)$ and mass eigenstates $\nu_i(t)$ are related by 3×3 unitary matrix U (Maki-Nakagawa-Sakata matrix) as

$$|\nu_\alpha(t)\rangle = \sum_i U_{\alpha i} |\nu_i(t)\rangle. \quad (1.11)$$

The unitary matrix U can be expressed in terms of tree mixing angles θ_{12} , θ_{23} , θ_{13} and one CP violating phase δ in the following standard notation

$$U = \begin{pmatrix} c_{12}c_{13} & s_{12}c_{13} & s_{13}e^{-i\delta} \\ -s_{12}c_{23} - c_{12}s_{23}s_{13}e^{i\delta} & c_{12}c_{23} - s_{12}s_{23}s_{13}e^{i\delta} & s_{23}c_{13} \\ s_{12}s_{23} - c_{12}c_{23}s_{13}e^{i\delta} & -c_{12}s_{23} - s_{12}c_{23}s_{13}e^{i\delta} & c_{23}c_{13} \end{pmatrix}, \quad (1.12)$$

where s_{ij}, c_{ij} stands for $\sin\theta_{ij}, \cos\theta_{ij}$, respectively.

The general probability formula in vacuum is written as

$$\left\{ \begin{array}{l} P(\nu_\alpha \rightarrow \nu_\beta) \\ P(\bar{\nu}_\alpha \rightarrow \bar{\nu}_\beta) \end{array} \right\} = \delta_{\alpha\beta} - 4 \sum_{i < k} \text{Re}(U_{\alpha j} U_{\beta j}^* U_{\alpha k}^* U_{\beta k}) \times \sin^2 \left(\frac{\Delta m_{jk}^2 L}{4E} \right) \quad (1.13)$$

$$\mp 2 \sum_{j < k} \text{Im}(U_{\alpha j} U_{\beta j}^* U_{\alpha k}^* U_{\beta k}) \times \sin \left(\frac{\Delta m_{jk}^2 L}{2E} \right), \quad (1.14)$$

where $\alpha, \beta = e, \mu, \tau$, and the minus and plus signs in front of the $\text{Im}(U_{\alpha j} U_{\beta j}^* U_{\alpha k}^* U_{\beta k})$ term correspond to neutrino and antineutrino channels, respectively. The exact survival probability for $P(\bar{\nu}_e \rightarrow \bar{\nu}_e)$ is given by

$$P(\bar{\nu}_e \rightarrow \bar{\nu}_e) = 1 - \sin^2 2\theta_{13} \sin^2 \frac{\Delta_{31}}{2} \quad (1.15)$$

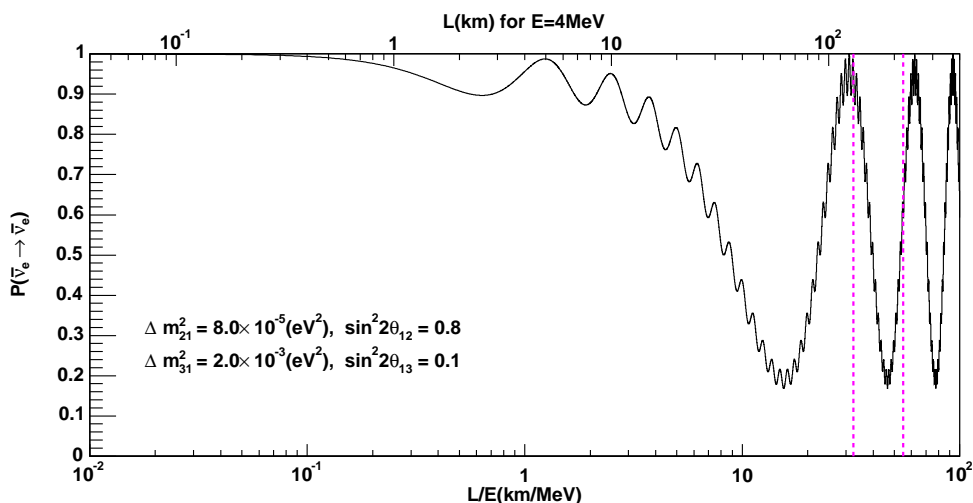
$$+ \frac{1}{2} s_{12}^2 \sin^2 2\theta_{13} \sin \Delta_{31} \sin \Delta_{21} \quad (1.16)$$

$$- (c_{13}^4 \sin^2 2\theta_{12} + s_{12}^2 \sin^2 2\theta_{13} \cos \Delta_{31}) \quad (1.17)$$

$$\times \sin^2 \frac{\Delta_{21}}{2}, \quad (1.18)$$

where,

$$\Delta_{ij} \equiv \frac{\Delta m_{ij}^2 L}{2E}, \quad (1.19)$$

Figure 1.1: Survival probability for $P(\bar{\nu}_e \rightarrow \bar{\nu}_e)$.

and the parametrization (1.12) is used.

The experimental result is $|\Delta m_{12}^2| \ll |\Delta m_{13}^2|$. The best fit value of $|\Delta m_{31}^2|$ is given by $|\Delta m_{31}^2| = 2.5 \times 10^{-3} \text{eV}^2$ [78]. The survival probability (1.18) for specific values is shown in Figure 1.1. In this case, the third and the fifth terms in (1.18) can be ignored. In KamLAND, Δ_{31} is about 50 and $\sin^2 \frac{\Delta_{31}}{2}$ is averaged to 1/2, the equation is simplified to,

$$P(\bar{\nu}_e \rightarrow \bar{\nu}_e) \cong \sin^4 \theta_{13} + \cos^4 \theta_{13} \left(1 - \sin^2 2\theta_{12} \sin^2 \frac{\Delta m_{21}^2 L}{4E} \right). \quad (1.20)$$

The short baseline reactor anti-neutrino experiments with baselines up to 1 km limits $\sin^2 \theta_{13}$ to be quite small, less than 0.03 [15]. In this case, (1.20) is approximated as

$$P(\bar{\nu}_e \rightarrow \bar{\nu}_e) \cong 1 - \sin^2 2\theta_{12} \sin^2 \frac{\Delta m_{21}^2 L}{4E}. \quad (1.21)$$

This implies that oscillations of $\bar{\nu}_e$ on large length can be simplified in terms of two flavors only.

1.2.3 Two flavour neutrino oscillations in matter (MSW effect) [13]

The evolution equation which describes $\nu_e - \nu_\mu$ oscillations in matter is written as

$$i \frac{d}{dt} \begin{pmatrix} \nu_e \\ \nu_\mu \end{pmatrix} = \begin{pmatrix} -\frac{\Delta m^2}{4E} \cos 2\theta_0 + \sqrt{2} G_F N_e & \frac{\Delta m^2}{4E} \sin 2\theta_0 \\ \frac{\Delta m^2}{4E} \sin 2\theta_0 & \frac{\Delta m^2}{4E} \cos 2\theta_0 \end{pmatrix} \begin{pmatrix} \nu_e \\ \nu_\mu \end{pmatrix}, \quad (1.22)$$

where ν_e and ν_μ are time dependent amplitudes of finding the electron and muon neutrino respectively, and N_e is the electron number density. In the case of constant density case, diagonalization of the effective Hamiltonian in (1.22) gives the mass eigenstates in matter

$$\nu_A = \nu_e \cos \theta + \nu_\mu \sin \theta, \quad (1.23)$$

$$\nu_B = -\nu_e \sin \theta + \nu_\mu \cos \theta, \quad (1.24)$$

where θ is the mixing angle in matter. It is given using the mixing angle in vacuum θ_0 and the mass difference Δm^2 as

$$\tan 2\theta = \frac{\frac{\Delta m^2}{2E} \sin 2\theta_0}{\frac{\Delta m^2}{2E} \cos 2\theta_0 - \sqrt{2} G_F N_e}. \quad (1.25)$$

The neutrino energies are written as

$$E_{A,B} = \frac{\sqrt{2}G_F N_e \pm \sqrt{\left(\sqrt{2}G_F N_e - \frac{\Delta m^2}{2E} \cos 2\theta_0\right)^2 + \left(\frac{\Delta m^2}{2E}\right)^2 \sin^2 \theta_0}}{2}. \quad (1.26)$$

Finally the probability of $\nu_e - \nu_\mu$ in matter is written as

$$P(\nu_e \rightarrow \nu_\mu; L) = \sin^2 2\theta \sin^2 \left(\pi \frac{L}{l_m} \right), \quad (1.27)$$

where l_m is the oscillation length in matter

$$l_m = \frac{2\pi}{E_A - E_B} = \frac{2\pi}{\sqrt{\left(\frac{\Delta m^2}{2E} \cos 2\theta_0 - \sqrt{2}G_F N_e\right)^2 + \left(\frac{\Delta m^2}{2E}\right)^2 \sin^2 2\theta_0}}. \quad (1.28)$$

In the low-density limit, θ and l_m approach the vacuum oscillation values.

Figure 1.2 shows the matter effect in KamLAND reactor $\bar{\nu}_e$ analysis [53]. The density of the crust is assumed to be $2.7\text{g}/\text{cm}^3$. For KamLAND LMAI solution, the effect is small. The density varies around 10% in various area in Japan. The 10% difference of the crust density gives 0.5% of difference for the reactor $\bar{\nu}_e$ event rate.

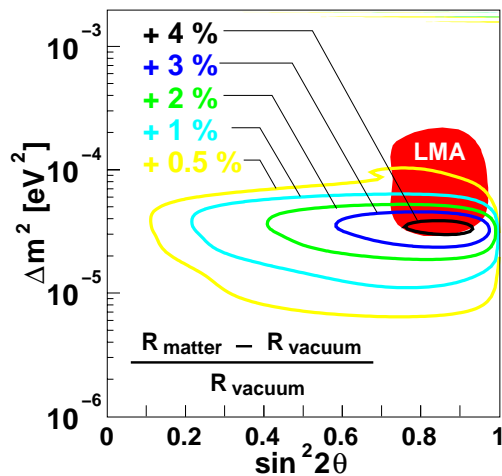


Figure 1.2: Matter effect in KamLAND reactor $\bar{\nu}_e$ analysis [53]. R_{matter} and R_{vacuum} mean reactor $\bar{\nu}_e$ event rate considered with/without matter effect. The density of the crust is assumed to be $2.7\text{g}/\text{cm}^3$.

1.3 Neutrino oscillation experiments

Figure 1.3 summarizes the regions of neutrino oscillation parameter space favored or excluded by various neutrino oscillation experiments including the first result from KamLAND [29]. In this section, these experiments using solar neutrinos, atmospheric neutrinos, accelerator neutrinos, and reactor neutrinos are summarized.

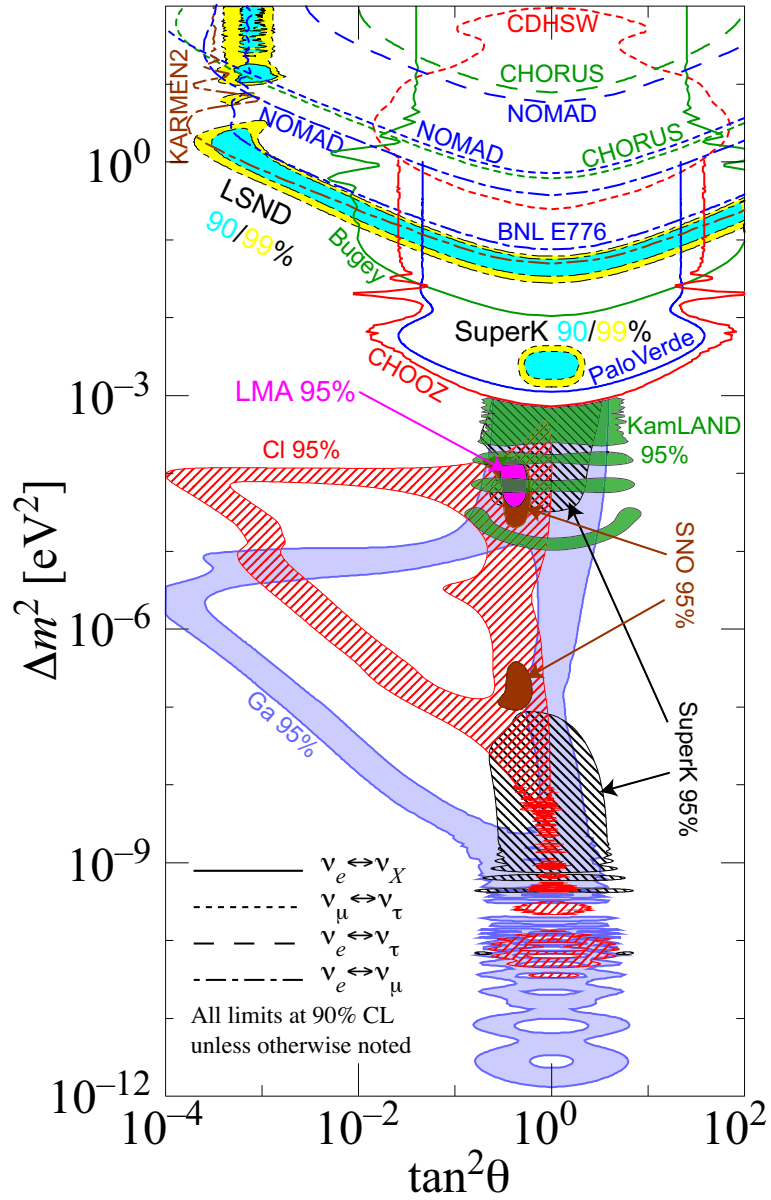


Figure 1.3: The regions of neutrino parameter space favored or excluded by various neutrino oscillation experiments [29]. The first result from KamLAND is also included.

1.3.1 Solar neutrino experiments

Solar Neutrinos

The solar energy is believed to be generated by thermonuclear reactions. These reactions are fusions of four hydrogens into a helium. In these processes energy is generated as γ -rays and two positrons and electron neutrinos are emitted,



According to the Standard Solar Model (SSM), two reaction chains in the sun are known. One is the pp cycle shown in Figure 1.4. These neutrino energy spectra based on the SSM are shown in Figure 1.5 and Table 1.2. Only the ${}^7\text{Be}$ neutrino and pep neutrino which have two body final states have monochromatic energies. The pp neutrinos with continuous energy have dominant contribution in the solar neutrinos, so the solar luminosity and ν_e are directly related and uncertainty of flux calculation is small. Another cycle is the carbon-nitrogen-oxygen (CNO) cycle, which produces helium nuclides from protons using carbon, nitrogen and oxygen nuclides as catalysts. This cycle is dominant in stars having larger mass and higher temperature cores than the sun. The recent results from the seven solar-neutrino experiments and a comparison with standard solar-model predictions [29] are listed in Table 1.3.

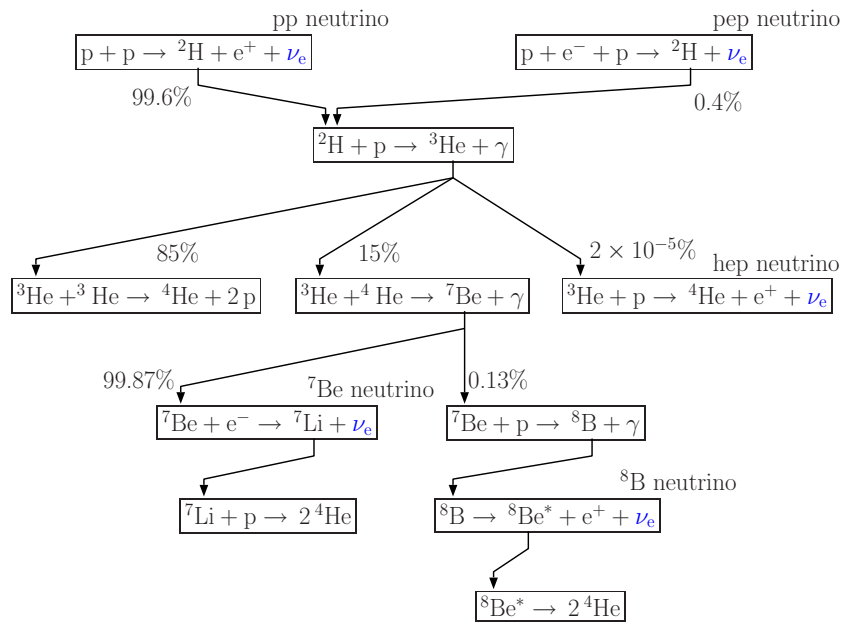


Figure 1.4: Solar neutrino generation in the pp chains.

The Homestake experiment

The first observation of the solar neutrinos was the Homestake [17] experiment, using reactions with ${}^{37}\text{Cl}$,



The ${}^{37}\text{Ar}$ is radioactive and extracted using a chemical method. The energy threshold of the reaction (1.30) is 0.814 MeV and the ${}^8\text{B}$ and pep neutrinos are detected. The solar neutrino

Neutrinos	Fraction	$\langle E_\nu \rangle$ (MeV)	E_ν^{\max} (MeV)
pp	0.909	0.26	0.42
pep	2×10^{-3}	1.44	-
hep	2×10^{-8}	9.62	18.77
^7Be	0.074	0.86 (90%) 0.38 (10%)	-
^8B	8.6×10^{-5}	6.71	~ 15

Table 1.2: Solar neutrino energy in the pp cycle.

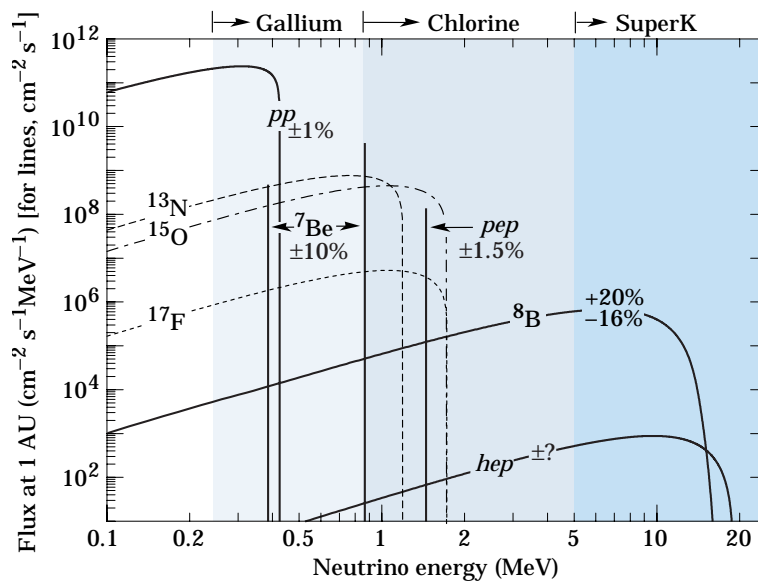


Figure 1.5: Solar neutrino flux predicted by the SSM [29]. The solid lines show neutrinos by the pp cycle. The dashed lines show neutrinos by the CNO cycle. The uncertainties in the fluxes from the various reactions are noted. The thresholds for the different classes of solar neutrino experiments are shown at the top of the figure.

capture rate shown in Table 1.3 is a combined result between 1970 and 1994 [18]. It is only about 1/3 of the BP2000 prediction [16].

The SAGE experiment and GALLEX experiment

Other experiments using radiochemical techniques are SAGE[19] and GALLEX[20]. In these experiments the reaction with ^{71}Ga



is used. The energy threshold of this reaction is 0.234 MeV, and the pp neutrinos are also detected in these experiments. GALLEX presented the observed capture rate is significantly less than the SSM prediction [21]. SAGE observed similar capture rate to that of GALLEX [22].

Kamiokande and Super-Kamiokande

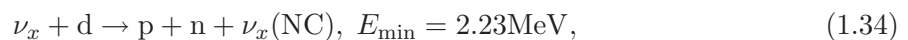
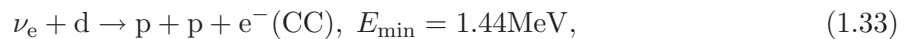
Experiments based on the water Cherenkov detectors are Kamiokande[23] and Super-Kamiokande[24]. These experiments use the neutrino-electron scattering reaction in H_2O ,



The analysis energy threshold is determined by the background rate and energy resolution. The Kamiokande experiment used 7.5 MeV and the Super-Kamiokande experiment uses 5.5 MeV for energy cuts, so only the ^8B neutrinos are detected in these experiments. The angular distributions of the recoil electrons in reaction (1.32) are used for detecting the direction of the neutrinos. This method is real time measurements of neutrinos. The Kamiokande-II Collaboration reported the first direct evidence that the Sun emits neutrinos [25]. The observed solar neutrino flux was also significantly less than the SSM prediction. At Super-Kamiokande, the solar-neutrino flux was measured as a function of zenith angle and recoil-electron energy [26]. The average solar-neutrino flux was smaller than, but consistent with, the Kamiokande-II result [27].

SNO

The SNO (Sudbury Neutrino Observatory)[28] experiment is located at the depth of 6,010 m of water equivalent in the INCO, Ltd. Creighton mine near Sudbury, Ontario in Canada. It detects the ^8B neutrino using a water Cherenkov detector with D_2O . In this experiment, three different reactions with the solar neutrinos as



and (1.32). The CC reaction is sensitive exclusively to electron-type neutrinos, while the NC is sensitive to all active neutrino flavors (ν_e, ν_μ, ν_τ). The ES reaction is sensitive to all flavors as well, but with reduced sensitivity to ν_μ and ν_τ . The CC reaction should directly determine the energy spectrum of the detected ν_e . The incident neutrino energy is related to the energy of the electron by the expression $E_\nu = E_e + 1.442\text{MeV}$. The angular distribution of CC scattering is $(1 - 1/3\cos\theta)$. The CC reaction is distinguished from the ES by this angular distribution. The NC reaction threshold is 2.2 MeV and it is detected by the 6.25 MeV γ -ray from neutron capture on deuterium. Sensitivity to these three reactions allows for the determination of the electron and non-electron active neutrino components of the solar flux.

The SNO reported results for pure D₂O in 2002 [56], as listed in Table 1.3. The fluxes $\phi(\nu_e)$ and $\phi(\nu_{\mu\text{or}\tau})$ deduced from these results were remarkably consistent as can be seen in Figure 1.6.

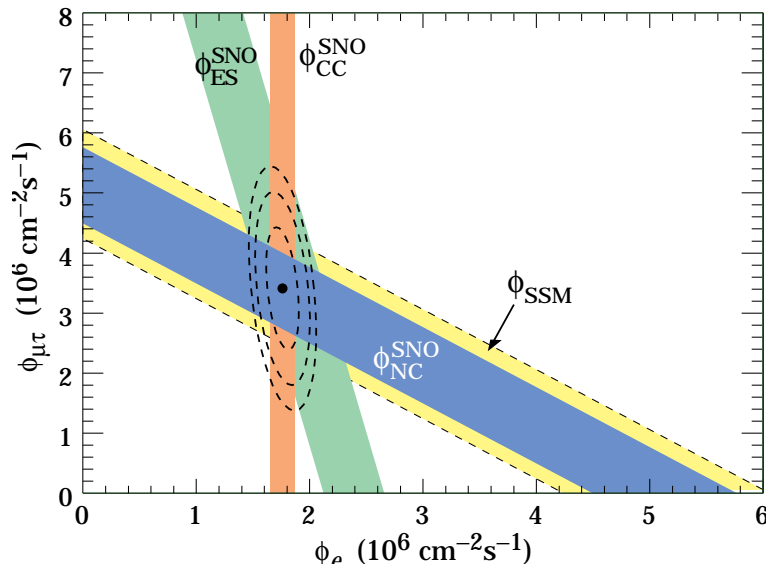


Figure 1.6: Fluxes of ⁸B solar neutrinos [29], $\phi(\nu_e)$, and $\phi(\nu_{\mu\text{or}\tau})$, deduced from the SNO's charged-current, ν_e elastic scattering, and neutral-current results for pure D₂O. The standard solar model prediction is also shown. The bands represent the 1σ error.

Solar global analysis

In September, 2003, SNO reported [57] results on the observed solar neutrino fluxes with NaCl added in heavy water: this improved the sensitivity for the detection of the NC reaction. Figure 1.7 shows the global analysis with the solar neutrino experiments [57]. This result constrains the allowed region of the LMA solution.

1.3.2 Atmospheric neutrino experiments

At the top of the earth's atmosphere, π 's are produced by reactions between primary cosmic rays and the nitrogen and oxygen nuclides. Atmospheric neutrinos are produced from pions and daughter muons

$$\pi^\pm(K^\pm) \rightarrow \mu^\pm + \nu_\mu(\bar{\nu}_\mu) \quad (1.35)$$

$$\mu^\pm \rightarrow e^\pm + \nu_e(\bar{\nu}_e) + \bar{\nu}_\mu(\nu_\mu). \quad (1.36)$$

Then, the number of atmospheric neutrinos are expected to be $\nu_\mu : \nu_e = 2 : 1$. In underground detectors, these neutrinos are observed using leptons created by the charged current interactions

$$\nu_e(\bar{\nu}_e) + A \rightarrow e^-(e^+) + X, \quad (1.37)$$

$$\nu_\mu(\bar{\nu}_\mu) + A \rightarrow \mu^-(\mu^+) + X. \quad (1.38)$$

Experiment	$^{37}\text{Cl} \rightarrow ^{37}\text{Ar}$ (SNU)	$^{71}\text{Ga} \rightarrow ^{71}\text{Ge}$ (SNU)	$^8\text{B}\nu$ flux ($10^6\text{cm}^{-2}/\text{s}^{-1}$)
Homestake	$2.56 \pm 0.16 \pm 0.16$		
GALLEX		$77.5 \pm 6.2^{+4.3}_{-4.7}$	
GNO		$65.8^{+10.2+3.4}_{-9.6-3.6}$	
SAGE		$70.8^{+5.3+3.7}_{-5.2-3.2}$	
Kamiokande			$2.80 \pm 0.19 \pm 0.33$ (ES)
Super-Kamiokande			$2.35 \pm 0.03^{+0.07}_{-0.06}$ (ES)
SNO (pure D ₂ O)			$1.76^{+0.06}_{-0.05} \pm 0.09$ (CC)
			$2.39^{+0.24}_{-0.23} \pm 0.12$ (ES)
			$5.09^{+0.44+0.46}_{-0.43-0.43}$ (NC)
SNO (NaCl in D ₂ O)			$1.59^{+0.08+0.06}_{-0.07-0.08}$ (CC)
			$2.21^{+0.31}_{-0.26} \pm 0.10$ (ES)
			$5.21 \pm 0.27 \pm 0.38$ (NC)
(BAHCALL)	$7.6^{+1.3}_{-1.1}$	128^{+9}_{-7}	$5.05(1.00^{+0.20}_{-0.16})$
(TURCK-CHIEZE)	7.44 ± 0.96	127.8 ± 8.6	4.95 ± 0.72

Table 1.3: Recent results from the seven solar-neutrino experiments and a comparison with standard solar-model predictions [29]

The zenith angle and the path length of neutrinos is obtained by the direction of the leptons. According to four experiments, IMB[31], Soudan 2[32], Kamiokande[33], and Super-Kamiokande[34], the ν_μ/ν_e ratio has been confirmed to be about 60%. The anomalous zenith-angle dependence of the atmospheric ν_μ and ν_e fluxes was first observed in Kamiokande, and has now been confirmed with much better statistical significance by Super-Kamiokande. In 1998, the discovery of neutrino oscillations was reported by the Super-Kamiokande collaboration. The distribution for ν_e agrees reasonably well with Monte Carlo calculations, but the upward ν_μ flux, which travels an extra distance of the earth's diameter relative to the downward flux, exhibits the pronounced deficit shown in Figure 1.8. The deficit and its variation with zenith angle is explained beautifully by $\nu_\mu - \nu_\tau$ oscillations, the case for which has only strengthened with updated results [86]. The confidence levels in $\Delta m^2 - \sin^2 2\theta$ parameter space for the neutrino oscillation fit to the Super-Kamiokande data is shown in Figure 1.9. The best fit point is at $\Delta m_{\text{atm}}^2 = 2.4 \times 10^{-3} \text{eV}^2$, $\sin^2 2\theta_{\text{atm}} = 1.0$.

1.3.3 Accelerator neutrino experiments

The neutrinos coming from the decay $\mu^+ \rightarrow e^+ \nu_e \bar{\nu}_\mu$ from μ^+ at rest were studied by the Liquid Scintillator Neutrino Detector (LSND) experiment [36]. While this decay does not include $\bar{\nu}_e$, an excess of $\bar{\nu}_e p \rightarrow e^+ n$ scattering was observed above the expected background. This excess is interpreted as due to oscillation of some of the $\bar{\nu}_\mu$ produced by μ^+ decay into $\bar{\nu}_e$. The corresponding allowed regions for oscillation parameters are shown in Figure 1.3. The related KARlsruhe Rutherford Medium Energy Neutrino (KARMEN) experiment sees no indication for such an excess and doesn't confirm the LSND experiment [37]. The preferred region from LSND is restricted by this result (labeled as KARMEN2). LSND result must be confirmed or refuted by other experiments such as MiniBooNE [38].

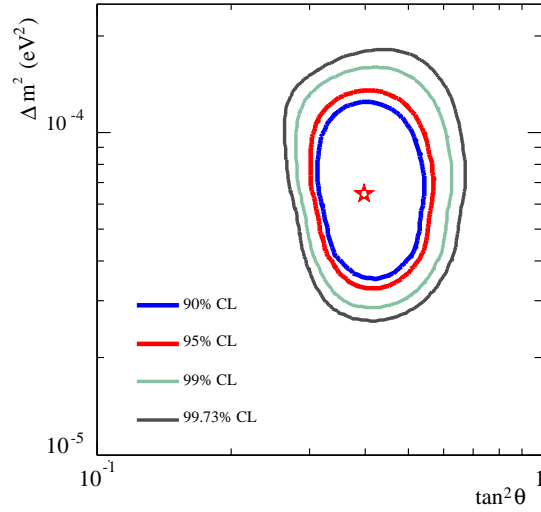


Figure 1.7: Solar neutrino global analysis [57]. This region corresponds to the LMA solution. The best-fit point is at $\Delta m^2 = 6.5 \times 10^{-5} eV^2$, $\tan^2\theta = 0.40$.

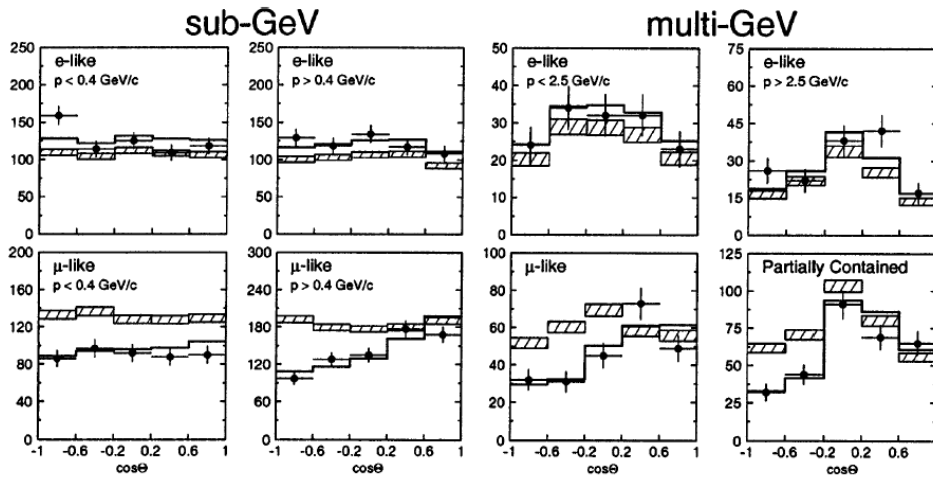


Figure 1.8: Zenith angle distributions of μ -like and e -like events for sub-GeV and multi-GeV data sets [9].

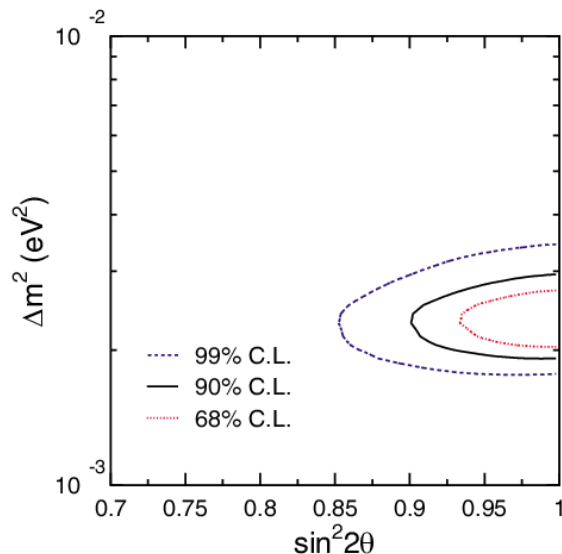


Figure 1.9: Allowed oscillation parameter regions for 2-flavor $\nu_\mu \leftrightarrow \nu_\tau$ oscillations [86].

1.3.4 Reactor $\bar{\nu}_e$ experiments

Nuclear reactors produce isotropically $\bar{\nu}_e$'s in the β -decay of neutron-fission fragments. The reactor neutrinos are produced and exposed at nuclear power plant as products of β -decay processes so that the reactor neutrinos are pure anti-electron neutrinos at production point. The low energy ($\sim O\text{MeV}$) of the reactor $\bar{\nu}_e$ makes them ideal for exploring oscillations with small mass differences and relatively large mixing angles. Since these neutrinos have a relatively low energy spectrum and low flux compared with solar neutrinos, all of the existing experiments which detect reactor neutrinos utilize liquid scintillator as a target and detect the signals induced by inverse β -decay process, having the relatively large cross section,

$$\bar{\nu}_e + p \rightarrow e^+ + n \quad (1.39)$$

$$\leftrightarrow n + p \rightarrow d + \gamma. \quad (1.40)$$

This reaction has a threshold of about 1.8 MeV. We can identify this process to detect the first scintillation light induced by positron and delayed γ -ray.

The reactor neutrino does not have sufficient energy to produce muons (or taus), and the neutral current reactions of the “oscillated” $\bar{\nu}_\mu$ or $\bar{\nu}_\tau$ have small cross sections and are indistinguishable from the many backgrounds present. So, we can only detect the anti-electron neutrino (disappearance). The reactor anti-neutrino flux and spectrum measured at a given distance L can be readily compared with the expectation at $L = 0$, thus testing the disappearance of $\bar{\nu}_e$. To identify the neutrino oscillation, the accurate determination of a deficit of events accompanied by a distortion of the $\bar{\nu}_e$ spectrum is essential.

A number of experiments using reactor $\bar{\nu}_e$'s to search for neutrino oscillations had been performed before KamLAND as listed in Table 1.4. At these experiments, neutrino disappearance was not found. By adjusting the baseline, we can obtain various information about oscillation parameters. Bugey [46] used baselines of 15, 40 and 95m. We can consider the measurement of the short baseline experiments as the direct determination of the reactor $\bar{\nu}_e$ spectrum. In case that the baseline length is chosen $O(1 \text{ km})$, the sensitivity of Δm^2 is comparable to $O(10^{-3} \text{ eV}^2)$.

Experiment	Baseline	Result
Palo Verde	0.75-0.89km	$1.01 \pm 0.024 \pm 0.053$
Palo Verde	0.75-0.89km	$1.04 \pm 0.03 \pm 0.08$
CHOOZ	1km	$1.01 \pm 0.028 \pm 0.027$
Bugey	15m	$0.988 \pm 0.004 \pm 0.05$
Bugey	15m	$0.987 \pm 0.014 \pm 0.027$
Bugey	40m	$0.994 \pm 0.010 \pm 0.05$
Bugey	95m	$0.915 \pm 0.132 \pm 0.05$

Table 1.4: Events(Observed/Expected) from reactor $\bar{\nu}_e$ experiments [29].

Two recent experiments, Chooz [48] and Palo Verde [49], used baselines of about 1km. These experiments are sensitive to the neutrino mass differences associated with the atmospheric neutrino. On the other hand, in case that the baseline length is chosen $O(100 \text{ km})$, the sensitivity of Δm^2 is comparable to $O(10^{-5} \text{ eV}^2)$.

Short baseline $L \sim O(1\text{km})$ experiments

The current data on neutrino oscillations suggest the need to include at least three neutrino flavors when studying results from experiments. The most general approach would involve five unknown parameters: three mixing angles and two independent mass differences. However, an intermediate approach consists of a simple generalization of the two-flavor scenario, assuming that $m_3^2 \gg m_1^2, m_2^2$ (i.e., $\Delta m_{13}^2 = \Delta m_{23}^2 = \Delta m^2$, while $\Delta m_{12}^2 \simeq 0$). This scenario is obviously compatible with the evidence based on the atmospheric neutrino anomaly ($\Delta m^2 \sim 3 \times 10^{-3} \text{ eV}^2$) and the solar neutrino deficit ($\Delta m^2 < 10^{-4} \text{ eV}^2$). In such a case the mixing angle θ_{12} becomes irrelevant, and one is left with only three unknown quantities; Δm^2 , θ_{13} , and θ_{23} . With this parametrization and assuming CPT symmetry, the $\bar{\nu}_e$ disappearance is written by

$$P(\bar{\nu}_e \rightarrow \bar{\nu}_x) = \sin^2 2\theta_{13} \sin^2 \frac{\Delta m^2 L}{4E_\nu}, \quad (1.41)$$

while $\nu_\mu \rightarrow \nu_\tau$ oscillations, responsible for the atmospheric neutrino results in this scenario, are described by

$$P(\nu_\mu \rightarrow \nu_\tau) = \cos^4 \theta_{13} \sin^2 2\theta_{23} \sin^2 \frac{\Delta m^2 L}{4E_\nu}. \quad (1.42)$$

Here the reactor-based neutrino oscillation experiments play a decisive role. The determination of the angle θ_{13} has obvious importance not only for the structure of the lepton mixing matrix U but for the observability of CP violation in the lepton sector.

Long baseline $L \sim O(100\text{km})$ experiments

The feature of long baseline (dominant of Δm_{12}^2 term) and low energy (no matter effect) reduce the disappearance probability as

$$P(\bar{\nu}_e \rightarrow \bar{\nu}_e) \sim \cos^4 \theta_{13} \left(1 - \sin^2 2\theta_{12} \sin^2 \frac{\Delta_{12}}{2} L \right) + \sin^4 \theta_{13} \quad (1.43)$$

$$\sim 1 - \sin^2 2\theta_{12} \sin^2 \frac{\Delta_{12}}{2} L. \quad (1.44)$$

According to (1.44), a condition for the minimum survival probability of reactor $\bar{\nu}_e$'s is written as

$$\Delta m^2(\text{eV}^2) = \frac{\pi}{2 \times 1.27} \cdot \frac{E(\text{MeV})}{L(\text{m})}. \quad (1.45)$$

In the case of reactor $\bar{\nu}_e$ experiments, $\langle E \rangle \sim 4\text{MeV}$, so in case of LMA solution is permitted to deviate from 1.

1.4 KamLAND experiment

Figure 1.10 shows locations of 18 nuclear power stations in Japan, including two prototype reactors. At these nuclear power stations there were 53 operatable power reactors, including one prototype reactor, when KamLAND started data taking in January 2002. Figure 1.11 shows distance distribution of the thermal output flux at KamLAND. Thermal outputs within the distance range $175 \pm 45\text{km}$ from KamLAND, which is 69 GW, have about half contribution to the total thermal output flux. According to (1.10), the sensitivity of Δm^2 for $\sim 180\text{km}$ is $\sim 10^{-5}\text{eV}^2$. This region includes the parameters of the LMA solution of the solar neutrino problem. Therefore, KamLAND has sensitivity to distortion of energy spectrum as well as deficit of $\bar{\nu}_e$ flux for the oscillation parameters in the LMA region. Figure 1.12 shows the expected sensitivity of KamLAND for various oscillation parameters in the LMA region. In this figure, the solid lines correspond to 5% systematic error and the dashed lines are 10% systematic error. The regions for the mass-squared difference are not so changed, but those for the mixing angle are affected because the number of events depend on the mixing angle directly. So, KamLAND can determine the solar neutrino problem using reactor $\bar{\nu}_e$'s. Figure 1.13 shows systematic error dependence of the significance for the neutrino disappearance for a specific event ratio. In this figure, the total systematic uncertainty is divided for the detector and the expected event calculation, and the detector systematics are assumed to be 5.5%. One can see the significance becomes worse for larger uncertainties than the detector systematics. According to these indications, the reactor $\bar{\nu}_e$ spectrum are required to be calculated more precisely than the detector systematics. The detail of the reactor $\bar{\nu}_e$ calculation is also described in this thesis.

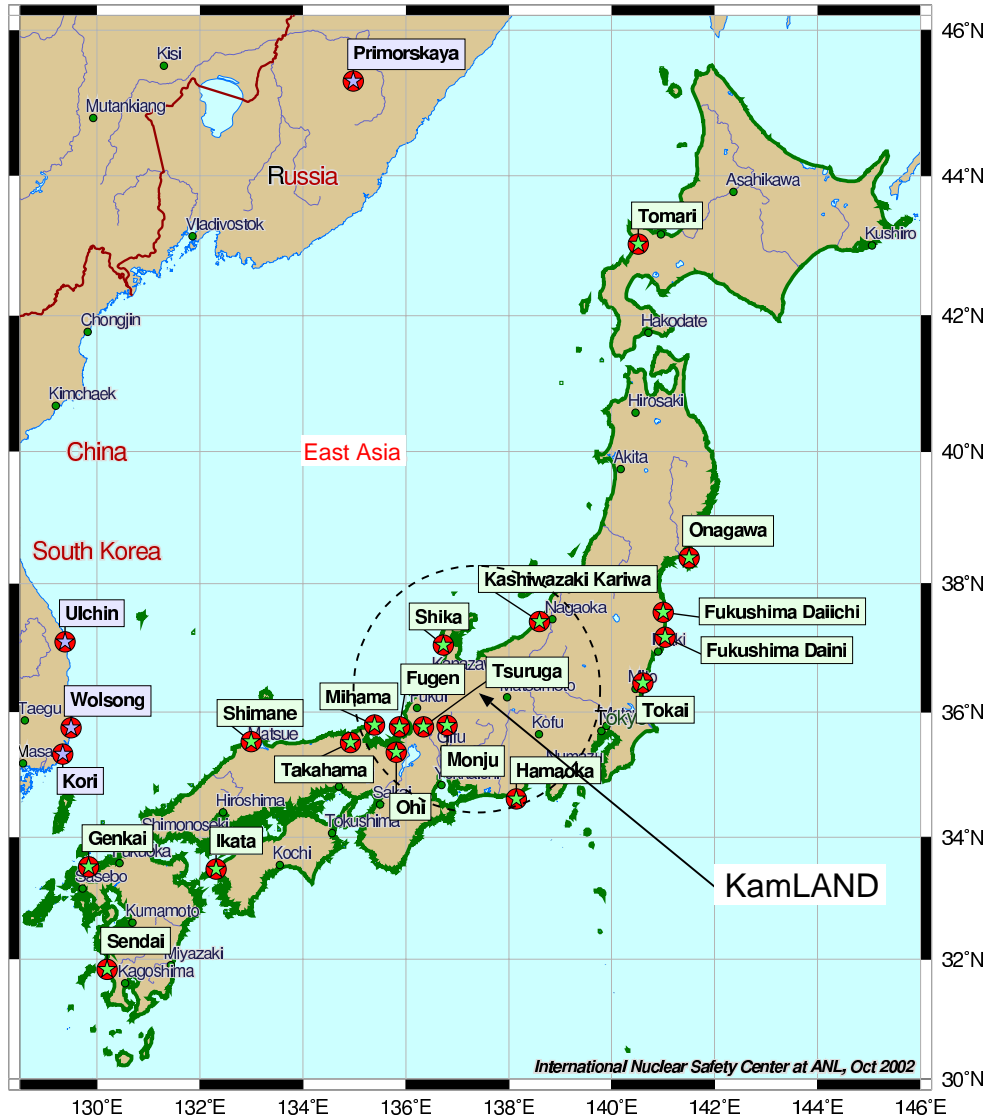


Figure 1.10: Map of Nuclear power reactors in Japan [69]. Some reactor locations may not represent the exact geographic location. At the end of January 2004, 52 commercial reactors in 16 power stations had been operatable. A prototype fast breeder reactor “Monju” has been under construction in 2004. Another prototype advanced thermal reactor “Fugen” ceased its operation in March 2003. The dashed circle corresponds to a distance of ~ 210 km from KamLAND.

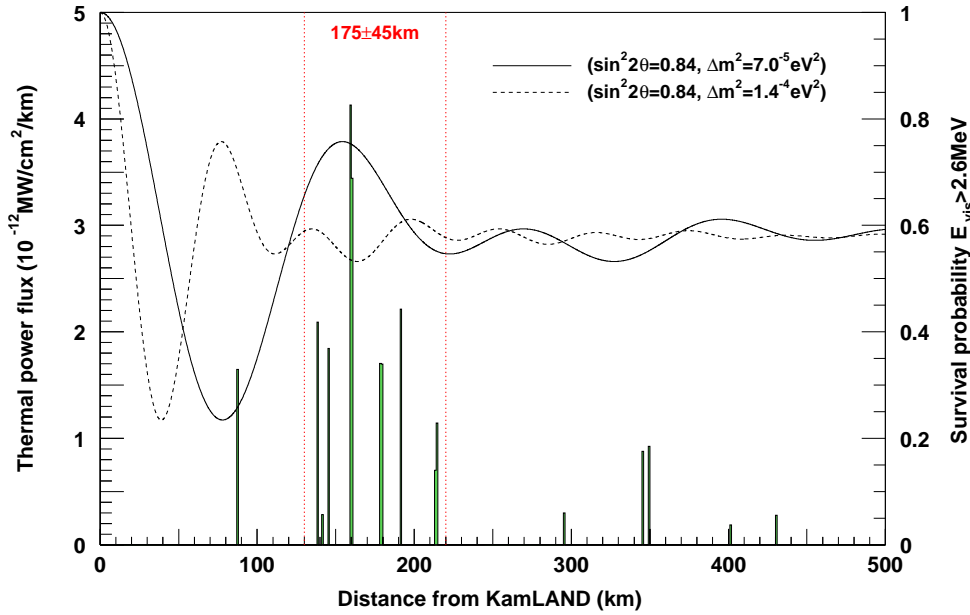


Figure 1.11: The reactor distance distribution for the thermal output flux at KamLAND. The solid curve is a survival probability of $\bar{\nu}_e$'s for typical parameters in the LMAI region. The dotted curve is for the LMAII region.

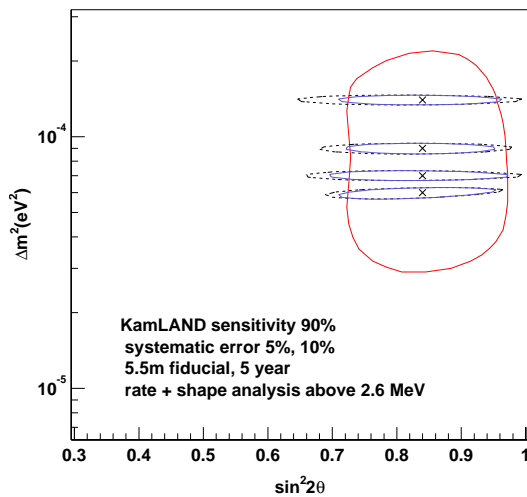


Figure 1.12: Sensitivity of KamLAND. Four islands are 90% allowed regions if oscillation parameters are at the cross points. The solid lines correspond to 5% systematic error and the dashed lines are 10%. The 95% allowed region of the LMA solution [39] before KamLAND is also shown.

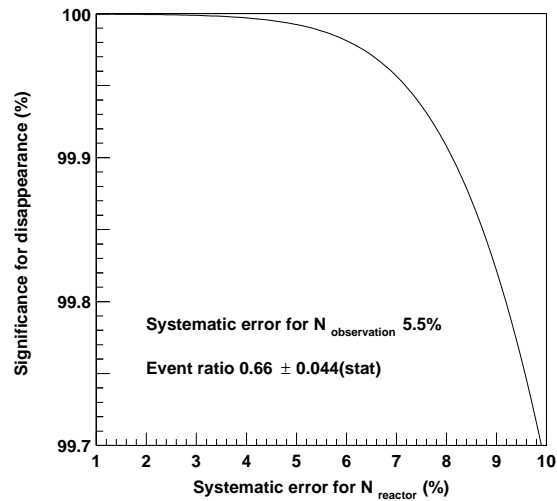


Figure 1.13: Statistical significance for the reactor neutrino disappearance as a function of the uncertainty of the expected number of reactor $\bar{\nu}_e$ events. The 5.5% detector systematics and specific event ratio are assumed.

Chapter 2

KamLAND experiment

The KamLAND detector was constructed in the Kamioka Mine in Kamioka Town, Hida City, Gifu Prefecture. It is a low energy $\bar{\nu}_e$ and ν_e detector using ultra-pure liquid scintillator and large photo-cathode photomultiplier tubes. The data taking started on January 22, 2002. The current main subject of the KamLAND experiment is to study the reactor $\bar{\nu}_e$'s.

In the section 2.1, $\bar{\nu}_e$ detection method using inverse β -decay reaction is described. In 2.2, a feature of the location of the KamLAND detector is shown. In 2.3, components of the detector are summarized.

2.1 Anti-neutrino detection method

2.1.1 Delayed coincidence technique

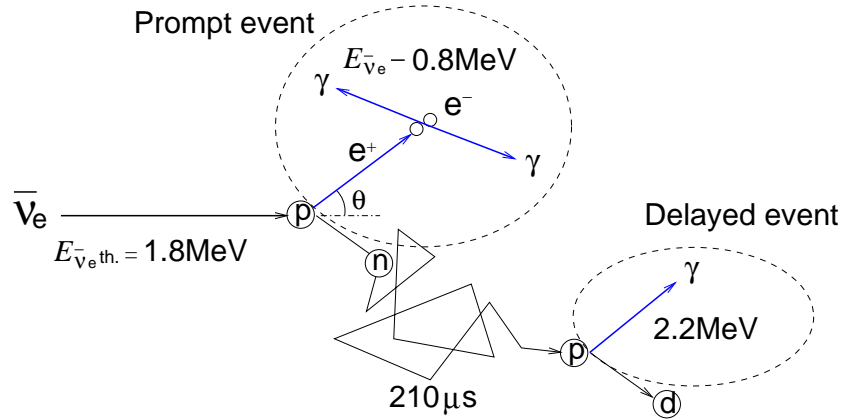


Figure 2.1: Delayed coincidence technique.

Electron anti-neutrinos are detected via inverse β -decay reaction,

$$\bar{\nu}_e + p \rightarrow e^+ + n, \quad (2.1)$$

in liquid scintillator (Figure 2.1). The $\bar{\nu}_e$ energy threshold of this interaction is approximately 1.8 MeV which comes from the mass difference of the neutron and the proton ($\Delta_{np} = 1.293 \text{ MeV}$)

and positron mass ($m_e = 0.511\text{MeV}$). The positron deposits its kinetic energy in the liquid scintillator by excitation and ionization and produces 2 γ -rays via pair annihilation;

$$e^+ + e^- \rightarrow 2\gamma(2 \times 0.511\text{MeV}). \quad (2.2)$$

The prompt event signal consists of the scintillation light from the energy deposition of the positron and annihilation γ -rays. The delayed event signal is the scintillation light comes from 2.2 MeV γ -ray from neutron capture on proton. The detection of the prompt event and the delayed event within a delayed time window and spacial correlation is an efficient tool to reduce the background.

Energy of prompt signal

The positron energy in the inverse β -decay reaction E_{e^+} is written as

$$E_{e^+} = E_{\bar{\nu}_e} - \Delta - T_n(\theta), \quad (2.3)$$

where $E_{\bar{\nu}_e}$ is the neutrino energy and $\Delta = M_n - M_p = 1.293\text{MeV}$ is the mass difference between the neutron and proton. $T_n(\theta)$ is the neutron kinetic energy with the scattering angle of the positron θ . Then, the energy of prompt signal is written as

$$E_{\text{prompt}} = E_{e^+} + m_e \quad (2.4)$$

$$= E_{\bar{\nu}_e} - \Delta + m_e - T_n(\theta) \quad (2.5)$$

$$= E_{\bar{\nu}_e} - 0.782\text{MeV} - T_n(\theta) \quad (2.6)$$

$$\approx E_{\bar{\nu}_e} - 0.78\text{MeV}. \quad (2.7)$$

Typically $T_n \sim \text{keV}$, and it's small compared with energy resolution of KamLAND detector. So, E_{prompt} has direct correspondence with $E_{\bar{\nu}_e}$.

2.1.2 Positron energy and cross section of the inverse β -decay reaction [42]

At zeroth order in $E_{\bar{\nu}_e}/M$, the positron energy is

$$E_e^{(0)} = E_{\bar{\nu}_e} - \Delta. \quad (2.8)$$

The differential cross section of the inverse β -decay is expressed as

$$\left(\frac{d\sigma}{d\cos\theta} \right)^{(0)} = \frac{\sigma_0}{2} \left[(f^2 + 3g^2) + (f^2 - g^2)v_e^{(0)}\cos\theta \right] E_e^{(0)} p_e^{(0)}, \quad (2.9)$$

where $v_e = p_e/E_e$ is the velocity of the positron, and the vector and axial-vector coupling constants are $f = 1$ and $g = 1.26$, and σ_0 is the normalizing constant, including the energy independent inner radiative corrections $\Delta_{\text{inner}}^{\text{R}}$,

$$\sigma_0 = \frac{G_F^2 \cos^2\theta_c}{\pi} (1 + \Delta_{\text{inner}}^{\text{R}}), \quad (2.10)$$

where G_F is the Fermi coupling constant, Cabibbo angle is $\cos\theta_c = 0.974$ and $\Delta_{\text{inner}}^{\text{R}} \simeq 0.024$.

The total cross section

$$\sigma_{\text{tot}}^{(0)} = \sigma_0 (f^2 + 3g^2) E_e^{(0)} p_e^{(0)} \quad (2.11)$$

$$= 0.0952 \left(\frac{E_e^{(0)} p_e^{(0)}}{1\text{MeV}^2} \right) 10^{-42} \text{cm}^2. \quad (2.12)$$

Because the energy-independent inner radiative corrections affect the neutron beta decay $n \rightarrow p + e^- + \bar{\nu}_e$ rate in the same way, the total cross section can also be written,

$$\sigma_{\text{tot}}^{(0)} = \frac{2\pi^2}{m_e^5 f^R \tau_n} E_e^{(0)} p_e^{(0)}, \quad (2.13)$$

where $\tau_n = 885.7 \pm 0.8\text{s}$ [44] is the measured neutron lifetime and $f^R = 1.7152$ is the phase space factor, including the Coulomb, weak magnetism, recoil, and outer radiative corrections, but not the inner radiative corrections.

At first order in $E_{\bar{\nu}_e}/M$, the positron energy depends upon the scattering angle as,

$$E_e^{(1)} = E_e^{(0)} \left[1 - \frac{E_{\bar{\nu}_e}}{M} \left(1 - v_e^{(0)} \cos\theta \right) \right] - \frac{y^2}{M}, \quad (2.14)$$

where, θ is the angle between the anti-neutrino and positron directions, and $y^2 = (\Delta^2 - m_e^2)/2$. For M the average nucleon mass is used. Using $1/M$ versus $1/M_p$ leads to an ignorable difference of $O((E_{\bar{\nu}_e}/M)^2)$.

The differential cross section at this order is

$$\left(\frac{d\sigma}{d\cos\theta} \right)^{(1)} = \frac{\sigma_0}{2} [(f^2 + 3g^2) + (f^2 - g^2)v_e^{(1)} \cos\theta] E_e^{(1)} p_e^{(1)} - \frac{\sigma_0}{2} \left[\frac{\Gamma}{M} \right] E_e^{(0)} p_e^{(0)}, \quad (2.15)$$

where

$$\begin{aligned} \Gamma = & 2(f + f_2)g \left[\left(2E_e^{(0)} + \Delta \right) \left(1 - v_e^{(0)} \cos\theta \right) - \frac{m_e^2}{E_e^{(0)}} \right] \\ & + (f^2 + g^2) \left[\Delta \left(1 + v_e^{(0)} \cos\theta \right) + \frac{m_e^2}{E_e^{(0)}} \right] \\ & + (f^2 + 3g^2) \left[\left(E_e^{(0)} + \Delta \right) \left(1 - \frac{1}{v_e^{(0)}} \cos\theta \right) - \Delta \right] \\ & + (f^2 - g^2) \left[\left(E_e + \Delta \right) \left(1 - \frac{1}{v_e^{(0)}} \cos\theta \right) - \Delta \right] v_e^{(0)} \cos\theta, \end{aligned} \quad (2.16)$$

the anomalous nucleon isovector magnetic moment is $f_2 = \mu_p - \mu_n = 3.706$.

The total cross section is written as,

$$\sigma(E_{\bar{\nu}_e}) = \left[\int_{-1}^1 \left(\frac{d\sigma(E_{\bar{\nu}_e})}{d\cos\theta} \right)^{(1)} d\cos\theta \right] \cdot \left(1 + \delta_{\text{outer}}^{\text{rad}} \right), \quad (2.17)$$

where, $\delta_{\text{outer}}^{\text{rad}}$ is the energy dependent outer radiative corrections to the total cross section are given by Ref. [43]. The dominant uncertainty of the cross section is the 0.1% error in τ_n . The total uncertainty after the corrections is 0.2% [43].

The energy threshold of the inverse β -decay in the laboratory frame is

$$E_{\bar{\nu}_e}^{\text{thr}} = \frac{(M_n + m_e)^2 - M_p^2}{2M_p} = 1.806\text{MeV}. \quad (2.18)$$

The $\bar{\nu}_e$ energy is calculated from the positron energy as

$$E_{\bar{\nu}_e} \simeq (E_e + \Delta) \left[1 + \frac{E_e}{M_e} \right] + \frac{\Delta^2 - m_e^2}{M_p}, \quad (2.19)$$

where $\cos\theta = 0$ is used as a good approximation of the average $\langle \cos\theta \rangle$.

2.1.3 Observed energy spectrum

The number of expected reactor $\bar{\nu}_e$ events is written as

$$N_{\text{expected, total livetime}} \equiv \int dE_{\bar{\nu}_e} n(E_{\bar{\nu}_e}) \quad (2.20)$$

$$= \int dE_{\text{prompt}} \frac{dE_{\bar{\nu}_e}(E_{\text{prompt}})}{dE_{\text{prompt}}} n(E_{\bar{\nu}_e}(E_{\text{prompt}})), \quad (2.21)$$

where the differential part is written by using (2.19) as

$$\frac{dE_{\bar{\nu}_e}}{dE_{\text{prompt}}} = 1 + \frac{2(E_{\text{prompt}} - m_e) + \Delta}{M}. \quad (2.22)$$

$n(E_{\bar{\nu}_e}(E_{\text{prompt}}))$ is the energy spectrum of the expected event. It is written using the number of target protons N_p , the cross section for the inverse β -decay reaction $\sigma(E_{\bar{\nu}_e})$, the detection efficiency $\varepsilon_{\text{detection}}$ and the $\bar{\nu}_e$ energy spectrum from all sources $\Psi(E_{\bar{\nu}_e})$ as,

$$n(E_{\bar{\nu}_e}) = N_p \sigma(E_{\bar{\nu}_e}) \varepsilon_{\text{detection}} \Psi(E_{\bar{\nu}_e}). \quad (2.23)$$

Figure 2.2 shows the energy spectrum of $\sigma(E_{\bar{\nu}_e})$, and typical $\Psi(E_{\bar{\nu}_e})$ (a.u.) and $n(E_{\bar{\nu}_e})$ (a.u.).

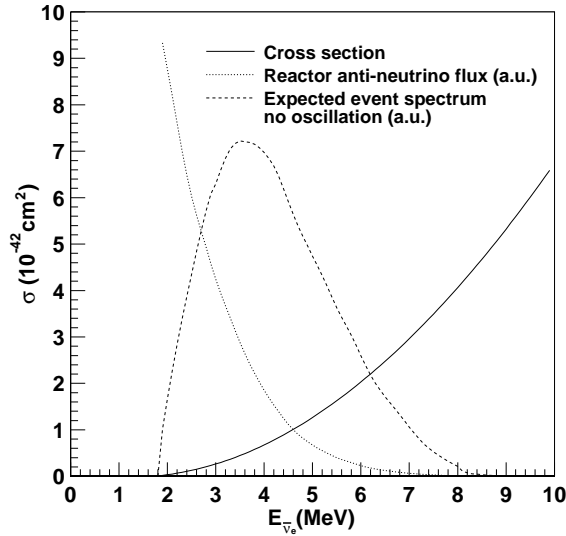


Figure 2.2: Observed spectrum calculated with the $\bar{\nu}_e$ spectrum and the cross section.

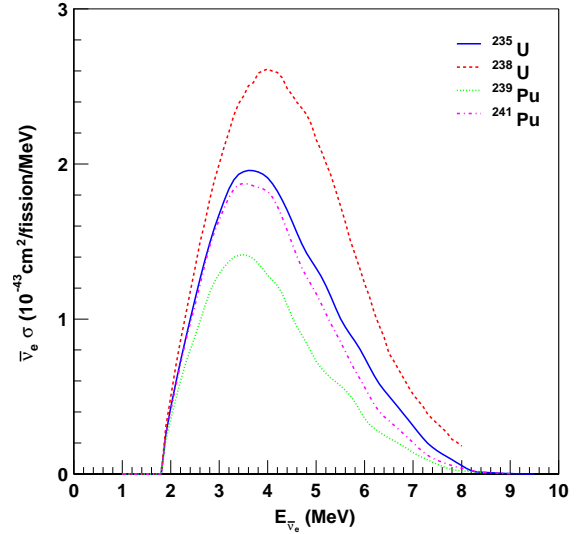


Figure 2.3: Observed spectrum for the $\bar{\nu}_e$ spectrum of each isotope per fission reaction.

At the KamLAND experiment, the total $\bar{\nu}_e$ energy spectrum $\Psi(E_{\bar{\nu}_e})$ is given as the summation of the contribution from each reactor,

$$\begin{aligned} \Psi(E_{\bar{\nu}_e}) &= \sum_{\text{reactor}} \frac{1 - P(\Delta m^2, \sin^2 2\theta, E_{\bar{\nu}_e}, L_{\text{reactor}})}{4\pi L_{\text{reactor}}^2} \\ &\times \sum_{\text{isotope}} \psi_{\text{isotope}}(E_{\bar{\nu}_e}) \int_{\text{total livetime}} dt f_{\text{reactor, isotope}}(t), \end{aligned} \quad (2.24)$$

where P is the neutrino oscillation probability written as (1.9), $\psi_{\text{isotope}}(E_{\bar{\nu}_e})$ is the $\bar{\nu}_e$ energy spectrum per fission at each fissile isotope and $f_{\text{reactor, isotope}}(t)$ is the fission reaction rate of each isotope and each reactor. The detail of the $\bar{\nu}_e$ spectrum is described in 6.1. Figure 2.3 shows the observed energy spectrum per fission at each fissile isotope.

The total neutrino flux is treated in this analysis as the summation with the all run time with weight of livetime efficiency η_{run} ,

$$\int_{\text{total livetime}} dt f_{\text{reactor, isotope}}(t) = \sum_{\text{run}} \eta_{\text{run}} \int_{\text{run time}} dt f_{\text{reactor, isotope}}(t), \quad (2.25)$$

where the livetime efficiency of each run is defined as the livetime divided by the run time.

At the KamLAND experiment, a prompt event energy analysis threshold of 2.6MeV is applied to avoid background $\bar{\nu}_e$'s from uranium and thorium decaying in the Earth (geo-neutrinos, Figure 2.4). Ratio of the number of expected reactor $\bar{\nu}_e$ events for $E_{\text{prompt}} > 2.6\text{MeV}$ in the Figure 2.3 is listed in Table 2.1. The observed energy spectrum is obviously effected by composition of the fissile isotopes.

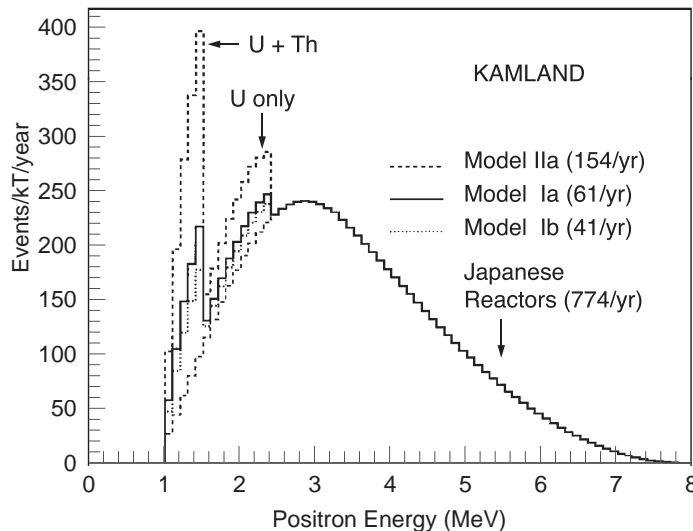


Figure 2.4: Expected reactor $\bar{\nu}_e$ energy spectrum with contributions of geo-neutrinos [30].

Isotope	^{235}U	^{238}U	^{239}Pu	^{241}Pu
Ratio	1.00	1.52	0.60	0.87

Table 2.1: Ratio of number of the expected $\bar{\nu}_e$ events for each isotope to that of ^{235}U . The energy range is $2.6\text{MeV} < E_{\text{prompt}} < 8.0\text{MeV}$.

2.2 Location of KamLAND

KamLAND is located at the site of the earlier Kamiokande, where is in the Kamioka Mine in Kamioka Town, Hida City, Gifu Prefecture. The Kamioka Mine is operated by Kamioka Mining

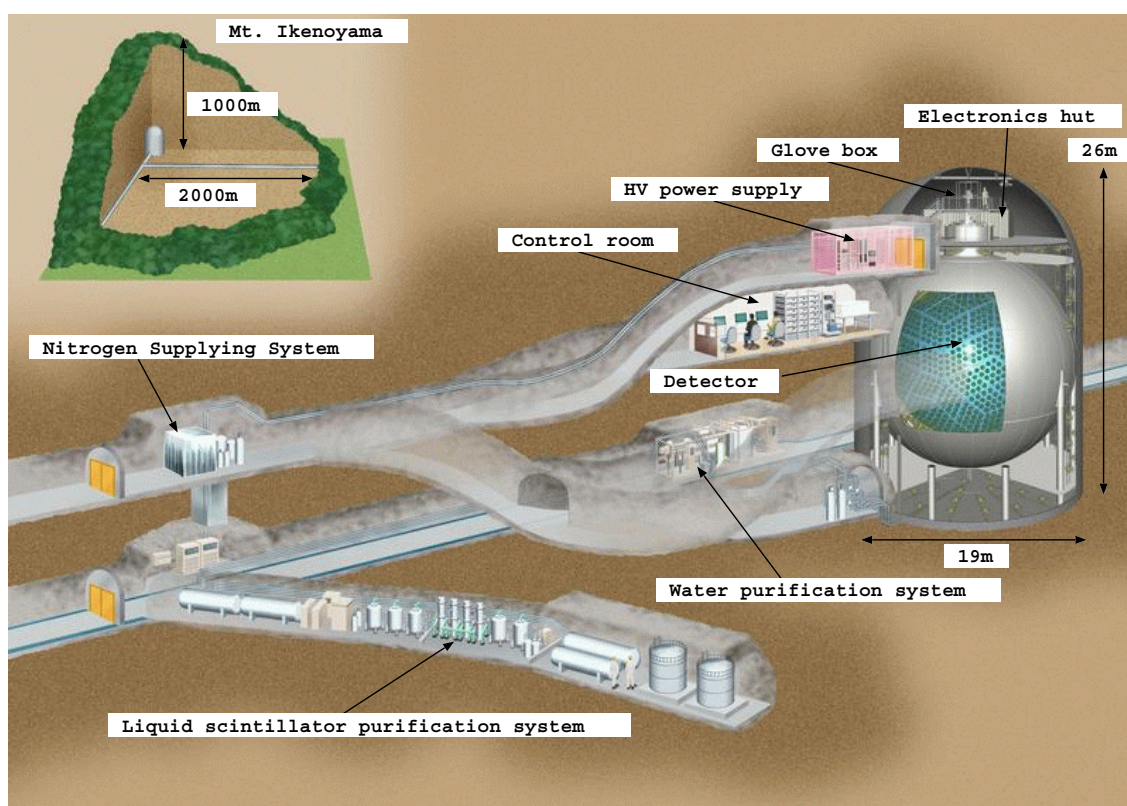


Figure 2.5: KamLAND Detector.

and Smelting Company. Figure 2.5 shows the schematic view of KamLAND. The detector has an elevation of 350m, and it lies nearly under the summit of Mt. Ikenoyama, 1350m high. The detector has a rock overburden of about 1000m in the vertical direction.

2.2.1 Coordinates of KamLAND

The coordinates of KamLAND detector in the Japan-19 Plane Orthogonal were provided by Kamioka Mining and Smelting Co., Ltd. After April 2002, the Japanese Geodetic Datum2000 and the GRS80 Ellipsoid are standard coordinate system and ellipsoid in Japan. The coordinates in the orthogonal coordinate system based on this coordinate system and ellipsoid were calculated by using coordinate transformation programs provided by the Geographical Survey Institute of the Ministry of Land, Infrastructure and Transport as Table 2.2.

Coordinate system and Ellipsoid	Coordinates		
	(X,Y) or (Latitude, Longitude)	Orthometric height	
Japan-19 Plane Orthogonal	VII-Plane	358.114m	
	X		46988.548m
	Y		13309.227m
Tokyo Datum, Bessel Ellipsoid	lat. 36°25'24.44462" N	358.114m	
	long. 137°18'54.39025" E		
Japanese Geodetic Datum2000 (ITRF94), GRS80 Ellipsoid	lat. 36°25'35.56182" N	358.114m	
	long. 137°18'43.49535" E		
	X		-3776988.520m
	Y		3483830.328m
	Z	3766616.070m	

Table 2.2: Coordinates of KamLAND detector.

2.3 Detector design

Figure 2.6 shows the sideview of KamLAND. At the center of the detector, 1 kton of ultrapure liquid scintillator is contained in a 13-m-diameter spherical balloon. A buffer oil in a 18-m-diameter spherical stainless-steel containment vessel is surrounding the balloon. An array of 1879 photomultiplier tubes (PMTs), mounted on the inner surface of the containment vessel, completes the inner detector (ID) system. A 3-mm-thick acrylic barrier at 16.6-m diameter helps to prevent radon emanating from PMT glass from entering the liquid scintillator. The containment vessel is surrounded by a 3.2 kton water-Cherenkov detector with 225 20-inch PMTs.

2.3.1 Liquid scintillator and buffer oil

The liquid scintillator for KamLAND which was made from three components shown in Table 2.3 provides the required properties as follows. Because the liquid scintillator is contained in 13-m-diameter spherical balloon, the attenuation length for the scintillation light is required to be longer than this. To detect the low energy neutrino events, a high light output and low content of the radioactive impurities are required. Long term stability and high flash point are also required.

The paraffin oil, represented as C_nH_{2n+2} , has high optical clarity for the scintillation light and high H/C ratio. Dodecane is used for the main component of the KamLAND liquid scintillator. Pseudocumene (1,2,4-Trimethylbenzene) is used to increase the scintillation light output. PPO

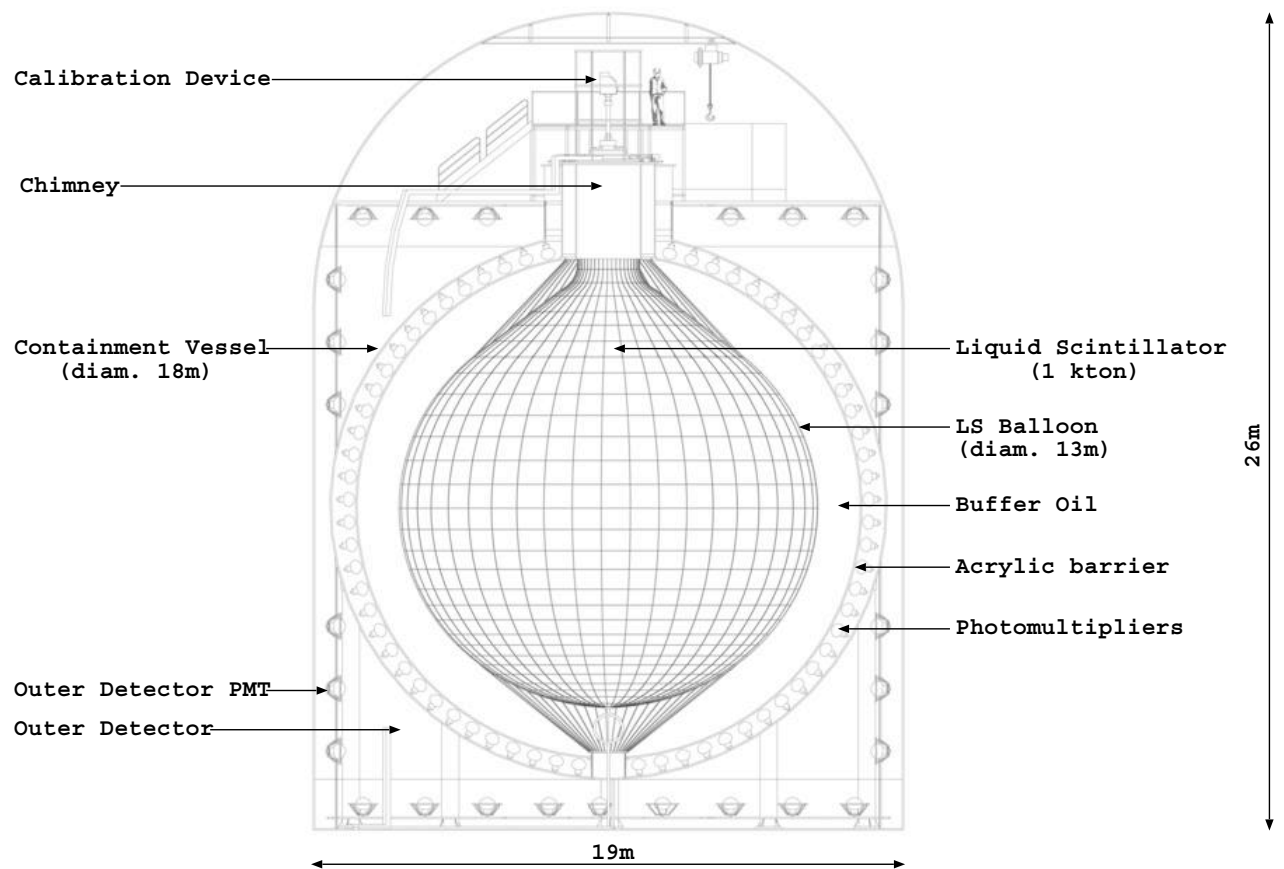


Figure 2.6: Sideview of KamLAND detector.

(2,5-Diphenyloxazole) is the common solute as a fluor. The characteristic of the liquid scintillator is shown in Table 2.4. The light output is 49 % anthracene and the light yield is about 300 p.e. per MeV when a signal occurs at the center of the detector.

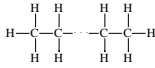
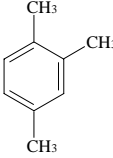
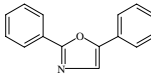
Parameters	Solvent			Solute
	Dodecane	Isoparaffin	Pseudocumene 1,2,4-Trimethylbenzene	PPO 2,5-Diphenyloxazole
Structure	$C_{12}H_{26}$ 	$C_nH_{2n+2}(n \sim 15)$	C_9H_{12} 	$C_{15}H_{11}NO$ 
Specific gravity (@ 15°C)	0.7526	0.7958	0.8796	-
Refractive index (@ 15°C, $\lambda = 589\text{nm}$)	1.4217	1.4410	1.5049	-
Flash point (°C)	83	78	54	-
Composition in LS	80.2%	-	19.8%	1.52g/l
Composition in BO	53%	47%	-	-

Table 2.3: Element of liquid scintillator for KamLAND [53].

In the outside of the liquid scintillator, non-scintillator oil (buffer oil) of a mixture of dodecane and isoparaffin oils is filled for absorbing external radiation. The specific gravity of the buffer oil is controlled to be 0.04% lighter than the liquid scintillator to cancel the weight and to keep the spherical shape of the liquid scintillator in a balloon (Table 2.4). During the filling procedure a water extraction and nitrogen bubbling method was used to purify the liquid scintillator and buffer oil.

	Liquid scintillator	Buffer oil
Liquid yield (p.e./MeV)	~ 300 @ center	-
Liquid output (% Anthracene)	49	-
Attenuation length (m @400nm)	~ 10	-
Specific density (g/cm ³ @ 15°C)	0.77754 ± 0.00010	0.77732 ± 0.00010
Refractive index (@ 14°C, $\lambda = 590\text{nm}$)	1.44087 ± 0.00015	1.43532 ± 0.00013
Flash point (°C) (Design value)	64	≥ 78

Table 2.4: Liquid scintillator and Buffer oil for KamLAND [53].

Number of target protons

The temperature of the liquid scintillator in the detector and the temperature coefficient of density expansion are 11.5°C and $7.41 \times 10^{-4}\text{g/cm}^3/\text{K}$ respectively. The fiducial mass corresponds to a 5.5m fiducial volume cut is 0.5437kton. The number of free target protons is 4.61×10^{31} in

the fiducial mass with a 99.985% natural abundance of ^1H (8.469×10^{31} atom/kton) and 30ppm of H_2O concentration in the liquid scintillator (2.0×10^{27} atom/kton).

Neutron capture on proton

The neutron from the inverse β -decay reaction is captured by not only protons but also other isotopes. The γ 's energies and capture probabilities are summarized in Table 2.5. The total probability of the neutron captured on protons is 99.48%.

Isotope	Cross section (barn)	γ energy (MeV)	Probability
^1H	0.332	2.22457	1
^2H	0.0005	6.2574	2.26×10^{-7}
^{12}C	0.0034	4.9468	5.15×10^{-3}
^{13}C	0.0009	8.1762	1.51×10^{-5}
^{14}N	0.0750	10.8348	4.23×10^{-5}
^{16}O	0.0002	4.1425	5.01×10^{-8}

Table 2.5: Neutron capture nuclei. The cross section and probability for neutron capture on isotopes are listed.

2.3.2 PMTs

The liquid scintillator of the central detector is surrounded by 1879 photomultiplier tubes (PMTs) mounted on the inner surface of an 18-m-diameter spherical stainless-steel vessel. These PMTs include 1325 specially developed fast PMTs with 17-inch-diameter photocathodes and 554 older Kamiokande 20-inch PMTs [54].

17-inch PMTs

To improve the timing resolution and the peak to valley ratio, a 17-inch PMT (R7250 from Hamamatsu) was developed based on the 20-inch PMT. Figures 2.7 and 2.8 show schematic views of the 17-inch PMT and 20-inch PMT. The characteristic of the 17-inch PMT and the installation procedure in the detector is described here.

The main components of the PMT is the photocathode, electron multiplier (dynode) and voltage divider circuit. Like the 20-inch PMT, the photocathode of the 17-inch PMT is the bialkali photocathode (Sb-K-Cs), which has a spectral response fits the spectra of the scintillation light. The outside region of the photocathode is disadvantageous for the photoelectron collection efficiency and the timing response. So, the photon acceptance of the 17-inch PMT is masked and reduced to the central 17 inches of the photocathode. The dynode of the 20-inch PMT is the venetian blind type, which has large size dynodes and generally used for the large photocathode PMT. On the other hand, the dynodes of the 17-inch PMT consist of one stage of box type and nine stages of linear focused type. The box type dynode has excellent photoelectron collection efficiency, and the linear focused type dynode has excellent timing response. Figure 2.9 and Table 2.6 show the voltage divider circuit of the 17-inch PMT. When the large light pulse is inputted in PMTs, current flows through the voltage divider and the effect of voltage losses is caused. To prevent saturation of the output current due to this effect, resistances of the 17-inch PMT are increased in the last few stages (R10-12). The total value of the resistances between the photocathode and the high voltage power supply is $5.35\text{M}\Omega$. The circuit of the

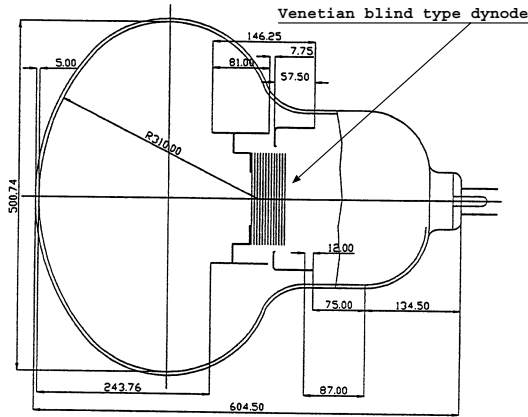


Figure 2.7: R3250 20-inch PMT from Hamamatsu.

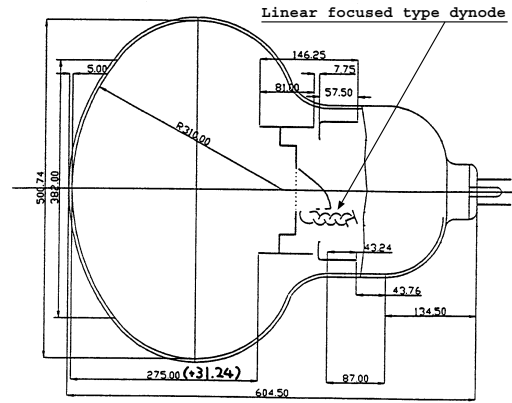


Figure 2.8: R7250 17-inch PMT from Hamamatsu.

voltage divider is connected to the base of the PMT and installed in an oil-proof housing made of acrylic (Figure 2.10).

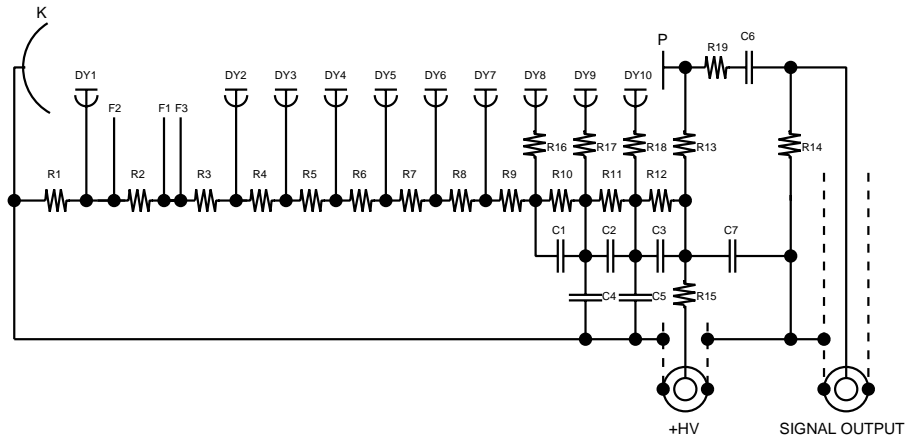


Figure 2.9: Circuit diagram of the voltage divider in the 17-inch PMT.

Parameters Table 2.7 shows parameters of the 17-inch PMT. Figure 2.11 shows the wavelength dependence of the quantum efficiency of the 17-inch PMT. The maximum spectral response is around 350-400nm.

The gain G for the one photoelectron of the PMT having N dynode stages is written as

$$G = \delta^N = (A \cdot E^\alpha)^N \sim \left(A \cdot \left(\frac{V}{A+1} \right)^\alpha \right)^N = K \cdot V^b, \quad (2.26)$$

where δ is the secondary electron emission ratio, A , K and b are constants, E is an interstage voltage, V is a voltage applied between the cathode and the anode of the PMT, and α is a coefficient determined by the dynode material and geometric structure. For the 17-inch PMT, b is ~ 6.5 .

Electrode	K	Dy1-F2	F1-3	Dy2	Dy3	Dy4	Dy5	Dy6	Dy7	Dy8	Dy9	Dy10	P
Resistance		R1	R2	R3	R4	R5	R6	R7	R8	R9	R10	R11	R12
Voltage division ratio		18.5	0.6	3.4	5	3.3	1.7	1	1	1	2	3	4
Resistance(k Ω)		2220	72	408	600	396	204	120	120	120	240	360	480
Resistance										R16	R17	R18	R13
Resistance(Ω)										50	50	50	100k
Condenser		C1~3	C4-5	C6-7						Resistance	R15	R19	R14
Capacity(F)		10n	1000p	4700p						Resistance(Ω)	10k	75	50

Table 2.6: Voltage divider circuit of the 17-inch PMT.

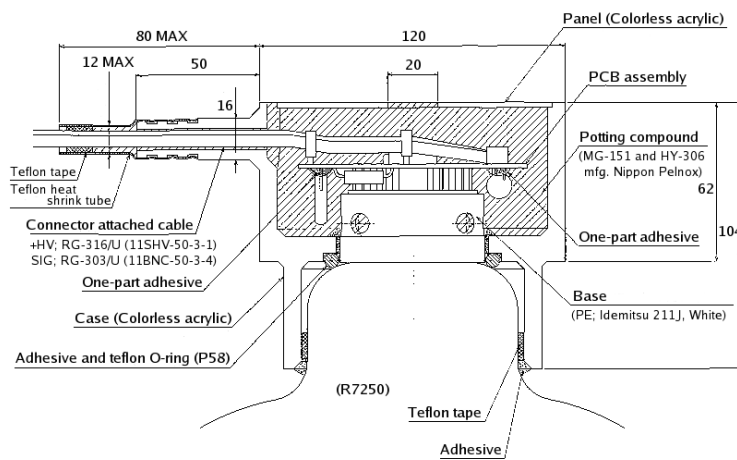


Figure 2.10: Oil-proof housing of 17inch PMT.

Parameters	Characteristics
Photocathode diameter	20 inches(ϕ 508mm)
Valid photocathode diameter	17 inches(ϕ 430mm)
Dynode structure	one stage of Box and 9 stages of Linear focused
Input window material	Borosilicate glass
Photocathode material	Bialkali
Spectral response range	300nm - 650nm
Maximum spectral response	420nm
Rise time(@ 1×10^7 Gain)	7ns
Electron transit time(")	110ns
Transit time spread (@ 1×10^7 Gain,1pe,full surface)FWHM	3.5ns

Table 2.7: Summary of the 17-inch PMT characteristics.

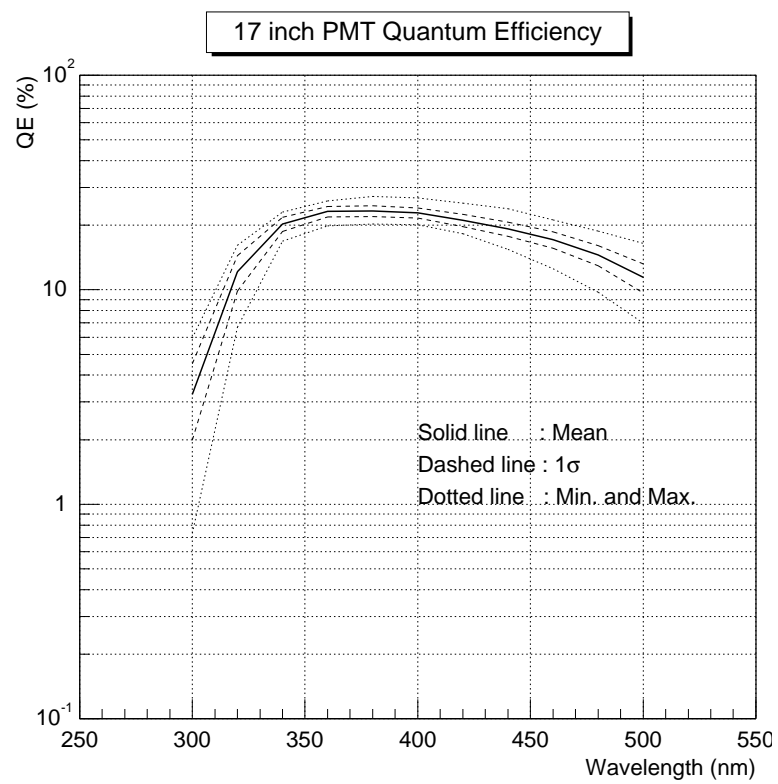


Figure 2.11: Quantum efficiency of 17inch PMTs.

A peak-valley ratio is defined as the ratio of the pulse height for one p.e. signal and valley located between the signal amplitude and dark current. The peak-valley ratio of the 17-inch PMT is ~ 4 , so the output pulse peak by one photoelectron can be determined from noise events.

TTS (Transit Time Spread) is defined as the FWHM of the electron transit time distribution. It effects the resolution of the event vertex determination in the detector. TTS depends on the number of incident photons. For the 17-inch PMT with linear focused type dynodes, TTS is about 4.4ns (FWHM, @1p.e.).

Installation of PMTs in the detector

The inner surface of the 18-m-diameter spherical stainless-steel vessel is divided into 30 diamond-shaped regions by stainless-steel frames. Each PMT was installed in a stainless-steel support and mounted on the surface by bolts. In a diamond-shaped region, 64 17-inch and 20-inch PMTs are mounted uniformly. To shield photocathodes from the light coming from outside, light shields are installed between PMTs.

Geomagnetic field eraser

To cancel the Earth’s magnetic field that causes decrease of the output levels of the PMTs, a set of compensating coils are embedded in the cavity walls. The remaining magnetic field at the position of PMTs is less than 50 mGauss. According to a prior measurement, the decrease of the output charges in this magnetic field is less than $\sim 8\%$ [55].

2.3.3 Front-End Electronics(FEE)

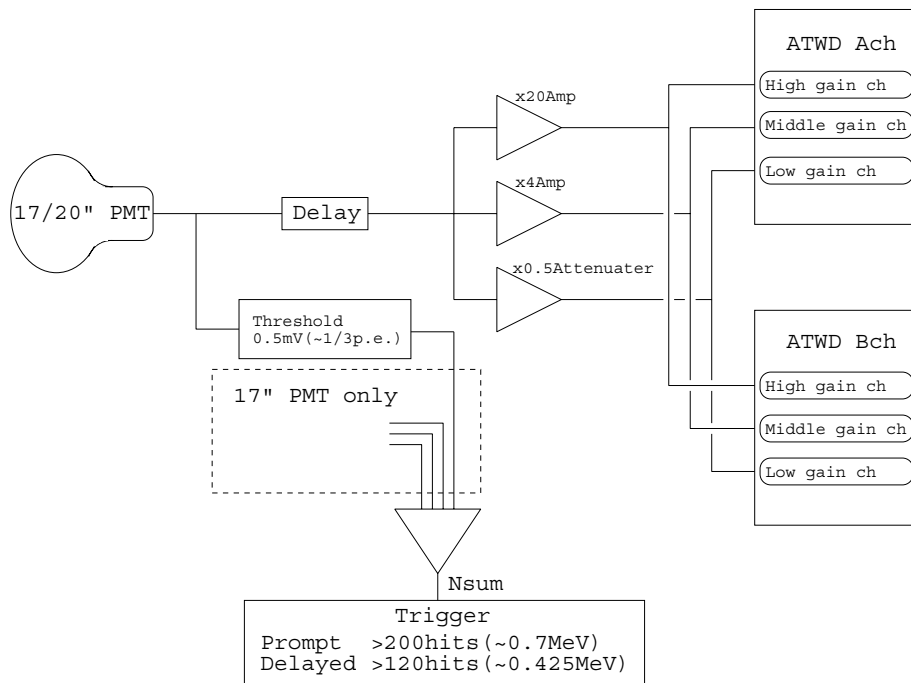


Figure 2.12: Schematic diagram of the front-end electronics.

The front-end electronics (FEE) for KamLAND is based on the Analog Transient Waveform Digitizers (ATWD). A schematic diagram of the front-end electronics is shown in Figure 2.12. One FEE board has 12 input channels for PMT signals.

An output signal from PMT is discriminated by the threshold adjusted to about 1/3 p.e. pulse height. The total number of the discriminated 17-inch PMTs (Nsum) is used for event triggers. The primary (prompt) trigger threshold is set at 200 PMT hits, corresponding to about 0.7MeV. This threshold is lowered to 120 hits, corresponding to about 0.4MeV for 1 msec after the primary trigger to observe lower energy delayed event.

To realize a large dynamic range required from thousands photoelectrons typically due to cosmic ray muon events to single photoelectron due to low energy neutrino events, each PMT channel has three different amplifiers. The highest gain is 20 times and designed for detecting single photoelectron events. Almost all events except for muon events have low energy, so this gain is used normally. The middle gain is 4 times and the lowest gain designed for muon events attenuates signals to 0.5 times.

To reduce dead time caused by digitizing signals, each PMT channel has two identical ATWD chips (A channel and B channel) connected from three amplifiers. Second ATWD is available to capture a waveform if the first one is busy.

Item	Value
Number of input channels	4
	High gain: $\times 20$
	Medium gain: $\times 4$
	Low gain: $\times 0.5$
	Clock: 40 MHz
Number of sampling channels	128
Sampling rate	670 MHz
ADC type	common-ramp 128 Wilkinson 10-bit
Clock for ADC	40 MHz

Table 2.8: Properties of ATWD

Each ATWD has four independent input channels which always acquire data in parallel. Some characteristics of ATWD is shown in Table 2.8. The four input channels correspond to the three different gains and an input for 40MHz test pulse used for a time interval calibration.

Acquisition of an input waveform is started by a discriminator signal on an array of 128. The acquisition of a waveform takes place in real time. A total time window is about 200ns and the time interval between each sample is approximately 1.5 ns. The time interval for each channel is calibrated at the beginning of each run using an internal 40MHz test pulse.

The ATWD chip has a common-ramp parallel Wilkinson 10-bit ADC (Analog-to-Digital Converter). When the trigger system sends a command, the stored voltages, not integrated charge, on arrays are converted to digital values. Each count of ADC for the high gain is approximately $120\mu\text{V}/\text{bit}$. Digitizing entire 128 samples of a waveform takes approximately $25\mu\text{sec}$ per gain channel. If the waveform from a higher gain saturates due to a large input pulse, the next gain is digitized.

2.3.4 Trigger system

Trigger command

The trigger system issues a 5 bit trigger command to the FEE. The trigger commands are separated to global trigger or forced trigger. The global trigger is decided based on the 4 bit NSUM information (the number of PMTs whose output level is higher than discriminator threshold) sent from each FEE board in normal data taking. When the global trigger is issued, the acquired waveforms are digitized. On the other hand, the forced trigger mode, mainly designed for calibration, forces both acquisition and digitization regardless of discriminator signals. The trigger information for each event is recorded.

Prompt and delayed trigger commands

For normal physics data taking, the basic global trigger is a prompt trigger and a delayed trigger. The prompt trigger (the primary ID trigger) threshold is set at 200 PMT hits of the ID NSUM, corresponding to about 0.7 MeV. The delayed trigger threshold is 120 hits of the ID NSUM, corresponds to above 0.4 MeV for 1 msec after the prompt trigger.

The energy dependent trigger efficiency of the prompt event is estimated using delayed trigger events. It is defined as the ratio of the number of delayed events with NSUM which is larger than the NSUM threshold for the prompt trigger to the number of all delayed events. The detection efficiency of reactor $\bar{\nu}_e$ is estimated to be 99.98% with a 0.9MeV threshold by convolving the efficiency curve and the expected reactor $\bar{\nu}_e$ spectrum assuming no anti-neutrino oscillation. The total trigger-related systematic uncertainty is estimated to be 0.02% including energy resolution and scale error. In the case of the delayed trigger, the energy dependent trigger efficiency is estimated by a similar method. According to special data with a trigger threshold of 50PMT hits, The detection efficiency is $\sim 100\%$ at 0.5MeV.

Other trigger commands

- ID prescale trigger
A global trigger to the ID FEE boards for a fraction of each second.
This is useful for the high rate data acquisition such as source calibration.
- OD trigger
The trigger threshold for the outer detector is set to provide $> 99\%$ tagging efficiency. The OD is separated into four regions, top, upper side, lower side and bottom.
These regions have nsum thresholds of 6, 5, 6 and 7, respectively.
- Supernova trigger
If there are 48 events with more than 772 total ID NSUM in 0.84 seconds, a supernova trigger is issued to the DAQ.
This trigger continues a predefined data acquisition state for 3 minutes to prevent DAQ hang up because of high event rates from the supernova.
- 1pps trigger
A GPS trigger is issued at the start of run and every 32 seconds thereafter.
The 1 pps trigger is based on the GPS 1 pps signal.
- History trigger
The ID history trigger is based on the total ID nsum being above the ID history trigger threshold 120, it is issued every 25ns.

2.3.5 Plastic balloon and balloon strap

The 1 kton of the liquid scintillator at the center of the detector is contained in a 13-m-diameter spherical balloon made of 135- μm -thick transparent plastic film. This balloon was developed taking into account some properties required for KamLAND experiment. These properties include the mechanical strength, the long term stability, chemical compatibility with the surrounding liquid scintillator, a high transparency of the scintillation light, low content of the radioactive impurities and low permeability of ^{222}Rn generated in the outer materials.

The balloon film is a laminate of EVOH/nylon/nylon/nylon/EVOH. The EVOH (Ethylene vinyl alcohol copolymer) is 15 μm thick and provides low gas permeability. The nylon is 25 μm thick and provides strength. Both materials have the chemical compatibility and low radioactive impurities (Table 2.9). Moreover, two axis extension was carried out to these films for increasing strength. The transparency for the 400 nm wavelength light is 96% (Figure 2.13). For ^{222}Rn , the diffusion constant is $5 \times 10^{-11}\text{cm}^2/\text{s}$ and the solubility is 3.9, which makes the density difference 1.8×10^{-6} between the buffer oil and the liquid scintillator under the equilibrium state [51].

The balloon was made of 44 20×1 m panels used the microwave welding. The spherical shape of the balloon is kept by the small difference of the liquid level between the inner and outer liquid. The tension of the balloon film is led by the density difference between these liquid. Currently, the density difference is controlled within 0.01% so the net weight of the liquid scintillator for the balloon is about 100 kg. The balloon is supported and constrained by a ‘‘cargo net’’ structure of Kevlar ropes. These Kevlar ropes are supported at the top of the stainless steel vessel. The strength per one Kevlar ropes is about 4000 kgf. The content of the radioactive impurities is shown in Table 2.9. The top of the balloon is a 2-m-diameter cylinder structure (chimney), used for introduction calibration materials.

		U	Th	^{40}K
Film	Content	0.018ppb	0.014ppb	0.27ppb
	Decay rate	0.02Bq	0.006Bq	7.2Bq(γ -ray 0.7Bq)
Kevlar rope	Content	0.08ppb	0.8ppb	1.2ppb
	Decay rate	0.1Bq	0.33Bq	31Bq(γ -ray 3Bq)

Table 2.9: Content of radioactive impurities in the balloon structure [51].

2.3.6 Veto detector

At the outside of the inner detector, a water-Cherenkov detector filling 3.2kton ultrapure water is located. This detector provides a tag for cosmic-ray muons using the 20-inch PMTs mounted on the walls. The geometric shape of the veto detector is a 19-m-diameter and 20-m-height cylinder separated into two regions by the equator of the spherical vessel for the inner detector. On the surface of the walls, 225 20-inch PMTs are mounted. To enhance the veto efficiency by considering flight-path of cosmic rays, the veto detector are divided into four regions using white reflective polyethylene sheets (Figure 2.14). The number of PMTs in each region is 50 PMTs on the top, 60 PMTs on the upper side, 60 PMTs on the lower side, and 55 PMTs on the bottom. The outer surface of the vessel and the cavity walls is covered by polyethylene sheets to increase the amount of the input light into the photocathodes.

Another function of this amount of water is absorption of γ -rays and neutrons from the surrounding rock. To shelter the water from ^{222}Rn coming from the rock, the surface of the cavity walls is covered by polyurethane.

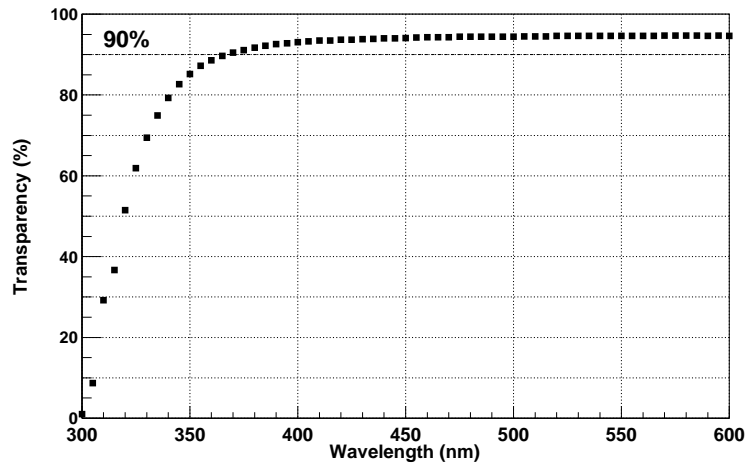


Figure 2.13: Transparency of balloon film

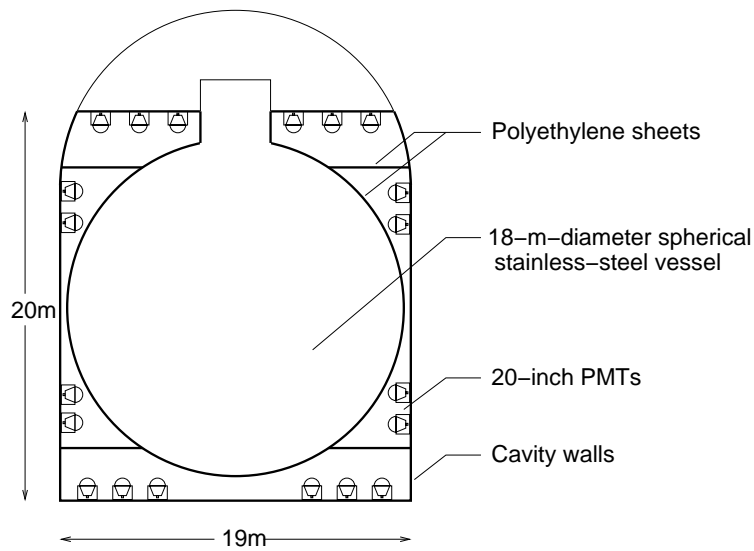


Figure 2.14: Veto counter

2.3.7 Purification system

The radioactive impurities in the liquid scintillator and buffer oil are removed by the purification system located in a shaft. The main components of the purification system is the water extraction system and the nitrogen purge system (Figure 2.15). The ionizing elements, ^{238}U , ^{232}Th and ^{40}K , are removed using the water extraction method. The oxygen, which decrease the light output of the liquid scintillator, ^{222}Rn and water are removed using the nitrogen purge method.

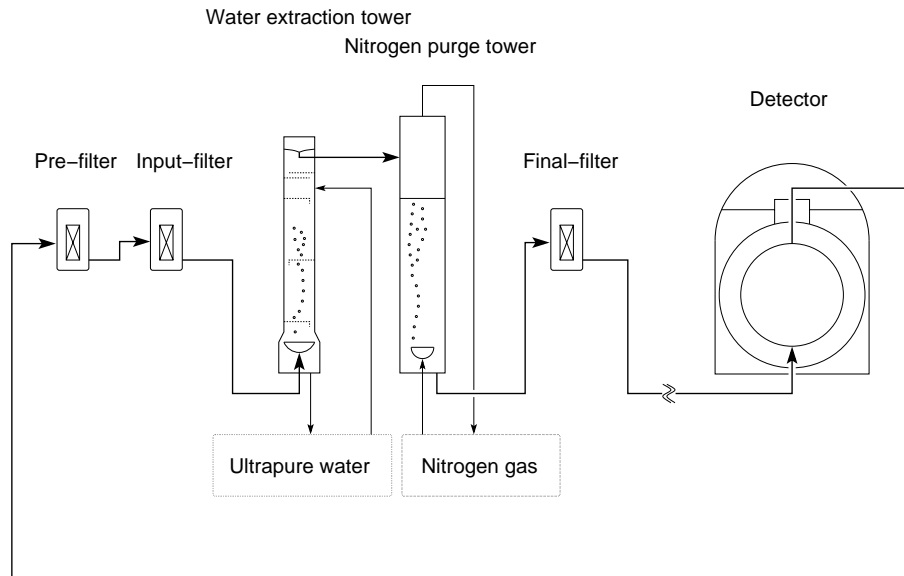


Figure 2.15: Purification system. Main components of the purification method are a water extraction and nitrogen bubbling.

2.3.8 Water purification system

The water purification system provides the ultrapure water to the water-Cherenkov detector and the water extraction system of the purification system (Figure 2.16). This system removes impurities such as salt from the natural water in the mine as the feed water using a reverse osmosis (RO) membrane.

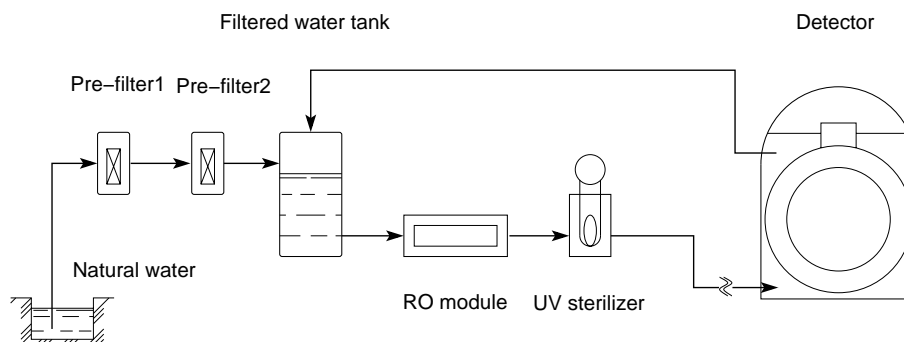


Figure 2.16: Water purification system. The RO membrane removes impurities.

2.3.9 Nitrogen supply system

The nitrogen supply system provides the nitrogen for the detector and the purification system (Figure 2.17).

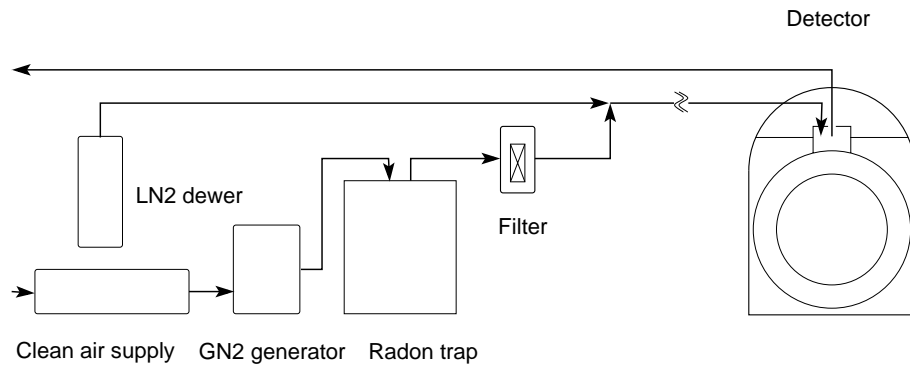


Figure 2.17: Nitrogen gas purification system. Normally, gas from only liquid nitrogen is supplied in the detector.

Chapter 3

Event reconstruction and detector calibration

In this section, event reconstruction at KamLAND are summarized. The data acquisition system at KamLAND returns the waveforms of all PMTs which detected photo-electrons. First of all, some basic analysis and calibrations are described; waveform analysis (3.1), gain calibration (3.2), bad channel selection (3.3) and timing calibration (3.4). Next, the reconstruction methods for vertex (3.5), energy (3.6), and muon track (3.7) are described. The vertex reconstruction mainly makes use of the timing information of each PMT. The total systematic uncertainty for determining fiducial volume is estimated to be 4.71% using the muon spallation events with isotropic vertex distribution in the detector. The energy reconstruction is based on the total charge sum of PMT hits. The systematic uncertainty for the energy scale is estimated to be 2.14% for using the 17 inch PMTs only, and 2.33% for the 17inch PMTs and the 20 inch PMTs. It is considered time and position dependence of reconstructed energies, and the non-linearity between the 17 inch PMT and the 20 inch PMT, and the contribution of the Cherenkov light, and the quenching effect. Systematic uncertainties, which have small contributions, for the noise event cut and the flasher event cut are also described.

3.1 Waveform analysis

The ATWDs acquire the output signals from the PMTs. After subtracting the pedestal value of each sampling channel, the waveform of each PMT is reproduced. as shown in Figure 3.1. The timing information is defined as the leading edge time. The charge is obtained by the sum of counts in the sampling channel between the leading edge and trailing edge. Multi-photon information is also fit by the same method and the time and the charge information are extracted similarly.

Each ATWD contains data even when there is no signal, which is called pedestal. To extract pure amplitude, the pedestal data must be subtracted. In ATWD, the charges are stored by 128 capacitances first, and then, the corresponding voltages are converted to digital data. The capacities of 128 capacitances are not identical and have some fluctuations. The pedestal subtraction is needed also to correct these fluctuations. Pedestal data are taken at the beginning of each run. When pedestal data are taken, triggers are randomly acquire empty waveforms. To estimate the pedestal value, 50 samples of the pedestal data except for the waveform which contains electronics noise or accidental hits are averaged. After pedestal data are subtracted, the remaining constant baseline shift is fit event by event, and removed.

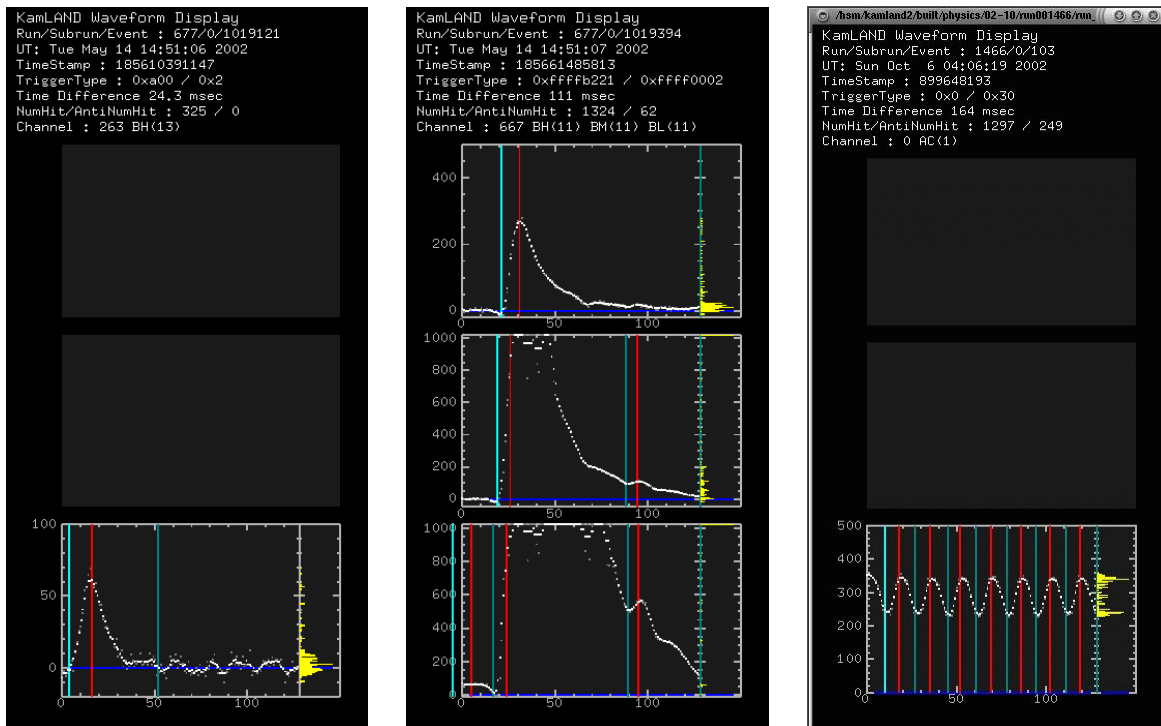


Figure 3.1: Example of waveforms for a small pulse (Left), a large pulse (Middle), and periodic test pulses (Right). The left panel shows a waveform only with high gain, the right panel shows waveforms with high, middle and low gain. The waveforms from the middle and low gain are saturated. The pedestal are already subtracted and the baseline is adjusted. The line at the peak position is the reconstructed peak position, the line before the peak position is the leading edge time, and the line after peak position is the trailing edge time. The timing information is defined as the leading edge time.

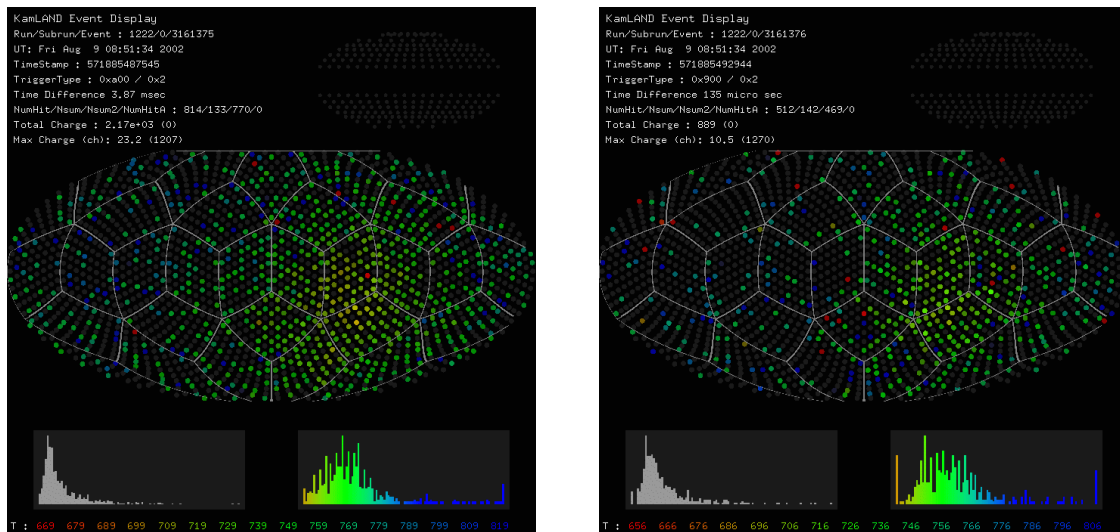


Figure 3.2: KamLAND event display. (Left) Prompt signal of $\bar{\nu}_e$ candidate events. (Right) Delayed signal of $\bar{\nu}_e$ candidate events. The inner detector is shown in the center of figures and the outer detector in the right upper region. Charge distribution is shown at the left bottom region, and timing distribution is at the right bottom region.

The time interval between each sample is about 1.49nsec, and it is well calibrated for each channel with frequent (daily) calibration at the beginning of each run using a internal 40MHz test pulse. Figure 3.1 (Right) shows the test pulses. The time bin width is written by

$$(\text{time bin width}) = 25\text{nsec}/(\text{peak} - \text{interval}). \quad (3.1)$$

The measurement result for each channel is iterated, and the time information of each channel is corrected.

Figure 3.2 shows examples of observed events at KamLAND detector. PMTs which detect photo-electrons are colored and the difference of colors corresponds to that of the fitted timing. Inner detector is shown in the center of the figure and outer detector in the right upper region. Charge distribution is shown at the left bottom region, and timing distribution is at the right bottom region. These reconstructed timing and charge information is made use of by the vertex fit or the energy fit.

3.2 Gain calibration

To correct the time variation of the PMT gain, charge distribution from each PMT for single photo-electron events is monitored. Single photo-electron events are selected by removing large pulse signals and noisy signals, and low energy background signals from normal data. For the 17 inch PMTs, the charge distribution for the single photo-electron events has a clear peak, so the charge for the single photo-electron is defined fitting the peak with Gaussian. For the 20 inch PMTs, however, the single photo-electron peak is not identified because of the difference of the dynode type. So, relative charge at high photon level between adjacent 17 inch PMTs and 20 inch PMTs is used to determine the gain of the 20 inch PMT.

Figure 3.3 shows the time variation of the mean single photo-electron charge. The gain increases by about 8% during ~ 22 month period. The variation is caused by ATWD hardware

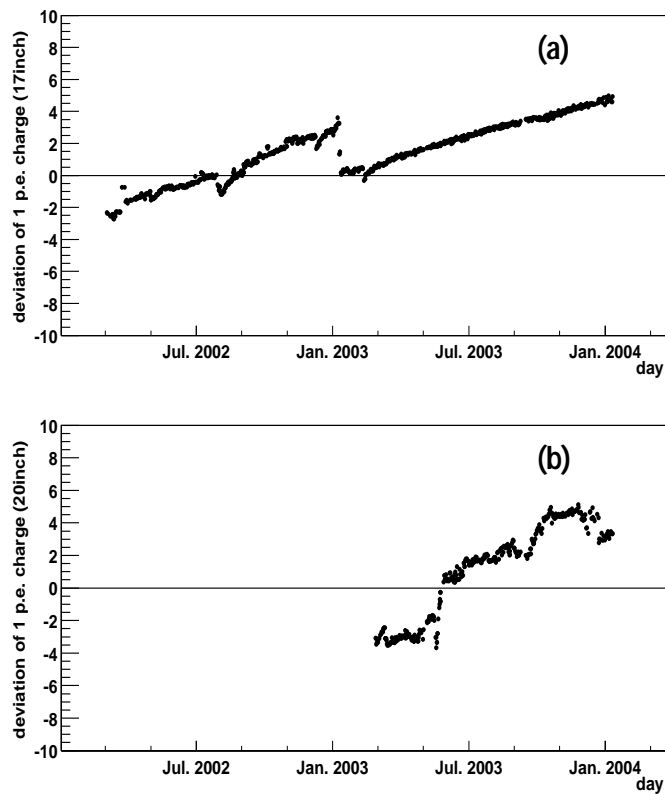


Figure 3.3: Time variation of the mean single photo-electron charge. for the 17 inch PMTs (a) and the 20 inch PMTs included in February 2003 (b). The single photo-electron charge is gradually increasing by about 8%. In January 2003, the gain for the 17 inch PMTs dropped due to the electronics upgrade. Since May 2003 the gain for the 20 inch PMTs rose by a gradual increase of the high voltage supplies.

changes, high voltage changes, and temperature change in the electronics. The variation of the gain of each channel is corrected run by run. The gradual rise and unstable gain are compensated by this correction. For a long run, with a run time longer than 20,000 sec, the gain is corrected by that run's, and for short runs, the gain is corrected by data from the nearest long run.

3.3 Bad channel selection

In the PMT channels, there are unstable channels, which have too many hits, no hits or strange charge occasionally. These abnormal signals are caused by malfunctioning PMTs or unstable high voltage supplies for each PMT or miss connection of signal cables. These unstable channels are categorized as "bad channels". To prevent systematic biases, the bad channels are masked in event reconstruction. Figure 3.4 shows the number of the bad channels in the inner detector and the outer detector. There are ~ 10 bad channels in the inner detector and more than 50 bad channels in the outer detector. The bad channels in the outer detector are mainly dead PMTs via a water leak. Bad channels are found by observing each channel's hit rate and charge. Selection criteria for the bad channels in the inner detector are as follows

- Hit rate ($< 1,000$ hits/10,000events).
Find low response channels by electronics failures.
- No-hit rate ($> 1,000$ no-hits/10,000events).
Find no response channels caused by the trouble for the PMT high voltage power supplies etc.
- Hit rate in high charge muon event (< 80 hits/100high-charge-muon).
Find excessively low gain channels.
- Difference of hit rate between A-ch and B-ch ($> 22\%$ difference in 10,000events).
Find bad-ch for which the ping-pong scheme in the FEE failed.
- ADC counts for single photo-electron is too low ($< \bar{Q}_{\text{adc}} \times 1/4$) or too high ($> \bar{Q}_{\text{adc}} \times 4$).
Find very low gain or very high gain channels. The \bar{Q}_{adc} is the mean ADC counts corresponding to single photo-electron of all 17 inch channels.
- Charge difference in high charge muon events.

$$\frac{1}{N_i} \sum_{j=1}^{N_i} \frac{(Q_i - Q_j)^2}{Q_j} > 400 \text{p.e.} (Q_j > 0, j : \text{neighbor PMTs}). \quad (3.2)$$

Find channels with a large gain difference by a comparison of the gain between neighboring channels.

For the outer detector, only criterion #1 applies.

3.4 Timing calibration

The timing of each waveform is defined as the leading edge time. To reconstruct the vertex position precisely, the relative timing of all PMT output signals are calibrated. The timing of signals varies due to difference of the transit time or cable length and so on. Figure 3.5 shows the schematic diagram of the timing calibration system. The laser pulses of 500nm wavelength

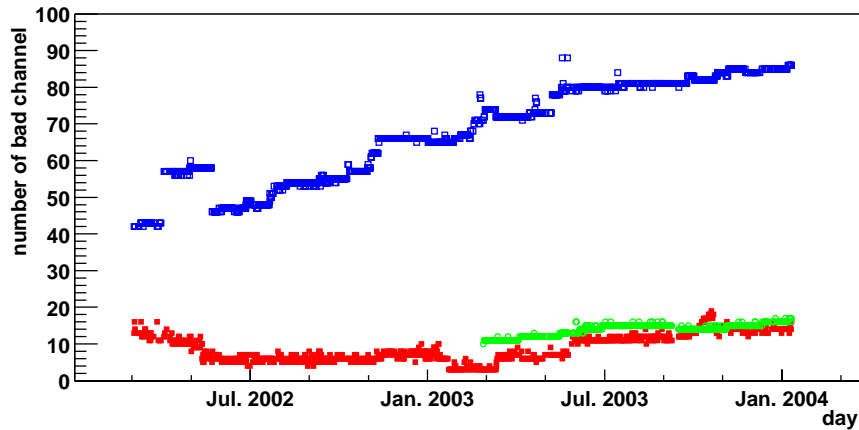


Figure 3.4: Time variation of the number of bad channels for the 17 inch PMTs (Red markers), the 20 inch PMTs (Green markers), and the 20 inch PMTs in the outer detector (Blue markers).

are introduced to a diffusing ball installed at center of the detector with a optical fiber. The diffusing ball is an 5-cm-diameter acrylic sphere containing magnesium oxide. It diffuses the laser pulse uniformly. The data acquisition is carried out by the output signal from a two inch PMT. The leading edge time of this PMT signal is used for determining the reference time.

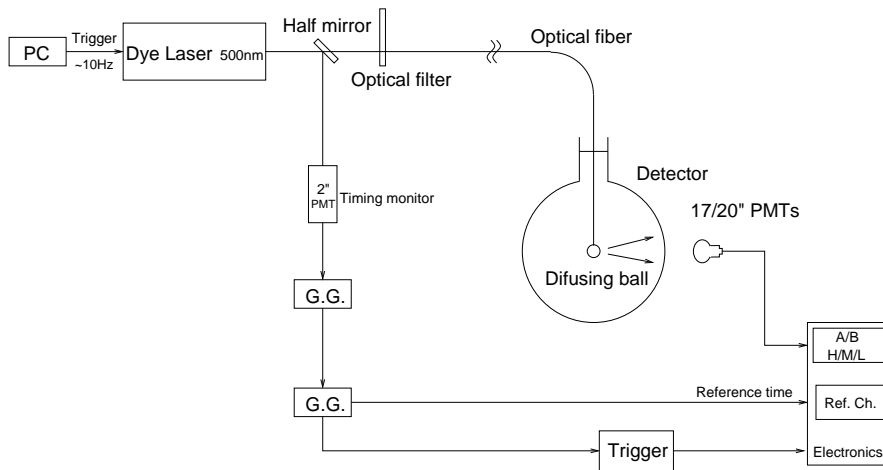


Figure 3.5: Schematic diagram of the timing calibration.

Examples of correlation between timing and charge at a 17inch PMT is shown in Figure 3.6 and that of a 20inch PMT is shown in Figure 3.7. The maximum count of the charge corresponds to ~ 100 photo-electrons. We can see the output charge dependence of the time. The reconstructed time t is corrected using two dimensional functions of the output charge q as $t(q) = p_0 + p_1 \cdot \log q + p_2 \cdot (\log q)^2$. The three parameters were calculated for each gain channel of all PMTs.

Figure 3.8 shows the time distribution of single photo-electron events. Before applying the result of the time calibration, the spreads of the time distribution of single photo-electron events

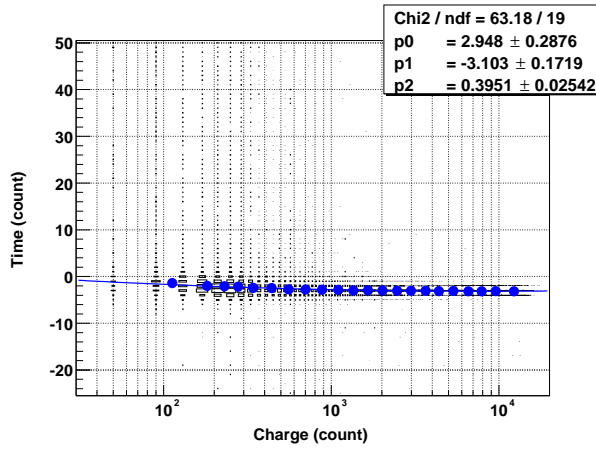


Figure 3.6: Correlation between time and charge of output signals from a 17inch PMT.

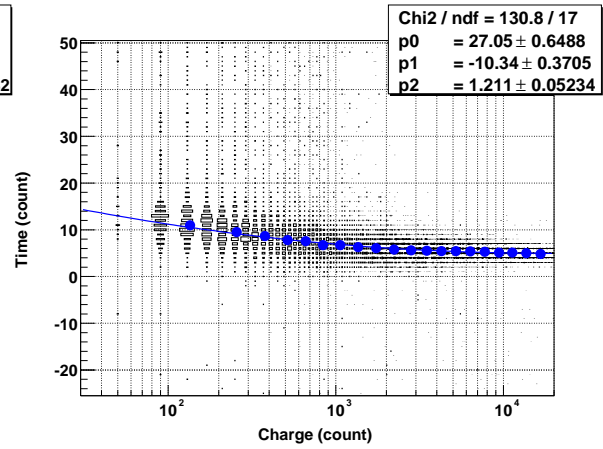


Figure 3.7: Correlation between time and charge of output signals from a 20inch PMT.

are 5.6ns for the 17inch PMTs and 8.2ns for the 20inch PMTs. After correcting the relative timing, the spreads are improved to 2.3ns and 4.7ns respectively.

3.5 Vertex reconstruction and fiducial volume

The vertex fitting program is essential to retrieve the correct vertex for each event. The vertex reconstruction is based on relative timing of PMT hits. The algorithm makes use of time of flight of the scintillation light and absolute position is tuned by radioactive sources, deployed on various z position. That result is used for the reconstruction of energy. Possible reconstruction biases affect a fiducial volume determination. Uncertainty of the fiducial volume is estimated from uniformities of spallation neutron and $^{12}\text{B}/^{12}\text{N}$ distributions.

3.5.1 Vertex reconstruction

The vertex reconstruction is based on the relative times of the PMT hits. When a vertex point (x, y, z) is assumed, the light emission time is calculated from each PMT hit,

$$t_i(x, y, z) = T_{\text{detected},i} - T_{\text{tof},i}(x, y, z), \quad (3.3)$$

where $T_{\text{detected},i}$ is the detected time of the photon, and $T_{\text{tof},i}$ is the time of flight which calculated from path length L_i and speed of light V shown in Figure 3.9,

$$T_{\text{tof},i} = \frac{L_i}{V} \quad (3.4)$$

$$L_i = \text{sqrt}(x - x_i)^2 + (y - y_i)^2 + (z - z_i)^2 \quad (3.5)$$

$$V = \frac{c}{n_{\text{eff}}}, \quad (3.6)$$

where n_{eff} is an effective index of refraction representing both the liquid scintillator and the buffer oil. In reality, T_{detected} depends on charge because of a multi photon effect. That charge

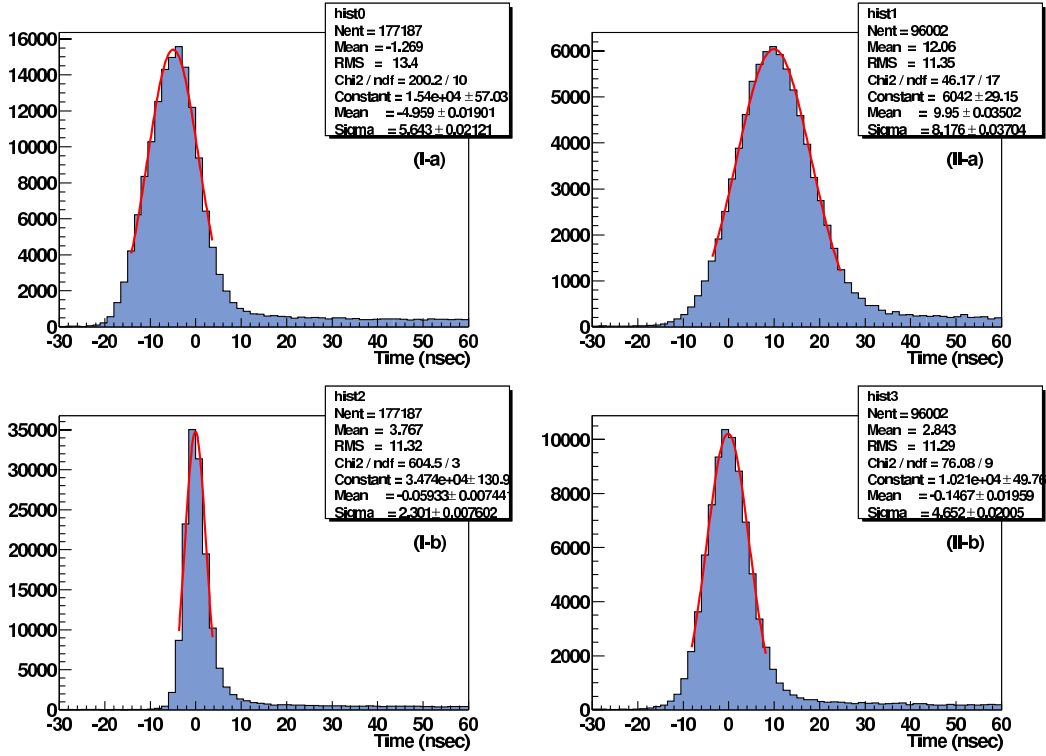


Figure 3.8: Timing distribution of 1 p.e. events. (I-a) and (II-a) are distributions of the 17-inch and 20-inch PMTs before the timing correction. (I-b) and (II-b) are distributions after the correction.

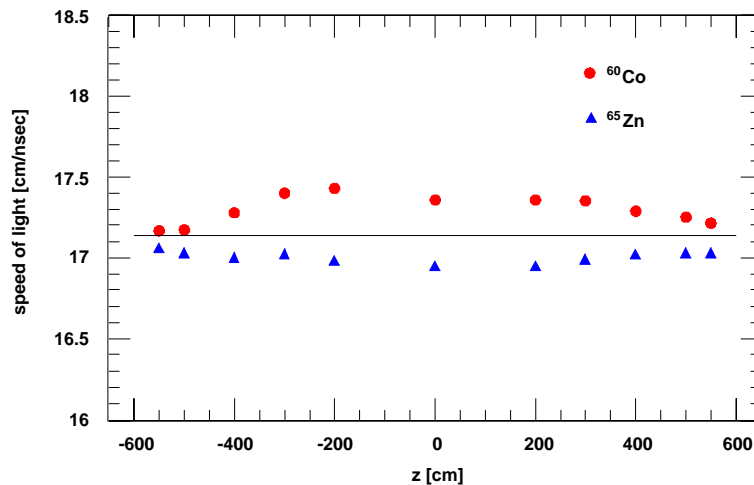


Figure 3.9: Measured speed of light for calibration sources at z positions, ^{60}Co and ^{65}Zn , at various z positions. The small energy dependence is due to a multi photon effect.

dependence is measured by source calibrations at various energies. At an ideal vertex point, there is no correlation between t_i and the space-time correlation coefficient dt_i/dx , expressed as [81],

$$\frac{dt_i}{dx} = -\frac{dT_{\text{tof},i}}{dx} \tag{3.7}$$

$$= -\frac{1}{dx} \left(\frac{L_i}{V} \right) \tag{3.8}$$

$$= \frac{x_i - x}{LV}, \tag{3.9}$$

and the covariance between t_i and dt_i/dx is,

$$\sigma_{t_i, \frac{dt_i}{dx}} = \sum_i w_i (t_i - \langle t_i \rangle) \left(\frac{dt_i}{dx} - \left\langle \frac{dt_i}{dx} \right\rangle \right) / \sum_i w_i \tag{3.10}$$

$$= \left(\sum_i w_i \left(t_i \frac{dt_i}{dx} \right) / \sum_i w_i \right) - \left(\langle t_i \rangle \left\langle \frac{dt_i}{dx} \right\rangle \right). \tag{3.11}$$

where w_i is the distance dependent weight for each PMT, $\langle t_i \rangle$ and $\langle dt_i/dx \rangle$ indicate their mean value. The first term in (3.11) works as a pull-push balance term for each PMTs with the deviation from the origin of time. The second term is a constant in a event, but it is independent of the pull-push balance term and related to the time profile of scintillation light emission. The vertex position is moved in order that the covariance for x, y, z converges on zero.

3.5.2 Deviation of the reconstructed vertex

Position estimation are monitored periodically with γ -ray and neutron sources along the central vertical axis (z-axis) of the scintillator volume. Figure 3.10 shows the vertical axis dependence of the reconstructed vertices deviations with source calibrations. In these calibrations, sources of ^{60}Co , ^{65}Zn , ^{68}Ge and Am-Be are used. All reconstructed points within the fiducial radius of 5.5m are within 5cm of the deployed positions. The vertex resolution for the ^{60}Co source is about 20 cm. Energy dependence of the resolution is estimated to be $\sim 30\text{cm}/\sqrt{E(\text{MeV})}$ from various energy sources.

3.5.3 Systematic uncertainty on the fiducial volume

The total volume of the liquid scintillator is $1171 \pm 25\text{m}^3$, as measured by flow meters during detector filling. The nominal 5.5-m-radius fiducial volume ($\frac{4}{3}\pi R^3$) corresponds to 0.595 ± 0.013 of the total LS volume. Figure 3.11 shows the summary of the fiducial volume ratio. The nominal value corresponds to the center vertical line.

The effective fiducial volume is defined by the cuts on the radial positions of the reconstructed event vertices. At present, only z-axis calibrations are available, so we assess the systematic uncertainty in the fiducial volume by studying uniformly-distributed muon spallation products, identified as delayed coincidences following muons. We measure the position distribution of the β -decays of ^{12}B ($Q = 13.4\text{MeV}$, $\tau_{1/2} = 20.2\text{ms}$) and ^{12}N ($Q = 17.3\text{MeV}$, $\tau_{1/2} = 11.0\text{ms}$), which are produced at the rate of about 60 $^{12}\text{B}/^{12}\text{N}$ events/kton-day. Figure 3.12 shows the time difference of $^{12}\text{B}/^{12}\text{N}$ events after muon events.

Fits to the energy distribution of these events indicate that the sample is mostly ^{12}B as shown in Figure 3.13; the relative contribution of ^{12}N is only $\sim 1\%$. Figure 3.14 shows vertex

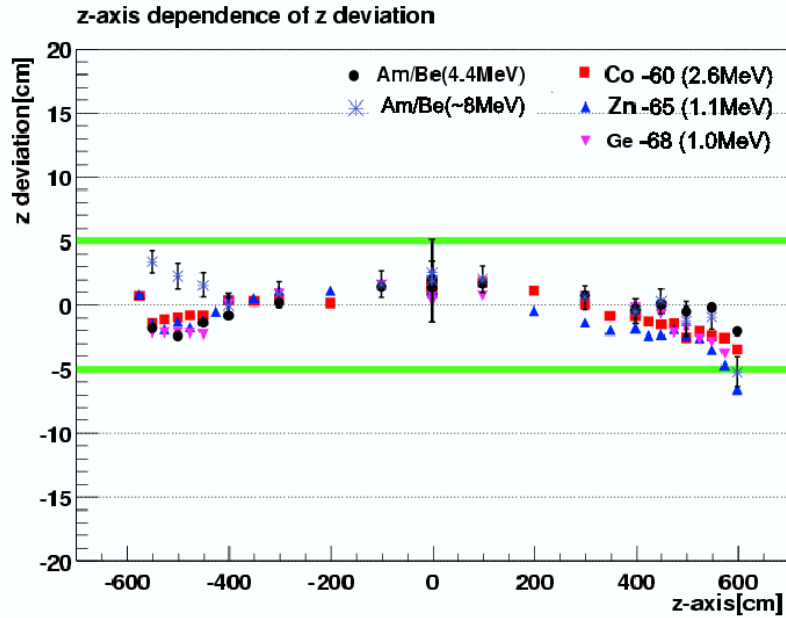


Figure 3.10: Z-deviations with source calibrations, $^{60}\text{Co}(2\gamma, 1.173 + 1.333\text{MeV})$, $^{65}\text{Zn}(1\gamma, 1.11552\text{MeV})$, $^{68}\text{Ge}(2\gamma, 0.511 \times 2\text{MeV})$, and Am-Be ($1\gamma, 4.438\text{MeV}$ and $1\gamma \sim 8\text{MeV}$ by neutron capture on Ni or Fe).

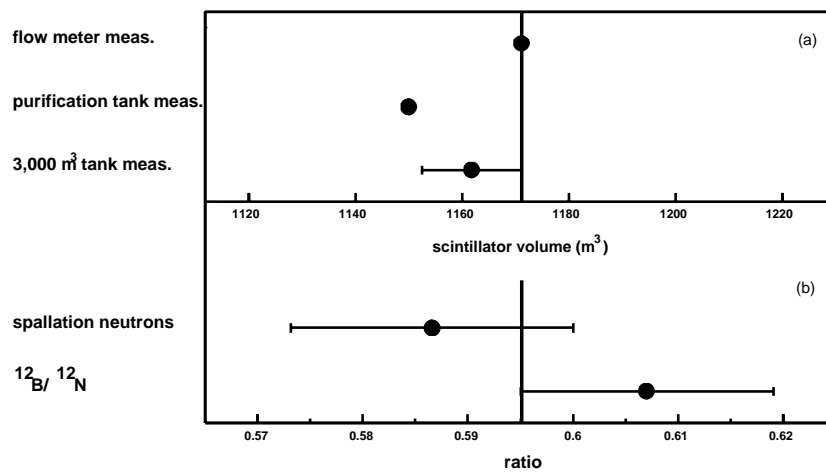
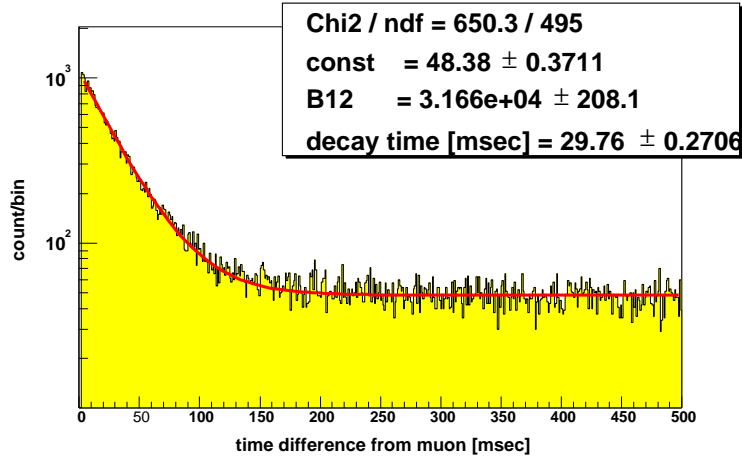
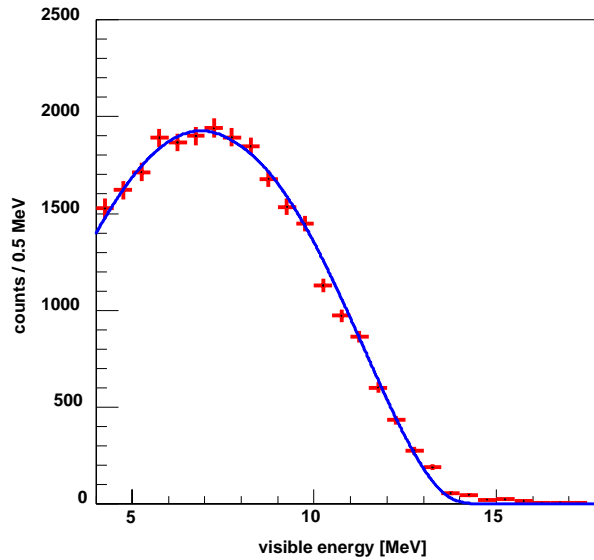


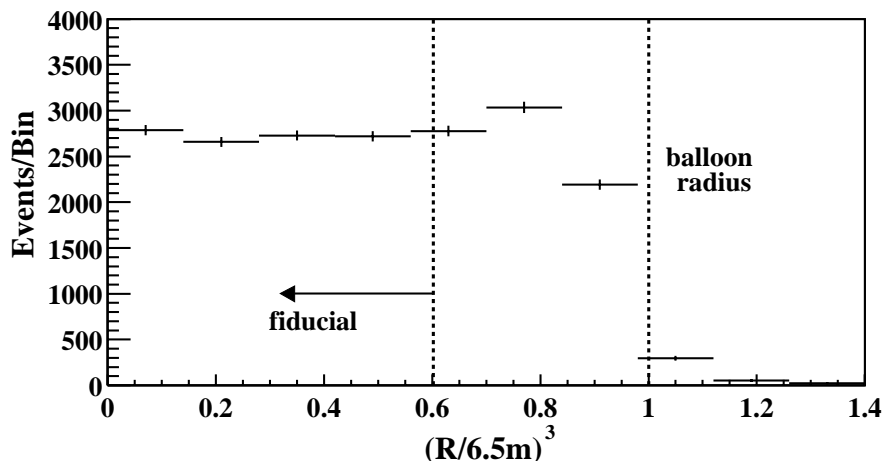
Figure 3.11: Systematic uncertainty on the fiducial volume.

Figure 3.12: $^{12}\text{B}/^{12}\text{N}$ events following muons.

distribution of $^{12}\text{B}/^{12}\text{N}$ events. The number of $^{12}\text{B}/^{12}\text{N}$ events reconstructed in the fiducial volume compared to the total number in the entire LS volume is $0.607 \pm 0.006(\text{stat}) \pm 0.006(\text{syst})$.

Figure 3.13: Energy distribution of $^{12}\text{B}/^{12}\text{N}$ events following muons.

As a consistency check, in a similar study of spallation neutrons the ratio $0.587 \pm 0.013(\text{stat})$ was found. The $^{12}\text{B}/^{12}\text{N}$ events typically have higher energy than $\bar{\nu}_e$ candidates, so an additional systematic error accounts for possible dependence of effective fiducial volume on reactor $\bar{\nu}_e$ energy. We constrain the variation to 2.7% by comparing the prompt and delayed event positions of delayed-neutron β -decays of $^9\text{Li}(Q = 13.6\text{MeV}, \tau_{1/2} = 178\text{ms})$ and $^8\text{He}(Q = 10.7\text{MeV}, \tau_{1/2} = 119\text{ms})$. The observed capture distance variation is a measure of the energy uniformity of the vertex finding algorithm. Combining the errors from the LS volume measurements, the $^{12}\text{B}/^{12}\text{N}$ volume ratio calibration, and the constraints on energy dependence, we obtain a 4.7% systematic

Figure 3.14: Vertex distribution of $^{12}\text{B}/^{12}\text{N}$ events.

error on the fiducial volume.

3.6 Energy reconstruction

The visible energy for each event is reconstructed from charge distribution of PMT hits, which depends on the vertex point, asymmetric geometry of the detector; particularly missing PMTs (~ 20 PMTs around chimney and ~ 5 PMTs at the bottom). The absolute energy scale is calibrated by the source calibration data. To account for time variation in the detector status, some basic corrections are performed before the visible energy estimation; the single photo-electron charge (Gain calibration), bad channel selection, the software discriminator threshold, and the dark hit subtraction.

3.6.1 Visible energy calculation

After reconstruction of the vertex point, the visible energy is calculated as a function of correction parameters,

$$E = \frac{\sum_i Q_i^{\text{observed}}}{\sum_i Q_i^{\text{expected}}} \times (\text{Const.}), \quad (3.12)$$

where Q_i^{observed} is the observed PMT charge (p.e.) and Q_i^{expected} is the expected PMT charge (arbitrary) written as

$$Q_i^{\text{expected}}(\theta, L_i, \eta_i, \xi_i, \lambda) = \frac{\eta_i \exp(-L_i/\lambda) \cos \theta_i}{L_i^2} \xi_i, \quad (3.13)$$

where θ_i is the angle of incidence, L_i is the distance to light generation point, η_i is the light loss by balloon shadow, λ is the light attenuation length, and ξ_i is the single photo-electron threshold effect. These parameters Table 3.1 are handled as follows.

1. Dark hit subtraction

Figure 3.15 shows the timing distribution of detected signals after subtracting time of flight event by event. The time of flight is calculated as “(Detected time) – (Distance from each

Parameter	Estimation/Correction
θ Angle of incidence	Vertex reconstruction
L Distance to light generation point	
- Dark hit of PMTs	Hits in the off-time window
η Light loss by balloon shadow	Geometrical information of the ropes Periodical ^{60}Co calibration
λ Light attenuation length	
ξ Single photo-electron threshold effect	Probability of 1p.e. detection

Table 3.1: Parameters and values for calculation of position dependent visible energy.

PMT to the reconstructed vertex point)/(Light velocity)”. Central 150 nsec time interval corresponds to the real hits for the scintillation light, and in other regions, the accidental dark hits are dominant.

To reduce the effect of the dark hit, PMT hits within the 150 nsec time window are used for the energy estimation. The contribution of dark hit charge (10-15p.e.) is about 3-5% for 1 MeV event. To reduce this contribution for the visible energy, the total charge in the 50 nsec off-time window is scaled to the 150 nsec width, and subtracted from the on-time window event by event.

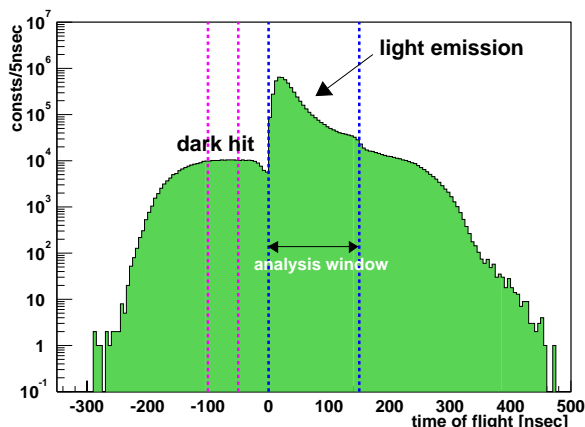


Figure 3.15: Timing distribution of detected signals after the correction for time of flight.

2. Shadow effect

As shown in Figure 2.6, the balloon containing the liquid scintillator is supported by a “cargo net” structure of ropes. The incident light on the PMTs is disturbed by the ropes (Shadow effect). Particularly, at the top and bottom of the balloon, the density of the ropes are high, so the shadow effect becomes larger. Moreover, the shadow effect to each PMT depends on the vertex position.

The shadow effect to each PMT at each event is calculated and corrected based on the geometrical information of the ropes. To calibrate the angular distribution of the output charge, the ^{60}Co source calibration is also performed at the center of the detector. The small time dependence of the shadow effect is calibrated by the weekly ^{60}Co source calibration.

3. Light attenuation length

As shown in Figure 2.6, the liquid scintillator is surrounded by the buffer oil and there are transparent acrylic plates in front of the PMTs. So, the intensity of the scintillation light is varied by the absorption in the scintillator or buffer oil, the reemission in the scintillator, and the slight reflection on the acrylic plates. The effective attenuation length including these effects is measured by the source calibration, and obtained to be 22m.

4. Single photo-electron efficiency [82]

The detection inefficiency of the single photo-electron causes the non-linearity of the visible energy.

Probability of 1 p.e. detection if there is no threshold effect

$$P(1) = \mu \exp(-\mu), \quad (3.14)$$

where μ is the mean number of photo-electrons,

$$\mu = \frac{1}{N_{\text{PMT}}} E \frac{dQ}{dE}. \quad (3.15)$$

The detection efficiency ϵ of 1 p.e. is a concern, and the probability of 0 p.e. and 1 p.e. and N p.e. ($N > 2$) detection efficiencies are,

$$P(0) = \exp(-\mu) + (1 - \epsilon)\mu \exp(\mu) \quad (3.16)$$

$$= \exp(-\mu) (1 + (1 - \epsilon)\mu) \quad (3.17)$$

$$P(1) = \epsilon \mu \exp(-\mu) \quad (3.18)$$

$$P(N) = \frac{\mu^N}{N!} \exp(-\mu) : (N \geq 2). \quad (3.19)$$

$$(3.20)$$

The visible energy (E_{vis}) is calculated by adding up charges, so

$$E_{\text{vis}} = Q(1) \times P(1) + \sum_{N \geq 2} (Q(N) \times P(N)). \quad (3.21)$$

Here, the normalization constant is omitted because it doesn't effect for the nonlinearity of energy. If there is no threshold effect, visible energy will be

$$\sum_{N \geq 1} (Q(N) \times P(N)) = \mu Q_1 \equiv E_{\text{vis-no-th.}}, \quad (3.22)$$

where Q_1 is the mean charge of 1 p.e. events with no threshold effect. Then, considering that only 1 p.e. events are affected by the threshold effect, E_{vis} is rewritten as,

$$E_{\text{vis}} = \mu Q_1 - \mu \exp(\mu) Q_1 + Q(1) \epsilon \mu \exp(-\mu) \quad (3.23)$$

$$= \mu Q_1 \left(1 - \exp(\mu) + \frac{Q(1)}{Q_1} \epsilon \exp(-\mu) \right) \quad (3.24)$$

$$= E_{\text{vis-no-th.}} \left(1 - \exp(\mu) \left(1 - \frac{Q(1)}{Q_1} \epsilon \right) \right). \quad (3.25)$$

Here, the $Q(1)$ is determined from the following relation.

$$Q_1 = Q(1) \epsilon + Q_{\text{loss}} (1 - \epsilon), \quad (3.26)$$

where Q_{loss} is the mean charge of the events under threshold, so, it should be less than 1/3 p.e. Finally,

$$E_{\text{vis}} = E_{\text{vis-no-th.}} (1 - \exp(-\mu)\delta), \quad (3.27)$$

$$\delta \equiv \frac{Q_{\text{loss}}}{Q_1} (1 - \epsilon). \quad (3.28)$$

The δ is determined using the real data. For the radioactive source $^{60}\text{Co}(2\gamma, 1.173 + 1.333\text{MeV})$ and $^{65}\text{Zn}(1\gamma, 1.11552\text{MeV})$, individual γ -ray energies are similar, so the effects of quenching and Cherenkov light work similarly. Therefore, it is useful to separate the threshold effect and the quenching and Cherenkov light effects. The residual energy non-linearity can be caused by the single photo-electron threshold effect, and the δ is measured to be 0.03.

Table 3.2 shows real energies and visible energies which reconstructed using the 17 inch PMTs only.

Source		Energy (MeV)	E_{vis} (MeV)	$\sigma/\sqrt{E_{\text{vis}}}$ (MeV) (%)
^{203}Hg	1 γ	0.279197	0.197	8.2
^{68}Ge	2 γ	0.511×2	0.846	7.9
^{65}Zn	1 γ	1.11552	1.021	7.2
^{60}Co	2 γ	1.173 + 1.333	2.346	7.3
$\text{np} \rightarrow \text{d}\gamma$	1 γ	2.22457	2.211	-
$\text{n}^{12}\text{C} \rightarrow ^{13}\text{C}\gamma$	1 γ	4.9468	5.061	-

Table 3.2: Correlation of calibration source energy with visible energy E_{vis} .

3.6.2 Systematic uncertainty of the visible energy calculation

The systematic uncertainty of the visible energy calculation is estimated from the deviation of the calculated energy caused by various condition. It is classified into the position and time dependence, and characteristic of the 17 inch PMT and the 20 inch PMT, and the effect of the Cherenkov light and the quenching of the scintillation light. The uncertainty from each component is as follows.

1. Time dependence

Figure 3.16 (a) shows the time variation of the energy deviation ($\Delta E/E$) of the neutron capture gamma event ($\text{np} \rightarrow \text{d}\gamma, 2.22457\text{MeV}$), which caused by the spallation neutron. Large gap appeared in January 2003, when electronics upgrade was performed, and other gradual variation is remained. These time dependent deviations are corrected run by run using the peak of 1.46 MeV ^{40}K gamma, which vertex is mainly near the balloon surface. Figure 3.16 (b) shows the time variation of the neutron capture gamma event after the correction. Moreover, this correction is performed to the visible energy of the calibration sources, $^{68}\text{Ge}(2\gamma, 0.511 \times 2\text{MeV})$, $^{65}\text{Zn}(1\gamma, 1.11552\text{MeV})$, and $^{60}\text{Co}(2\gamma, 1.173 + 1.333\text{MeV})$. For all energies, the deviation of the visible energy is less than 1.3%.

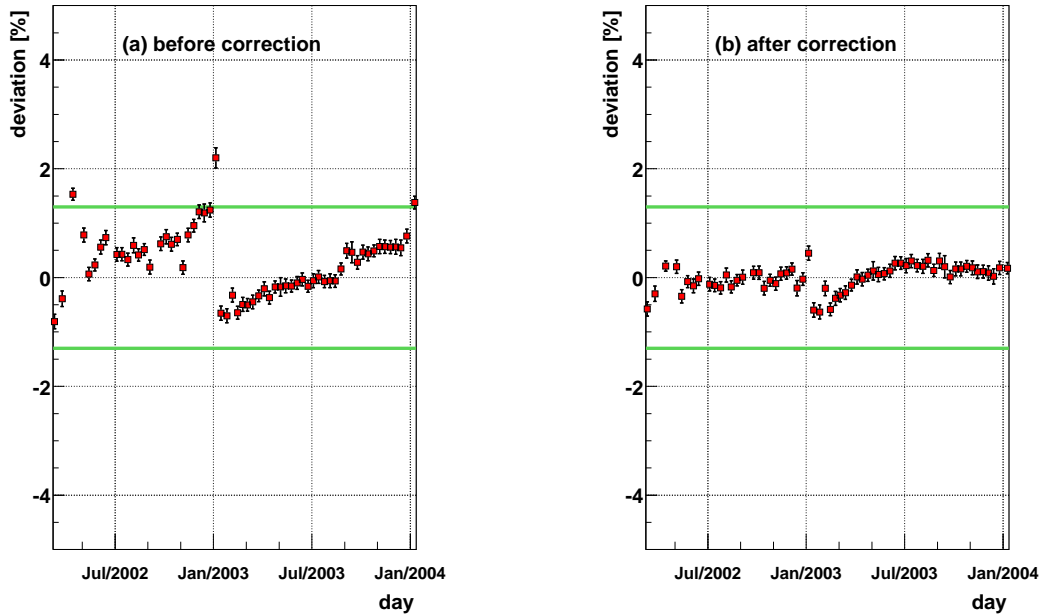


Figure 3.16: Time dependence of the visible energy of the neutron capture gamma event. (a) Before correction. (b) After correction.

2. Position dependence

Figure 3.17 shows the position dependence of the energy deviation of the neutron capture gamma event for the radius (a), and the z-axis (b). At the top and bottom region, the local variation increases. The fiducial radius is 5.5m, so the deviation of the visible energy is less than 0.3% with the radius and 0.92% for the z-axis. Moreover, the position dependence of the visible energy is studied using the calibration sources, $^{203}\text{Hg}(1\gamma, 0.279197\text{MeV})$, $^{68}\text{Ge}(2\gamma, 0.511 \times 2\text{MeV})$, $^{65}\text{Zn}(1\gamma, 1.11552\text{MeV})$, and $^{60}\text{Co}(2\gamma, 1.173 + 1.333\text{MeV})$. At all the visible energies, the position dependence of the energy deviations is checked less than 0.92%.

3. Non-linearity for 20 inch PMTs

Data taking at KamLAND is classified into two kinds of period, one is using 1325 17 inch PMTs only and another is using additional 554 20 inch PMTs. Therefore, the energy dependent uncertainty of the visible energy corresponding to the available PMTs is occurred. This uncertainty is mainly caused by the difference of the charge response between the 17 inch PMT and the 20 inch PMT. Particularly, the 17 inch PMT has enough charge resolution to recognize the single photo-electron peak. So, the energy calibration using the radioactive sources is performed with the 17 inch PMTs only. Then, reconstructed energy with the 20 inch PMTs is tuned using that with the 17 inch PMTs. The visible energy as using both of the 17 inch PMTs and the 20 inch PMTs is combined as

$$E_{\text{vis}} = (1 - \alpha)E_{\text{vis},17\text{inch}} + \alpha E_{\text{vis},20\text{inch}}, \quad (3.29)$$

where $E_{\text{vis},17\text{inch}}$ is the reconstructed visible energy using the inch PMTs, and $E_{\text{vis},20\text{inch}}$ is the reconstructed visible energy using the 20inch PMTs, and α is a combining factor.

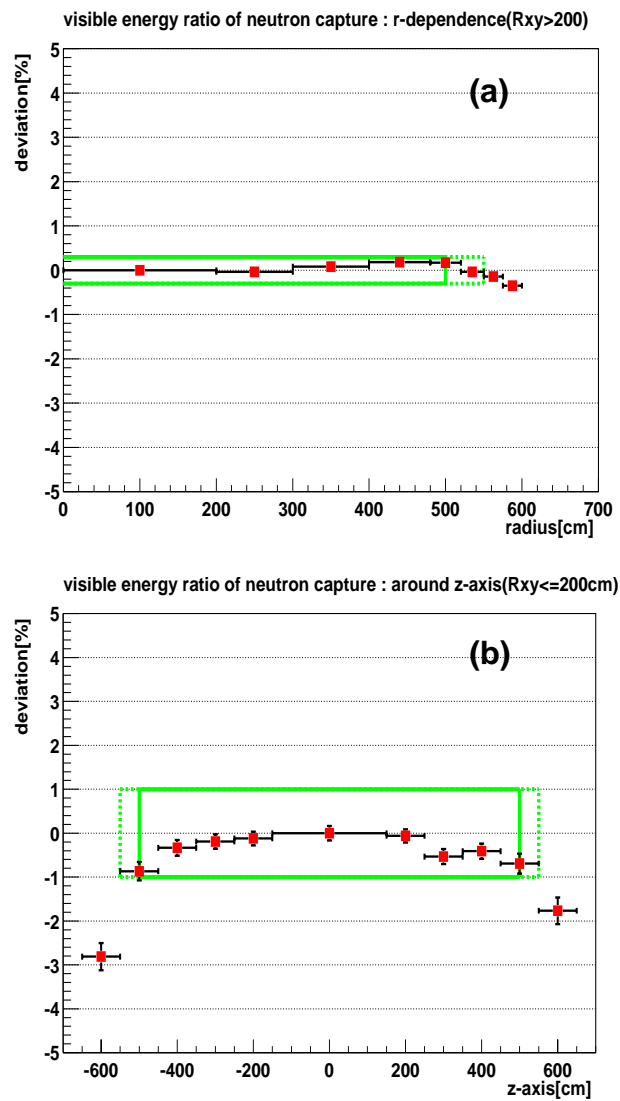


Figure 3.17: Position dependence of the energy deviation of the neutron capture gamma event. (a) With the radius. (b) With the z-axis.

The α is determined to be 0.3 to get the best energy resolution. Figure 3.18(Left) shows the visible energy resolution for various combining factors.

The uncertainty from commissioning the 20 inch PMTs is estimated using the calibration sources, ^{214}Po , ^{68}Ge , ^{65}Zn , ^{60}Co , and Am – Be(2.22457MeV, 4.438MeV and – 8MeV). Figure 3.18(Right) shows the energy deviation of the combined energy (using the 17 inch PMTs and the 20 inch PMTs) to the energy with the 17 inch PMTs only. The deviations are less than 0.8% for the whole energy region.

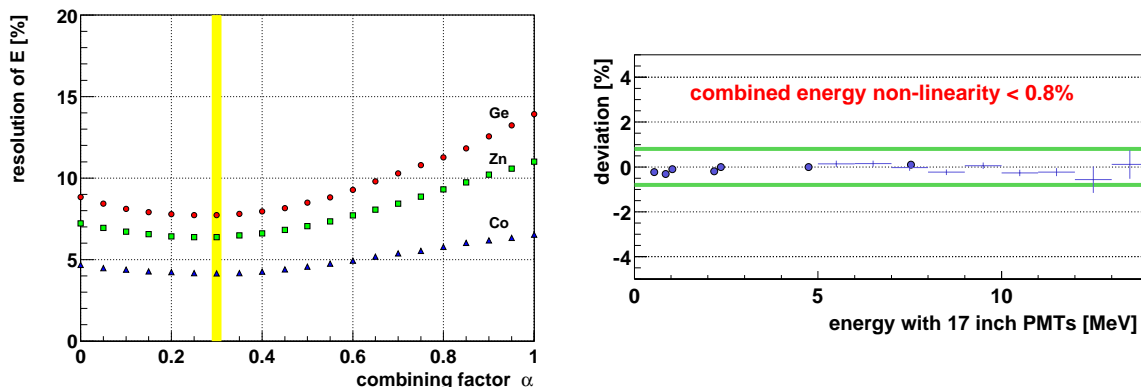


Figure 3.18: Energy non-linearity from characteristics between the 17inch PMT and the 20 inch PMT. (Left) Combining factor dependence of the energy resolution. (Right) Energy deviation of the combined energy (using the 17 inch PMTs and the 20 inch PMTs) to the energy with the 17 inch PMTs only. The energies depend on the calibration sources, ^{214}Po , ^{68}Ge , ^{65}Zn , ^{60}Co , and Am – Be(2.22457MeV, 4.438MeV and – 8MeV).

4. Cherenkov light / Birk's constant in the quenching effect

The direct contribution of Cherenkov light can be ignored because the dominant wavelength is below the absorption wavelength of the scintillator. However, the scintillator reemits absorbed Cherenkov light and this contribution has an energy dependence. Since its magnitude depends on the energy loss dE/dx of the charged particle, the contribution is related to the recoil energy of an electron for γ -rays, and it is necessary to consider pair-annihilation. The limit and range of this contribution is tuned by altering the contribution of the quenching effect described as follows.

The light output in the liquid scintillator dL/dx is written with the energy loss dE/dx as

$$\frac{dL}{dx} = \frac{L_0 \frac{dE}{dx}}{1 + k_B \frac{dE}{dx}}, \quad (3.30)$$

where L_0 is a coefficient between luminescence for a low ionization density and energy loss in the scintillator, and k_B is a quenching parameter (Birk's constant [83]), which corresponds to the ionization quenching caused by high ionization density with heavily ionizing particles. For electrons, the energy non-linearity is smaller than heavily ionizing particles as alphas and protons.

The contribution from the quenching and Cherenkov light are tuned using five gamma sources (^{68}Ge , ^{65}Zn , ^{60}Co , $\text{np} \rightarrow \text{d}\gamma$, and $\text{n}^{12}\text{C} \rightarrow ^{13}\text{C}\gamma$) and electrons from the β -decays of ^{12}B and ^{12}N . The two γ 's of ^{68}Ge and ^{60}Co are treated as one γ ray whose energy

is the effective mean of them. The recoil energies of electrons are calculated with a MC simulation. Figure 3.19 (Left) shows the fitting result for the non-linear visible energies of the data points. The fitting parameters are Birk's constant and Cherenkov light intensity. The function of the visible energy for the best fit parameters is shown in Figure 3.19 (Right top), and the energy deviation for the 1σ C.L. is shown in Figure 3.19 (Right bottom). The combination of uncertainties for the Cherenkov light and Birk's constant effect is estimated to be 1.0%.

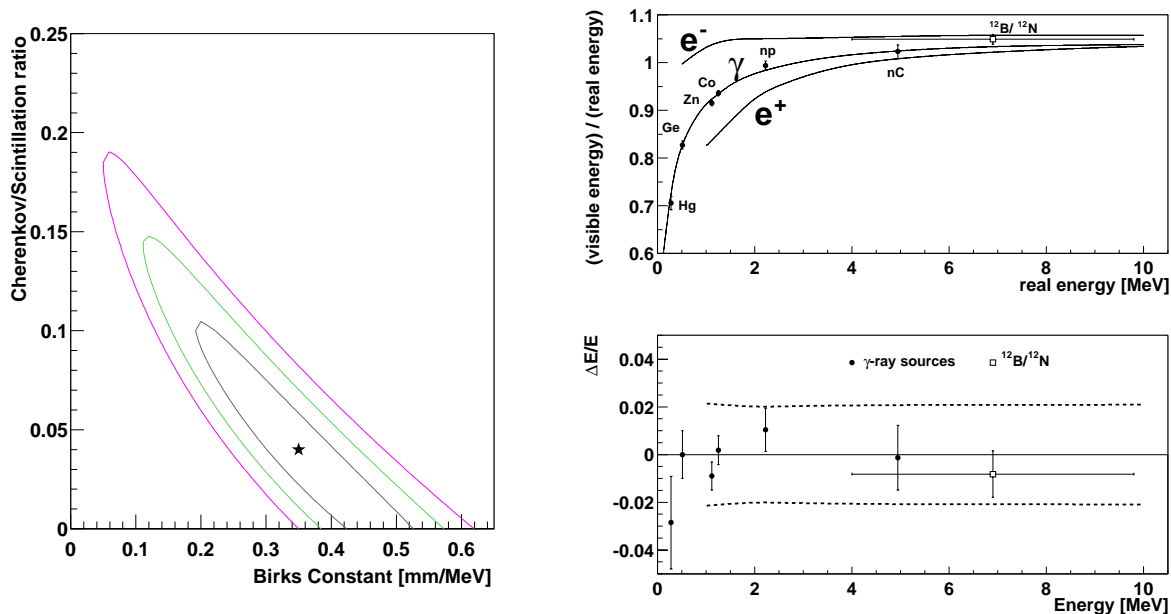


Figure 3.19: Non-linearity of the visible energy to the real energy. (Left) (Right top) (Right bottom)

The systematic uncertainties in the energy scale at the 2.6MeV prompt event energy analysis threshold are listed in Table 3.3. The total value is 1.88% with the 17 inch PMTs only and 2.04% with the 17 inch and 20 inch PMTs. The uncertainties correspond to 2.14% and 2.33% uncertainty in the number of events respectively in an unoscillated reactor $\bar{\nu}_e$ spectrum.

Parameters	Uncertainty (%)	
	17inch only	17inch and 20inch
Time dependence	1.3	1.3
Position dependence	0.92	0.92
20-inch PMT non-linearity	-	0.8
Cherenkov/Birks	1.0	1.0
Total	1.88	2.04

Table 3.3: Systematic uncertainty in the energy scale at $E_{\text{prompt}} = 2.6\text{MeV}$.

3.7 Muon track reconstruction

The KamLAND detector is located at an average rock overburden of 2,700 m.w.e. resulting in 0.34 Hz of cosmic ray muons which go through the inner detector. The cosmic ray muons passing into the detector produce various radioactive isotopes as spallation products via their interactions with scintillator materials. In particular, spallation neutrons, ^8He and ^9Li make correlated background events for the delayed coincidence signal around muon tracks. To reject the correlated background for the $\bar{\nu}_e$ event, the muon track information is very useful. Moreover, if the muon interacts with the scintillator materials and produces many spallation products, a higher energy deposition than usual occurs. The residual charge information reflects this energetic muon information very strongly. In this section, the selection criteria for muons, the tracking algorithm and the definition of the residual charge are described.

3.7.1 Selection criteria

Selection criteria for muon events are as follows,

- (A) $Q_{\text{ID}} \geq 10,000\text{p.e.}$
Total charge sum of the 17 inch PMTs in the inner detector is greater than 10,000 p.e. The event rate with this selection criteria is 0.31-0.32 Hz.
- (B) $Q_{\text{ID}} \geq 500\text{p.e.}$ and $N_{\text{OD}} \geq 5\text{hits}$
Total charge sum of the 17 inch PMTs in the inner detector is greater than 500 p.e. and the number of hits in the outer detector is greater than 5 hits. When a muon go through only the buffer oil region, the muon emits only Cherenkov photons resulting in the lower charge sum. The event rate with this selection criteria is 0.027-0.028 Hz.

Figure 3.20 shows the time interval between muon events (a), and the charge distribution of muon events (b). The muon rate is estimated to be about 0.34 Hz. There are two clear peaks in the charge distribution, which correspond to “through going muons” (scintillation light + Cherenkov light) and “clipping muons” (Cherenkov light), respectively. The clipping muon is defined to be a muon that passes through the inner detector but not through the scintillator.

3.7.2 Muon track reconstruction

The muon track reconstruction is based on the timing information of PMT hits. A muon event generates the Cherenkov photons and scintillation photons along its track in the detector as shown in Figure 3.21. The Cherenkov photons are emitted to the Cherenkov angle θ related to the index of refraction when the later reemission photons are ignored. In the scintillation photon case, the PMTs detect photons in all directions. The observed time at each PMT is expressed as a function of l , which corresponds to the muon path length for earliest photons [81],

$$t = t_0 + \frac{l}{c} + \frac{z-l}{\cos\theta} \cdot \frac{n}{c} \quad (3.31)$$

$$= t_0 + \frac{l}{c} + \sqrt{(z-l)^2 + \rho^2} \cdot \frac{n}{c}, \quad (3.32)$$

where t_0 is the time when a muon entered to the detector, and n is the index of refraction, and the velocity of the muon is approximated to be the speed of light.

Thus, the minimum of t calculated by the equation $dt/dl = 0$,

$$\cos\theta = \frac{1}{n}. \quad (3.33)$$

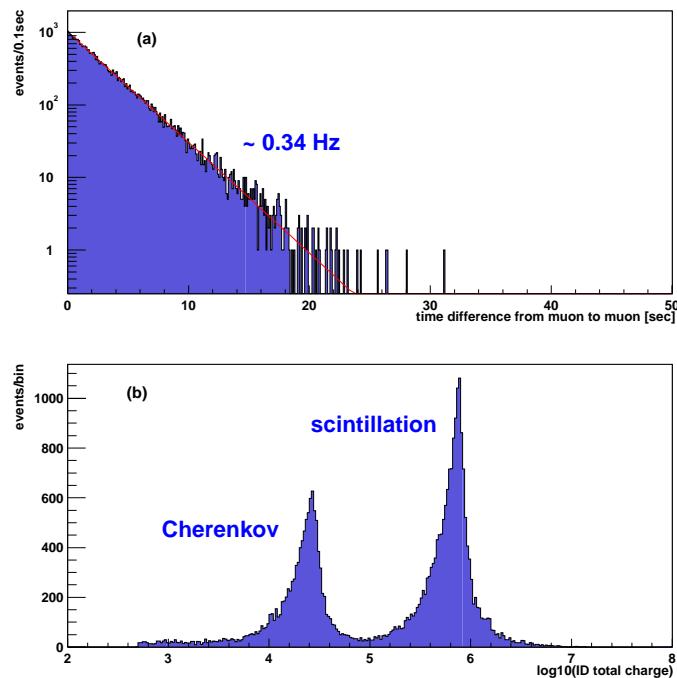


Figure 3.20: (a) Time difference from muon to muon, and the muon rate is estimated to be about 0.34 Hz. (b) Charge distribution of muons. It has two clear peaks, “through going muons” (scintillation light and Cherenkov light) and “clipping muons” (Cherenkov light).

This angle indicates the angle from which the earliest photons come, and it is exactly same as the Cherenkov angle when the velocity of the muon is the same as the speed of light. It allows the simplification of the optical system using only earliest photons. The muon track is reconstructed to get the most balanced track which reproduce the time of PMT hits. In order to avoid the complicated time information, the PMTs out of the range of the Cherenkov angle are not used for the reconstruction. The index of refraction of the liquid scintillator and the buffer oil is measured to be 1.4-1.6 in the various wavelength relevant to the scintillation light. In order to consider the difference of the pass length in the scintillator and buffer oil for each track, that parameter is tuned within the measured value.

When the stopping muon, which stop in the detector, or multi muon events are reconstructed, the above algorithm is not appropriate. The muon which has too small charge sum for the reconstructed track length is classified into the “miss-reconstructed muon”. The miss-reconstructed “through going muon” rate is about 0.2% for all muons. The muon which has too large charge sum for the track length is classified into the “showering muon”, and its fraction is about 1.5% of all muons.

3.7.3 Residual charge

Figure 3.22 shows correlations between the total charge in the inner detector and the muon track length, in the liquid scintillator and in the buffer oil, without miss-reconstructed muons. There are linear correlation between the total charge and the track length. Here, the correlations are

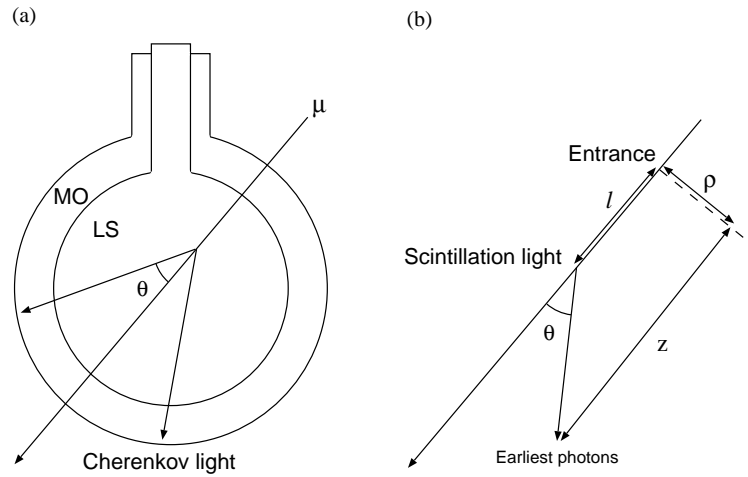


Figure 3.21: Muon track reconstruction. (a) Cherenkov photons are emitted with the Cherenkov angle θ related to the index of refraction. (b) In the scintillation photon case, the PMTs detect photons in all directions, however, the earliest photons come from the θ which corresponds to the Cherenkov angle.

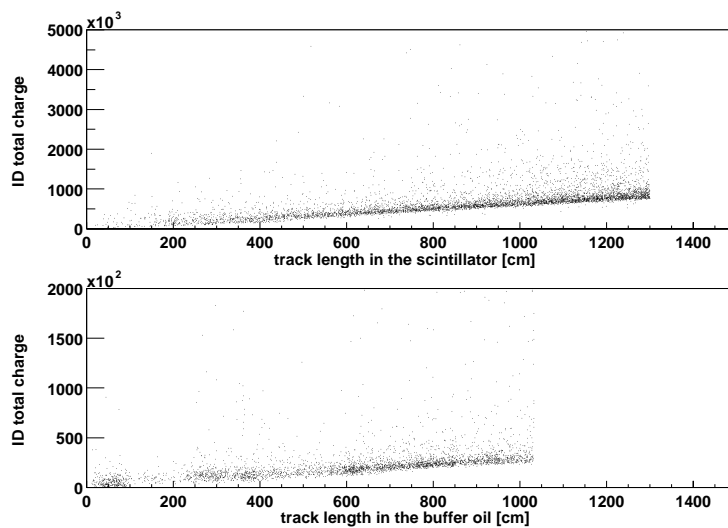


Figure 3.22: Correlations between the total charge in the inner detector and the muon track length, in the liquid scintillator (upper) and in the buffer oil (lower).

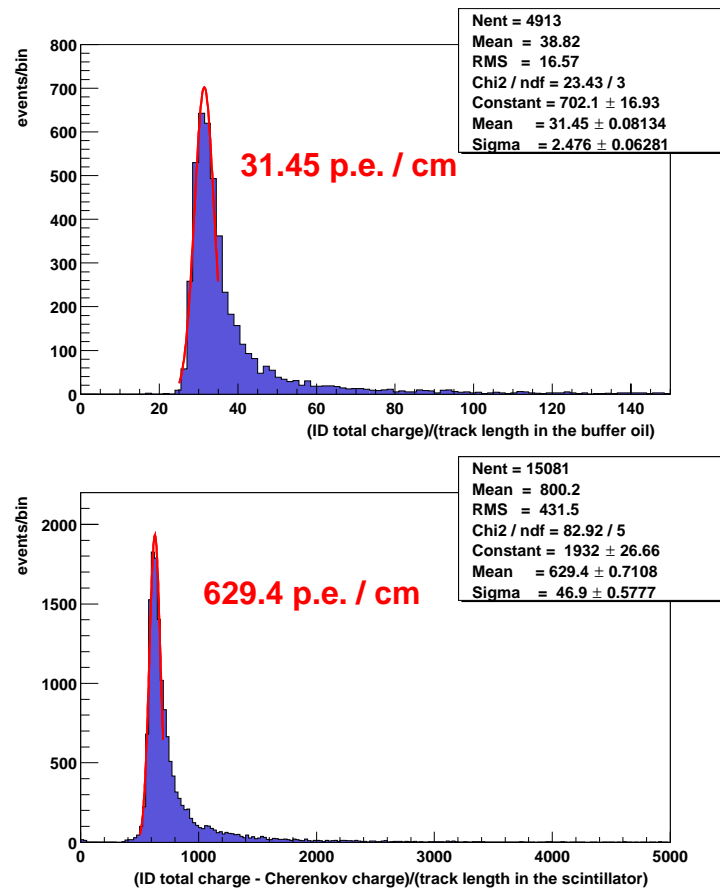


Figure 3.23: Normalized charge by reconstructed muon track length. Upper figure is $(dQ/dX)_{\text{Cherenkov}}$ for clipping muons and lower is $(dQ/dX)_{\text{scintillation}}$ for through going muons.

defined as,

$$\left(\frac{dQ}{dX}\right)_{\text{Cherenkov}} = \frac{Q_{\text{ID}}}{X_{\text{ID}}} : (\text{for clipping muon}) \quad (3.34)$$

$$\left(\frac{dQ}{dX}\right)_{\text{scintillation}} = \frac{Q_{\text{ID}} - L_{\text{ID}} \left(\frac{dQ}{dX}\right)_{\text{Cherenkov}}}{L_{\text{scintillation}}} : (\text{for through going muon}) \quad (3.35)$$

where Q_{ID} , L_{ID} and $L_{\text{scintillation}}$ are the total charge sum of the inner detector, and the reconstructed track length for the inner detector, and the scintillator region. Figure 3.23 shows the distribution of normalized charge by reconstructed muon track length in the buffer oil and in the scintillator. The ideal light emission per length is approximated by the mean of a Gaussian fit with a lower edge,

$$\left(\frac{dQ}{dX}\right)_{\text{Cherenkov}}^{\text{ideal}} = 31.45 \text{ p.e./cm} \quad (3.36)$$

$$\left(\frac{dQ}{dX}\right)_{\text{scintillation}}^{\text{ideal}} = 629.4 \text{ p.e./cm}. \quad (3.37)$$

The $(dQ/dX)_{\text{scintillation}}$ is about 20 times higher than the $(dQ/dX)_{\text{Cherenkov}}$.

In this thesis, the parameter of the residual charge ΔQ is often used because it has a good correlation with the production rate of spallation products. The residual charge is defined as,

$$\Delta Q = Q_{\text{ID}} - L_{\text{ID}} \cdot \left(\frac{dQ}{dX}\right)_{\text{Cherenkov}}^{\text{ideal}} - L_{\text{scintillation}} \cdot \left(\frac{dQ}{dX}\right)_{\text{scintillation}}^{\text{ideal}}. \quad (3.38)$$

The tracking performance is also verified by the correlation between spallation neutrons and reconstructed muon tracks. The efficiency within 2 m and 3 m from the muon track is evaluated to be 90.7% and 93.8% respectively. The reconstructed track information is used for the background estimation and reduction (spallation cut).

3.8 Noise event selection (Noise cut)

The ‘‘noise event’’ (Left panel of Figure 3.24) is defined as the event which has no timing cluster in PMT hits. It is selected using a following criterion,

$$n100 \leq (\text{nhit} + 50)/2, \quad (3.39)$$

where the ‘‘nhit’’ means the number of PMT hits in a event and ‘‘n100’’ means the number of the maximum PMT hits within a 100 nsec time window in a event. Most of noise events are created by unstable conditions of the data taking, the ringing problem of the electronics after muons or the data transfer problem during unexpectedly high trigger rate.

The accidental noise rate is calculated using the trigger rate ($\sim 250\text{Hz}$) of the low threshold special run, in which threshold is a 100 trigger hit, i.e. a half level of the normal run,

$$(\text{accidental noise rate}) = 250 \text{ Hz} \times 250 \text{ Hz} \times 100 \text{ nsec} \sim 6 \times 10^{-3} \text{ Hz},$$

and its rate is almost consistent with the actual noise rate $\sim 5 \times 10^{-3} \text{ Hz}$. The inefficiency for the normal run due to the noise selection cut is calculated using its trigger rate $\sim 21\text{Hz}$,

$$(\text{inefficiency by noise cut}) = 21 \text{ Hz} \times 100 \text{ nsec} \sim 2 \times 10^{-4} \%,$$

and assigned as the systematic uncertainty.

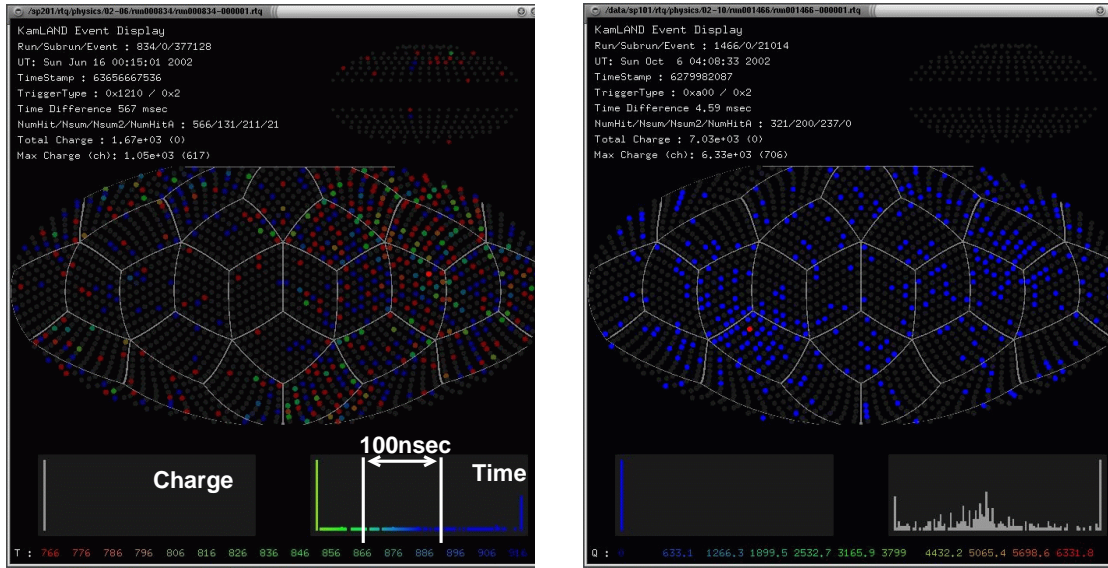


Figure 3.24: Event displays of a typical noise event (Left) and a typical flasher event (Right).

3.9 Flasher event selection (Flasher cut)

The “flasher event” (Right panel of Figure 3.24) is caused by light emission from the PMT presumably due to discharge in dynodes. The surrounding PMTs detect the light from the flasher PMT. The flasher signal mimics the high energy event up to ~ 20 MeV, however, they are easy to select using the maximum of the PMT charge. The selection criteria are,

- Total charge in the inner detector ≥ 2500 p.e.
- Ratio of the maximum of the PMT charge to the total charge sum ≥ 0.6 .

The flasher event rate is 3×10^{-3} Hz, which corresponds to $\sim 0.01\%$ of total low energy events. Therefore, the inefficiency of the flasher cut is estimated to be less than 0.01%.

Chapter 4

Background estimation

There are various radioactivities in the detector, and some of them are coming into the detector from outside of produced by the spallation of cosmic-ray muon. Main radioactive impurities which contained in the scintillator are ^{238}U (including ^{222}Rn and ^{210}Pb), ^{232}Th , ^{40}K and ^{85}Kr . Incoming radioactivities are γ -ray of ^{40}K and ^{208}Tl , cosmic-ray muon, fast neutron. ^{40}K is mainly emitted from the rope of the scintillator balloon. ^{208}Tl is emitted from the surrounding rock or the surface of the PMTs. The cosmic-ray muons create various spallation products, neutron, ^{12}B , ^{12}N , ^9B , ^8B , ^8Li and neutron emitters (^8He and ^9Li). The fast neutron is produced in the rock or in the outer detector by the muon spallation and comes into the inner detector. Some of their characteristic decay makes correlated events, and these are background for the $\bar{\nu}_e$ event. Moreover, accidental coincidence makes uncorrelated background. Its contribution is estimated by using same selection criteria as $\bar{\nu}_e$ without the condition for time window cut. On the other hand, to avoid background $\bar{\nu}_e$'s from uranium and thorium decaying in the Earth (geo-neutrinos [30], Figure 2.4), a prompt event energy analysis threshold of 2.6MeV is applied for the reactor $\bar{\nu}_e$ event selection.

The estimated background events in the total livetime are summarized in Table 4.1. The total number of background events is 17.8 ± 7.3 .

4.1 Single event distribution

Figure 4.1 shows vertex distributions of various energy regions. The veto for 2 msec following muons has already applied for all plots in this figure. The most intensive region is the top of the detector around the chimney because there are various stainless steel materials to hang the scintillator balloon. The spallation products like ^{12}B , ^{12}N are dominant above several MeV energy range. The life time of them is longer than 2 msec. The vertex distribution of them

Background	2.6MeV threshold
Accidental	2.69 ± 0.02
Fast neutrons	< 0.89
Spallation	4.8 ± 0.9
$^{13}\text{C}(\alpha, n)^{16}\text{O}$	10.3 ± 7.1
Total	17.8 ± 7.3

Table 4.1: Summary of background estimation.

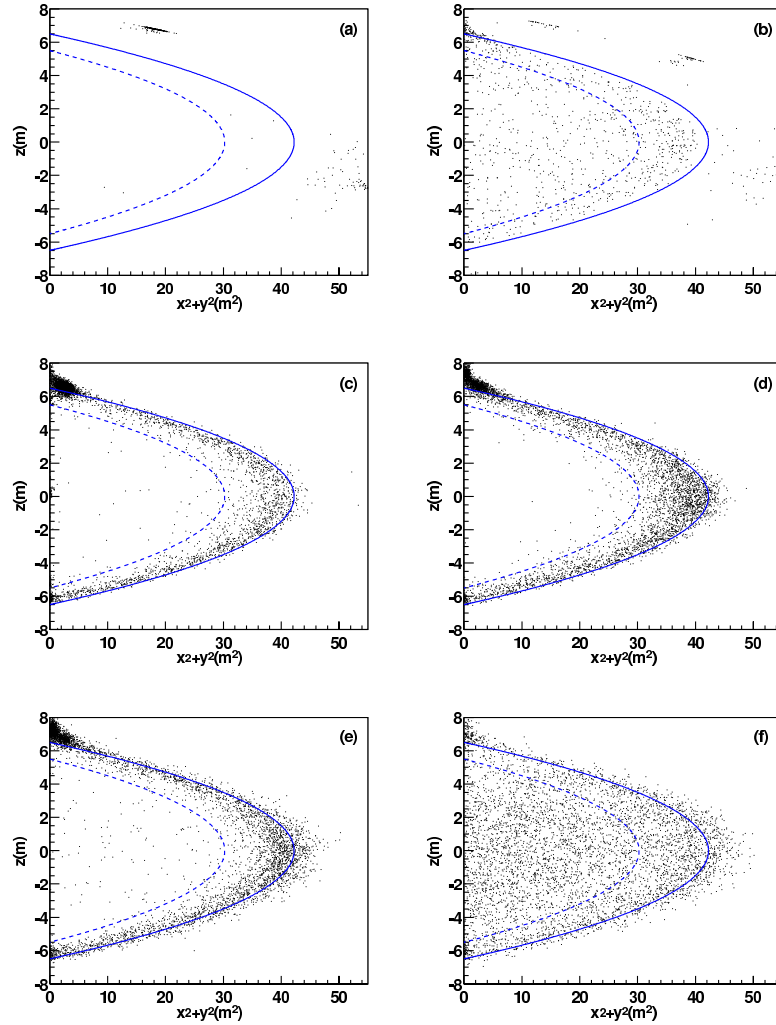


Figure 4.1: Vertex distribution of each energy range in the whole volume. The energy ranges are (a) $>15\text{MeV}$, (b) $7\text{-}15\text{MeV}$, (c) $3\text{-}7\text{MeV}$, (d) $2\text{-}3\text{MeV}$, (e) $1\text{-}2\text{MeV}$, and (f) $0.5\text{-}1\text{MeV}$. Intensive region is exists around the equator and outside of the scintillator balloon in higher energy. There are considered to be stop or clipping muon events because there is no PMT in the outer detector around equator and the water buffer is thin. The most intensive region is the top of the detector around the chimney. The event distribution is uniform at long life (> 2 msec) spallation products energy region or below 1 MeV region. External radiations from ^{40}K and ^{208}Tl are dominant at MeV order energy region.

looks uniform, while there are small affection from the stop muons around the equator. From one to several MeV energy range, many events are observed near the balloon edge as shown in Figure 4.1 (c)-(e).

The most probable explanation for the Figure (c) is the radiation from the dust on the surface of the balloon inside, for example $\beta + \gamma$ decay of ^{208}Tl (^{232}Th chain) gives about 5 MeV energy deposition in the scintillator. The Figure (c) and (d) indicate the attenuation of external radiations, γ -rays from ^{208}Tl (2.62 MeV) and ^{40}K (1.46 MeV). The most of 2.62 MeV γ -rays of ^{208}Tl are emitted from the outside of the detector, because many radioactive isotopes like ^{238}U and ^{232}Th are contained in the surrounding rock and the ^{208}Tl is the daughter isotope of the ^{232}Th . Its event rate is about 3 Hz. On the other hand, the most of 1.46 MeV γ -rays of ^{40}K are emitted from the inside of the balloon ropes. The balloon ropes contain $8.3 \times 10^{-10}\text{g/g}$ of ^{40}K , and its decay rate is 21.6 Bq (γ -ray 2.3 Bq). This must be the delayed event of the accidental background because the cut condition of the delayed energy is 1.8-2.6 MeV in $\bar{\nu}_e$ selection.

Below 1 MeV, the distribution of events is uniform as in the Figure (f). The most of them are ^{85}Kr and ^{210}Bi (^{210}Pb). The half-life time of ^{85}Kr is $\tau = 10.756\text{y}$ and it decays to ^{85}Rb via β -decay (99.5%, $Q_\beta = 687\text{keV}$) or $\beta + \gamma$ (0.43%, $Q_\beta = 173\text{keV} + E_\gamma = 514\text{keV}$). The ^{210}Pb , which is the daughter isotope of ^{222}Rn (^{238}U), is contained in the detector. The half-life time of it is $\tau = 22.3\text{y}$ and it decays to ^{210}Bi ($Q_\beta = 64\text{keV}$). The ^{210}Bi decays to ^{210}Po via β -decay ($\tau = 5.013\text{d}$, $Q_\beta = 1.163\text{MeV}$).

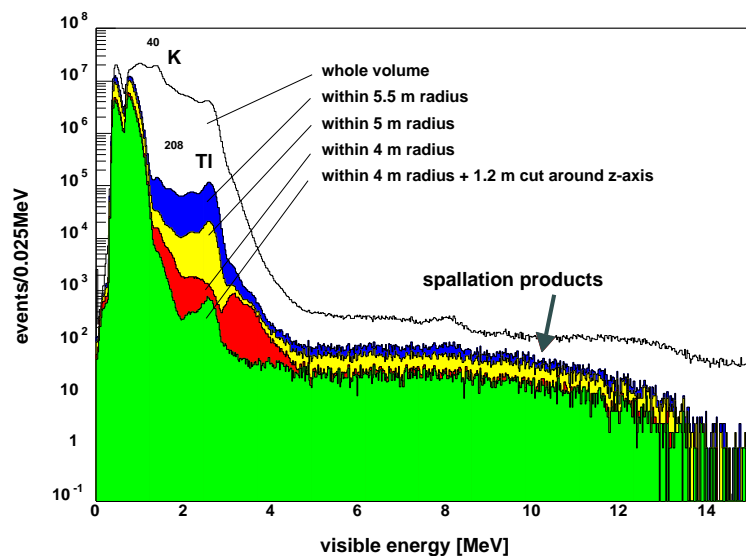


Figure 4.2: Energy spectra of single events with fiducial radius. External radiations, γ -rays from ^{208}Tl (2.62MeV) and ^{40}K (1.46MeV) are strongly suppressed by the cut of the fiducial radius. Along the central z-axis intensive radiations are observed around 1.5-4 MeV.

Figure 4.2 shows the energy spectrum at various fiducial volume conditions. From the top, whole volume, $R < 5.5\text{m}$, 5m, 4m fiducial cuts are plotted. The lowest histogram shows the histogram of the 4 m cut and the central cylindrical cut with 1.2 m radius. A bump around 0.8 MeV indicates the prompt trigger threshold and that around 0.5 MeV indicates the delayed trigger threshold. Peaks around 1.46 MeV correspond to the γ of ^{40}K from balloon surfaces, ropes or outside the balloon. Peaks around 2.62 MeV is the γ of ^{208}Tl from balloon surfaces or the surrounding rock. Due to the energy resolution ($\sigma/\sqrt{E(\text{MeV})} \sim 7.5\%$), the observed

energy of the 2.62 MeV γ -ray has the distribution. γ -rays from ^{208}Tl , which is originally $\simeq 3$ Hz, are strongly suppressed by the fiducial volume cut, and the single rate becomes $\simeq 0.01$ Hz. The dominant sources above 5 MeV are the spallation products from muon. The histogram of 4 m fiducial show the similar event rates as that of 5 m fiducial at the energy region larger than 3 MeV. This is why the dominant background sources are concentrated in the center. There are three thermometers and their cables along the z-axis. Furthermore, some radon can be contaminated and emanated from the top of the detector into these regions when calibration device is put on along the z-axis. The bottom histogram labeled “4 m + cylinder 1.2 m cut” means the cylindrical region with radius 1.2 m along z-axis is cut to remove events of these regions. This histogram shows the dominant sources from 3 MeV to 4 MeV is coming from the center regions.

4.2 Background for reactor $\bar{\nu}_e$ selection

4.2.1 Accidental background

The accidental background is estimated by the same cut as the $\bar{\nu}_e$ selection criteria except for the different time window. To reduce the statistical error from the accidental background estimation, a wider time window is used. The time window for delayed events is between 10 msec to 20 sec after prompt events. The time window later than 10 ms is determined to remove the neutron capture events which capture time is $\sim 210\mu\text{sec}$. The position difference between the prompt and delayed events is $\Delta R < 2\text{m}$. The event energies are required to be $2.6\text{MeV} < E_{\text{prompt}}$ and $1.8\text{MeV} < E_{\text{delayed}} < 2.6\text{MeV}$. The fiducial radius is $R < 5.5\text{m}$ and the spallation cut is performed.

Figure 4.3 shows the time and energy spectrum of the accidental events for 5.5 m fiducial volume. Time spectrum is flat in the whole time window of 10 msec and 20 sec as expected for random coincidence. This rate is extrapolated into the $\bar{\nu}_e$ selection time window of $0.5\mu\text{sec}$ and $1000\mu\text{sec}$. The events around 1 MeV caused by ^{210}Bi β -decays in the LS, there are no contribution in 2.6 MeV threshold analysis. The events around 2.6 MeV are caused by ^{208}Tl γ generated in the rock. Fiducial cut criteria are decided by the ^{208}Tl γ background rate. The total accidental events are estimated to be 2.69 ± 0.02 above 2.6 MeV threshold. This means that the rate of the accidental background is 0.0052 events/day at 2.6 MeV threshold. This accidental background rate is small enough compared with the reactor $\bar{\nu}_e$ rate (~ 0.7 events/day) in no oscillation case.

4.2.2 ^9Li and ^8He spallation products

There are several nuclei from ^{12}C in the liquid scintillator produced by interaction with cosmic ray muons which emit neutron after β -decays as shown in Table 4.2. The isotopes with long lifetime are more critical for delayed coincidence analysis, because backgrounds from the shorter-lived isotopes are easily removed by the spallation cut. The selection criteria for these isotopes are same one as that of $\bar{\nu}_e$ without the spallation cut. Prompt energy spectrum is shown in Figure 4.4. From this figure, dominant source from the neutron emitter is ^9Li .

To estimate the contribution of these backgrounds within the reactor $\bar{\nu}_e$ samples, decay time of the ^9Li nuclei was studied. The $^8\text{He}/^9\text{Li}$ samples are divided into two cases, showering and non-showering muon induced events. Showering muon is defined as such that the residual charge of muon is larger than 10^6 p.e. and non-showering muon is defined that residual charge of muon is less than 10^6 p.e. As these elements are mainly produced by showering muons, the

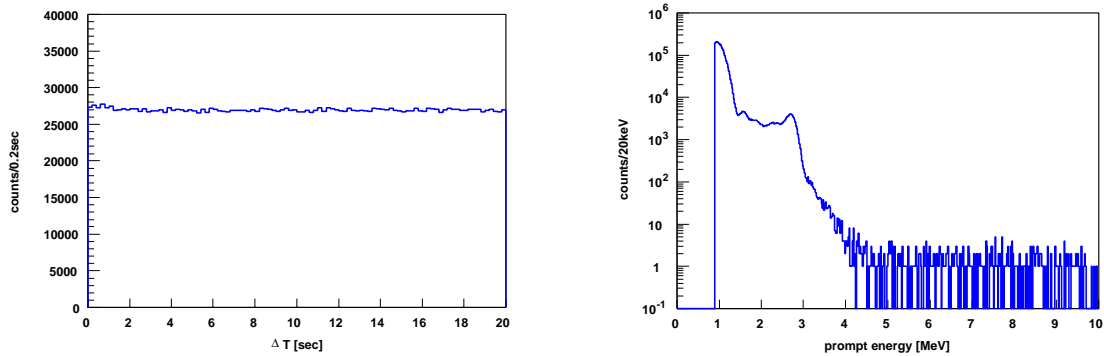


Figure 4.3: Accidental time and energy spectrum for 5.5 m fiducial volume. Time spectrum is flat in the whole time window of 10 msec and 20 sec. The events around 1 MeV are caused by ^{210}Bi β -decays in the LS and the events around 2.6 MeV are caused by ^{208}Tl γ generated in the rock.

Isotope	Production reaction	Half-life (msec)	Decay mode	Energy (MeV)	Fraction of decays
^8He	$^{12}\text{C}(\gamma, 4\text{p}), ^{12}\text{C}(\pi^-, \text{n}3\text{p})$	119	β^-	10.7	0.84
			$\beta^- + \text{n}$		0.16
^9Li	$^{12}\text{C}(\gamma, 3\text{p}), ^{12}\text{C}(\pi^-, \text{n}2\text{p})$	178	β^-	13.6	0.52
			$\beta^- + \text{n}$		0.48
^{11}Li	$^{12}\text{C}(\gamma, 2\pi^+\text{p}), ^{12}\text{C}(\pi^-, \pi^+\text{p})$	8.5	β^-	20.6	0.07
			$\beta^- + x\text{n}$		0.92
^{12}Be	$^{12}\text{C}(\gamma, 2\pi^+), ^{12}\text{C}(\pi^-, \pi^+)$	11.4	β^-	11.7	-
			$\beta^- + \text{n}$		-

Table 4.2: Nuclei emit neutron after β -decays which mimic delayed coincidence signal. These nuclei are produced by the interaction between cosmic ray muons and the ^{12}C in the liquid scintillator.

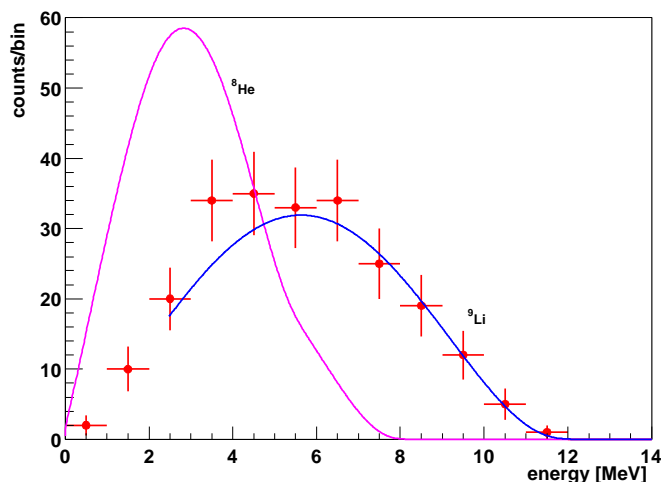


Figure 4.4: Prompt energy spectrum of ${}^9\text{Li}/{}^8\text{He}$ events within 500 msec following showering muons. The blue line and purple line are the theoretical lines of ${}^9\text{Li}$ β -decay and ${}^8\text{He}$ β -decay respectively.

cut condition for those is more severe. Total volumes are vetoed for 2 seconds. On the other hand, 3m cylindrical cut along to the muon track for non-showering muons are applied for 2 seconds.

Figure 4.5(a) shows the time distribution for showering muon in fiducial volume and Figure 4.5(b) shows that for non-showering muon with the distance within 3m from the muon track. As clearly shown, the event rate from showering muons is more than that of non-showering ones. These data are fit by exponential function plus constant background. The decay time of ${}^8\text{He}$ and ${}^9\text{Li}$ are fixed to the each lifetime, 171.7 msec and 257.2 msec respectively. The production ratio of ${}^8\text{He}$ to ${}^9\text{Li}$ is free parameter. Total events from showering muons are estimated to be 350 ± 30 , and those from non-showering muons are 86 ± 17 within 3 m from the muon track.

To estimate the background rates after the spallation cut, tracking efficiency of the muon fitter is used. Figure 4.5(d) shows the distance distribution of spallation neutron ($\mu + {}^{12}\text{C} \rightarrow \mu + n + \text{Nuclei}$) events for non-showering muons. For non-showering muons, 3 m cylindrical cut along the muon track are applied for 2 sec. The efficiency of the muon tracking within 3 m is estimated to be 93.8%. This means that 6.2% of total spallation events remains after spallation cut. The remained background rates are estimated to be $(86 \pm 17) \times 0.062/0.938 = 5.7 \pm 1.1$ per whole data samples. For showering muons, all volume veto are applied for 2 sec. The event rate at the 2.6MeV energy threshold is calculated from 0.9MeV threshold result by using the expected energy spectrum. 85% of the total events are contaminated into the energy threshold 2.6MeV, The remained background after the spallation cut is estimated to be 4.8 ± 0.9 events at 2.6 MeV energy threshold.

Figure 4.5(c) shows the decay time of events from the non-showering muon with the distance more than 3m away from the muon track. The solid line is also fitting result and it is consistent with estimated value.

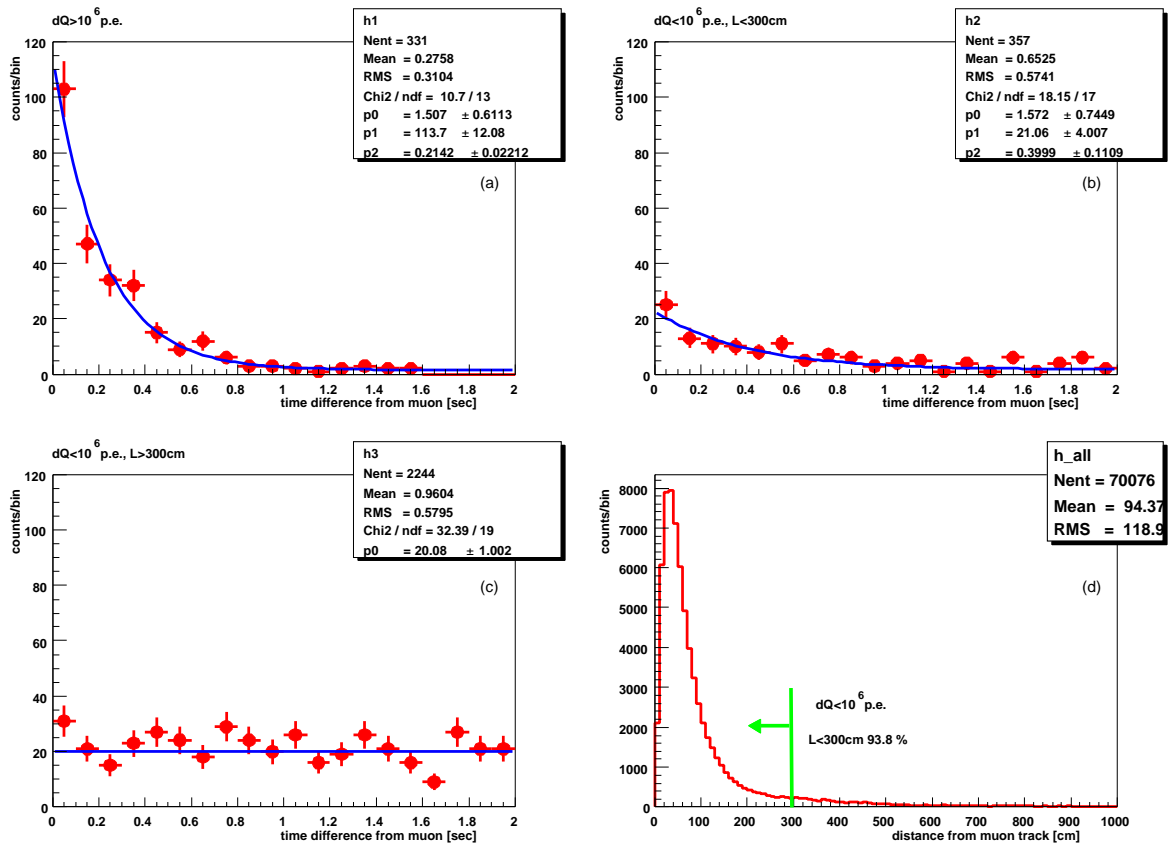


Figure 4.5: (a) Time distribution of showering muon events. (b) Time distribution of non-showering muon events within 3m radius cylinder around the muon track. The fitting results by the exponential plus constant background function are also shown. The decay time is fixed to be the lifetime of ${}^9\text{Li}$. (c) Time distribution of non-showering muon events without 3m from the track. (d) Distance distribution of non-showering muon event.

4.2.3 Fast neutron

Fast neutrons mimic delayed coincidence because it interacts proton and the recoiled proton emits scintillation light and the neutron are finally captured by proton and emits 2.22 MeV γ -rays. Most external fast neutrons are produced by muons which pass through both the outer detector and the surrounding rock. This background is studied by detecting delayed coincidence events tagged with a muon which passed only in the outer detector (triple coincidence). Decay electron from primary muon decay (Michel electron following muon) which concentrates around the scintillator balloon edge is observed as well as the fast neutron. The lifetime of the decay electron is $2.197\mu\text{sec}$ and it can be separated with the time interval cut less than $10\mu\text{sec}$. The event selection cuts for the time difference and position difference between the prompt and delayed event are $10\mu\text{sec} < \Delta T < 1000\mu\text{sec}$ and $\Delta R < 2\text{m}$, respectively. The event energies are required to be $2.6\text{MeV} < E_{\text{prompt}} < 14\text{MeV}$ and $1.8\text{MeV} < E_{\text{delayed}} < 2.6\text{MeV}$. The fiducial radius is $R < 5.5\text{m}$ and the spallation cut is performed. The OD hits are required to be more than 5.

Figure 4.6 (a) shows the time correlation between prompt and delayed signal. The fitted value of capture time is $214.9 \pm 23.7\mu\text{sec}$, which is consistent with the estimation from spallation neutrons by muons ($211.2 \pm 2.6\mu\text{sec}$). Figure 4.6 (b) shows the energy spectrum of neutron capture γ signal. Figure 4.6 (c) shows the prompt event vertex position as a function of distance from the detector center. The attenuation length of neutron from outside to inside are estimated from the radius distribution. The fitting result of the attenuation length is $29.7 \pm 3.4\text{ cm}$, and the worst case (33.1 cm) of this fit are used for estimation of the fast neutron contamination in the fiducial volume. The total number of events of fast neutrons is estimated to be less than 4.3 events. These events can be rejected for the $\bar{\nu}_e$ analysis using the OD hits. However, the outer detector has small inefficiency. The efficiency of the outer detector is larger than 92%, so the miss-tagging events is less than 0.37. Figure 4.6 (d) shows the energy spectrum of recoiled proton by the fast neutron. These samples don't indicate any distinctive shapes and are consistent with the flat distribution.

The fast neutron contribution from rock surrounding the detector are calculated by simple simulation. The total ratio of neutron contribution, (neutron from muon not going through anti-counter but going through surrounding rock) / (neutron from muon going through anti-counter), is 0.11. So the contribution from rock is less than 0.52 events. The upper limit of fast neutron background events for the reactor $\bar{\nu}_e$ detection is estimated to be less than 0.89.

4.2.4 $^{13}\text{C}(\alpha, n)^{16}\text{O}$

A correlated background comes indirectly from α decays in the liquid scintillator. Special runs to observe the decay of ^{222}Rn daughter ^{210}Po establish that there were $(1.47 \pm 0.20) \times 10^9$ α decays during the livetime of data taking. At the construction of the KamLAND detector ^{222}Rn existed in the detector, and now, it is thought the daughter nuclei ^{210}Pb (half-life 22.3y) is in the radiation equilibrium.

The target nuclei of (α, n) reaction are listed in Table 4.3. The target which has large energy threshold or small natural abundance is negligible. Figure 4.7 shows the total cross sections of (α, n) reactions for various target nuclei, and their cross sections are normalized with the number of target, which is calculated from the composition of liquid scintillator and the natural abundance. The α energy emitted from ^{210}Po is 5.304 MeV, so the dominant reaction is $^{13}\text{C}(\alpha, n)^{16}\text{O}$. For ^{13}C , abundance in the KamLAND liquid scintillator is measured as $(^{13}\text{C}/^{12}\text{C}) = 0.0109293 \pm 0.0000011$. It is consistent with the natural abundance of ^{13}C , 1.10%.

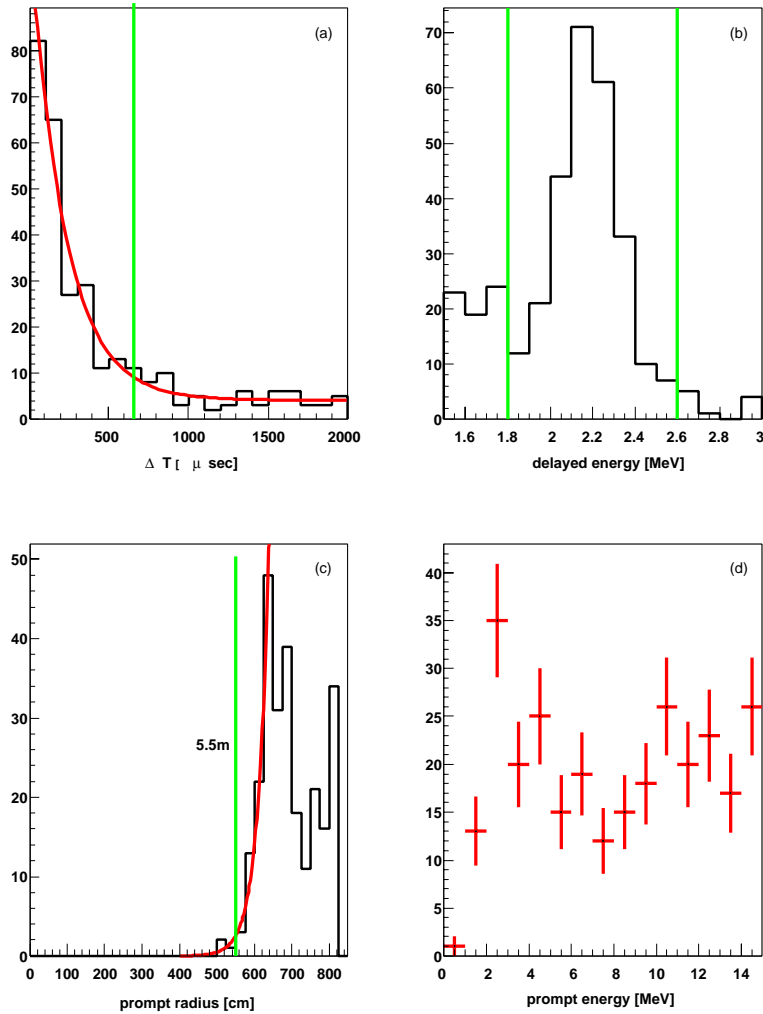


Figure 4.6: Fast neutron candidates. (a) Time correlation between prompt events and observed events. The observed mean capture time is $214.9 \pm 23.7 \mu\text{sec}$. (b) The energy distribution of the delayed neutron captured gamma events. (c) Distance distribution of the prompt events. The fitting result of the attenuation length is 29.7 ± 3.4 cm. (d) Energy distribution of the prompt events.

Target nuclei	Q value (MeV)	Threshold (MeV)	Natural abundance (%)
^1H	-23.68	115.4	99.985
^2H	-4.19	12.50	0.015
^3H	-4.78	11.12	-
^{12}C	-8.50	11.34	98.90
^{13}C	2.22	0	1.10
^{14}C	-1.82	2.34	-
^{14}N	-4.73	6.09	99.634
^{15}N	-6.42	8.13	0.366
^{16}N	1.52	0	-
^{16}O	-12.13	15.17	99.762
^{17}O	0.59	0	0.038
^{18}O	-0.70	0.85	0.200
^{19}O	5.71	0	-

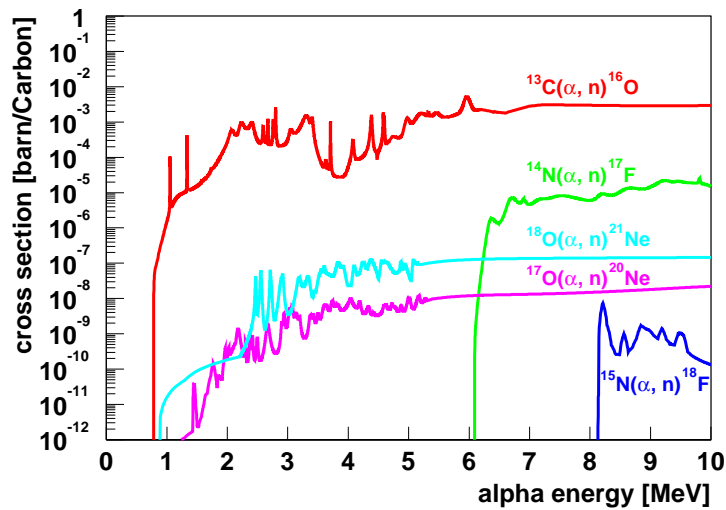
Table 4.3: Target nuclei of (α, n) reaction [58, 59].

Figure 4.7: Total cross sections of (α, n) reactions for nuclei, ^{13}O , ^{14}N , ^{15}N , ^{15}N , ^{17}O , and ^{18}O . The cross sections are normalized with the number of target, which is calculated from the composition of liquid scintillator and the natural abundance. The dominant reaction is $^{13}\text{C}(\alpha, n)^{16}\text{O}$ at the α energy 5.304 MeV, emitted from ^{210}Po .

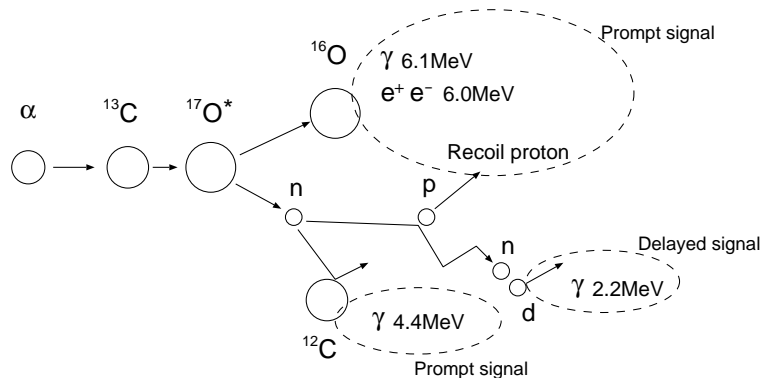


Figure 4.8: $^{13}\text{C}(\alpha, n)^{16}\text{O}$ correlated background. The first excited state of ^{16}O emits the 6.049 MeV e^+e^- with initial pair creation, and the second excited state of that emits the 6.130 MeV γ -ray. The 4.4MeV γ -ray is emitted from γ decays following neutron inelastic scattering on ^{12}C , $^{12}\text{C}(n, n\gamma)^{12}\text{C}$. The observed energy of recoil protons from neutron-proton elastic scattering is mostly quenched below 2.6MeV. The 2.2 MeV γ -ray from thermal neutron capture on protons performs as the delayed signal.

The signal of the 5.3MeV α -particle is quenched below the energy threshold, but the secondary reaction $^{13}\text{C}(\alpha, n)^{16}\text{O}$ produces events above 2.6MeV as shown in Figure 4.8. The $^{13}\text{C}(\alpha, n)^{16}\text{O}$ reaction may populate states in ^{16}O at 6.05, 6.13, 6.92 and 7.12 MeV, with spins and parities 0^+ , 3^- , 2^+ and 1^- respectively; the 6.05 MeV state decays by pair emission (internal pair creation) and the other three states by gamma emission. The Q value of $^{13}\text{C}(\alpha, n)^{16}\text{O}$ reaction is 2.216 MeV, so 5.304 MeV α particle may produce the 6.05, 6.13 MeV states and the grand state of ^{16}O .

Figure 4.9 (a) shows the cross section of $^{13}\text{C}(\alpha, n)^{16}\text{O}$ with a function of the α energy in the laboratory system. The number of $^{13}\text{C}(\alpha, n)^{16}\text{O}$ reaction is calculated as follows,

$$N = \int_{E_0}^0 dE_\alpha \left(-\frac{dN}{dE_\alpha} \right), \quad (4.1)$$

$$-\frac{dN}{dE_\alpha} = n_{\text{target}} I_{\text{source}} \sigma(E_\alpha) \left(-\frac{dX}{dE_\alpha} \right), \quad (4.2)$$

$$E_\alpha : \alpha \text{ energy} \quad (4.3)$$

$$E_0 : \text{Incident } \alpha \text{ energy} \quad (4.4)$$

$$n_{\text{target}} : \text{Number of target} \quad (4.5)$$

$$I_{\text{source}} : \text{Source intensity} \quad (4.6)$$

$$\sigma(E_\alpha) : (\alpha, n) \text{ cross section} \quad (4.7)$$

$$\frac{dX}{dE_\alpha} : \text{Stopping power.} \quad (4.8)$$

Figure 4.9 (b) shows stopping power of the liquid scintillator in KamLAND.

The neutron energy depends on the scattering angle, because the recoiled ^{16}O carry away a portion of the reaction energy. For 5.304 MeV α , the neutron energy distribution has the width of 2.65 MeV between forward scattering and backward scattering. The angular distribution of neutron can be expressed by a Legendre-polynomial [60, 61]. The neutron energy spectrum is

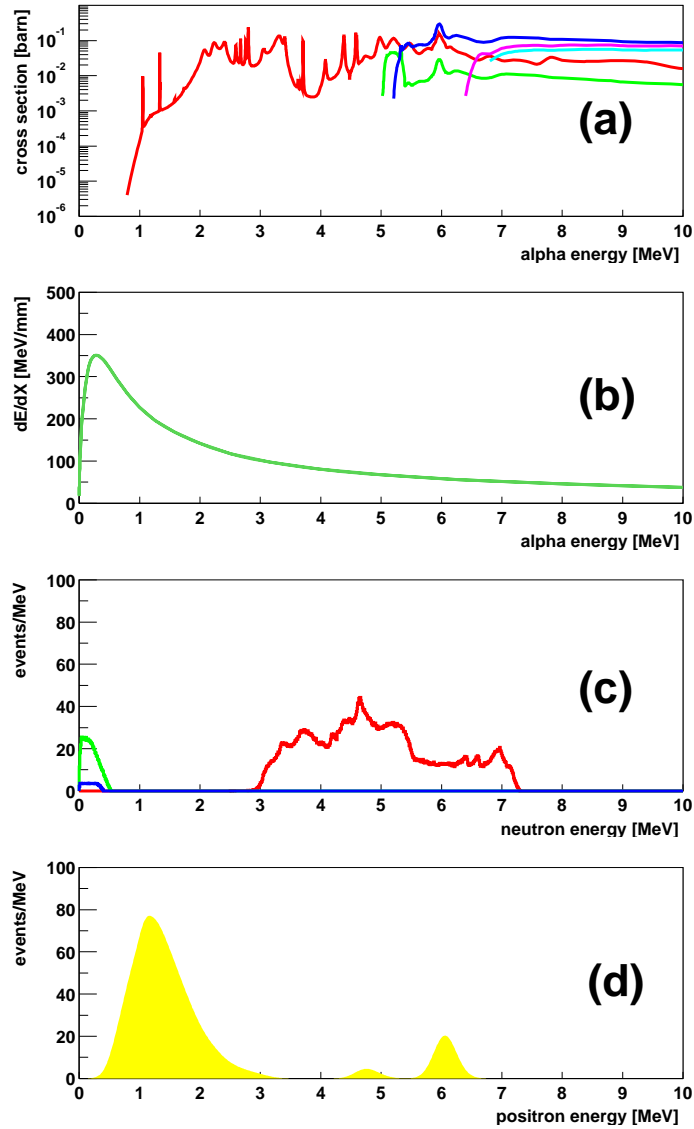


Figure 4.9: Energy spectra for $^{13}\text{C}(\alpha, n)^{16}\text{O}$ background. (a) Cross section of $^{13}\text{C}(\alpha, n)^{16}\text{O}$ with a function of the α energy in the laboratory system. The red, green, blue, pink and sky blue lines are cross section for grand, first excited, second excited, third excited, fourth excited state of ^{16}O , respectively. (b) Stopping power of the liquid scintillator in KamLAND. (c) Neutron energy distribution of $^{13}\text{C}(\alpha, n)^{16}\text{O}$ in positron scale. The recoil of protons can be simulated with the MC. The quenching factor of proton is calculated from the Birk's constant, which is estimated by the energy of ^{210}Po , ^{214}Po , and ^{212}Po .

calculated as follows,

$$n(E_n) = \int_{E_0}^0 dE_\alpha \int d\Omega \delta(\Omega, E_\alpha, E_n) n_{\text{target}} I_{\text{source}} \frac{d\sigma}{d\Omega} \left(-\frac{dX}{dE_\alpha} \right) \quad (4.9)$$

$$\frac{d\sigma}{d\Omega} = \sum_{\nu} A_{\nu} P_{\nu}(\cos\theta) \quad (4.10)$$

$$E_n : \text{Neutron energy} \quad (4.11)$$

$$\Omega : \text{Scattering solid angle} \quad (4.12)$$

$$\delta(\Omega, E_\alpha, E_n) : 1(\text{Conservation of momentum}) \text{ or } 0 \quad (4.13)$$

$$A_{\nu} : \text{Coefficients of Legendre - polynomial} \quad (4.14)$$

$$P_{\nu}(\cos\theta) : \text{Legendre - polynomial.} \quad (4.15)$$

The neutron energy distribution are shown in Figure 4.9 (c).

The recoil of protons can be simulated with the MC. The quenching factor of proton is calculated from the Birk's constant, which is estimated by the energy of ^{210}Po , ^{214}Po and ^{212}Po . Figure 4.9 (d) shows the energy distribution of $^{13}\text{C}(\alpha, n)^{16}\text{O}$ in positron scale. The 6.049 MeV e^+e^- by internal pair creation and 6.130 MeV γ are observed at 2.6 MeV energy threshold as well as the 4.438 MeV γ by $^{12}\text{C}(n, n\gamma)^{12}\text{C}$. The (α, n) background is summarized in Table 4.4. The conservative error for the (α, n) background each energy is assigned as follows. For the recoil protons, 32% scale error is assigned, corresponding to the decay rate of ^{210}Po , cross section of the $^{13}\text{C}(\alpha, n)^{16}\text{O}$ reaction for the grand state of ^{16}O , and the angular distribution of the neutron. As error for the quenching factor of proton, 10% is assigned. For the γ -ray from $^{12}\text{C}(n, n\gamma)^{12}\text{C}$ reaction, 32% scale error is assigned, corresponding to the decay rate of ^{210}Po , cross section of the $^{13}\text{C}(\alpha, n)^{16}\text{O}$ reaction for the grand state of ^{16}O , the angular distribution of the neutron, and cross section of the $^{12}\text{C}(n, n\gamma)^{12}\text{C}$ reaction. For the e^+e^- and γ -ray from the excited state of ^{16}O , 100% scale error is assigned, corresponding to the decay rate of ^{210}Po and cross section of the $^{13}\text{C}(\alpha, n)^{16}\text{O}$ reaction for the first and second state of ^{16}O . The total number of expected events is 10.31 ± 7.14 at 2.6 MeV energy threshold.

Source	Energy	Events	Events (>2.6MeV)	Error
Recoil proton	Low energy	67.30	1.5	$1.5 \times 32\%$
γ -ray from $^{12}\text{C}(n, n\gamma)^{12}\text{C}$	~ 4.4 MeV	1.71	1.71	$1.71 \times 32\%$
e^+e^- from first excited state of ^{16}O	~ 6 MeV	6.18	7.1	$7.1 \times 100\%$
γ -ray from second excited state of ^{16}O	~ 6 MeV	0.92		
Total			10.31	7.14

Table 4.4: Summary of the $^{13}\text{C}(\alpha, n)^{16}\text{O}$ backgrounds.

Chapter 5

Event selection

Event selections for the reactor neutrino analysis are described in this chapter. The various selection criteria are applied for the data set to improve the quality of data samples. Total data set consists of physics runs taken during March 9, 2002 to January 11, 2004. The condition of the KamLAND detector livetime during those period is described in Sec. 5.1. Livetime calculation is shown in Sec. 5.2. Efficiencies for the $\bar{\nu}_e$ detection are described in Sec. 5.3. Event selection criteria and final samples are shown in Sec. 5.4.

5.1 Data collection

Total data set used for this reactor neutrino analysis consist of physics runs taken during March 9, 2002 to January 11, 2004. The run is a basic unit of the KamLAND data set and is updated once a day in case of normal condition. Physics run is taken all day long except for the detector calibration, hardware and software maintenances, etc. Figure 5.1 shows the KamLAND detector operation conditions during the whole data sample. Integrated time taking physics data is 574.1 days. At the beginning of the data taking, the hardware and software maintenances were performed frequently. Currently, the detector calibration is the main reason for the time not taking physics data. After subtracting bad runs, bad period selections, and the deadtime by the spallation cut, the total livetime is (515.1 ± 0.3) days, used for the reactor $\bar{\nu}_e$ analysis.

There are tree detector conditions in this period (Table 5.1). After improvement of the electronics, response to input of large signals were changed. The PMT array was upgraded by commissioning 554 20-inch PMTs. The photo-cathode coverage increased from 22% to 34% and improving the energy resolution from $7.3\%/\sqrt{E(\text{MeV})}$ to $6.2\%/\sqrt{E(\text{MeV})}$.

5.2 Livetime calculation

To calculate the expected number of $\bar{\nu}_e$ events for the $\bar{\nu}_e$ detection time at the detector, livetime is essential value. The period for each run is classified with

- Runtime : Time of the data taking period for each run, defined as

$$(\text{Runtime}) = (\text{Time of the last event in the run}) - (\text{Time of the first event in the run}).$$

The uncertainty of the runtime is estimated to be ~ 5 msec. It depends on the event rate of ~ 200 Hz for the history trigger. It corresponds to $6 \times 10^{-6}\%$ for the typical 24 hours runtime.

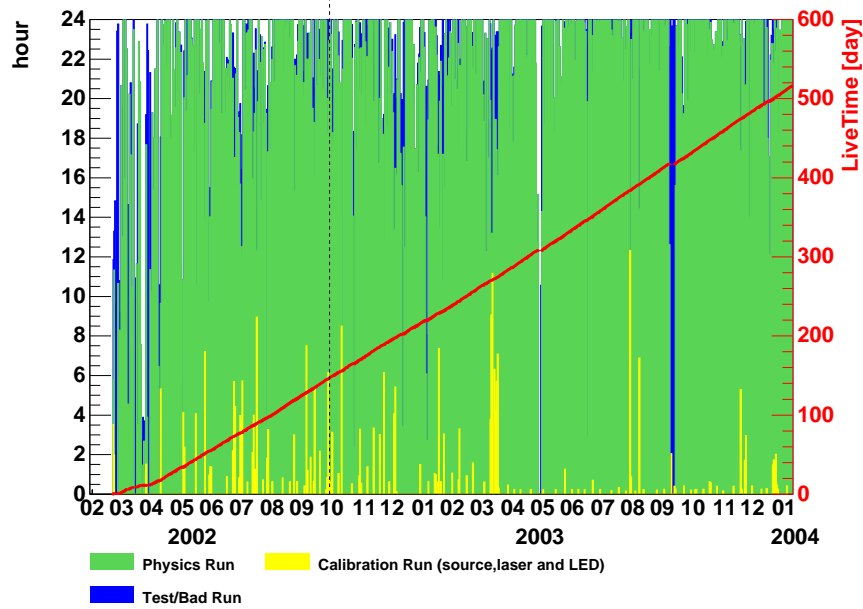


Figure 5.1: History of the operation at KamLAND. The red line shows the total livetime.

	I	II	III	Total
Period (Start)	March 9, 2002	January 10, 2003	February 27, 2003	
(End)	January 10, 2003	January 11, 2004	January 11, 2004	
Used electronics	First generation	Second generation	Second generation	
Used PMTs	17-inch only	17-inch only	17 and 20-inch	
Fiducial radius		5.5 m		-
Fiducial mass		543.7 tons		-
Number of targets		4.61×10^{31}		-
Run time (days)	244.86	43.35	285.87	574.09
Livetime (days)				
(w/ Spallation cuts)	218.40	38.87	257.87	515.14
Detection efficiency (%)	89.82	89.82	89.83	-

Table 5.1: Summary of measurement periods for the reactor neutrino analysis.

- Deadtime : Time of no data taking period or data taking is incorrect.
- Vetotime : Unused period at the analysis for the background rejection.

5.2.1 Deadtime

The deadtime is classified to four types

- Bad run
The data quality is very poor. For example, the number of bad-channels in the ID 17 inch PMTs is many or has cluster distribution. It is caused by problems of HV power supplies or electronics, or strange values of the trigger rate or muon rate. These runs are not used conservatively.
- Bad period (half-badrun)
A part of the run period is worse condition like a bad run. Typically, this period is within a few hours before or after some trouble.
- Trigger dead period
The trigger is disable to fire. The disable flag is recorded in data files when the trigger module is busy and disable to work, and the enable flag is recorded when the trigger status is recovered. Another possible deadtime comes from the broken data packet by network problems. That is tagged by the large time intervals ($> 100\text{msec}$) between each history event.
- Noisy period
The multiple noise events are usually coming within $150 \mu\text{sec}$ after muons because of the ringing on FEE. If there are no muons before a cluster of noise events, there is a possibility that muons are missed by indistinct deadtime. The missing muon is tagged by plural noise events within 1 msec without any muon, and that period is considered as the deadtime, conservatively. Another method to tag missing muon is to look for missing waveform, $N_{\text{hit}} < N_{\text{sumMax}}$.
There is a possibility muons (possibly energetic muons) come into the detector while the deadtime, therefore, whole volume of the detector should be vetoed for 2 sec, conservatively. Only for the missing waveform case, the trigger hit information (N_{sumMax}) is used in order to decide the veto time width,

$$\begin{aligned} \text{low energy muon } (200 \leq N_{\text{sumMax}} \leq 1200) &: 2 \text{ msec veto} \\ \text{high energy muon } (N_{\text{sumMax}} \geq 1200) &: 2 \text{ sec veto.} \end{aligned}$$

The trigger is sending a special flag periodically per sec, and it is called 1 PPS trigger. This is not coming during the Supernova trigger mode, but it is enable during this period from run876. This 1 PPS trigger helps to check the uncertainty of the dead time because “(run time) – (dead time) – (Supernova trigger period)” should be equal to “(number of 1 PPS trigger \times 1sec)”. Unknown dead time ratio is defined,

$$1 - \frac{(\text{Number of 1 PPS trigger}) \times 1\text{sec}}{(\text{Run time}) - (\text{Dead time}) - (\text{Supernova trigger period})} \quad (5.1)$$

and the percentage is 100 times of it. Figure 5.2 shows its percentage for each run. Average of indistinct deadtime is 0.06%.

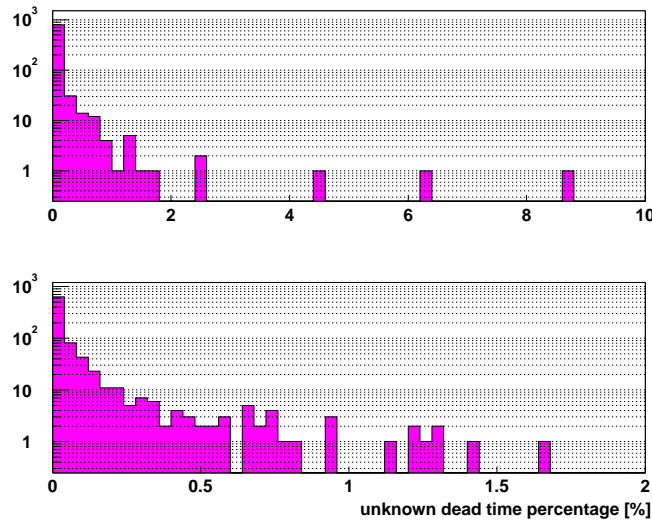


Figure 5.2: Ratio of unknown deadtime in percentage. It is much less than 2% for almost all run, but it is more than 2% in some runs.

5.2.2 Vetotime

The veto for the detector is applied after every muon event and after every deadtime. The muon is classified four grades and three different types of veto are applied for each muon,

- Low charge muon ($Q \leq 40,000\text{p.e.}$)
Whole volume of the detector is vetoed for 2 msec.
- Energetic muon ($Q > 40,000\text{p.e.}$ and $\Delta Q \geq 10^6\text{p.e.}$)
Whole volume of the detector is vetoed for 2 sec.
- Miss reconstructed muon ($Q > 40,000\text{p.e.}$ and $\text{Badness} \geq 100$)
Whole volume of the detector is vetoed for 2 sec.
- Well reconstructed muon (but not energetic one, $Q > 40,000\text{p.e.}$ and $\text{Badness} < 100$ and $\Delta Q < 10^6\text{p.e.}$)
Whole volume of the detector is vetoed for 2 msec, and then cylindrical volume around muon track within 3 m ($\Delta L \leq 3\text{m}$) is vetoed for 2 sec. The cylindrical veto is only applied to the delayed event.

Where Q means the total charge sum of ID 17 inch PMTs for each muon event, and ΔQ means the residual charge. The badness is the grade of reconstruction. The 9.7% of runtime in the fiducial volume (5.5 m fiducial radius) is vetoed by the spallation cut.

5.2.3 Livetime

The livetime is calculated using runtime and deadtime and veto information for each run. To consider the overlap of each veto in time and volume, the simple MC simulation is used. The MC events are distributed uniformly for the position and time in the fiducial volume and runtime,

so the ratio of livetime/runtime is given by

$$\frac{\text{Livetime}}{\text{Runtime}} = \frac{\text{Number of events}(R < 5.5\text{m})\text{with applying all cut}}{\text{Number of events}(R < 5.5\text{m})}. \quad (5.2)$$

The uncertainty of this calculation is verified by the statistic of the generated events. About 9.2×10^8 events were generated, and the vetoed events were about 10% of the total generated events. The error for the ratio of the vetoed events to the total generated events is $\sim 1.0 \times 10^{-5}$. Therefore, the uncertainty of the calculation is 0.001%. Figure 5.3 shows the ratio of livetime to runtime for each run except for the bad run. The livetime for almost all runs are less than 24 hours. The total livetime from March 9, 2002 to January 11, 2004 is 515.1 days.

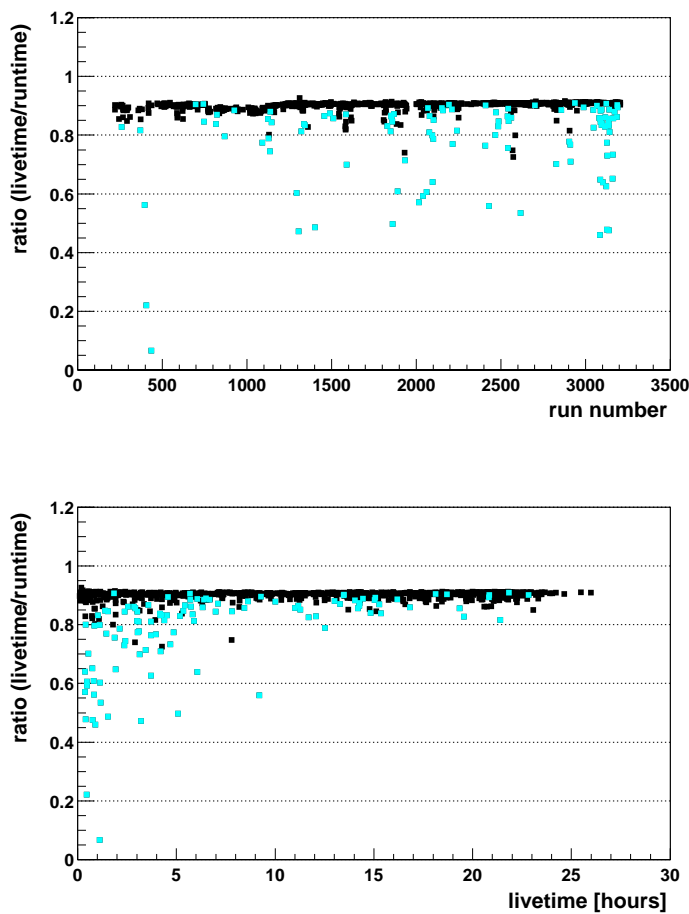


Figure 5.3: Ratio of livetime/runtime for each run. The sky blue markers indicate half-bad runs. The small ratio indicates the noisy run, which has much noisy period. The average efficiency for the runtime is about 90%.

The total systematic uncertainty for the livetime is addressed with a quadratic sum of uncertainty of the runtime $6 \times 10^{-6}\%$, the deadtime finding error 0.06% and the uncertainty of the calculation 0.001%,

$$\sqrt{(6 \times 10^{-6})^2 + 0.06^2 + 0.001^2} \simeq 0.06\%.$$

5.3 Detection efficiency

Table 5.2 lists the detection efficiencies in the $\bar{\nu}_e$ events selection. The systematic uncertainty of event selection is 1.6% and the event selection efficiency of all cuts is $(89.8 \pm 1.5)\%$. The trigger efficiency (2.3.4) and the probability of a thermal neutron capture on proton (2.3.1) are described already. In this section, efficiencies for the delayed coincidence selection, space correlation, time correlation, and delayed energy cut are described.

Parameter	Efficiency (%)
Space correlation	91.32 ± 1.49
Time correlation	98.89 ± 0.05
Trigger efficiency	-
Delayed energy	$99.98^{(I,II)}, 99.99^{(III)}$
Neutron capture on proton	99.48
Total	$89.82^{(I,II)}, 89.83^{(III)}$

Table 5.2: Detection efficiency above 2.6 MeV prompt energy threshold. “(I,II)” means the analysis period I and II, “(III)” means the analysis period III.

5.3.1 Space correlation

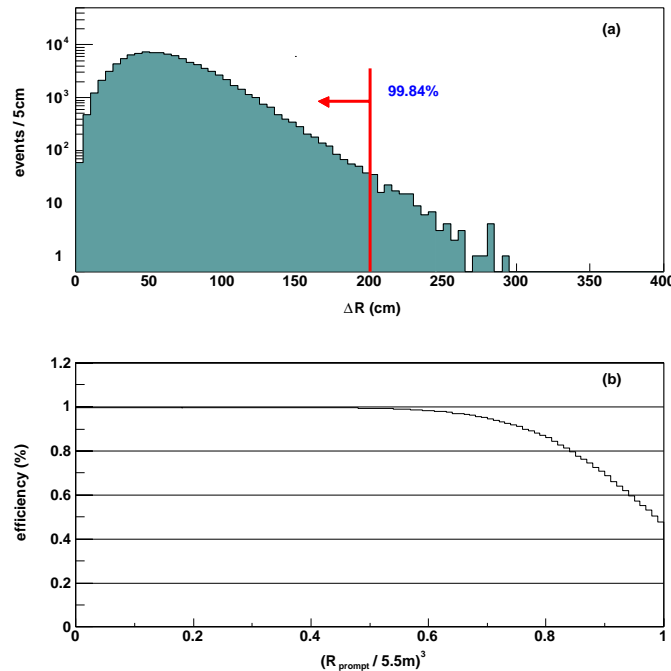


Figure 5.4: (a) Space correlation between prompt and delayed events generated by the MC. The assumed resolution is $\sigma_{x,y,z} = 30\text{cm}\sqrt{E(\text{MeV})}$ estimated from the source calibration for various energies. (b) Efficiency for the delayed vertex is within 2 m from the prompt vertex and within 5.5 m fiducial volume as a function of the prompt vertex.

Space correlation between prompt and delayed events is evaluated with a help of a detector simulation. For the delayed events, to simulate the recoil neutron by the reactor $\bar{\nu}_e$, neutrons around 10-20 keV are generated. The diffusion length of recoil neutron is evaluated to be ~ 9 cm. The assumed vertex resolution is $30\text{cm}/\sqrt{E(\text{MeV})}$ estimated from the source calibration for various energies. Figure 5.4 (a) shows the space correlation between prompt and delayed events, and the events within 200 cm is 99.84%. This result can be checked by the Am-Be calibration using the delayed coincidence of the 4.44 MeV γ -ray and the neutron captured 2.22 MeV γ -ray. The overall efficiency of the neutron capture event within 200 cm in the Am-Be source calibration at various z position is $99.69 \pm 0.11\%$. It is consistent with the prediction of the MC within 0.5%. Selection criteria for the delayed vertex in the $\bar{\nu}_e$ selection are the diffusion cut $\Delta R < 2\text{m}$ and the fiducial cut $R_{\text{delayed}} < 5.5\text{m}$. The vertex dependence of the space efficiency is shown in Figure 5.4 (b). The inefficiency of the space correlation is dominated by the escape effect from the fiducial radius. The efficiency of those selection is 91.32% in the MC, while it is 1.49% smaller in the Am-Be calibration. The difference is addressed as the systematic error in the $\bar{\nu}_e$ selection, conservatively.

$$(\text{Efficiency of space correlation}) = 91.32 \pm 1.49\%. \quad (5.3)$$

Moreover, the efficiency is consistent within 2% even if the vertex resolution is 10 cm better or worse.

5.3.2 Time correlation

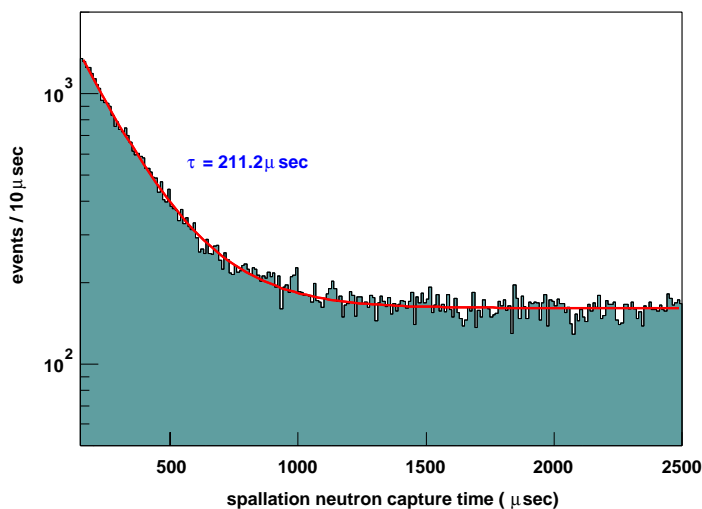


Figure 5.5: Time difference from muons to spallation neutron capture candidates. The mean capture time is fitted to be $211.2 \pm 2.6\mu\text{sec}$.

Time correlation between prompt and delayed events is evaluated using the capture time of spallation neutrons after muon events, $\mu + {}^{12}\text{C} \rightarrow xn + \text{nuclei}$. Figure 5.5 shows the time difference from muons to spallation neutron capture candidates. To avoid the electronics unstable condition due to the multiple neutrons, high energy muons are not used. The mean capture time is evaluated to be $211.2 \pm 2.6\mu\text{sec}$ using the fitting by the exponential curve with accidental

backgrounds. Therefore, the efficiency of the time correlation is calculated as

$$(\text{Efficiency of time correlation}) = \frac{1}{\tau} \int_{0.5\mu\text{sec}}^{1000\mu\text{sec}} dt \exp(-t/\tau) \quad (5.4)$$

$$= 98.89 \pm 0.05\%. \quad (5.5)$$

Moreover, the events generated with the MC have the mean capture time $\sim 212.5\mu\text{sec}$, which agrees with the capture time with the spallation neutrons. The uncertainty associated with the time correlation cut is dominated by the upper time cut $< 1000\mu\text{sec}$.

5.3.3 Delayed energy

The selection efficiency of the delayed energy cut is $1.8\text{MeV} < E_{\text{delayed}} < 2.6\text{MeV}$ (visible energy) is calculated using the energy resolution σ at the neutron capture peak.

$$(\text{Efficiency of delayed energy cut}) = \frac{1}{\sqrt{2\pi}\sigma} \int_{1.8\text{MeV}}^{2.6\text{MeV}} dE \exp\left(-\frac{(E - 2.21)^2}{2\sigma^2}\right). \quad (5.6)$$

The energy resolution are different between the period I, II and III, due to the 20 inch PMT commissioning. Therefore the efficiencies for the both periods are calculated to be

$$\text{Period I, II (17inchPMTs only)} \rightarrow 99.98\%, \quad (5.7)$$

$$\text{Period III (17inchPMTs + 20inchPMTs)} \rightarrow 99.99\%, \quad (5.8)$$

and the effect of the resolution uncertainties is negligible.

5.4 Reactor $\bar{\nu}_e$ event selection

5.4.1 Event selection criteria

To select inverse β -decay events by $\bar{\nu}_e$'s, the delayed coincidence method is used. Based on the study of the background and efficiency study, $\bar{\nu}_e$ selection criteria are decided as follows,

1. Analysis threshold for the prompt energy, $2.6\text{MeV} < E_{\text{prompt}} < 8.5\text{MeV}$

To avoid geo-neutrino backgrounds.

2. Delayed coincidence between the positron and delayed neutron

- (a) Time difference, $0.5\mu\text{s} < \Delta T < 1000\mu\text{s}$

Neutron capture time is evaluated to be $211.2 \pm 2.6\mu\text{sec}$, using the capture time of spallation neutrons after muon events, Therefore, 99.89% of neutron is captured within the time window $0.5\mu\text{s} < \Delta T < 1000\mu\text{s}$, and the systematic error for the selection efficiency is 0.05%. The detection efficiency of very short time interval less than about 300nsec from previous event is too low abnormally. Conservatively, within $0.5\mu\text{sec}$ should be ignored.

- (b) Position difference, $\Delta R < 2\text{m}$

The 91.32% of neutron is captured within 2 m distance and 5.5 m fiducial radius by the MC simulation. Systematic uncertainty is 1.6% compared with the Am-Be source calibration.

- (c) Delayed event energy, $1.8\text{MeV} < E_{\text{delayed}} < 2.6\text{MeV}$

The detection efficiency is evaluated to be 99.98% and 99.99% for the 17 inch PMTs only and including the 20 inch PMTs.

3. Fiducial cut

- (a) Fiducial radius, $R < 5.5\text{m}$

The radial positions of the prompt and delayed event are both required to be less than 5.5m.

4. Spallation cut

Delayed neutron emitters in spallation products are eliminated by the following cuts. The deadtime introduced by all muon cuts is $(9.7 \pm 0.1)\%$.

- (a) Low charge muon ($Q \leq 40,000\text{p.e.}$)

A 2-msec veto is applied for the entire fiducial volume following the muon.

- (b) Energetic muon ($Q > 40,000\text{p.e.}$ and $\Delta Q \geq 10^6\text{p.e.}$)

A 2-sec veto is applied for the entire fiducial volume following the muon.

- (c) Miss reconstructed muon ($Q > 40,000\text{p.e.}$ and badness ≥ 100)

A 2-sec veto is applied for the entire fiducial volume following the muon.

- (d) Well reconstructed non-energetic muon ($Q > 40,000\text{p.e.}$ and badness < 100 and $\Delta Q < 10^6\text{p.e.}$)

A 2-msec veto is applied for the entire fiducial volume following the muon. Delayed events within 2 sec and 3 m from a muon track are rejected.

5. Multiple neutron cut

- (a) Single neutron, $N_{\text{delayed-neutron}} = 1$

The multiple neutron events can be caused by the spontaneous fission of ^{238}U (SF branch: 5.45×10^{-5}), and the upper limit of ^{238}U decay rate is estimated from the ^{234}Pa decay rate. The spontaneous fission of ^{238}U is calculated to be less than 2 events for the total livetime of 515.1 day. The inefficiency from this cut is equivalent to the probability of the accidental coincidence for the events which has uniform distribution for time and space. It is estimated to be $< 0.01\%$ for 5.5 m fiducial volume.

5.4.2 Event reduction

Reduction	Runtime / Events	Reduction factor
	597.7 day	
1 Bad-run and deadtime reduction	570.3 day (1.43×10^9 events)	0.95
2 Noise and flasher cut	1.16×10^9 events	0.81
3 Muon separation	1.14×10^9 events	0.98
4 Muon veto	1.13×10^9 events	0.99
5 Delayed coincidence selection	12,766 events	1.1×10^{-5}
6 Fiducial cut	593 events	0.046
7 Spallation cut	261 events	0.44
8 Multiple neutron cut and upper prompt energy cut	258 events	0.99

Table 5.3: $\bar{\nu}_e$ event reduction.

The $\bar{\nu}_e$ events are selected using the reduction procedure as listed in Table 5.3. Figure 5.6 shows the prompt energy and delayed energy distribution, illustrating reduction of the delayed coincidence events by the fiducial cut, spallation cut, multiple neutron cut and upper prompt energy cut. The delayed coincidence selection is the most effective in the event reduction. After the spallation cut, the remaining candidates below 20 MeV are 261 events. After the multiple neutron and upper energy cut, the remaining candidates are 258 events.

The vertex distribution of the delayed coincidence events is shown in Figure 5.7. The final samples have almost uniform distribution. The profiles of $\bar{\nu}_e$ candidates are shown in Figure 5.8 and Figure 5.9. Their correlation is clear in all parameters. The mean neutron capture energy is 2.218 ± 0.010 MeV by the Gaussian fit. Its deviation from the real capture energy is only 0.3%. It demonstrates the stability of the overall energy scale.

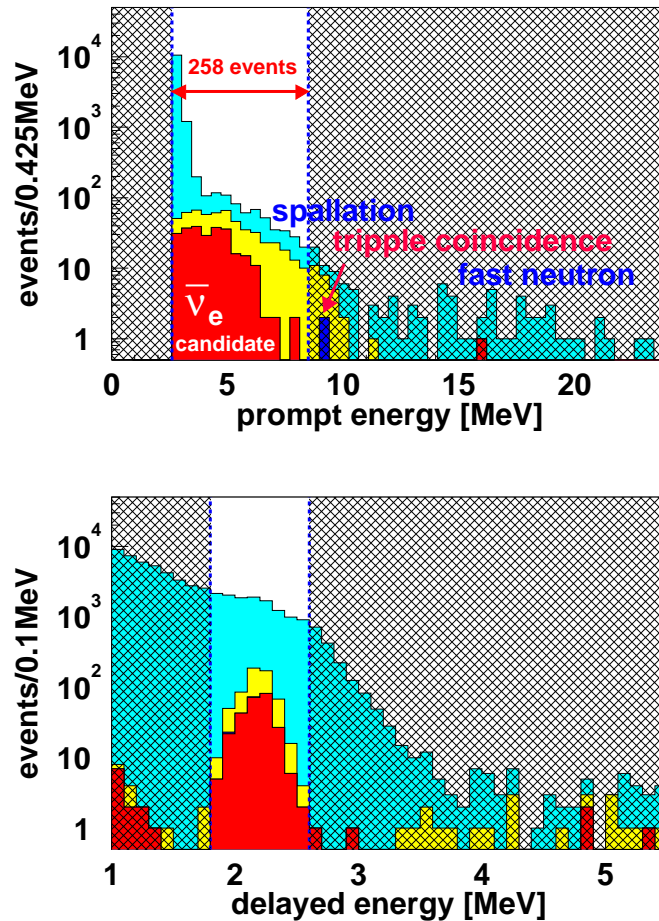


Figure 5.6: Prompt energy and delayed energy distribution. The reduction of the delayed coincidence events by the fiducial cut, spallation cut, multiple neutron cut and upper prompt energy cut are performed. The final sample is 258 events for the total livetime of 515.1 day.

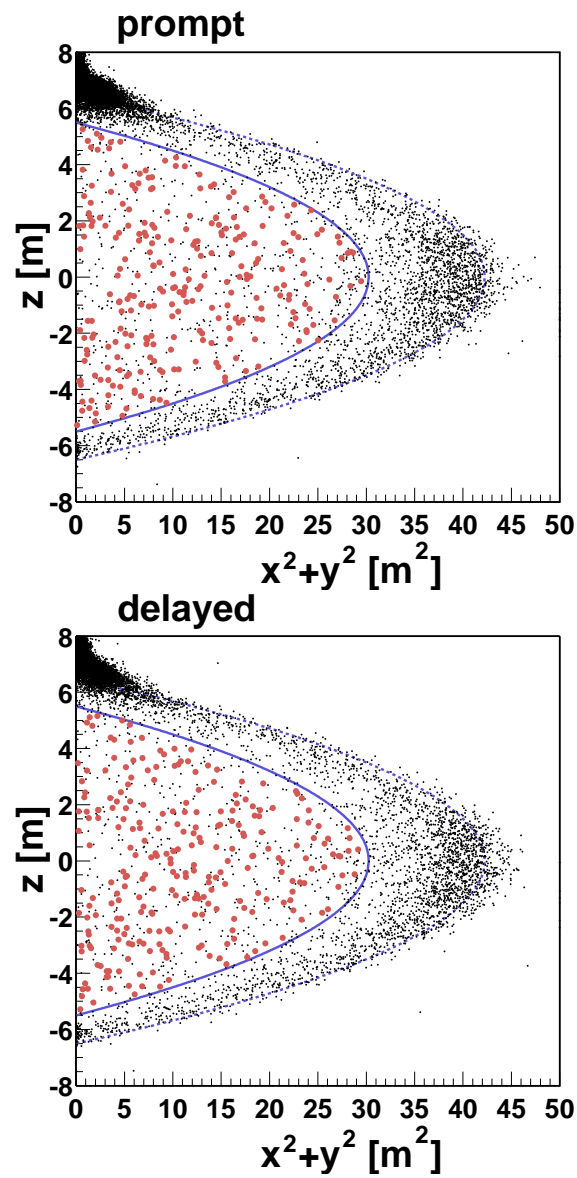


Figure 5.7: Vertex distribution of the delayed coincidence events. The regions with event rates higher than other regions are seen at around $z \sim \pm 6.5\text{m}$ and around balloon surfaces. The red markers mean after the fiducial cut, spallation cut, multiple neutron cut and upper prompt energy cut. The final samples distribute almost uniformly.

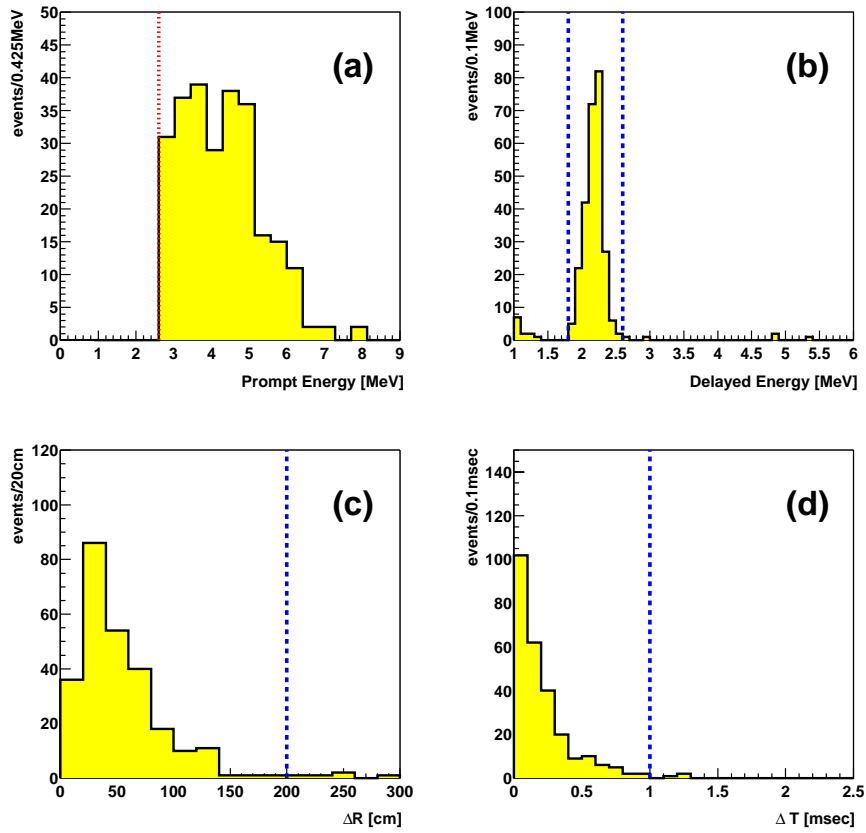


Figure 5.8: Profiles of $\bar{\nu}_e$ candidates. (a) Prompt energy. (b) Delayed energy. (c) Space correlation. (d) Time difference. The selection cuts for undisplayed parameters are applied. Lines indicate the selection criteria.

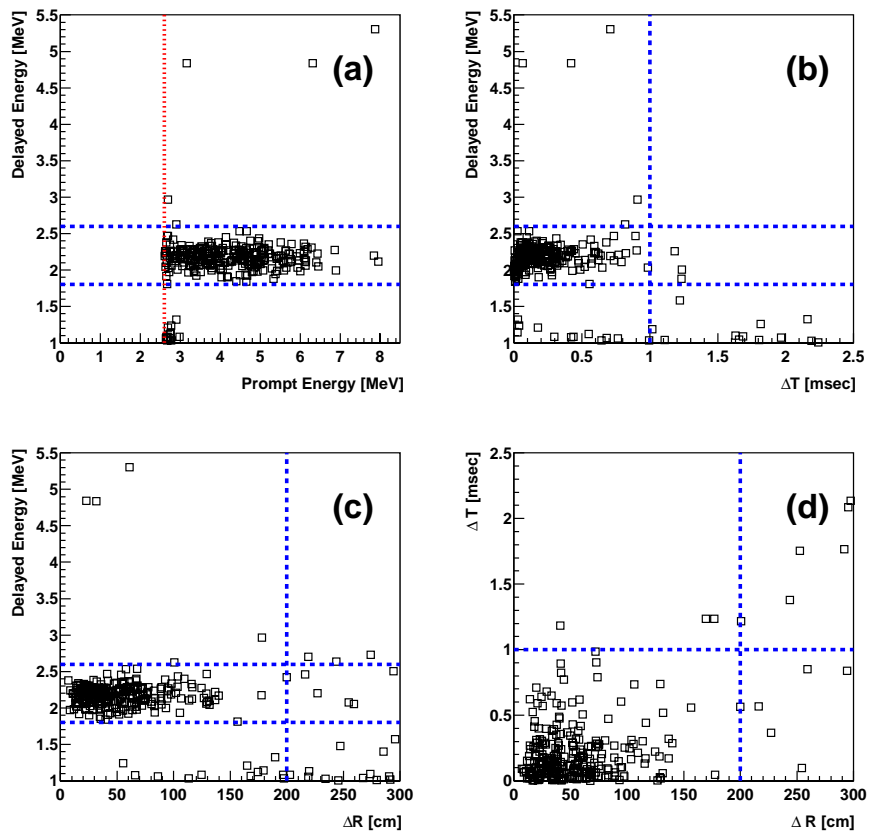


Figure 5.9: Profiles of $\bar{\nu}_e$ candidates. (a) Prompt energy vs Delayed energy. (b) Time difference vs Delayed energy. (c) Space correlation vs Delayed energy. (d) Space correlation vs Time difference. The selection cuts for undisplayed parameters are applied. Lines indicate the selection criteria. Events around 5 MeV in the delayed energy are the carbon capture candidates. The accidental events are concentrated at $E_{\text{prompt}} \sim 2.6\text{MeV}$.

Chapter 6

Fission rate calculation

In the data taking period at KamLAND between March 2002 and January 2004, 52 commercial reactors and one prototype reactor existed in Japan as operatable electric-power producing reactors. Generation rate of reactor $\bar{\nu}_e$'s has correlation with the fission rate for each fissile element. The contribution to the reactor $\bar{\nu}_e$ flux at KamLAND from each reactor was 0.1% to 7% if it operated with a rated output. Therefore, to predict reactor $\bar{\nu}_e$ events at KamLAND with precision of $< 1\%$, we need to know the time dependent reactor $\bar{\nu}_e$ spectrum created in all these reactors precisely. In this chapter, calculation method of reactor $\bar{\nu}_e$ spectrum which has been used for the KamLAND analysis is described. At first, generation of the reactor $\bar{\nu}_e$ is described in 6.1.

In 6.2, burnup parameter which shows the time dependence in the reactor core is described. The time evolution of the fission rate for each fissile element is shown by the differential equation about the concentration of nucleus in the reactor core (burnup equation). The burnup equation is dependent on the neutron flux distributed spatially in the core. In the real reactor core, the total fission rate is $\sim 10^{20}$ fission/s, and it is impossible to trace these large number of reactions. So, the burnup equation is used to simulate time evolution of the fuel.

In 6.3, calculating of the time-dependent fission rate for each fission element in the real core by using the general reactor core analysis method is described. It is impossible to trace three-dimensional neutron density in actual cores. So, this reactor core analysis method is based on “two-dimensional multi-group fuel-assembly analysis” and “three-dimensional few-group full core analysis”.

To perform this method we need data such as structure of reactor core, design of fuel and status of control rods, so it is difficult to simulate all 52 Japanese commercial reactors. So, we developed a new simple method which can calculate the fission rate for each fissile element with required accuracy. In 6.4, this simple method is described.

In 6.5, the systematic uncertainty for the energy spectrum of the reactor $\bar{\nu}_e$ calculated by this simple method is described.

On the other hand, the fission rate in the one prototype reactor, Fugen of the Japanese Nuclear Cycle Development Institute (JNC), was calculated by JNC using their detailed method and were provided for the KamLAND experiment. The reactor $\bar{\nu}_e$ contribution from Japanese research reactors and reactors outside of Japan is described in Chapter7.

6.1 Reactor neutrino

Reactor $\bar{\nu}_e$'s are produced in the β -decay of neutron-rich fission fragments in reactor cores. The production rate of reactor $\bar{\nu}_e$'s is obtained with $\bar{\nu}_e$ energy spectra of four fission elements per fission reaction and fission rates correlated with total released energy. In nuclear power reactors, the electric energy is produced by converting the thermal energy produced by the fission reaction in cores. The fission fragments emit $\bar{\nu}_e$'s with β -decay reactions. The thermal power of the largest power reactors in Japan is about 4000MW per one unit. In this case, the fission reaction rate is $\sim 10^{20}$ fission/s and $\sim 6 \times 10^{20}$ $\bar{\nu}_e$'s are emitted per one second. So, nuclear power reactors are intense sources of $\bar{\nu}_e$'s.

6.1.1 Fission elements in reactor cores

In electric-power producing reactors, the nuclear fission reaction is continued to maintain the rated electric outputs. At Japanese commercial reactors, ^{235}U enriched uranium oxide (UO_2) is used as nuclear fuel. The fission reaction, $^{235}\text{U} + n \rightarrow X_1 + X_2 + x n$, produces two fragments and ~ 2 fission neutrons. The fission neutrons interact and lose their energy through elastic scattering with moderator water around the nuclear fuel. Then, the thermal neutrons are absorbed by ^{235}U and some of them cause the chain of fission reactions. Fast neutrons are absorbed by ^{238}U and cause fission reactions. On the other hand, ^{238}U absorbs neutrons which energy range is 1eV to 1keV and become ^{239}U . ^{239}U repeats the beta decay and neutron absorption as shown in Table 6.1. In these elements, ^{239}Pu and ^{241}Pu have large thermal fission cross section. So, ^{235}U , ^{238}U , ^{239}Pu and ^{241}Pu are main components of fission elements in nuclear fuel.

Mass number	Atomic number			
	92	93	94	95
241			$\boxed{^{241}\text{Pu}}$	$\xrightarrow[13.6\text{y}]{\beta} ^{241}\text{Am}$
240			$\uparrow (n, \gamma)$ ^{240}Pu	
239	^{239}U	$\xrightarrow[23.5\text{m}]{\beta} ^{239}\text{Np}$	$\xrightarrow[2.35\text{d}]{\beta} \boxed{^{239}\text{Pu}}$	
238	$\boxed{^{238}\text{U}}$	$\uparrow (n, \gamma)$	$\uparrow (n, \gamma)$	

Table 6.1: Main components of the U-Pu chain in nuclear fuel.

Figure 6.1 shows the time dependence of fission rates in one of the Palo Verde reactor cores using same nuclear fuel as Japanese commercial reactors. It is calculated by a reactor core analysis code. The contribution of four fission elements is dominant, and that of ^{240}Pu and ^{242}Pu is of order 0.1% or less.

6.1.2 Neutrino energy spectrum of each fission element

Most of the fission fragment are neutron rich nuclei and unstable, then undergo β -decays. Each fission fragment undergoes β -decay ~ 3 times, so $\sim 6\bar{\nu}_e$'s are produced per fission reaction. The

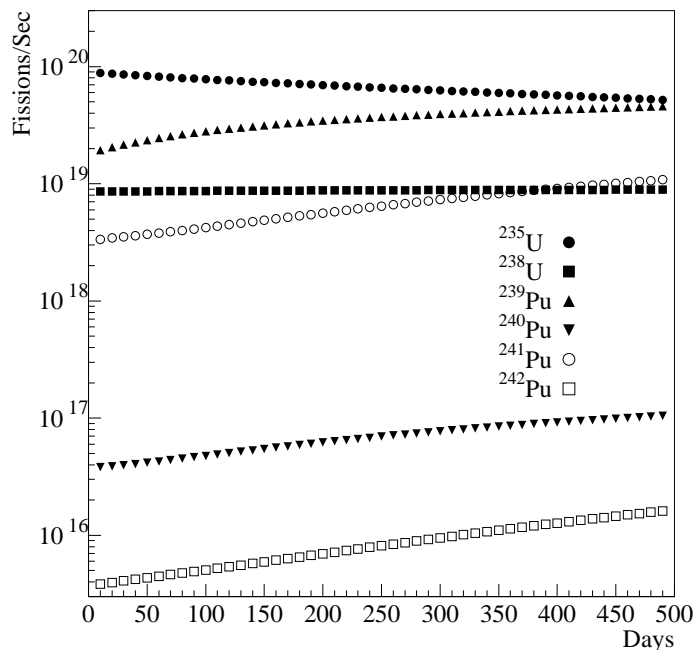


Figure 6.1: Fission rates at a unit of the Palo Verde reactor cores [40]. This reactor core corresponds to the equilibrium core described in Chapter 6.

nuclei which created in this decay procedure is called the fission products. Figure 6.2 shows the fission product yield. The distributions have two steep peaks at $Z \sim 40$ and $Z \sim 55$.

Figure 6.3 shows the reactor $\bar{\nu}_e$ spectra per fission and its error taken from Ref. [45]. The neutrino spectra for ^{235}U , ^{239}Pu and ^{241}Pu were converted from observed β spectrum from the fission products, by fitting under assumption of 30 hypothetical beta-branches. These measurements were performed in about one day. On the other hand, some nuclides in the fission products as ^{144}Ce , ^{106}Ru and ^{90}Sr have long life time ($\tau \gtrsim 1\text{year}$). The small additional contribution of $\bar{\nu}_e$'s from these long lived nuclides is not included in the $\bar{\nu}_e$ spectra. About the neutrino spectrum for ^{238}U , there is not measurement because fast neutrons are needed to let ^{238}U fission. So, the energy spectrum is calculation. According to a short baseline reactor $\bar{\nu}_e$ experiment, Bugey, the experimental accuracy on the absolute neutrino flux including the cross section calculation is 1.4% to be compared with an accuracy of 2.7% on the expected flux [46]. Moreover, at the Bugey 3 measurements, the measured neutrino spectra favor a model of reactor neutrino spectrum based on the ILL experiment [47].

The total neutrino production rate is written,

$$F(t, E_{\bar{\nu}_e}) = \sum_{\text{nucleus}} f_{\text{nucleus}}(E_{\bar{\nu}_e}) R_{\text{nucleus}}(t) + \Delta F_{\text{long}}(t, E_{\bar{\nu}_e}), \quad (6.1)$$

where $f_{\text{nucleus}}(E_{\bar{\nu}_e})$ is the neutrino energy spectrum per fission of each fissile element, $R_{\text{nucleus}}(t)$ is the fission reaction rate of each fissile element and $\Delta F_{\text{long}}(t, E_{\bar{\nu}_e})$ is the contribution from long lived nuclides, As described in 7.6, this contribution is small above an 3.4MeV reactor $\bar{\nu}_e$ analysis threshold of KamLAND. To calculate the reactor $\bar{\nu}_e$ flux at KamLAND, we need to know the time dependent fission rates of each element in all Japanese reactors.

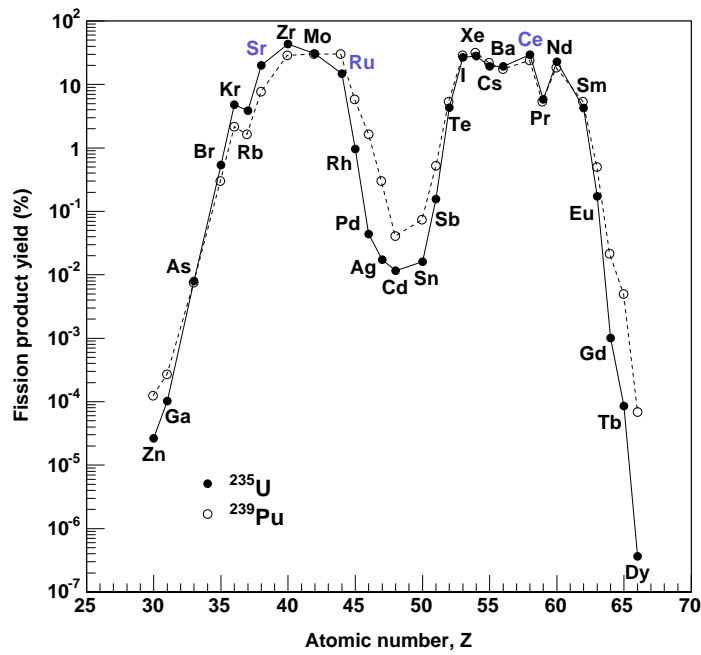


Figure 6.2: Fission product yield curve [41]. Normalized to 200% for the two fragments per fission reaction. The horizontal axis shows the atomic number. The nuclides with colored labels include the long lived nuclides in the isotopes. (Contribution from these nuclides to the $\bar{\nu}_e$ flux at KamLAND is described in 7.4.)

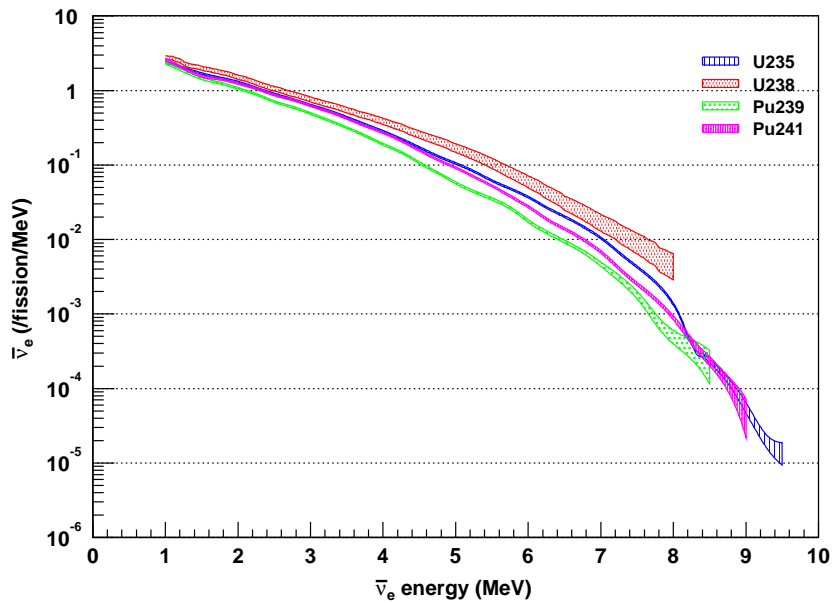


Figure 6.3: Reactor neutrino energy spectrum [45].

6.1.3 Energy released per fission reaction

To estimate fission reaction rates in nuclear fuel, the total released energy by fission in reactors is available. The thermal output of actual reactors, however, includes additional instantaneous energy provided by the radiative capture and the resultant gamma ray emission of fission neutrons. The average energy released per fission with a thermal neutron in ^{235}U is listed in Table 6.2.

Forms	Released energy (MeV)	Available energy (MeV)
Fission fragments	168	168
Decay of fission products		
β -rays	8	8
γ -rays	7	7
$\bar{\nu}_e$'s	12	0
Prompt γ -rays	7	7
Kinetic energy of fission neutrons	5	5
Capture γ -rays	0	3-12
Total	207	198-207

Table 6.2: The released energy and available energy per fission with a thermal neutron in ^{235}U [65].

The released energy per fission can be calculated based on the mass difference between the reactants before fission and the fission fragments and fission neutrons. These fission fragments undergo β -decay and release an energy. The total released energy per fission is ~ 200 MeV. On the other hand, we can measure the available energy collected by coolant. Obviously, the ~ 10 MeV of $\bar{\nu}_e$ energy is not absorbed in reactors. The additional energy from capture γ -rays of fission neutrons is ~ 10 MeV, so the average total energy transformed into heat is ~ 200 MeV per fission.

Parameters	BWR	PWR
Nuclear fuel	UO ₂	
^{235}U enrichment	3 ~ 5%	
Moderator	Light water	
Coolant	Light water	
Control material	B ₄ C	Hf/Ag – In – Cd
Loop of coolant	1	2
Generation of steam	Core	Steam generator
Pressure and temperature in cores	70 atm., 285°C	157 atm., 320°C
Pump for coolant	Recirculation pump	Primary coolant pump
Exchanged fuel volume ratio	1/4	1/3
Refueling	Once a year	
Control method for steady-state power operation	Coolant flow control (Control rod)	Density of neutron absorber
Control method for start-up and shutdown	Control rod Coolant flow	Density of absorber Control rod
Number of core in Japan	29	23

Table 6.3: Parameters of BWR and PWR.

6.1.4 Core thermal output

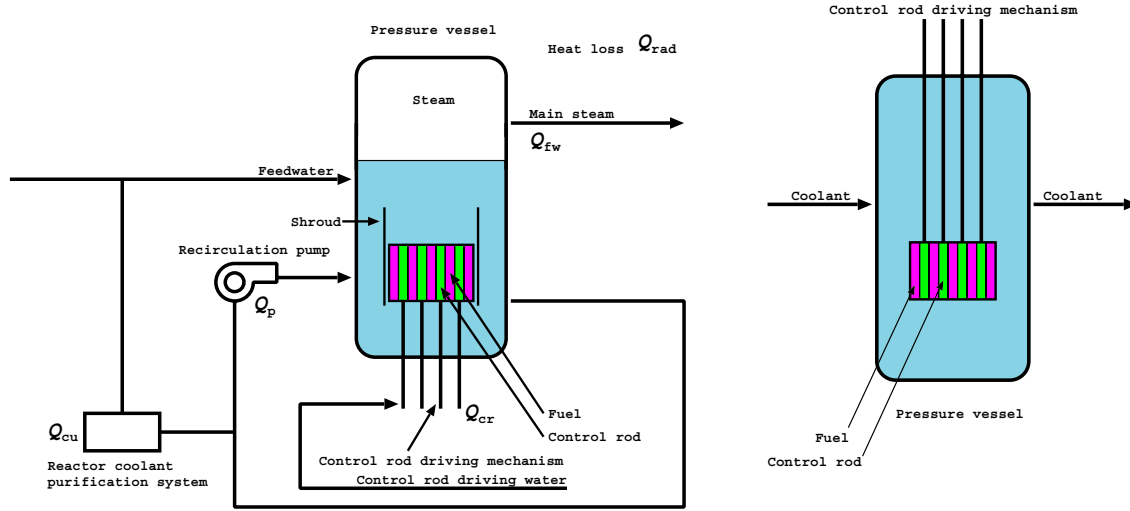


Figure 6.4: Heat balance at BWR (Left) and PWR (Right) cores. BWRs have additional loops for controlling the coolant flow.

To calculate generation rates of reactor \bar{v}_e 's, correlation between the “core thermal output” and the fission reaction rates are needed. The core thermal output is defined as thermal energy generated in reactor cores. At BWRs, the core thermal output is same as the reactor thermal output. At PWRs, however, the reactor thermal output includes the core thermal output and relatively small heat from the reactor coolant pumps. The core thermal output is calculated by considering heat balance of reactor cores. Figure 6.4 shows a schematic diagram of heat balance at BWR and PWR cores. BWRs have additional loops of the recirculation water. So, the case of BWRs are shown here. The core thermal output Q_{ctp} is written as

$$Q_{ctp} = Q_{fw} - Q_{cr} + Q_{cu} + Q_{rad} - Q_p, \quad (6.2)$$

where, Q_{fw} is thermal energy taken out from cores by cooling water, Q_{cr} is input energy from control rod driving mechanism, Q_{cu} is thermal energy taken by reactor coolant purification system, Q_{rad} is heat loss with radiation and Q_p is input energy from recirculation pumps. In these terms, contribution from Q_{fw} is dominant and other terms are less than 1%. Therefore, uncertainty of the calculated core thermal output is dominated by accuracy of Q_{fw} . Q_{fw} is written as valance of enthalpy of the steam Q_{out} and feedwater Q_{in} ,

$$Q_{fw} = Q_{out} - Q_{in} \quad (6.3)$$

$$= w_{out} h_{out} - w_{in} h_{in}, \quad (6.4)$$

where, $w_{out} \sim w_{in}$ are flow of coolant (feedwater or main steam, [kg/h]), $h_{out} = h_g(p_{core})$ is specific enthalpy ([J/kg]) of main steam which is obtained as specific enthalpy of saturated steam of temperature determined by reactor pressure p_{core} , and $h_{in} = h_f(T_{in})$ is specific enthalpy of feedwater which is obtained as specific enthalpy of saturated water of feedwater temperature

T_{in} . According to consideration of propagation of uncertainty, uncertainty of Q_{fw} is written as

$$\begin{aligned}\sigma_{Q_{\text{fw}}}^2 &\approx \sigma_w^2 \\ &+ \left(\frac{Q_{\text{out}}}{Q_{\text{fw}}}\right)^2 \left(\frac{p_{\text{core}}}{h_g}\right)^2 \left(\frac{\partial h_g}{\partial p_{\text{core}}}\right)^2 \sigma_{p_{\text{core}}}^2 \\ &+ \left(\frac{Q_{\text{in}}}{Q_{\text{fw}}}\right)^2 \left(\frac{T_{\text{in}}}{h_f}\right)^2 \left(\frac{\partial h_f}{\partial T_{\text{in}}}\right)^2 \sigma_{T_{\text{in}}}^2,\end{aligned}\quad (6.5)$$

where σ_w , $\sigma_{p_{\text{core}}}$ and $\sigma_{T_{\text{in}}}$ are uncertainties of the flow of coolant, reactor pressure and the feedwater temperature, these values are $< 2\%$. In the three terms of (6.5), uncertainty of flow of coolant is dominant, because sensitivity to pressure of specific enthalpy of saturated steam ($\partial h_g / \partial p_{\text{core}}$)/ h_g is small, and temperature of coolant becomes high enough to consider influence of feedwater temperature to be small ($Q_{\text{in}} < Q_{\text{fw}} < Q_{\text{out}}$). The accuracy of flow of coolant is determined by uncertainty of feedwater flowmeters, which are calibrated within 2%. Therefore, in the KamLAND experiment, 2% is used as a value of uncertainty of core thermal output data provided by electric power companies.

6.2 Time evolution of the fission rate

6.2.1 Burnup

A basic parameter which indicate the condition of the nuclear fuel in reactor core is ‘‘burnup’’. Burnup is defined as the time integrated thermal output per nuclear fuel mass (GWd/t). The composition of isotopes changes with the increases of the burnup.

At Japanese commercial reactors, a particular nuclear fuel keeps fission reaction for ~ 3 years and a thermal output per nuclear fuel mass is designed to be 30MW/t. Therefore, at the end of the operation period, burnup reaches 3year \cdot 30MW/t \sim 30GWd/t. And a typical rated thermal output is about 3GW. In this case, mass of the nuclear fuel is (3GW)/(30MW/t) \sim 100t.

6.2.2 Burnup equation

The time variation of an isotope which has an atomic number i and a mass number j in reactors can be written as the difference between the production rate and the disappearance rate,

$$\frac{dN^{i,j}(t)}{dt} = \sigma_\gamma^{i,j-1} N^{i,j-1}(t)\phi(t) + \lambda^{i-1,j} N^{i-1,j}(t) - \sigma_a^{i,j} N^{i,j}(t)\phi(t) - \lambda^{i,j} N^{i,j}(t), \quad (6.6)$$

where $\phi(t)$ is the averaged neutron flux, N is a density of the isotope, λ is a beta decay constant. σ_a is a neutron absorption cross section includes the fission reaction cross section, the radiative capture cross section and cross section for other reactions, $\sigma_a = \sigma_f + \sigma_\gamma + \sigma_{\text{other}}$, these cross sections have energy dependence. The equation (6.6) is called burnup equation.

The dominant terms of the burnup equations which is related to four main fissile isotopes in

the nuclear fuel shown in Table 6.1 are written as follow,

$${}^{235}\text{U} : \frac{dN_{235\text{U}}(t)}{dt} = -\phi(t)(\sigma_{235\text{U}}^{\text{f}} + \sigma_{235\text{U}}^{\gamma})N_{235\text{U}}(t) \quad (6.7)$$

$${}^{238}\text{U} : \frac{dN_{238\text{U}}(t)}{dt} = -\phi(t)\sigma_{238\text{U}}^{\gamma}(\eta + 1)N_{238\text{U}}(t) \quad (6.8)$$

$${}^{239}\text{U} : \frac{dN_{239\text{U}}(t)}{dt} = \phi(t) (\sigma_{238\text{U}}^{\gamma}N_{238\text{U}}(t)) - \lambda_{239\text{U}}N_{239\text{U}}(t) \quad (6.9)$$

$$(N_{238\text{U}} \gg N_{239\text{U}}) \quad (6.10)$$

$${}^{239}\text{Np} : \frac{dN_{239\text{Np}}(t)}{dt} = \lambda_{239\text{U}}N_{239\text{U}}(t) - \lambda_{239\text{Np}}N_{239\text{Np}}(t) \quad (6.11)$$

$${}^{239}\text{Pu} : \frac{dN_{239\text{Pu}}(t)}{dt} = -\phi(t)(\sigma_{239\text{Pu}}^{\text{f}} + \sigma_{239\text{Pu}}^{\gamma})N_{239\text{Pu}}(t) + \lambda_{239\text{Np}}N_{239\text{Np}}(t) \quad (6.12)$$

$$(N_{239\text{Pu}} > N_{239\text{Np}}) \quad (6.13)$$

$${}^{240}\text{Pu} : \frac{dN_{240\text{Pu}}(t)}{dt} = \phi(t) (\sigma_{239\text{Pu}}^{\gamma}N_{239\text{Pu}}(t) - \sigma_{240\text{Pu}}^{\gamma}N_{240\text{Pu}}(t)) \quad (6.14)$$

$${}^{241}\text{Pu} : \frac{dN_{241\text{Pu}}(t)}{dt} = \phi(t) \left(\sigma_{240\text{Pu}}^{\gamma}N_{240\text{Pu}}(t) - (\sigma_{241\text{Pu}}^{\text{f}} + \sigma_{241\text{Pu}}^{\gamma})N_{241\text{Pu}}(t) \right), \quad (6.15)$$

where η is the ratio of the fission rate of ${}^{238}\text{U}$ caused by the fast neutron flux $\psi(t)$ to the radiative capture; $\eta \equiv \psi(t)\sigma_{238\text{U}}^{\text{f}}/\phi(t)\sigma_{238\text{U}}^{\gamma}$. The typical value of the neutron flux is $\phi \sim 10^{14}/\text{cm}^2/\text{s}$. Constants of the isotopes are listed in Table 6.4. $\phi\sigma$ for the isotopes at the typical neutron flux is also listed. A particular nuclear fuel exists in the core for 3-5 years, so lifetime of β -decay nuclides ${}^{239}\text{U}$ and ${}^{239}\text{Np}$ is fully short compared with that period.

Isotopes	Constants	$\phi\sigma$ (@ $\phi = 10^{14}/\text{cm}^2/\text{s}$) or λ (1/s)
${}^{235}\text{U}$	$\sigma_{235\text{U}}^{\text{f}}$	582.6b
	$\sigma_{235\text{U}}^{\gamma}$	98.38b
${}^{238}\text{U}$	$\sigma_{238\text{U}}^{\gamma}$	2.680b
	$\sigma_{238\text{U}}^{\text{f}}$	14.3b
${}^{239}\text{U}$	$\sigma_{239\text{U}}^{\gamma}$	22.5b
	$\sigma_{239\text{U}}^{\text{f}}$	23.45m
	$T_{1/2,239\text{U}}$	4.9×10^{-4}
${}^{239}\text{Np}$	$\sigma_{239\text{Np}}^{\gamma}$	36.8b
	$T_{1/2,239\text{Np}}$	2.357d
${}^{239}\text{Pu}$	$\sigma_{239\text{Pu}}^{\text{f}}$	748.1b
	$\sigma_{239\text{Pu}}^{\gamma}$	269.3b
	$T_{1/2,239\text{Pu}}$	24110y
${}^{240}\text{Pu}$	$\sigma_{240\text{Pu}}^{\text{f}}$	0.063b
	$\sigma_{240\text{Pu}}^{\gamma}$	289.5b
	$T_{1/2,240\text{Pu}}$	6564y
${}^{241}\text{Pu}$	$\sigma_{241\text{Pu}}^{\text{f}}$	1012b
	$\sigma_{241\text{Pu}}^{\gamma}$	358.5b
	$T_{1/2,241\text{Pu}}$	14.35y

Table 6.4: Constants of the isotopes.

In actual operating reactor cores, the neutron flux $\phi(t)$ has three-dimensional distribution and it is adjusted to maintain stable operation by the control of the coolant flow rate or density

of the neutron absorber. A thermal output Q at the reactor core is given by the fission rate and the energy released per fission for each fissile element. When the space distribution is averaged, the neutron flux in cores is written as follows,

$$Q = \phi(t)V_U(Q_{235\text{U}}^f\sigma_{235\text{U}}^fN_{235\text{U}}(t) + Q_{238\text{U}}^f\eta\sigma_{238\text{U}}^\gamma N_{238\text{U}}(t) + Q_{239\text{Pu}}^f\sigma_{239\text{Pu}}^fN_{239\text{Pu}}(t) + Q_{241\text{Pu}}^f\sigma_{241\text{Pu}}^fN_{241\text{Pu}}(t)), \quad (6.16)$$

where Q_{nuclei}^f is the available energy released per fission and V_U is the volume of the nuclear fuel. Examples of Q_{nuclei}^f using the reactor core analyses are listed in Table 6.5. In ^{235}U and ^{239}Pu , which are main components in fuel, there are differences of $\sim 0.5\%$. This difference depends on analysis codes and mechanism of the reactors.

	^{235}U	^{238}U	^{239}Pu	^{241}Pu
Bugey experiment [46]	201.8	205.0	210.3	212.6

Table 6.5: Available energy per fission reaction.

Figure 6.5 shows the time evolution of the number densities based on the burnup equations. In this example, initial conditions are as follows, fuel enrichment is 3.0%, $\eta = 0.1$, $\phi(t=0) = 3.0 \times 10^{13}/\text{cm}^2/\text{s}$, and fuel is completely UO_2 (density $10.4\text{g}/\text{cm}^3$) at $t=0$. The neutron flux was adjusted to keep the rated thermal output for the whole period. It is clear that densities of ^{239}U and ^{239}Np are saturated after a few days and those of Pu gradually increase. Particularly, ^{241}Pu accumulates slowly. Figure 6.6 shows the time evolution of the fission reaction rate of the main fissile isotopes. The neutron flux is also shown. In this plot, the time development has direct correlation with burnup. After one year, the absolute burnup is $\sim 15\text{GWd}/\text{t}$.

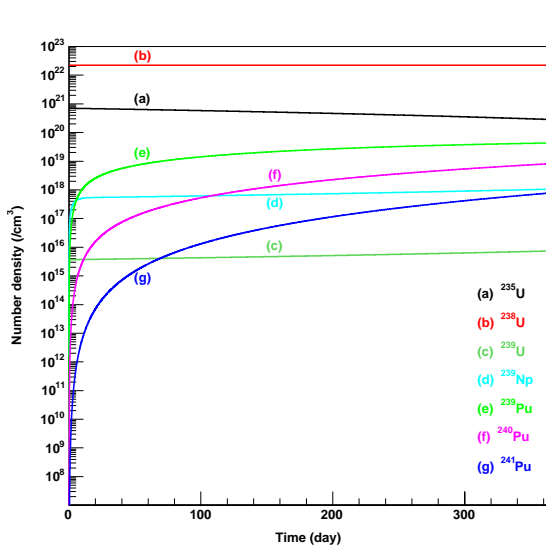


Figure 6.5: Time evolution of the number densities obtained by the burnup equations.

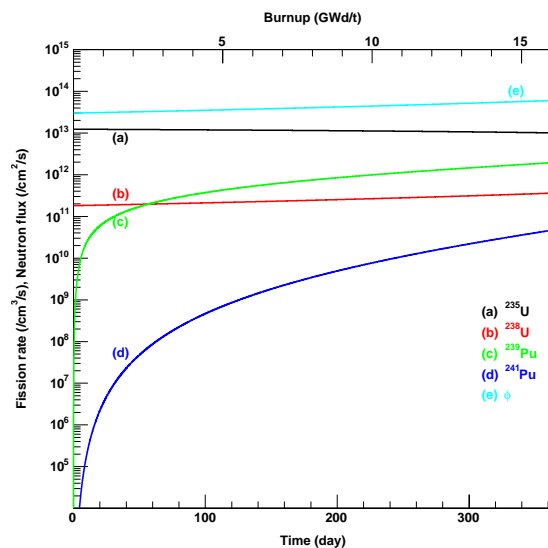


Figure 6.6: Time evolution of the fission reaction rates. The neutron flux is also shown.

The total fission rate at the typical reactor is $(3\text{GW})/(200\text{MeV}/\text{fission}) \sim 10^{20}$ fission/s. It

is actually impossible to trace the time dependence of these large number of nuclei in reactor cores. In the next chapter, the general reactor core analysis method is described.

6.3 Fission rate calculation using the reactor core analysis method [63, 64]

6.3.1 Reactor core analysis method

Detail reactor core simulation traces the fission rate for each fissile element in reactor cores under the actual operating conditions. In this analysis, a Core Management System for BWRs and PWRs which originated by Studsvik of America and developed by Tokyo Electric Power Co. (TEPCO) was used. This system is based on the CASMO-4[66]/SIMULATE-3[67] core fuel management methodology. These two analysis codes are as follows,

1. CASMO-4 is a simple fuel-assembly nuclear characteristics analysis code based on a multi-group two-dimensional transport theory. It is used to obtain nuclear constants (burnup dependent macroscopic cross sections library) from the burnup calculation, in which nuclear fuel is homogenized for each assembly.
2. SIMULATE-3 is a coupled three-dimensional neutronics/thermal-hydraulics analysis code to perform full reactor core calculations using nuclear constants and reactor operating conditions. It determines the detailed power shape or flux distribution based on a two-group three-dimensional nodal diffusion analysis. Using the nuclei composition in nuclear fuel and the neutron energy spectrum, the time evolution and the three-dimensional distribution of the fission rate for each fissile element is calculated.

The fission reaction rate R^i of nuclide i is written as

$$R^i = \sum_{x \in \text{core}(\text{bundle} \times 24 \text{axial})} \left(\frac{P_x}{P_{\text{seg} \equiv x}} R_{\text{seg} \equiv x}^i(E, V, H_v, C, H) \right), \quad (6.17)$$

P_x : Output at node x in cores

$P_{\text{seg} \equiv x}$: Standard output at node x in cores
for the fuel-assembly analysis

$R_{\text{seg} \equiv x}^i$: Fission reaction rate of nuclide i
at node x in cores for the fuel-assembly analysis

E : Burnup at node x in cores

V : Void fraction

H_v : Void fraction hysteresis

C : Control rod pattern

H : Spectrum history.

6.3.2 Burnup dependence at typical reactors

To develop a simplified calculation method described in next section, the detailed simulation was performed by TEPCO for some operation periods of typical reactor cores in Japan. In Table 6.6, target reactors which were chosen as BWR and ABWR at the Kashiwazaki-Kariwa

	BWR-5			ABWR	PWR	
	core1	core2	core3	core4	(Hypothetical core)	
Cycle1	*	*	*	-	-	*
Cycle2	*	*	*	-	-	*
Cycle3	*	*	*	-	*	-
Cycle4-	-	-	4-6	13	4	8-10

Table 6.6: Typical reactor cores used for the detailed calculation. The reactor cores with asterisks and numbers of the cycle were analyzed using the reactor core analysis method.

Nuclear Power Station and a typical PWR are listed. The target nuclear fuel was chosen as typical uranium based nuclear fuel.

Figure 6.7 shows the burnup dependence of the relative fission rate. The burnup dependence of each isotope except for cycle1 and cycle2 has almost same dependence. To perform this method we need detailed data such as structure of reactor core, design of fuel and status of control rods, so it is difficult to do this detailed method to all Japanese commercial reactors. However, the tendency in Figure 6.7 indicates the possibility that the fission rate of each fissile element in any reactor cores can be represented using the burnup evolution in reference core. A new simplified method to calculate the fission rate for each fission element using macroscopic approximation is described in next section.

6.4 Fission rate calculation using simplified method [63, 64]

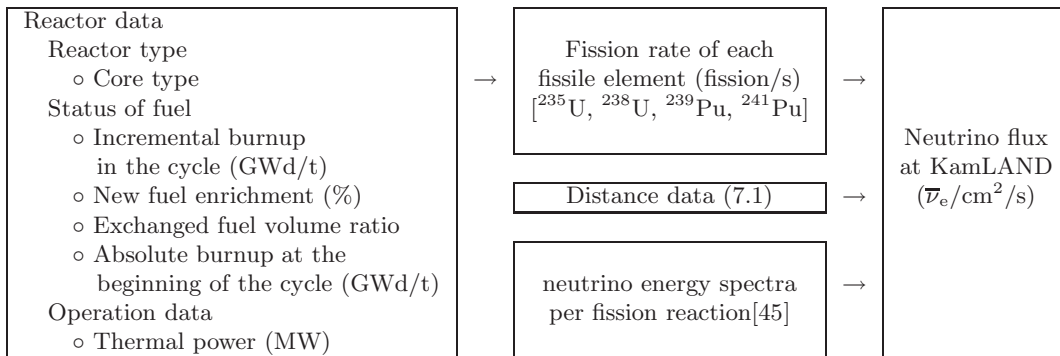


Table 6.7: Reactor data for neutrino flux calculation.

The flowchart of the simplified calculation method is shown in Table 6.12. At the simple method, new fuel part and other fuel part in cores are approximated using “initial core” and “equilibrium core” respectively. In 6.4.1, reactor operation data which shows condition of nuclear fuel in a reactor core is described.

The fission rate of each element is obtained as correction and combination of referential fission rate spectra of initial cores and equilibrium cores. The tree-dimensional distribution in cores is homogenized. The correction parameters are new fuel enrichment, exchanged fuel volume ratio and absolute burnup at beginning of cycle (BOC). Finally, the fission rate is scaled using the thermal output. In 6.4.2, burnup dependence in reference cores is described. It was calculated by the detailed method showed in 6.3.

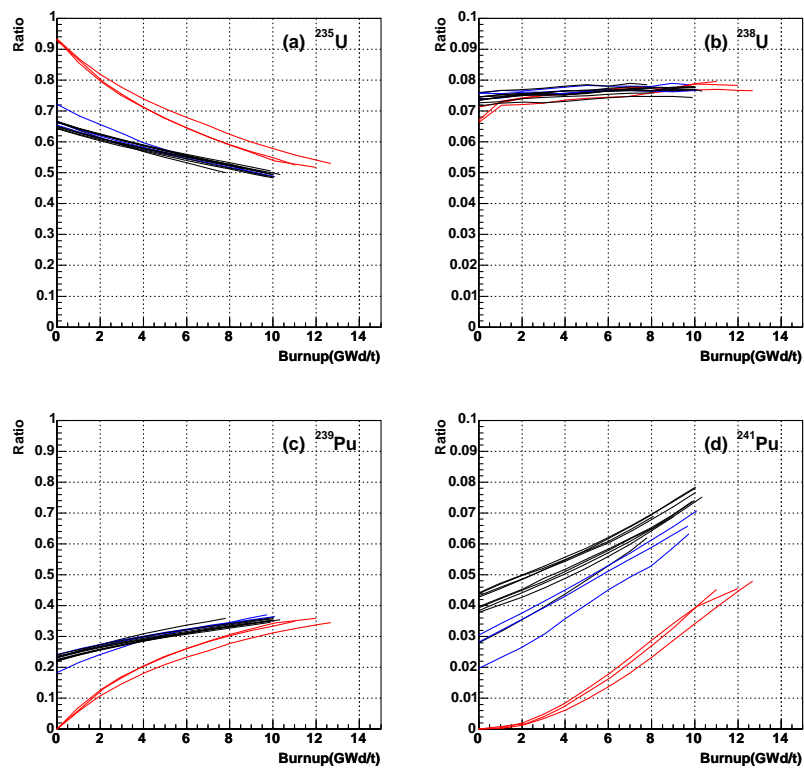


Figure 6.7: Relative fission yields for typical reactor cores by the detailed calculation. The ratio of number of fission reaction in the total number of fission reaction is shown. The red lines show first cycle reactor cores, the blue lines show second cycle reactor cores and the black lines show > 3 cycle cores.

The correction and combination use a small number of operation parameters (shown in Table 6.7), which usually handled in nuclear power plants. These corrections are described in 6.4.3, 6.4.4 and 6.4.5.

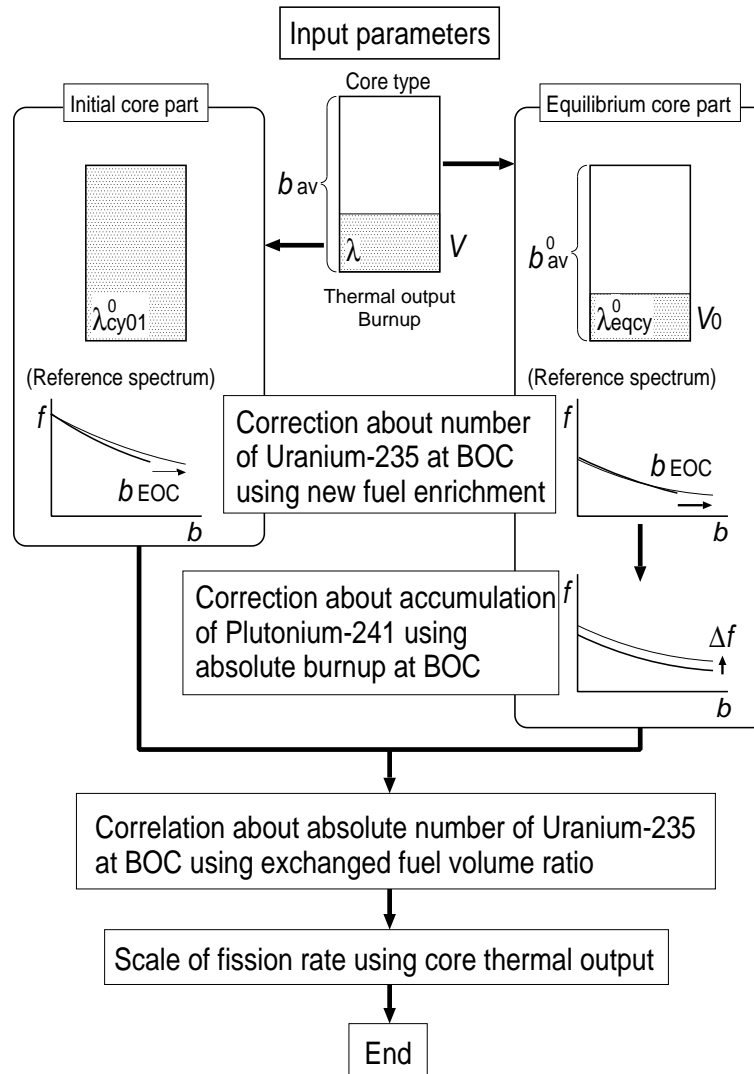


Figure 6.8: Flow chart of the simple method of the fission rate calculation.

6.4.1 Reactor operation data for simplified method [63, 64]

Reactor operation parameters used for the simplified method are as follows. These data are recorded in reactors and provided by all the reactors in Japan.

Reactor core type

Core type of commercial reactors in Japan is categorized into BWR(Boiling Water Reactor) and PWR(Pressurized Water Reactor), according to differences in the steam generating mechanism. There are two types of BWR; regular BWR and ABWR(Advanced Boiling Water Reactor). Design structure of core and condition of fuel are also different in each type. So,

BWR(includes ABWR) and PWR are treated separately when the fission rate is calculated by simplified method.

Cycle number

Japanese commercial reactors stop operation for regular maintenance and refueling about once a year. Usually, one fourth of the total nuclear fuel are exchanged in BWR's and one third for PWR's. "Cycle number" means how many times fuel exchange took place. In the first operation period with completely new fuel which doesn't include Pu, the cycle number is one. This core is called "Initial core". After exchanging fuel repeatedly, cores in which nuclide composition has similar time evolution is called "Equilibrium core". Because the nuclide composition is different obviously between initial cores and equilibrium cores, these cores are treated separately in the simplified strategy.

New fuel enrichment ϵ

"New fuel enrichment" shows the rate of the uranium in fuel. This parameter indicates the number density of ^{235}U in the new fuel.

Exchanged fuel volume ratio V

This parameter shows the ratio of exchanged fuel volume in the total fuel volume. This parameter indicates the absolute number of ^{235}U in the new fuel.

Reactor core thermal output Q

The thermal energy released by fission reaction in reactor core written as $Q(t) = \sum Q_i f_i(t)$, where Q_i is the energy released per fission reaction and f_i is the fission reaction rate.

Incremental burnup in the cycle b

Incremental burnup from the beginning of the cycle written as

$$b = \frac{1}{M} \int dt Q(t), \quad (6.18)$$

where, M is the mass of fuel and $Q(t)$ is the core thermal output.

Absolute burnup at the beginning of the cycle b_{av}

Average of absolute burnup in total fuel at the beginning of the cycle.

Mass of fuel M

The total mass of the fuel.

6.4.2 Burnup dependence in reference cores

Reference reactor cores which have the typical parameters were chosen as Table 6.8 based on the results of the detailed simulation. The four kinds of reference cores were simulated by the core type (BWR or PWR) and the cycle number (Initial core or Equilibrium core).

Core	Constant	BWR	PWR
Initial core	New fuel enrichment (%)	2.03	2.38
	Exchanged fuel volume ratio (%)	100	
	Absolute burnup at BOC (GWd/t)	0	
	Proportionality coefficient of new fuel enrichment and burnup at EOC (GWd/t/%)	6.50	
	Burnup at EOC (GWd/t)	10.0	12.0
Equilibrium core	New fuel enrichment (%)	3.44	3.45
	Exchanged fuel volume ratio (%)	28.0	33.0
	Absolute burnup at BOC (GWd/t)	15.15	12.10
	Proportionality coefficient of new fuel enrichment and burnup at EOC (GWd/t/%)	3.50	
	Burnup at EOC (GWd/t)	10.0	12.0

Table 6.8: Constants of the reference reactor cores for the detailed calculation and the simplified calculation.

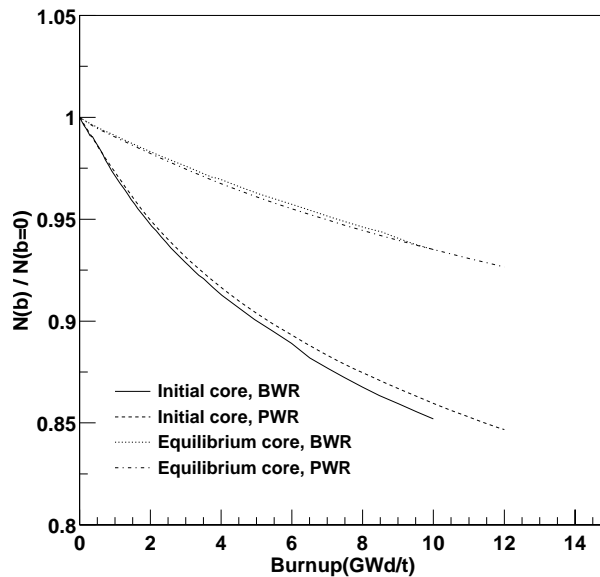


Figure 6.9: Burnup effect at the number of expected events which is normalized at beginning of cycle. Each line corresponds to the different core status.

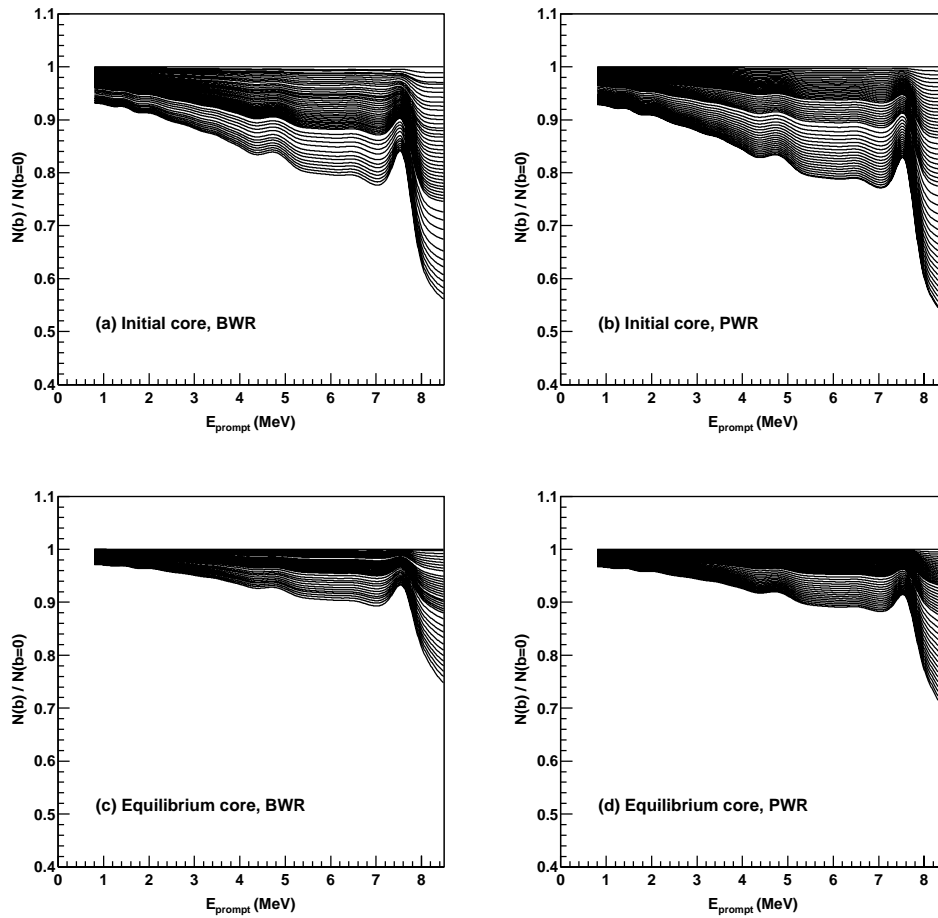


Figure 6.10: Burnup dependence of the expected energy spectra. The energy spectra are normalized for the energy spectrum at beginning of cycle. At BWR, the range of burnup is 0GWd/t to 12GWd/t. At PWR, 0GWd/t to 10GWd/t. The energy spectrum decreases with increase of the burnup. Note that above $E_{\text{prompt}} > 7.2$ MeV, the $\bar{\nu}_e$ spectra for some isotopes are not available. (see Figure 6.3)

Figure 6.9 shows the burnup effect of the event rate calculated for $2.6\text{MeV} < E_{\text{prompt}} < 8.6\text{MeV}$. Nuclear fuel which has large burnup includes higher concentration of ^{239}Pu than fuel in the beginning of the cycle. Therefore, the neutrino flux decreases due to the difference of the energy spectrum per fission reaction. Figure 6.10 shows the variation of the expected energy spectrum. In the high energy region, the neutrino flux decreases due to the difference of the $\bar{\nu}_e$ spectra of ^{235}U and ^{239}Pu .

6.4.3 Correction for variation of new fuel enrichment

At first, correlation between the reference spectra and ^{235}U number density at initial condition is considered. This parameter is presented as new fuel enrichment ϵ . The reference spectra shown in Figure ?? are normalized by total thermal output. Let us now consider time variation of fission rates per total thermal output at $t_1 = t_0 + \Delta t$ using the burnup equations and the neutron flux at $t_0 = 0$. We are assuming that fission isotopes are only ^{235}U and ^{239}Pu and number of ^{238}U is constant as a simple case. The burnup equations are written as

$$^{235}\text{U} : \quad \frac{dN_{235\text{U}}}{dt} = -\phi(t)\sigma_{235\text{U}}^f N_{235\text{U}}(t), \quad (6.19)$$

$$^{239}\text{Pu} : \quad \frac{dN_{239\text{Pu}}}{dt} = \phi(t) \left(\sigma_{238\text{U}}^\gamma N_{238\text{U}} - \sigma_{239\text{Pu}}^f N_{239\text{Pu}}(t) \right). \quad (6.20)$$

As initial conditions, $N_{235\text{U}}(0) = N_{235}^0$ and $N_{239\text{Pu}}(0) = 0$. The neutron flux at $t_0 = 0$ is determined by the thermal output Q^0 as

$$\phi(0) = \frac{Q^0}{Q_{235\text{U}}^f \sigma_{235\text{U}}^f N_{235\text{U}}^0}. \quad (6.21)$$

At short time after, $t_1 = \Delta t$, the number density of ^{235}U is written as

$$N_{235\text{U}}(\Delta t) = N_{235\text{U}}^0 \exp(-\phi(0)\sigma_{235\text{U}}^f \Delta t) \quad (6.22)$$

$$\approx N_{235\text{U}}^0 - \frac{Q^0}{Q_{235\text{U}}^f} \Delta t, \quad (6.23)$$

the fission rate of ^{235}U is

$$N_{235\text{U}}^f(\Delta t) = \phi(0)\sigma_{235\text{U}}^f N_{235\text{U}}(\Delta t) \quad (6.24)$$

$$\approx \frac{Q^0}{Q_{235\text{U}}^f} \left(1 - \frac{Q^0 \Delta t}{Q_{235\text{U}}^f N_{235\text{U}}^0} \right). \quad (6.25)$$

Therefore, for the short time period Δt , $N_{235\text{U}}^f$ can be written as a function of burnup $b \propto \Delta t$ and enrichment ϵ ,

$$N_{235\text{U}}^f = N_{235}^f \left(\frac{b}{\epsilon} \right). \quad (6.26)$$

So, the fission rate as the burnup $f(b)$ is assumed to be same formula

$$f\left(\frac{b_0}{\epsilon_0}\right) = f\left(\frac{b}{\epsilon}\right), \quad (6.27)$$

where b_0 and ϵ_0 are burnup and enrichment for the reference core and b and ϵ are burnup and enrichment in any cores. Then the fission rate for ϵ and b is scaled using the reference spectra for the enrichment ϵ_0 ,

$$f(\epsilon, b) = f\left(\epsilon_0, \frac{\epsilon_0}{\epsilon} b\right). \quad (6.28)$$

In actual case, the relation is not so simple and it is assumed,

$$f(\epsilon, b) = f\left(\epsilon_0, \frac{\epsilon_0}{\epsilon} (1 + \delta)b\right), \quad (6.29)$$

where δ is a correction factor. At the development of the simple calculation method, the scale factor,

$$\eta \equiv \frac{\epsilon_0}{\epsilon}(1 + \delta), \quad (6.30)$$

was determined using the detailed simulation as follows. At a burnup at EOC in reference cores b_{EOC} and that in any reactors $b'_{\text{EOC}} = b_{\text{EOC}} + \Delta b_{\text{EOC}}$ shown in Figure 6.11, η is written as

$$\eta = \frac{b_{\text{EOC}}}{b'_{\text{EOC}}}, \quad (6.31)$$

$$\Delta b_{\text{EOC}} = \frac{b_{\text{EOC}}}{\epsilon_0} \Delta \epsilon, \quad (6.32)$$

where, $\epsilon = \epsilon_0 + \Delta \epsilon$.

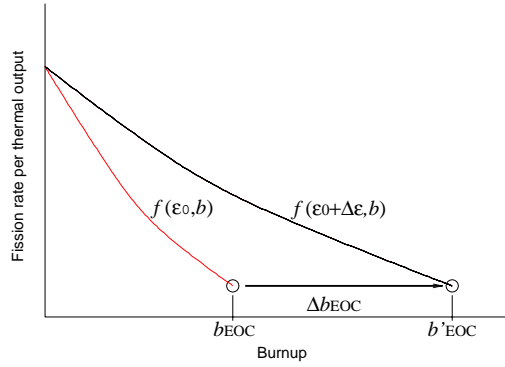


Figure 6.11: Burnup at end of cycle (EOC). For the reference spectrum (red line), b_{EOC} is determined as a typical burnup at the end of cycle.

Δb_{EOC} can be written using differential coefficients,

$$f(\epsilon_0, b_{\text{EOC}}) \equiv f(\epsilon_0 + \Delta \epsilon, b_{\text{EOC}} + \Delta b_{\text{EOC}}) \quad (6.33)$$

$$= f(\epsilon_0, b_{\text{EOC}}) + \frac{\partial f}{\partial \epsilon}(\epsilon_0) \Delta \epsilon + \frac{\partial f}{\partial b_{\text{EOC}}}(b_{\text{EOC}}) \Delta b_{\text{EOC}}, \quad (6.34)$$

then,

$$\Delta b_{\text{EOC}} = - \frac{\frac{\partial f}{\partial \epsilon}(\epsilon_0)}{\frac{\partial f}{\partial b_{\text{EOC}}}(b_{\text{EOC}})} \Delta \epsilon \quad (6.35)$$

$$\equiv \beta(\epsilon_0, b_{\text{EOC}}) \Delta \epsilon. \quad (6.36)$$

$\beta(\epsilon_0, b_{\text{EOC}})$ is determined using the detailed simulation. The constants of b_{EOC} and $\beta(\epsilon_0, b_{\text{EOC}})$ correspond to “Burnup at EOC” and “Proportionality coefficient of new fuel enrichment and burnup at EOC” in the Table 6.8. According to these values, relative expression of scale factors $\beta(\epsilon_0, b_{\text{EOC}})/b_{\text{EOC}}$, are 0.65/% and 0.54/% for the initial BWR and PWR cores, and 0.35/% and 0.29/% for the equilibrium BWR and PWR cores.

Using (6.31) and (6.36), (6.29) is written as

$$f(\epsilon_0 + \Delta \epsilon, b) = f\left(\epsilon_0, b \frac{1}{1 + \frac{\beta(\epsilon_0, b_{\text{EOC}})}{b_{\text{EOC}}} \Delta \epsilon}\right). \quad (6.37)$$

This equation indicates possibility that the fission rate at burnup b might be approximated using burnup dependence of the fission rate in a reactor core which enrichment is ϵ_0 .

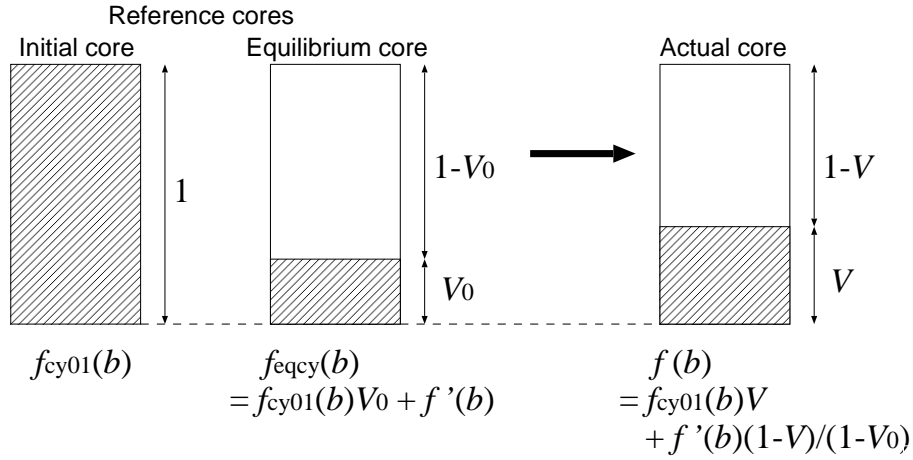


Figure 6.12: Fuel volume correction model.

6.4.4 Correction for exchanged fuel volume ratio

The new fuel enrichment is the relative amount of ^{235}U in new fuel component. The exchanged fuel volume ratio represents initial absolute number of ^{235}U in reactor cores.

Here the fission rate per thermal energy as functions of burnup for the referential initial core and the referential equilibrium core are $f_{cy01}(b)$ and $f_{eqcy}(b)$ (Figure 6.12). We assume the thermal power in the core is uniform. The fission rate is written as linear combination of $f_{cy01}(b)$ and $f_{eqcy}(b)$:

$$f(b) = f_{cy01}(b)V + f'(b)\frac{1-V}{1-V_0}, \quad (6.38)$$

$$f'(b) = f_{eqcy}(b) - f_{cy01}(b)V_0. \quad (6.39)$$

6.4.5 Correction for absolute burnup at the beginning of the cycle

The previous corrections using new fuel enrichment and exchanged fuel volume ratio have same formation for each fissile isotope. However, each fissile isotope has some characteristic time evolution of the fission reaction rate. So, an additional correction for each isotope is required. Particularly, the number of ^{241}Pu , which is created by two neutron absorptions of ^{239}Pu , depends on the number of irradiated neutrons. In the case of equilibrium cores, it is correlated with the number of fission reaction before the cycle. So, the absolute burnup at the beginning of the cycle b_{av} is used for correction for the nuclide composition at the beginning of the cycle as

$$f(b) = af_{cy01}(b) + bf'_{eqcy}(b) \quad (6.40)$$

$$= af_{cy01}(b) + b(f_{eqcy}(b) + \Delta f(b_{av})). \quad (6.41)$$

Here

$$\Delta f(b_{av}) \equiv \kappa \left(\frac{b_{av}}{b_{av}^0} - 1 \right), \quad (6.42)$$

where κ is correction factor for each fissile element and b_{av}^0 is the absolute burnup at the beginning of the cycle in the referential equilibrium core and b_{av} is in the target core. The correction factors

were decided by the least square method as Table 6.9. At actual reactor cores, $0 \lesssim (b_{av}/b_{av}^0 - 1) \lesssim 0.4$. So, effect of this correction is $\lesssim 5\%$ except for ^{241}Pu in BWRs, for which the fission rate is corrected $\lesssim 30\%$.

Isotopes	BWR		PWR	
	κ (fission/MW)	$\kappa/f_{\text{eqcy}}(b=0)$	κ (fission/MW)	$\kappa/f_{\text{eqcy}}(b=0)$
^{235}U	-7.90×10^{14}	-0.039	1.22×10^{15}	0.059
^{238}U	-7.81×10^{13}	-0.035	-9.83×10^{13}	-0.041
^{239}Pu	1.20×10^{14}	0.018	-7.74×10^{14}	-0.118
^{241}Pu	7.75×10^{14}	0.660	5.82×10^{13}	0.059

Table 6.9: Correction factors for the absolute burnup at BOC.

Using all corrections in 6.4.3, 6.4.4 and 6.4.5, the fission rate for a fissile isotope per thermal output in the target core is written as

$$f^{\text{isotope}}(\epsilon, b, V, b_{av}) = f_{\text{cy01}}^{\text{isotope}}(b') \frac{V - V_0}{1 - V_0} + \left(f_{\text{eqcy}}^{\text{isotope}}(b') + \kappa^{\text{isotope}} \left(\frac{b_{av}}{b_{av}^0} - 1 \right) \right) \frac{1 - V}{1 - V_0}, \quad (6.43)$$

$$b' = b \frac{b_{\text{EOC}}}{b_{\text{EOC}} + \beta(\epsilon_0, b_{\text{EOC}}) \Delta \epsilon}. \quad (6.44)$$

The relative difference of the calculated fission rate is shown in Figure 6.13 (without the correction for b_{av}) and Figure 6.14 (with the correction for b_{av}). The difference of the detailed method and simple method is less than 3%. It is clearly seen that the difference of ^{241}Pu decreases with the correction.

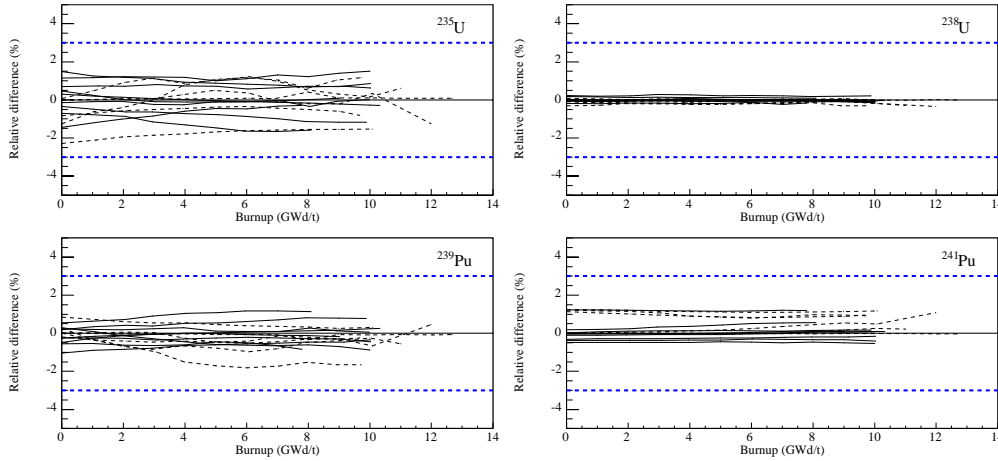


Figure 6.13: Comparison between fission rate calculated by detailed method and simple method without the correction for b_{av} . The relative difference is obtained as $(F(b)^{\text{isotope}}_{\text{simple}} - F(b)^{\text{isotope}}_{\text{detailed}}) / \sum_{\text{isotope}} F(b)^{\text{isotope}}_{\text{detailed}}$. Each line is the burnup dependence of a reactor core.

6.5 Systematic error of the simple method

Systematic uncertainty of the $\bar{\nu}_e$ obtained by the simple method includes uncertainty of the absolute value of the reactor thermal output and the relative fission rate for each fissile nuclide.

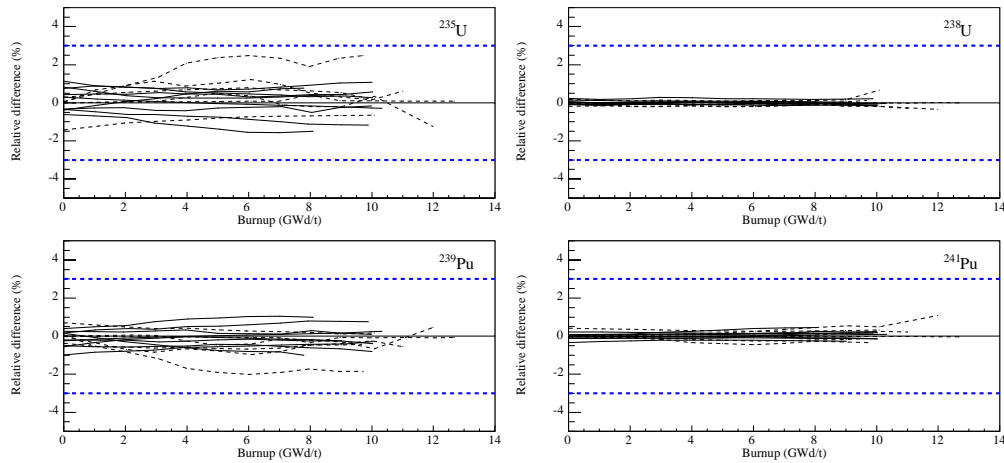


Figure 6.14: Comparison between fission rate calculated by detailed method and simple method with the correction for b_{av} . The relative difference is obtained as $(F(b)_{simple}^{isotope} - F(b)_{detailed}^{isotope}) / \sum_{isotope} F(b)_{detailed}^{isotope}$. Each line is the burnup dependence of a reactor core.

Figure 6.15 shows the difference of the $\bar{\nu}_e$ energy spectrum using the reactor anti-neutrino energy spectrum per fission. A systematic uncertainty in the $\bar{\nu}_e$ flux is less than 1%.

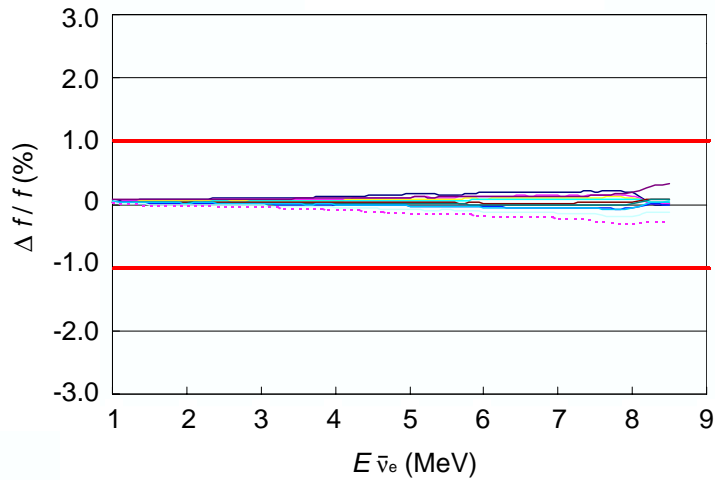


Figure 6.15: Comparison of anti-neutrino energy spectrum between the detailed method and simple method at a typical equilibrium core. Each line corresponds to burnup from 0GWd/t to 10GWd/t.

Chapter 7

Expected reactor anti-neutrino event estimation

In this chapter, the energy spectrum of the expected reactor $\bar{\nu}_e$ events at KamLAND is estimated. The reactor $\bar{\nu}_e$ flux is calculated using the fission rate flux for each fissile element from reactors. Handling of the reactors is classified into three groups as shown in Table 7.1.

About Japanese power reactors shown in Figure 7.2, the operation data provided by each reactor are used for calculating the fission rate using the method described in the Chapter 6. In section 7.1, the status of each reactor for the analysis period and the real operation data are described. The fission rate of a prototype reactor is provided by the operator directly.

About Korean commercial reactors, the daily electricity generation is used to calculate fission rate. In section 7.2, the fission rate of each reactor is calculated by using the assumption that the reactors have same average fuel composition and thermal efficiency as the Japanese commercial reactors.

In Japan, there are a few number of research reactors whose rated outputs are much smaller than power reactors. In section 7.3, contribution from these reactors and power reactors located in other countries are estimated.

Spent nuclear fuel includes some long live nuclides. These nuclides emit $\bar{\nu}_e$'s which are not included in the reactor $\bar{\nu}_e$ energy spectrum shown in the Figure 6.3. The maximum energy of these $\bar{\nu}_e$'s is higher than the analysis threshold. In section 7.4, additional effect from spent nuclear fuel generated in Japanese power reactors are estimated.

Finally, the energy spectrum of the expected event is calculated by using information about the run time, the livetime and the cross section at KamLAND. In section 7.5, the total reactor $\bar{\nu}_e$ flux at KamLAND is described. In section 7.6, the expected event at KamLAND and systematic uncertainty of each component of $\bar{\nu}_e$ flux estimation are described.

7.1 Japanese commercial reactors

7.1.1 Basic parameters

During the measurement period at KamLAND between March 2002 and January 2004, 52 commercial reactors in 16 electric power stations operated in Japan. Some basic parameters about Japanese power reactors are shown in Table 7.2. There are two prototype reactors. Fugen is ATR (Advanced Thermal Reactor) and stopped its operation in March 2003. Monju is FBR (Fast breeder Reactor) and it was under construction until January 2004. Thermal output shown in Table 7.2 is “rated thermal output” (same as “reactor thermal output” as full operation).

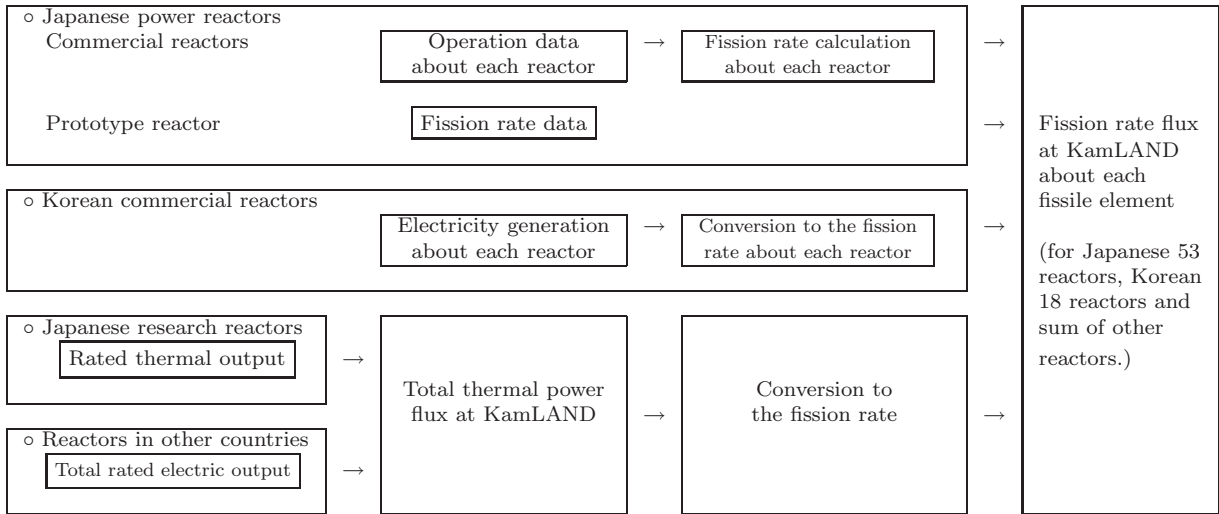


Table 7.1: Handling of each reactor in the fission rate calculation at KamLAND

Figure 7.1 shows history of a total thermal output of power reactors which existed as operable reactors in Japan. First reactor started operation in 1969. When KamLAND started data taking, almost all reactors have operated for several years at least. This means that the almost all reactor cores became “equilibrium cores”, in which the individuality of the time development of nuclear fuel is small. This feature supports to calculate the production rate of the reactor $\bar{\nu}_e$'s which depend on the state of reactor cores by macroscopic variables precisely. The detail of estimation of the reactor $\bar{\nu}_e$'s is described in Chapter 7.

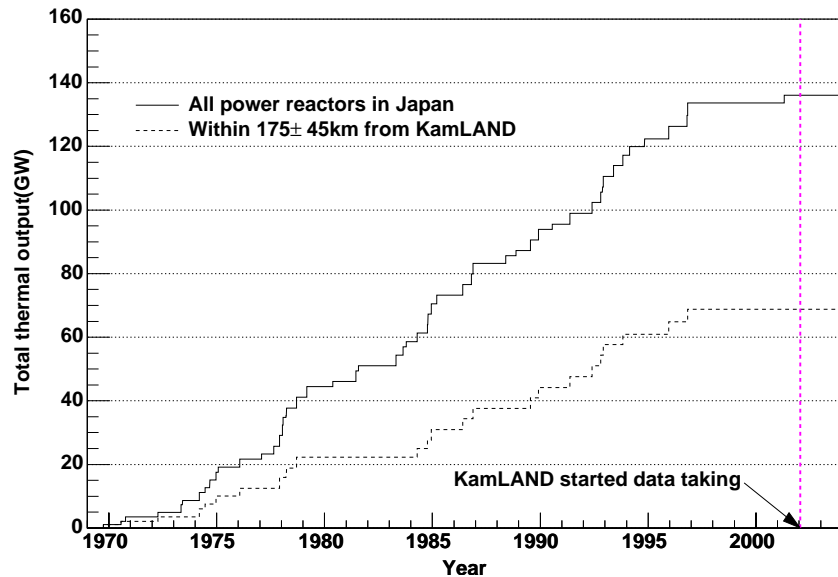


Figure 7.1: History of a total thermal output of electric-power producing reactors in Japan. The red dashed line is the start of the data taking at KamLAND.

Reactor core type

All Japanese commercial reactors are light water reactors (LWRs). 52 LWRs are separated to 29 boiling water reactors (BWRs) and 23 pressurized water reactors (PWRs) based on the water cooling type. Both type of LWRs use 3-5% enriched ²³⁵U fuel.

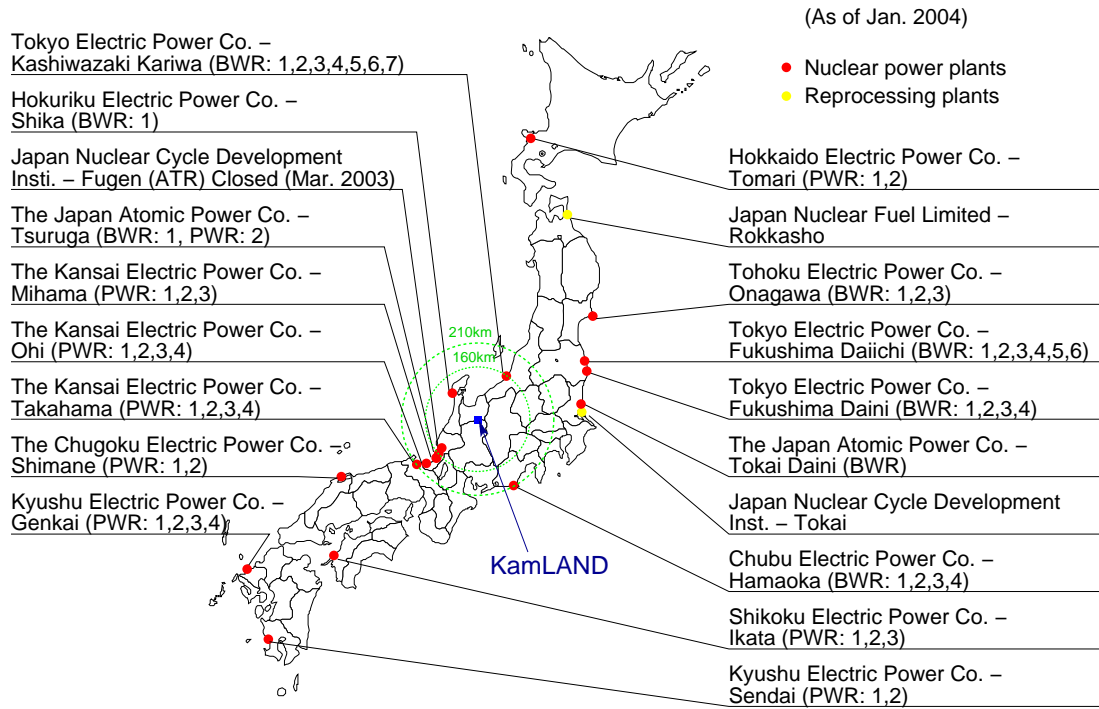


Figure 7.2: Nuclear power plants in Japan. Two reprocessing plants described in 7.4 are also shown.

Rated electric output

Electric output shown in Table 7.2 is “rated electric output” defined as capacity of each unit. In summer, temperature of seawater used as cooling water is higher than winter, therefore thermal efficiency falls. In this thesis, ratio of rated thermal output and rated electric output is used as rated thermal efficiency. Figure 7.3 shows rated thermal efficiencies of Japanese power reactors. The mean value of BWRs is 0.336 and that of PWRs is 0.340.

Coordinates of cores and distance to KamLAND

To calculate distance from each reactor to KamLAND, coordinates of power reactors in Japan with the Tokyo Datum and the Bessel Ellipsoid were used. (These coordinates are consistent with publicly available values in Ref. [71].) These coordinates were converted to values in the ITRF94 and GRS80 Ellipsoid by using the same coordinate transformation programs as coordinates at KamLAND described in 2.2. The orthometric height of all reactors was assumed to be 0.0m. The distance between KamLAND and each reactor was calculated by using the coordinates in the orthogonal coordinate system and shown in Table 7.2. The uncertainty of the distances was studied based on the comparison with coordinates of the reactors taken from an

	Reactor name	Reactor type	Thermal output (MW)	Electric output (MW)	Distance (km)	Power company
00	Hamaoka-1	BWR	1593	540	214	Chubu
01	Hamaoka-2	BWR	2436	840	214	Chubu
02	Hamaoka-3	BWR	3293	1100	214	Chubu
03	Hamaoka-4	BWR	3293	1137	214	Chubu
04	Shimane-1	BWR	1380	460	401	Chugoku
05	Shimane-2	BWR	2436	820	401	Chugoku
06	Tokai2	BWR	3293	1100	295	Genden
07	Tsuruga-1	BWR	1064	357	138	Genden
08	Tsuruga-2	PWR	3423	1160	138	Genden
09	Tomari-1	PWR	1650	579	783	Hokkaido
10	Tomari-2	PWR	1650	579	783	Hokkaido
11	Shika-1	BWR	1593	540	88	Hokuriku
12	Fugen	ATR	557	165	139	JNC
13	Monju	FBR	714	280	142	JNC
14	Mihama-1	PWR	1031	340	146	Kansai
15	Mihama-2	PWR	1456	500	146	Kansai
16	Mihama-3	PWR	2440	826	146	Kansai
17	Ohi-1	PWR	3423	1175	179	Kansai
18	Ohi-2	PWR	3423	1175	179	Kansai
19	Ohi-3	PWR	3423	1180	179	Kansai
20	Ohi-4	PWR	3423	1180	179	Kansai
21	Takahama-1	PWR	2440	826	191	Kansai
22	Takahama-2	PWR	2440	826	191	Kansai
23	Takahama-3	PWR	2660	870	192	Kansai
24	Takahama-4	PWR	2660	870	192	Kansai
25	Genkai-1	PWR	1650	559	754	Kyusyu
26	Genkai-2	PWR	1650	559	755	Kyusyu
27	Genkai-3	PWR	3423	1180	755	Kyusyu
28	Genkai-4	PWR	3423	1180	755	Kyusyu
29	Sendai-1	PWR	2660	890	830	Kyusyu
30	Sendai-2	PWR	2660	890	830	Kyusyu
31	Ikata-1	PWR	1650	566	561	Shikoku
32	Ikata-2	PWR	1650	566	561	Shikoku
33	Ikata-3	PWR	2660	890	561	Shikoku
34	Onagawa-1	BWR	1593	524	430	Tohoku
35	Onagawa-2	BWR	2436	825	431	Tohoku
36	Onagawa-3	BWR	2436	825	431	Tohoku
37	Fukushima1-1	BWR	1380	460	349	Tokyo
38	Fukushima1-2	BWR	2381	784	349	Tokyo
39	Fukushima1-3	BWR	2381	784	349	Tokyo
40	Fukushima1-4	BWR	2381	784	349	Tokyo
41	Fukushima1-5	BWR	2381	784	350	Tokyo
42	Fukushima1-6	BWR	3293	1100	350	Tokyo
43	Fukushima2-1	BWR	3293	1100	345	Tokyo
44	Fukushima2-2	BWR	3293	1100	345	Tokyo
45	Fukushima2-3	BWR	3293	1100	345	Tokyo
46	Fukushima2-4	BWR	3293	1100	345	Tokyo
47	KashiwazakiKariwa-1	BWR	3293	1100	159	Tokyo
48	KashiwazakiKariwa-2	BWR	3293	1100	159	Tokyo
49	KashiwazakiKariwa-3	BWR	3293	1100	159	Tokyo
50	KashiwazakiKariwa-4	BWR	3293	1100	160	Tokyo
51	KashiwazakiKariwa-5	BWR	3293	1100	161	Tokyo
52	KashiwazakiKariwa-6	BWR	3926	1356	161	Tokyo
53	KashiwazakiKariwa-7	BWR	3926	1356	160	Tokyo

Table 7.2: Power reactors in Japan.

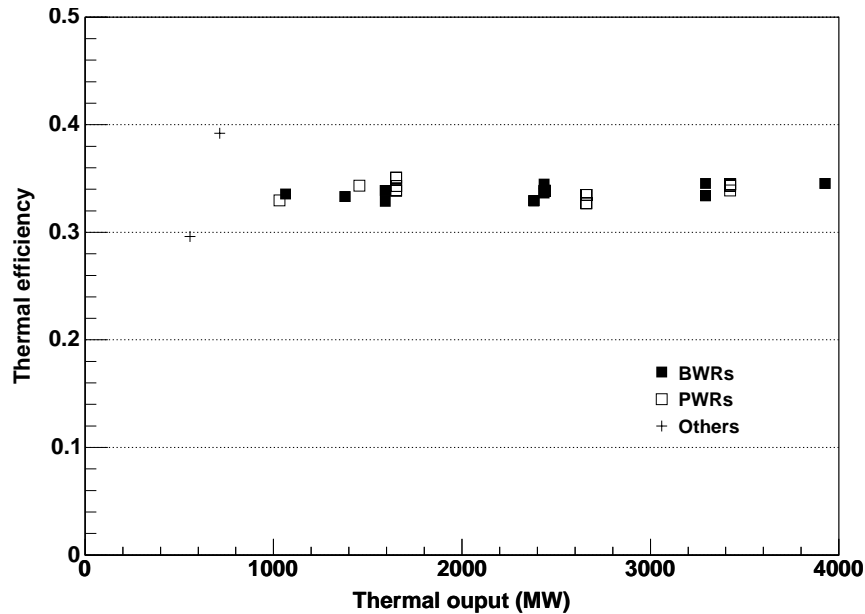


Figure 7.3: Rated thermal efficiencies of Japanese power reactors.

ordinary topographical map [52]. In this study, discrepancies were found to be within 70m. The difference of the number of expected reactor $\bar{\nu}_e$ events caused by the discrepancies is $< 0.1\%$.

The $\bar{\nu}_e$ flux is represented using unit of flux as $P_{\text{thermal}}/4\pi L^2$, where P_{thermal} is the thermal output and L is the distance to KamLAND. In this thesis, this value is called as ‘‘Thermal output (or power) flux’’. ‘‘Electric output flux’’ and ‘‘Neutrino flux’’ are similarly defined. Figure 7.4 shows thermal output flux of each reactor. This figure includes Korean reactors described later. All reactors have contribution of more than $\sim 0.1\%$, and about half of all reactors are distributed from 1% to 7%. Therefore, in the KamLAND experiment, it is required that time variation of thermal output of all these reactors are tracked.

7.1.2 Operation data of each reactor

Reactor operation data as input parameters for the time dependent fission rate calculation are provided by the electric power companies and compiled at Tohoku University. The data period of the reactor data described in this section is from March 6, 2002 to January 24, 2004.

Figure 7.5 shows operation period of reactors including Korean reactors. (Handling of Korean commercial reactors are described in the next section.) Generally, the operation of reactors stops once a year for refueling and regular maintenance. The reactor operation data are classified into two groups as listed in Table 7.3. One is nuclear fuel status which are fixed for each operation period and another is time dependent operation data including the thermal output.

Nuclear fuel parameters

Figure 7.6 shows cycle number distribution of 102 cores existed in all Japanese commercial reactors. Except for one initial core and one second cycle core, all cores are the equilibrium cores. This reactor is at a distance of 431km from KamLAND, and the contribution is $\sim 0.4\%$.

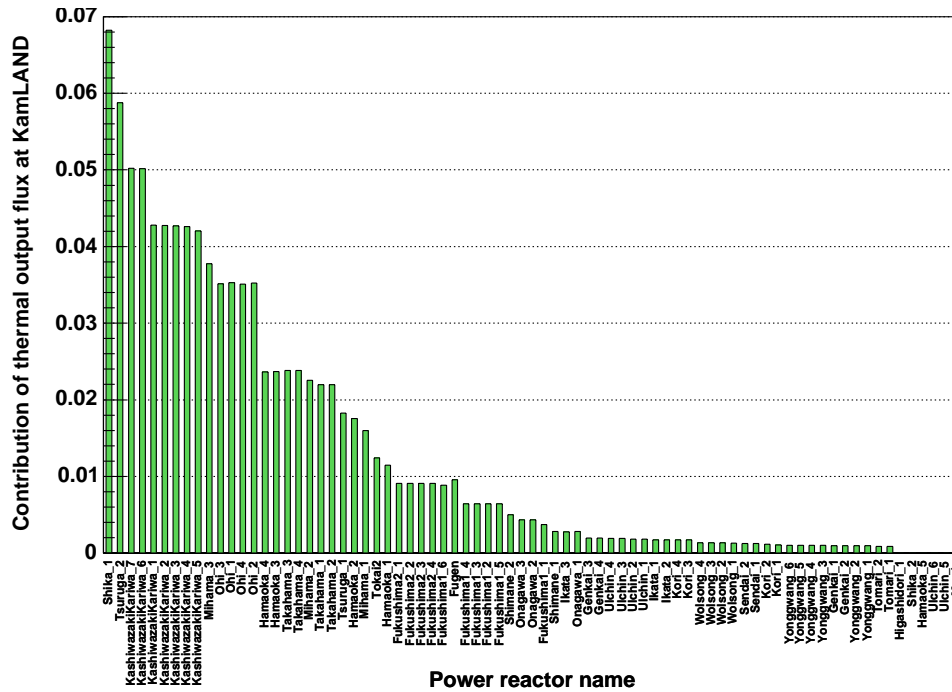


Figure 7.4: Contribution of rated thermal output flux at KamLAND from Japanese and Korean reactors.

Time dependence	Parameters
Fixed	<input type="checkbox"/> Reactor type (BWR or PWR)
Fixed for every cycle	<input type="checkbox"/> Cycle number <input type="checkbox"/> New fuel enrichment <input type="checkbox"/> Exchanged fuel volume ratio <input type="checkbox"/> Absolute burnup at the beginning of the cycle
Variable	<input type="checkbox"/> Reactor core thermal output <input type="checkbox"/> Incremental burnup in the cycle

Table 7.3: Time dependence of the operation data parameters.

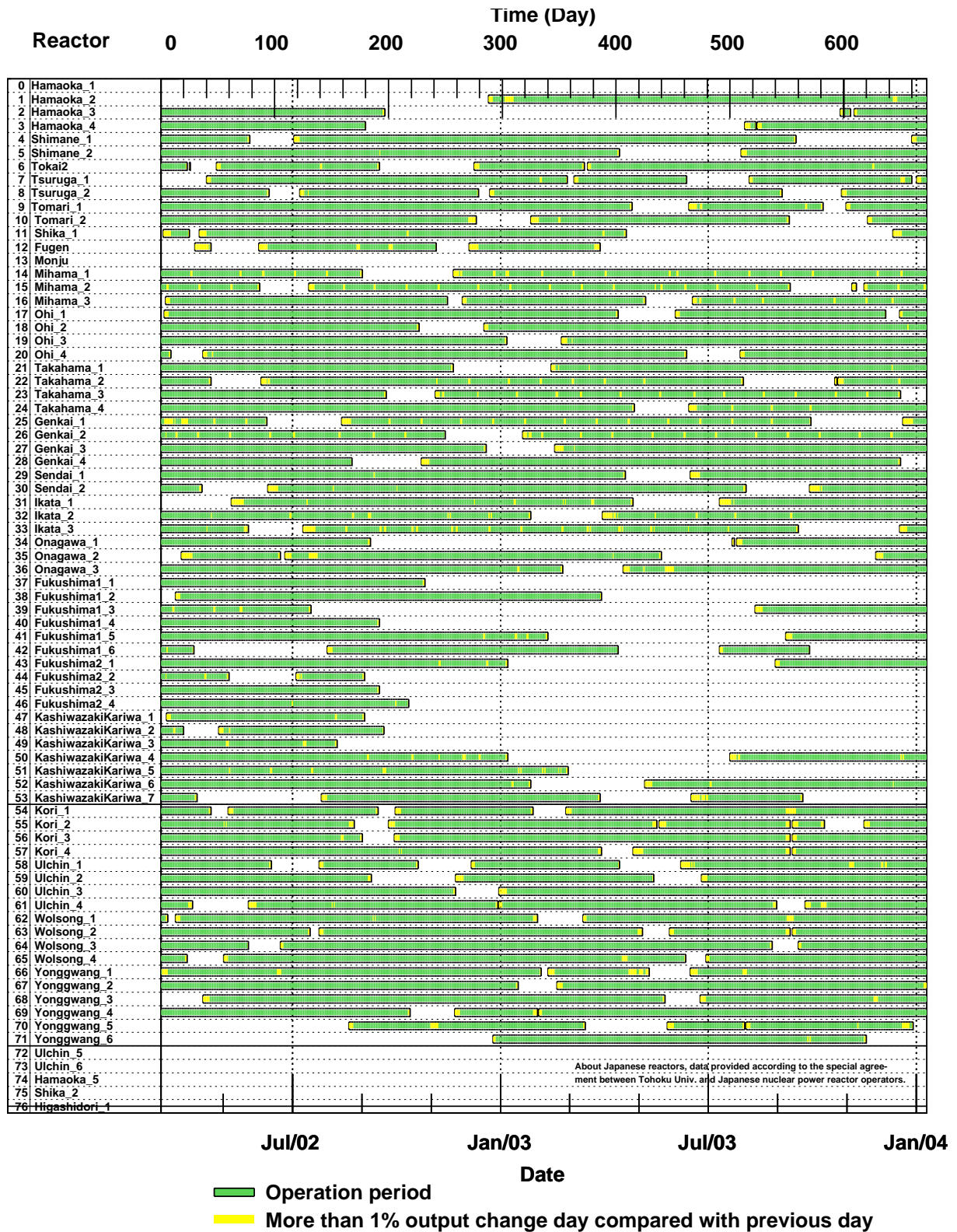


Figure 7.5: Reactor operation status. Horizontal bars show operation periods. The reactor number of 0 to 53 correspond to Japanese power reactors. The reactor number of 54 to 71 correspond to Korean commercial reactors. The reactor number of more than 72 correspond to reactors under construction.

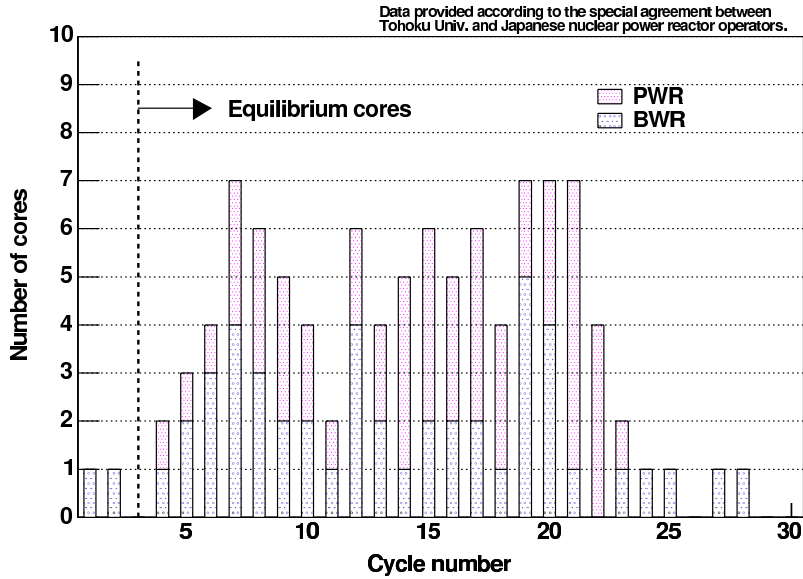


Figure 7.6: Cycle number distribution of reactor cores existed in the KamLAND analysis period. Almost all reactors were the equilibrium cores described in Chapter 6.

Time-dependent operation data

Thermal output	Operation status
Stable	<input type="checkbox"/> Steady-state operation
Varies	<input type="checkbox"/> Normal start-up
	<input type="checkbox"/> Normal shutdown
	<input type="checkbox"/> Intermediate shutdown
	<input type="checkbox"/> Control rod pattern adjustment (BWR)
	<input type="checkbox"/> Turbine steam free test (PWR)
	<input type="checkbox"/> Coastdown operation
	<input type="checkbox"/> Other irregular operation

Table 7.4: Operation status of power reactors.

The operation data of reactors are categorized as listed in Table 7.4. The nuclear fuel parameters described previously are time independent in a operation cycle. However, values of the thermal output and incremental burnup calculated from the thermal output depend on the operation status. To reproduce the operation status, the time interval of data points about these parameters in a cycle is classified in Table 7.5.

The steady-state operation Currently, there are two operation methods at Japanese commercial reactors. One method is to keep the electric output constant by adjusting the thermal output to correct the seasonal variation of the efficiency (Constant electric output operation). Another method keeps the thermal output constant (Constant thermal output operation).

Operation	Thermal output		Burnup	
	Interval	Value	Interval	Value
Stable output	□ One week	Instant value	Same point as the thermal output	
	□ One day	Average for one day	One day	Instant value at 24:00
Changed output	□ About one hour	Instant value	No data	
	□ About one hour	Instant value of the electric output	No data	
	□ Changing point of data	Instant value	Same point as the thermal output	
	□ One day	Average for one day	One day	Instant value at 24:00

Table 7.5: Time interval of the operation data.

The period of output change Change of the thermal output mainly takes place at the time of regular shutdown and start-up. Sometimes, shutdown for the maintenance without refueling is performed (Intermediate shutdown). Figure 7.7 shows the thermal output curve at a normal start-up and Figure 7.8 shows a normal shutdown. At the end of the operation cycle, some reactors gradually reduce the thermal output for about one month due to the decrease of the neutron flux (Coastdown operation).

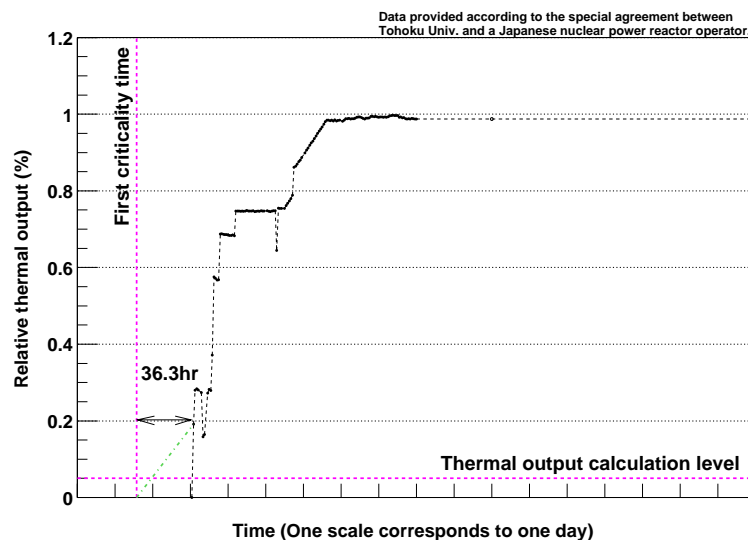


Figure 7.7: Example of the thermal output at the start-up.

At BWRs, the thermal output calculation using the flow of coolant is not performed for the output of less than 5 – 10% of the rated value . About PWRs, the calculation is mainly performed until the output decreases to 0. To determine the time when nuclear fission reaction started or stopped, the following arbitrary standard was used. The start time or stop time is determined as,

1. If the time of 0 thermal output is included in data, that time,
2. If the additional information about start-up time or shutdown time can be available, that time,
3. When it corresponds to neither of the cases, the time of one hour before or after of the last data point.

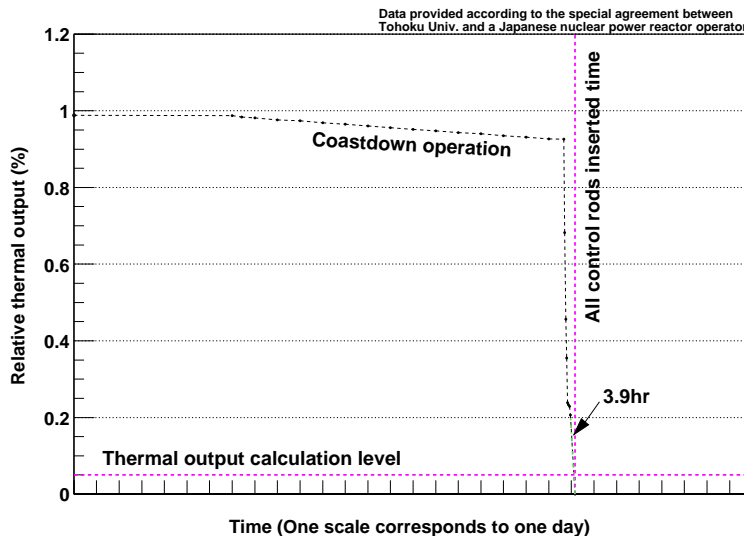


Figure 7.8: Example of the thermal output at the shutdown.

Where, the shutdown time is defined as the time of all control rods fully inserted, and the start-up time is defined as the time of starting of criticality. The normal shutdown and start-up for the regular maintenance is performed once in a year. If all BWRs, which have $\sim 50\%$ contribution of $\bar{\nu}_e$ flux at KamLAND operate with a output of 10% for two days, the influence of the unknown operation period on the total $\bar{\nu}_e$ flux for one year is $50\% \times 10\% \times 2\text{days}/1\text{year} < 0.1\%$. So, this effect can be considered to be negligible.

In other case, the thermal output decreases to $\sim 80\%$ for a few hours when the control rod pattern is adjusted to maintain a rated output (at BWRs) or the turbine steam free test (at PWRs).

For some reactors, values of the electric output were provided instead of the thermal output in the period when outputs were changed. In this case, the electric output was converted to the thermal output using the rated thermal efficiency. The contribution of $\bar{\nu}_e$ at KamLAND from one of these reactors is $\sim 0.2\%$, so the influence is negligible.

If the time dependent burnup data were not provided, it was calculated using the previous data point as $B(t_1) = B(t_0) + \langle P \rangle \cdot \Delta t / M$, where B is the burnup, $\langle P \rangle$ is the average output, Δt is the time between t_0 and t_1 , and M is the mass of fuel.

An example of the operation data of a typical BWR provided by a nuclear power reactor operator is shown in Figure 7.9. This figure includes one operation cycle completely. The burnup at the end of cycle is about 10GWd/t, which is typical value for BWRs.

7.1.3 Comparisons between the thermal output and the electric output

To cross check the time dependence of the thermal output data, the compiled data are compared with electric power record publicly available.

The data of the electric generation of each nuclear power station were taken from Japan Atomic Industrial Forum, INC (JAIF) web page [72]. The relation between the rated thermal efficiency λ_{rated} defined using the rated thermal output Q_{rated} and the electric output E_{rated} listed in Table 7.2 and the time dependent real thermal efficiency of each power station $\lambda_{\text{real}}(t)$

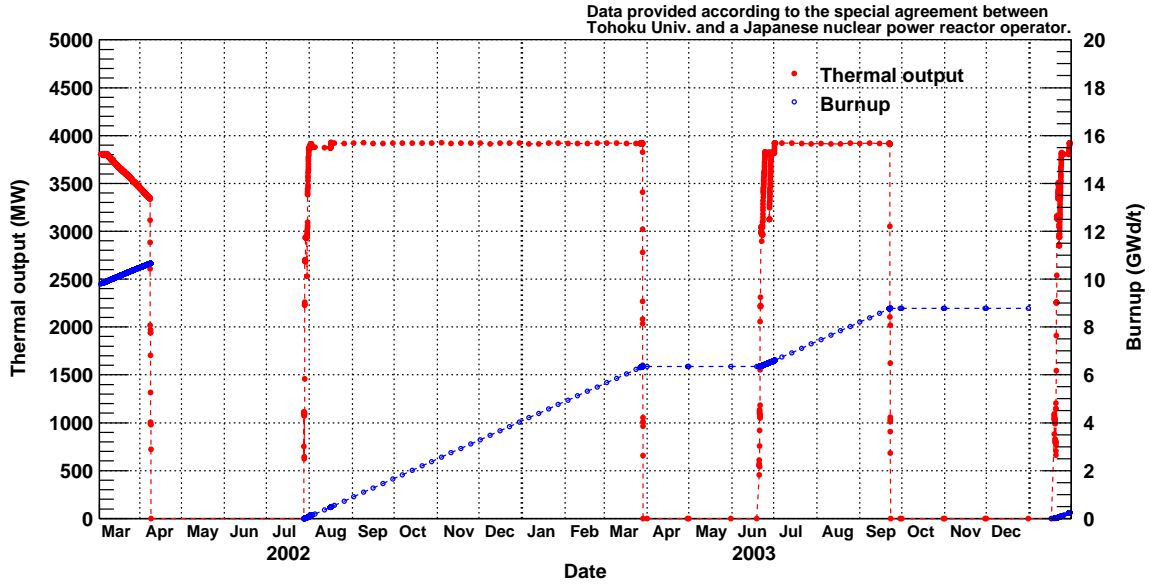


Figure 7.9: Example of the thermal power data of a typical BWR. The red dots show the thermal power (MW), the blue circles show the burnup data. From April 2002 to July 2002, this nuclear power station stopped operation for refueling and regular maintenance. After restarting operation, from April 2003 to June 2003 this nuclear power station stopped operation for irregular maintenance. At this period, the condition of the fuel was not changed. In September 2003, this operation cycle was finished. After refueling, new operation cycle was started.

is written as

$$\frac{E_{\text{rated}}}{Q_{\text{rated}}} \equiv \lambda_{\text{rated}} \leq \lambda_{\text{real}}(t) \equiv \frac{E_{\text{real}}(t)}{Q_{\text{real}}(t)}, \quad (7.1)$$

where $Q_{\text{real}}(t)$ and $E_{\text{real}}(t)$ are actual thermal and electric output at each power station. The λ_{rated} for each power station is shown in Figure 7.3. The efficiencies are around 33 to 34%. The capacity of the electricity generation (E_{rated}) was designed for being able to achieve it in summer season, when the thermal efficiency decreases because the sea water used as the cooling water is warmer than winter. So, the actual thermal efficiency $\lambda_{\text{real}}(t)$ is expected to be higher than the rated thermal efficiency λ_{rated} as written in (7.1).

Figure 7.10 shows a certain monthly electric generation of each power station converted from the thermal output data and JAIF data directly. These values are consistent with each other and it is clearly seen that the JAIF data are slightly higher than the KamLAND data.

To combine the contribution from each reactor, the electricity generation flux of each reactor was summed at a location of KamLAND. The upper panel of Figure 7.11 shows the two kinds of data of the electric generation flux at KamLAND. “JAIF data” means the total average electric output (power) flux at KamLAND $f_{e,\text{JAIF},\text{month}}$ calculated by using the electricity generation data taken from JAIF as

$$f_{e,\text{JAIF},\text{month}}(\text{MW}/\text{cm}^2) = \sum_{\text{reactor}} \frac{P_{e,\text{reactor},\text{month}}}{4\pi L_{\text{reactor}}^2}, \quad (7.2)$$

where $P_{e,\text{reactor},\text{month}}$ is the time average monthly electric output and L_{reactor} is distance to KamLAND. “KamLAND data” means the total average electric output flux at KamLAND $f_{e,\text{KamLAND},\text{month}}$ calculated by using the thermal output data provided by the electric power

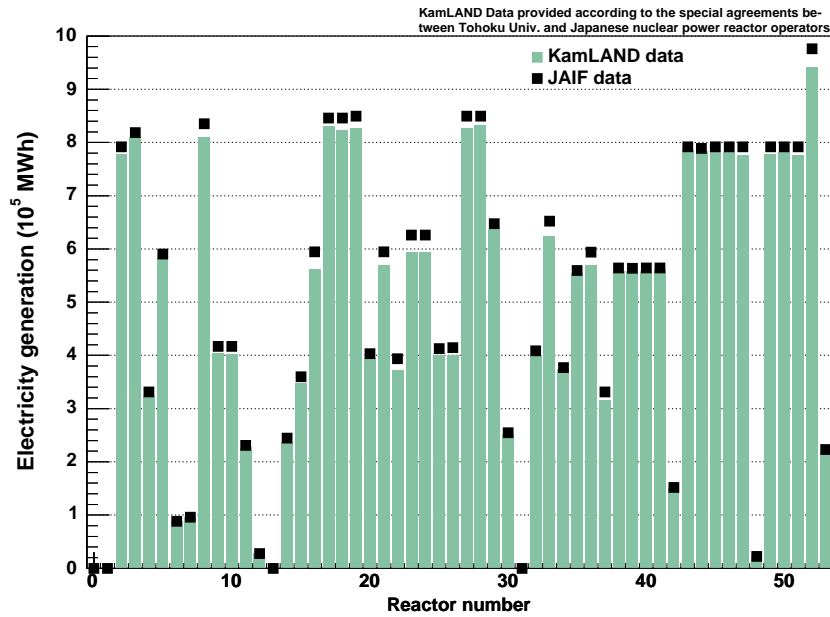


Figure 7.10: Comparisons between the electricity generation using KamLAND data and JAIF data. This figure uses the data in April 2002.

companies and the rated thermal efficiencies as

$$f_{e,\text{KamLAND,month}}(\text{MW}/\text{cm}^2) = \sum_{\text{reactor}} \frac{\int dt p_{t,\text{reactor,month}}(t)}{4\pi L_{\text{reactor}}^2 T_{\text{month}}}, \quad (7.3)$$

where $p_{t,\text{reactor,month}}(t)$ is the thermal output and T_{month} is time per each month. This figure shows that agreement of the electric power data and thermal power data is pretty good over the whole period.

The lower panel of Figure 7.11 shows the ratio of $f_{e,\text{JAIF,month}}$ to $f_{e,\text{KamLAND,month}}$. It is clear that the actual electric output is 1-2% higher than the converted electric output. It can be explained by the margin of the rated thermal efficiency, as it was mentioned before. Moreover this figure shows a seasonal dependence. It can be explained by the thermal efficiency is low in summers and high in winters. The difference of the thermal efficiency between summer and winter is generally about 3%. In this figure, the variation of the ratio of the thermal efficiency is about 2% and it correspond to this effect. In summer season when the actual thermal efficiency is close to the rated thermal efficiency, there is about 1% disagreement about two data. This may be explained as the designed margin. Although the thermal output flux in 2003 decreased to the half in 2002 (The upper panel of Figure 7.11), we can see two data corresponds within the range of the same variation.

7.1.4 Fission rate of each reactor

The fission reaction rate of each element is obtained by putting the time dependent operation data in the calculation method described in 6.4. An example of the fission reaction rate of each element in a typical power reactor is shown in Figure 7.12. It is clear that the rate of ^{239}Pu increases with the burnup and after refueling the rate of ^{235}U recovers.

Figure 7.13 shows the relative fission reaction rate flux of all Japanese power reactors at KamLAND. The time variation in each reactor is mostly canceled. In particular, ^{238}U and ^{241}Pu

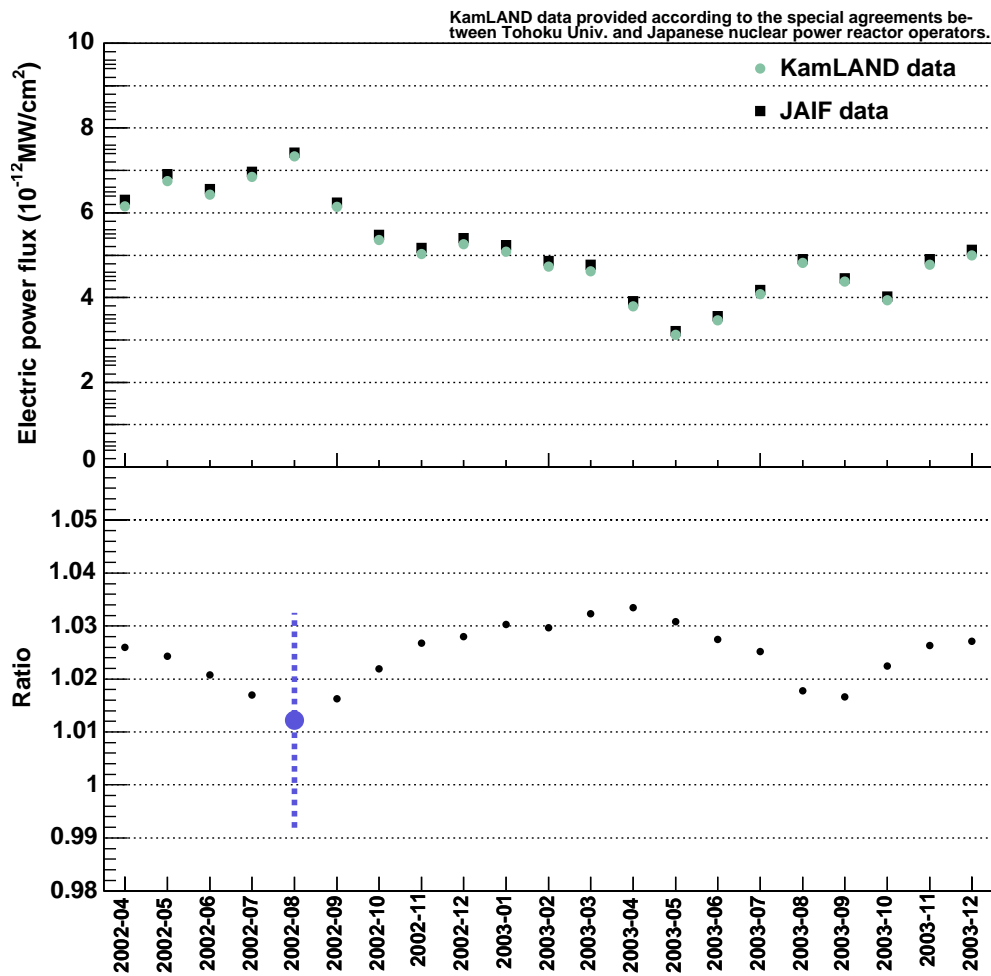


Figure 7.11: Electricity generation comparisons between the KamLAND data and the JAIF data. Upper panel shows the time variation of the electric output (power) flux at KamLAND by two data. Lower panel shows the time variation of the ratio of the JAIF data to the KamLAND data.

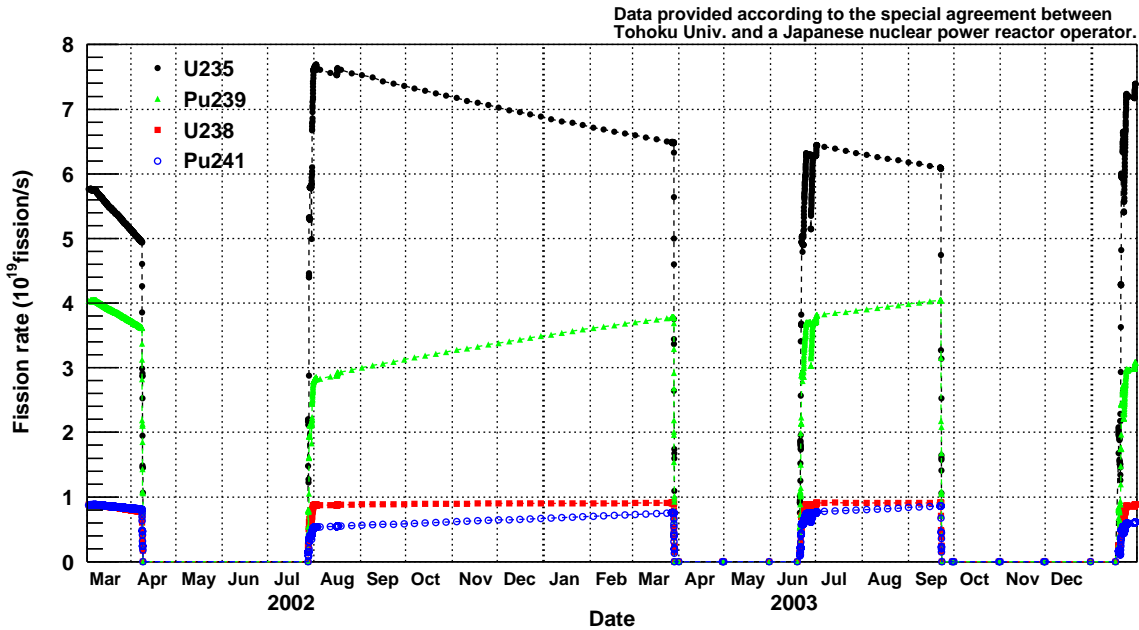


Figure 7.12: Example of the fission rate of each element at a typical reactor. Each color show each fission element; (Black: ^{235}U , Green: ^{239}Pu , Red: ^{238}U , Blue: ^{241}Pu). In this figure, operation data correspond to 7.9.

are stable. The average value in the analysis period is $^{235}\text{U} : ^{238}\text{U} : ^{239}\text{Pu} : ^{241}\text{Pu} = 0.563 : 0.079 : 0.301 : 0.057$.

7.2 Korean commercial reactors

7.2.1 Korean power reactors

In the measurement period at KamLAND between March 2002 and January 2004, 18 commercial reactors which has been located in 4 electric power stations existed in South Korea as operatable electric-power producing reactors (Figure 7.14). All these reactors are PWRs. Basic parameters are listed in Table 7.6.

7.2.2 Operation data of each reactor

The fission rate in the south korean commercial reactors (PWRs) was calculated by using the electric generation of each reactor and assuming the same averaged relative fission reaction rate and thermal efficiency as the Japanese PWRs. The daily electric generation data were taken from Web pages of the Korea Hydro and Nuclear Power Co., LTD. [73]. Figure 7.15 shows the time variation of the electricity generation at the Korean nuclear power stations. The operation pattern is same as the power reactors in Japan (also see corresponded reactors in Figure 7.5).

7.2.3 Fission rate of each reactor

To convert the electricity generation to the fission reaction rate of each element, the thermal efficiency and relative fission reaction rate and energy released by the fission reaction were substituted as following values.

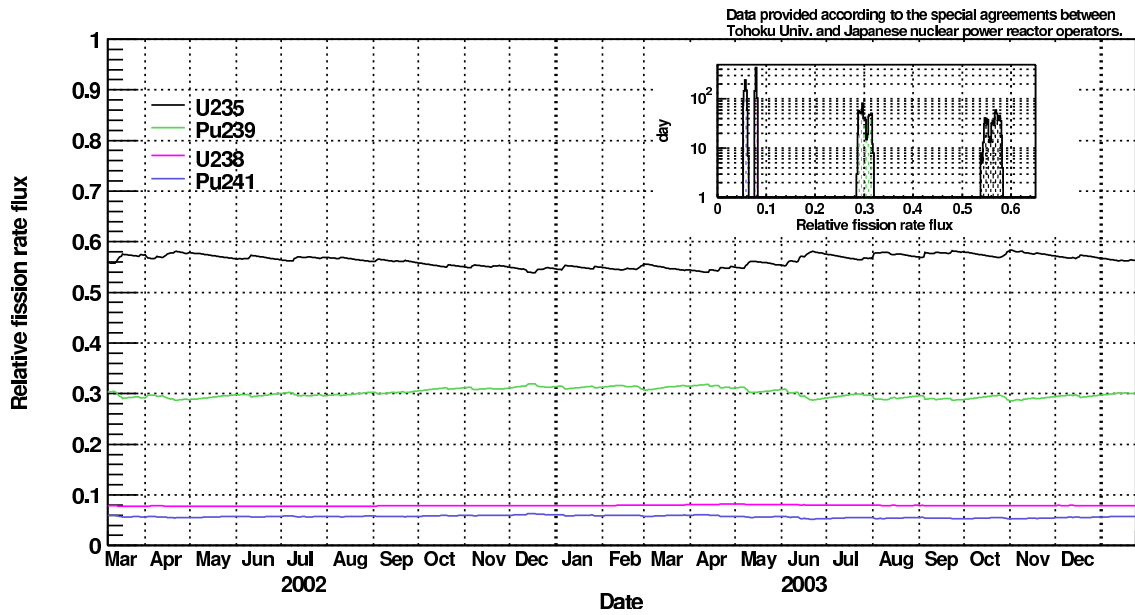


Figure 7.13: Relative fission reaction rate flux at KamLAND from all Japanese power reactors.

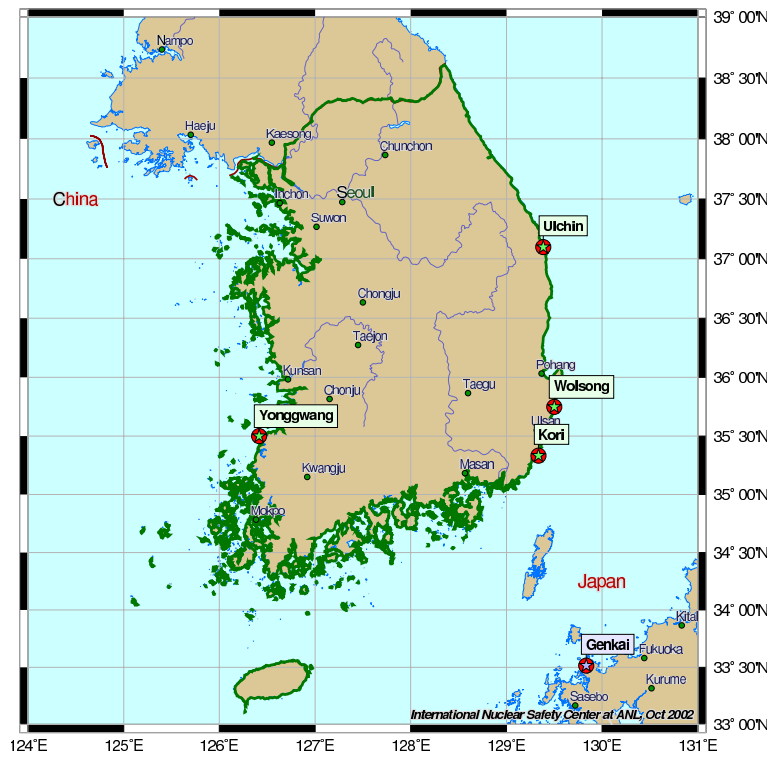


Figure 7.14: Nuclear power stations in South Korea [69].

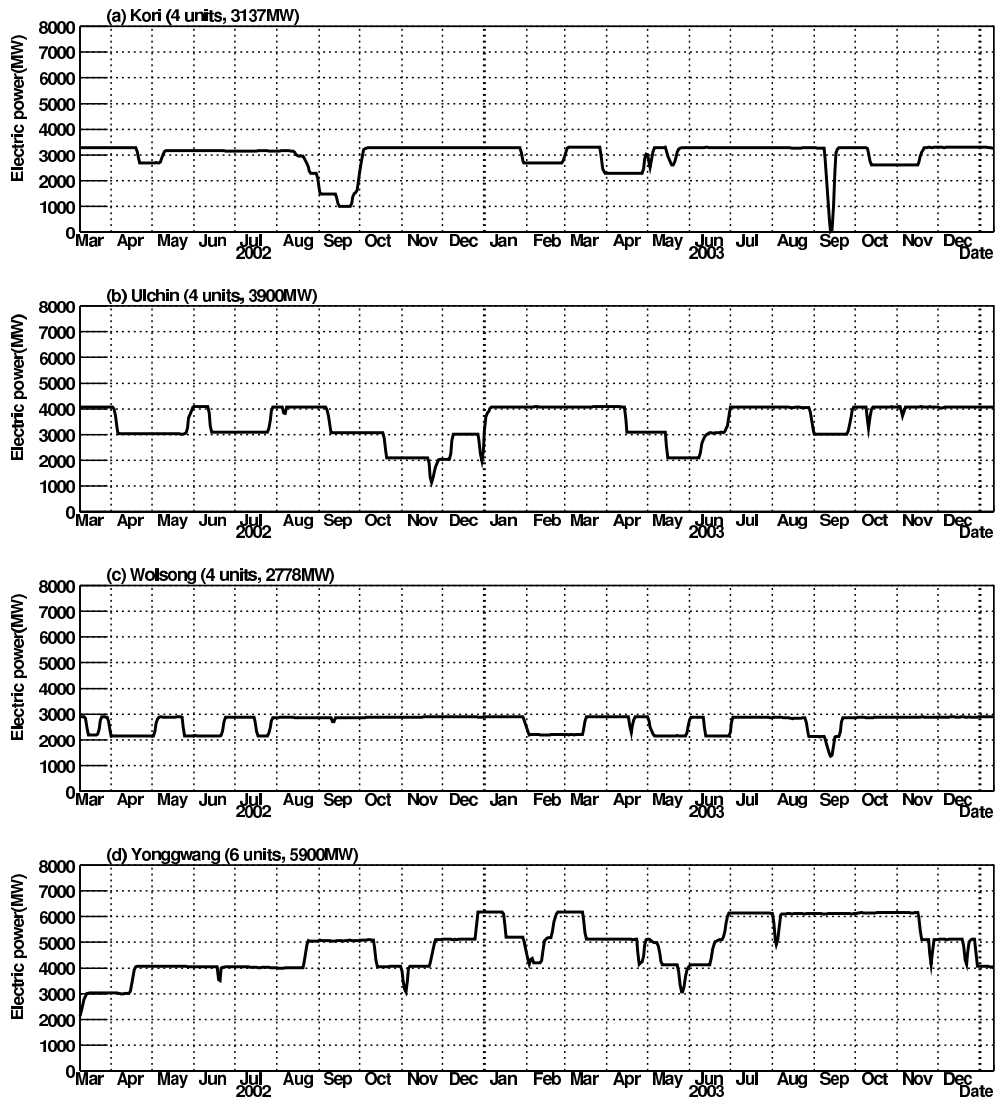


Figure 7.15: The time variation of the electricity generation at the Korean nuclear power stations. In this figure, all units at each power station are added.

	Reactor name	Reactor type	Thermal output (MW)	Electric output (MW)	Distance (km)	Power company
54	Kori-1	PWR	1727	587	734.5	KHNP
55	Kori-2	PWR	1913	650	734.5	KHNP
56	Kori-3	PWR	2796	950	734.5	KHNP
57	Kori-4	PWR	2796	950	734.5	KHNP
58	Ulchin-1	PWR	2796	950	711.8	KHNP
59	Ulchin-2	PWR	2796	950	711.8	KHNP
60	Ulchin-3	PWR	2943	1000	711.8	KHNP
61	Ulchin-4	PWR	2943	1000	711.8	KHNP
62	Wolsong-1	PWR	1995	678	708.6	KHNP
63	Wolsong-2	PWR	2060	700	708.6	KHNP
64	Wolsong-3	PWR	2060	700	708.6	KHNP
65	Wolsong-4	PWR	2060	700	708.6	KHNP
66	Yonggwang-1	PWR	2796	950	986.4	KHNP
67	Yonggwang-2	PWR	2796	950	986.4	KHNP
68	Yonggwang-3	PWR	2943	1000	986.4	KHNP
69	Yonggwang-4	PWR	2943	1000	986.4	KHNP
70	Yonggwang-5	PWR	2943	1000	986.4	KHNP
71	Yonggwang-6	PWR	2943	1000	986.4	KHNP

Table 7.6: Korean commercial reactors

- Thermal efficiency of 0.340,
as the averaged rated thermal efficiency of the Japanese PWRs.
- ($^{235}\text{U} : ^{238}\text{U} : ^{239}\text{Pu} : ^{241}\text{Pu}$) = (0.574 : 0.081 : 0.293 : 0.052),
as the averaged relative fission reaction rate at the Japanese PWRs.
- The energy shown in Table 6.5,
as the energy released by the fission reaction in the PWRs taken from [46].

According to Figure 6.9, at equilibrium cores the burnup dependence of the $\bar{\nu}_e$ event rate is less than 10%. Therefore, the systematic uncertainty of $\bar{\nu}_e$'s from Korean reactors was assigned as 10% of the contribution to all events at KamLAND.

7.3 World reactors

Figure 7.16 shows position of power reactors in the world. At end of 2002, a total electric output in the world is 373.727GW[70], corresponding to a thermal output of about 1100GW. Basic parameters about research reactors in Japan are listed in Table A.1. Parameters of commercial reactors in countries other than Japan and South Korea are listed in Table A.2. Figure 7.17 shows the thermal output flux at KamLAND. In this figure, the thermal output corresponds to the rated thermal output or conversion from the rated electric output. Contribution from outside Japan and South Korea is 0.6% and Japanese research reactors have 0.1% contribution.

The sum of the $\bar{\nu}_e$ contribution from reactors located in other countries was estimated using the rated outputs and a typical relative fission reaction rate and thermal efficiency as follows.

- The thermal output flux at KamLAND of $1.7 \times 10^{-13}\text{MW}/\text{cm}^2$,
as the conversion of the rated electric output of world reactors using a thermal efficiency of 0.34 and the rated thermal output of the Japanese research reactors.

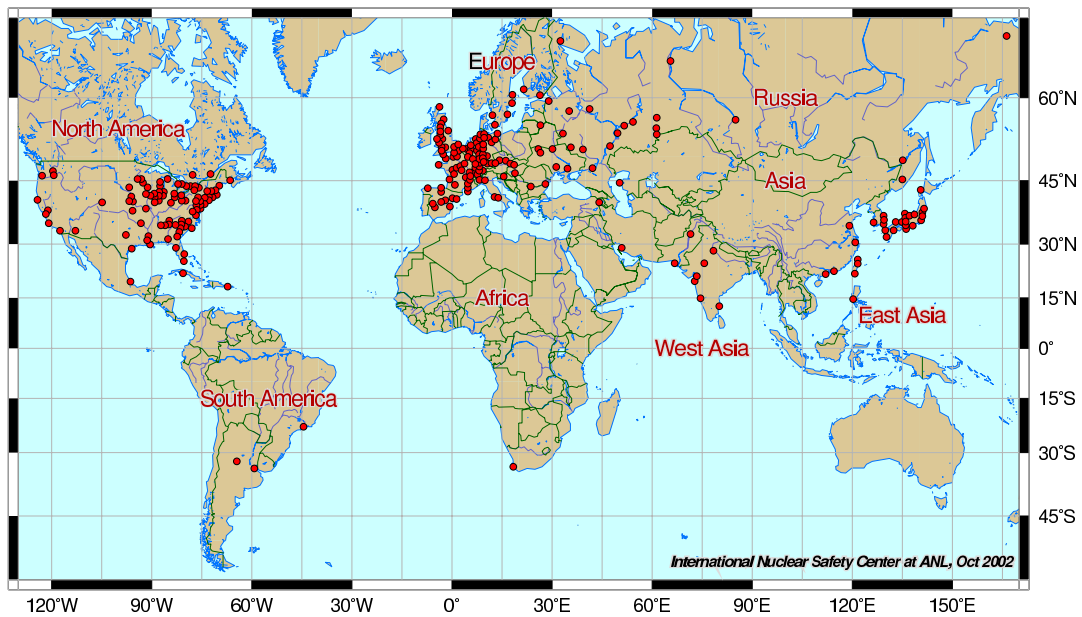


Figure 7.16: Map of nuclear power reactors in the world [69]. Some reactors which not reached construction status are included in this map.

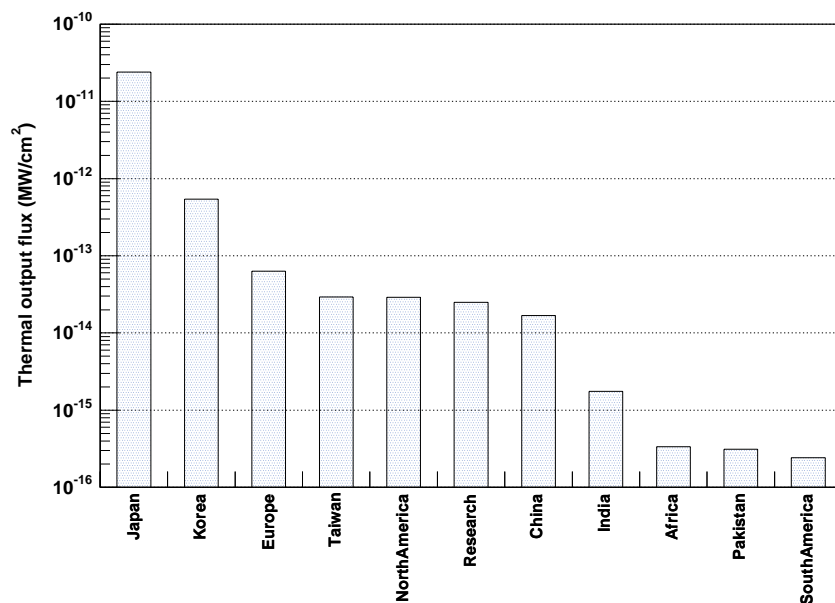


Figure 7.17: Contribution from reactors out of japan to thermal output flux.

- $(^{235}\text{U} : ^{238}\text{U} : ^{239}\text{Pu} : ^{241}\text{Pu}) = (0.573 : 0.080 : 0.293 : 0.054)$,
as a combination of the averaged relative fission rate of Japanese PWRs and BWRs using the ratio of BWRs and PWRs in LWRs in the world. According to the Atomic Energy Commission [74], 86% of the commercial reactors in the world are LWRs. And, 74% of LWRs are PWRs and 26% are BWRs.
- The energy shown in Table 6.5,
as the energy released by the fission reaction in the PWRs taken from [46].

The fission rate flux at KamLAND from these reactors including the Japanese research reactors is listed in Table 7.7.

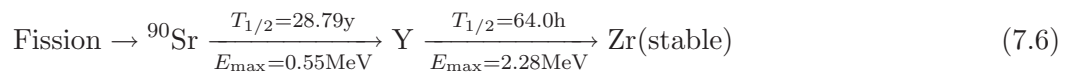
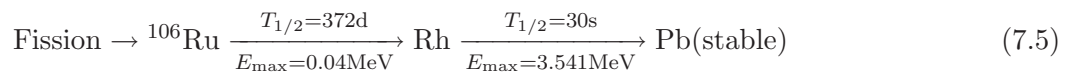
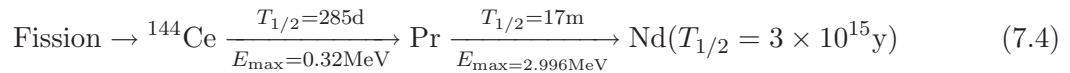
	Isotopes			
	^{235}U	^{238}U	^{239}Pu	^{241}Pu
fission/cm ² /s	2.9×10^3	4.0×10^2	1.5×10^3	2.7×10^2

Table 7.7: Fission rate flux at KamLAND from reactors outside of Japan and South Korea.

7.4 Contribution from long lived nuclides

The $\bar{\nu}_e$ energy spectra per fission shown in Figure 6.3 were obtained by the exposure of about one day. Therefore, contribution of the β -decay of long lived nuclides is not included. In this section, the long lived nuclides in nuclear fuel are investigated.

Some long lived nuclides are listed in Table 7.8. In these nuclides, ^{144}Ce (7.4), ^{106}Ru (7.5) and ^{90}Sr (7.6) have daughter nuclides which Q values are higher than the energy threshold of inverse β -decay (Figure ??).



The spent fuel from nuclear power plants have been transported to reprocessing facilities in the country or overseas, or stored in interim storage facilities in the country or power plants. Distances between Japanese reprocessing facilities and KamLAND are larger than those of main reactors. So, if it is considered that all nuclear fuel have been stored in power plants from the start of operation, the $\bar{\nu}_e$ contribution is maximum. To estimate the accumulation of the nuclear fuel in each power station in Japan and South Korea, the electricity generation was traced from the the first criticality (Table 7.9).

The time dependent decay rate of each daughter nuclide in each core is calculated using the fission reaction rate of each element converted from the electricity generation and the rated

Nuclide	Half life	Decay	Energy (MeV)
^3H	12.3y	β	0.019
^{85}Kr	10.76y	β	0.687
$^{90}\text{Sr} - ^{90}\text{Y}$	28.1y, 64h	β	0.546, 2.28
^{95}Nb	35d	β	0.926
$^{106}\text{Ru} - ^{106}\text{Rh}$	367d, 30s	β	0.039, 3.54
^{137}Cs	30y	β	1.18
$^{144}\text{Ce} - ^{144}\text{Pr}$	284d, 17.3m	β	0.319, 3.0
^{147}Pm	4.4y	β	0.22
^{99}Tc	$2 \times 10^5\text{y}$	β	0.29
^{129}I	$1.7 \times 10^7\text{y}$	β	0.19

Table 7.8: Long lived nuclides in fission products.

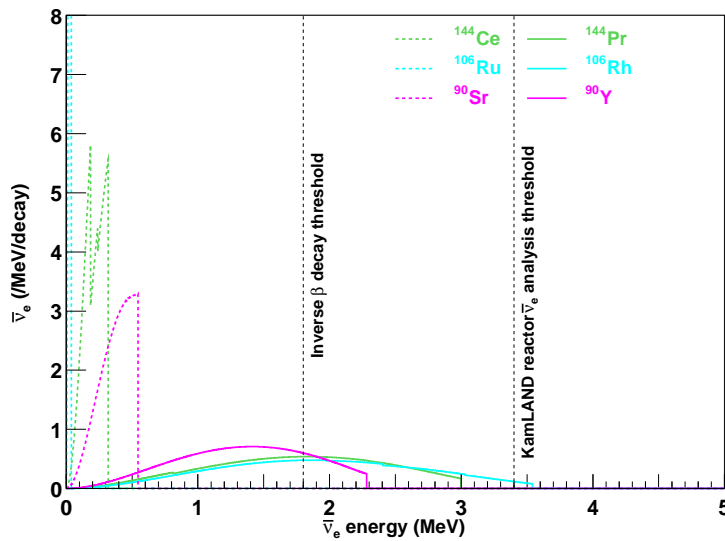


Figure 7.18: $\bar{\nu}_e$ energy spectra from long lived nuclides. The end points correspond to the q values.

Period	Data
April, 1969 - March, 1977	Annual generation [75]
April, 1977 - March, 1993	Annual generation [76]
April, 1993 - March, 2000	Monthly generation [76]
April, 2000 - March 6, 2002	Monthly generation [72]

Table 7.9: Reference of the electricity generation at Japanese power reactors.

thermal efficiency as

$$\frac{dN_i(t)}{dt} = \sum_a k_a R_a(t) - \lambda_i N_i(t) \tag{7.7}$$

$$\frac{dN_{i+1}(t)}{dt} = \lambda_i N_i(t) - \lambda_{i+1} N_{i+1}(t), \tag{7.8}$$

where N_i and N_{i+1} are the number density of the parent nuclides and daughter nuclides, λ is the decay constant and R_a is the fission reaction rate of each element. The k_a is yield of the parent nuclides from each fission reaction listed in Table 7.10.

Fission fragment	Fission nuclides			
	²³⁵ U	²³⁸ U	²³⁹ Pu	²⁴¹ Pu
¹⁰⁶ ₄₄ Ru	0.40	2.55	4.31	6.18
¹⁴⁴ ₅₈ Ce	5.48	4.50	3.74	4.39
⁹⁰ ₃₈ Sr	5.82	3.12	2.10	1.57

Table 7.10: Yields of fission fragments (in %)[50].

Figure 7.19 shows the sum of the time variation of the decay rate of each daughter nuclide in each core. The decay rate of ¹⁴⁴Pr and ¹⁰⁶Rh and yield of ¹⁴⁴Ce and ¹⁰⁶Ru are corresponded with each other. On the other hand, the decay rate of ⁹⁰Y is not saturated yet. Figure 7.20 shows the contribution from the long lived nuclides in the measurement period of KamLAND. In the current analysis for $\bar{\nu}_e$'s above 3.4MeV, the time variation of the contribution from ¹⁴⁴Pr and ¹⁰⁶Rh is considered to be the time dependence of ¹⁴⁴Ce and ¹⁰⁶Ru. And, systematic uncertainty is assigned as $\pm 50\%$.

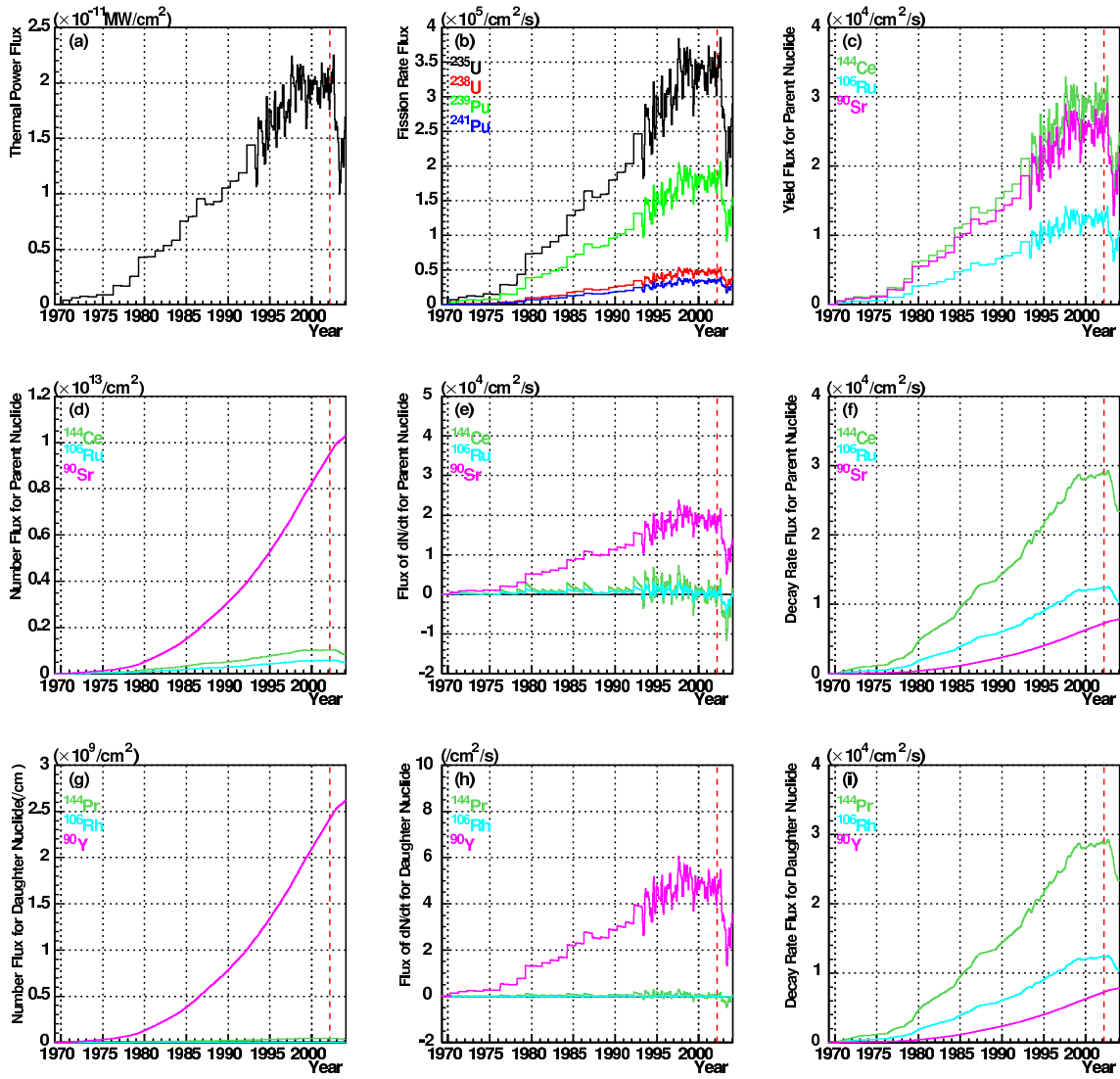


Figure 7.19: Contribution from Long lived nuclides at KamLAND. The red dashed lines show the start of measurement at the KamLAND experiment. (a): The time variation of the total thermal output (power) flux at KamLAND from all Japanese power reactors. (b): The flux of the fission reaction rate of each element. (c): The yields of ^{144}Ce , ^{106}Ru and ^{90}Sr as parent nuclides corresponding to the fission rate of each element. (d): The accumulation of the parent nuclides. (e): The variation of the parent nuclides. (f): The decay rate of the parent nuclides. (g): The accumulation of ^{144}Pr , ^{106}Rh and ^{90}Y as daughter nuclides. (h): The variation of the daughter nuclides. (i): The decay rate of the daughter nuclides. This rate corresponds to the generation rate of $\bar{\nu}_e$.

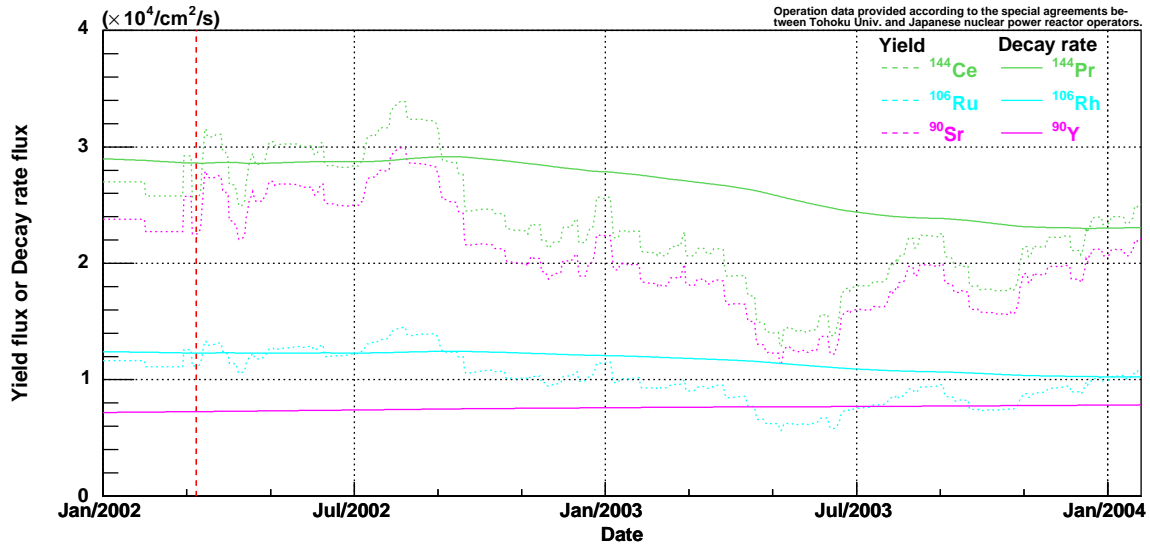


Figure 7.20: Contributions from long lived nuclides at KamLAND.

7.5 Anti neutrino flux at KamLAND

Figure 7.21 shows the time variation of the thermal output (power) flux at KamLAND. The total integrated thermal power flux of all reactors over the detector livetime was 701 Joule/cm².

Figure 7.22 shows the time variation of the reactor $\bar{\nu}_e$ ($1.8\text{MeV} < E_{\bar{\nu}_e} < 8.0\text{MeV}$) flux at KamLAND. After the latter half of 2002, a number of Japanese reactors were off. Particularly, the flux decreased to about half in May 2003. This reduction was mainly due to shutdown of Kashiwazaki Kariwa Nuclear Power Station located at a distance of 160km from KamLAND. Figure 7.23 shows the time variation of the weighted mean of distance from each reactor to KamLAND calculated as $L(t) = (\sum L_{\text{reactor}} P_{\text{reactor}}(t)) / (\sum P_{\text{reactor}}(t))$, where L_{reactor} is the distance of each reactor and $P_{\text{reactor}}(t)$ is the thermal output flux. For this calculation, the reactor sites in Shika, Kashiwazaki-Kariwa, around Wakasa-bay sites, Hamaoka, Tokai-Daini, Fukushima-Daini and Fukushima-Daiichi are included. We can see mean of distance was about 180km in the whole period and sensitive to operation of one reactor “Shika” at 88 km which has largest single contribution to the flux.

7.6 Reactor $\bar{\nu}_e$ events at KamLAND assuming no anti-neutrino oscillation

For the total detector livetime of 515.1days the expected reactor $\bar{\nu}_e$ energy spectrum is shown in Figure 7.24 and 7.25. Number of expected events in the absence of anti-neutrino disappearance is 365.3 and itemized in Table 7.11. The contribution from Japanese research reactors and reactors outside of Japan is 4.5%. The contribution to the $\bar{\nu}_e$ flux from Korean reactors is $(3.4 \pm 0.34)\%$, the estimation of the systematic uncertainty is described previously. Other reactors give an $(1.1 \pm 0.5)\%$ contribution. In this case and about the long lived nuclides, 50% uncertainty is assigned.

Figure 7.26 shows the expected reactor $\bar{\nu}_e$ events for the long lived nuclides. The number of expected events is listed in Table 7.12. We can see good agreement between the approximation using the yields of the parent nuclides and the precise calculation using the decay rates of the



Figure 7.21: The thermal power flux from reactors at KamLAND.

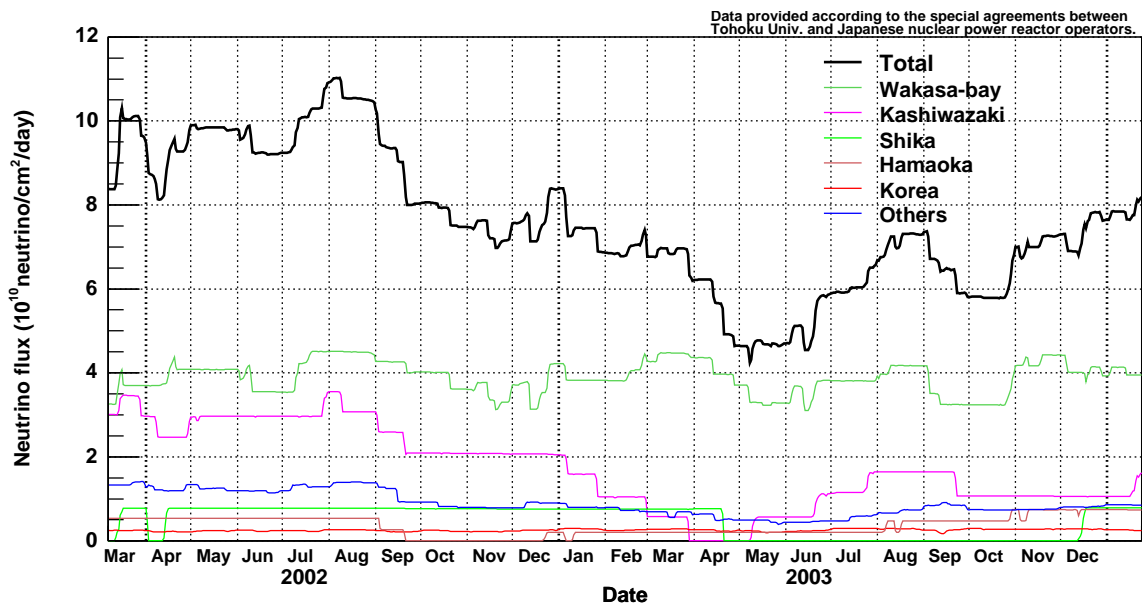


Figure 7.22: The reactor neutrino flux at KamLAND. The colored lines show contribution from each region where reactors are located.

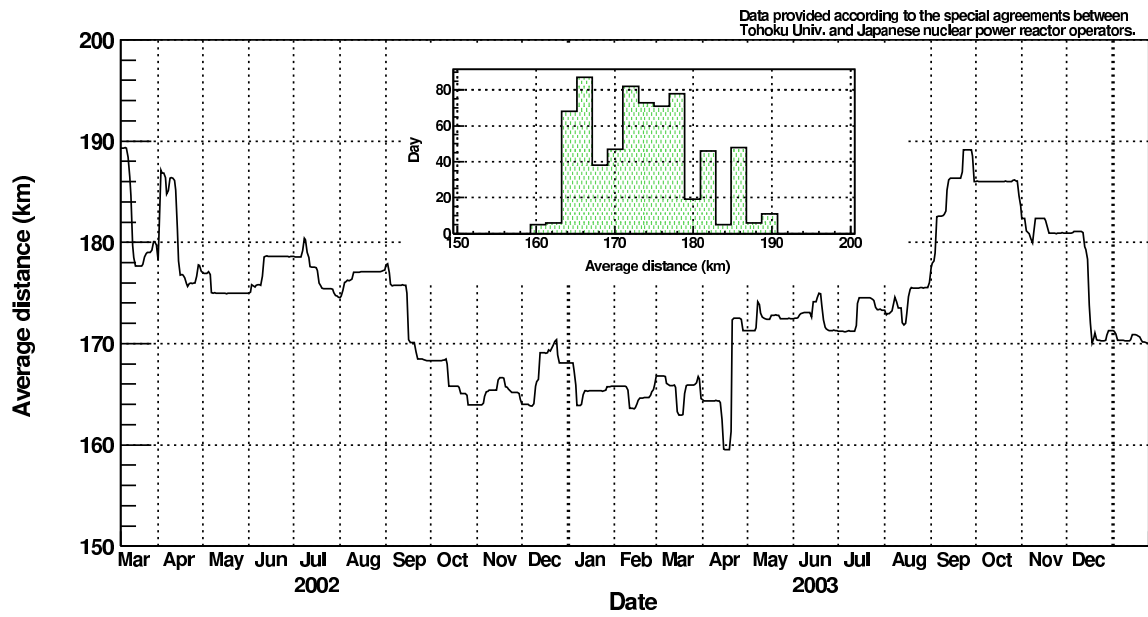


Figure 7.23: Time variation of the mean of distance. Average distance in this period is 173.6km.

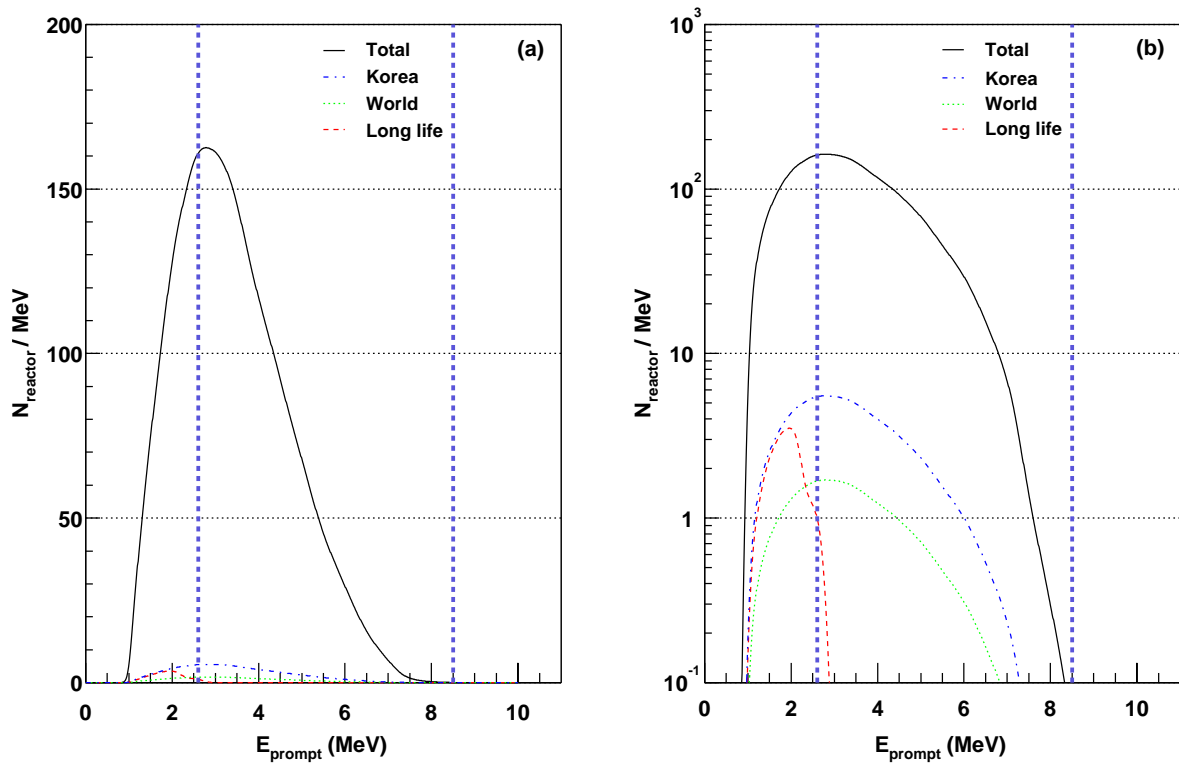
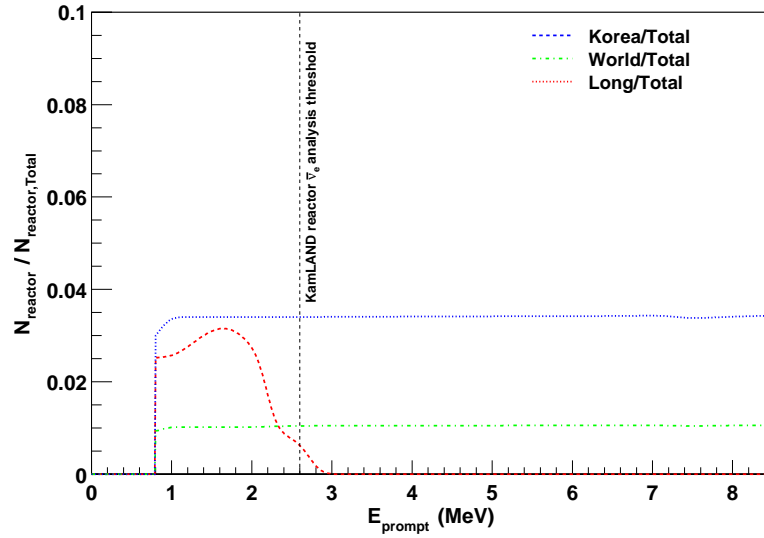


Figure 7.24: Expected reactor $\bar{\nu}_e$ energy spectrum.


 Figure 7.25: Expected reactor $\bar{\nu}_e$ energy spectrum.

	$N_{\text{no-osc}}$	Contribution (%)	Uncertainty
Total	365.2	100.00	(summarized in next chapter)
Korean reactors	12.46	3.41	$\times 10\%$
Other reactors	3.843	1.05	$\times 50\%$
Long lived nuclides	0.153	0.0419	$\times 50\%$

Table 7.11: Number of expected events in the absence of anti-neutrino disappearance.

daughter nuclides.

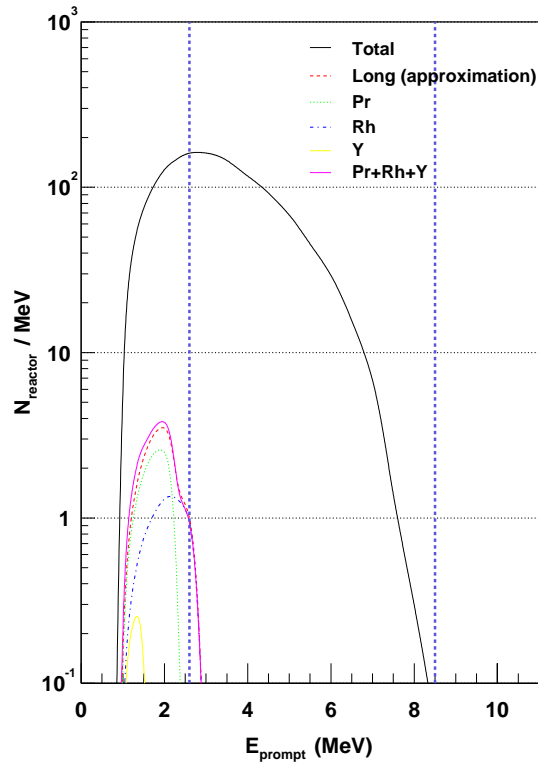


Figure 7.26: Expected reactor $\bar{\nu}_e$ energy spectrum for the long lived nuclides. “Long” uses the yields of ^{144}Ce and ^{106}Ru . “Pr”, “Rh” and “Y” correspond to using decay rates of ^{144}Pr , ^{106}Rh and ^{90}Y respectively. The decay rates are calculated using the time evolution of the reactor output.

The systematic uncertainties relate to reactors are summarized in Table 7.13. The uncertainty of $\bar{\nu}_e$ spectrum per fission (2.5%) are taken from Ref. [45]. The contribution from fission products which have long β -decay lifetimes (but shorter than the long lived nuclides) is estimated to be an additional uncertainty of 0.01%. This uncertainty was calculated as the difference of the total $\bar{\nu}_e$ yield associated with shifting the run time by one day.

Figure 7.27 shows the time and distance distribution of the expected reactor $\bar{\nu}_e$ events at KamLAND. It is clear that the contribution from a distance of about $\sim 160\text{km}$ decreases in 2003. The contribution from a distance of less than 100km is also decreased.

Conditions		Ratio of number of events	
		0.9MeV Thre.	2.6MeV Thre.
(a) Yields	Total	1.0000	1.0000
	Long life	0.0067	0.0004
(b) Decay rates	Long life	0.0074	0.0004

Table 7.12: Ratio of number of expected events for the long live nuclides. The total number of expected events for each analysis threshold is defined as 1.0. (a) uses the yields of ^{144}Ce and ^{106}Ru . (b) uses the decay rates of ^{144}Pr , ^{106}Rh and ^{90}Y calculated using the time evolution of the reactor output.

Parameters	Uncertainty (%)	
Thermal power of Japanese reactors	2.0	from flowmeters (Sec 6.1)
Korean reactors	0.34	3.41% contribution \times 10%
Other reactors	0.53	1.05% contribution \times 50%
Distance from reactors	< 0.1	$< \pm 70\text{m}/180\text{km}$
Chemical composition of fission elements	< 1.0	Fission rate calculation
Reactor neutrino spectra	2.54	[45], $\Delta N_{\text{no-oscillation}}$
Longlife nuclei	0.02	0.04% contribution \times 50%
Timelag	0.01	$\Delta N_{\text{no-oscillation}}$
Cross section	0.2	[42], [43]
Number of targets	< 0.1	from density

Table 7.13: Systematic uncertainties relate to reactors.

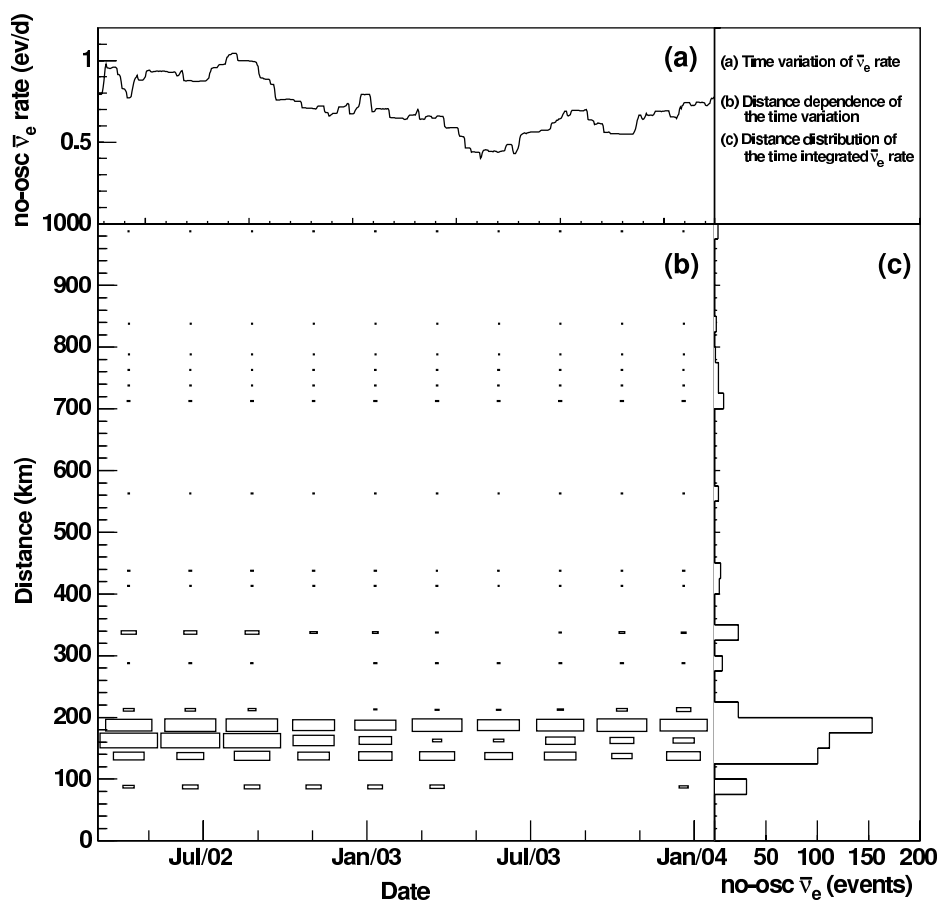


Figure 7.27: Time and distance variation of the expected reactor $\bar{\nu}_e$ events at KamLAND.

Chapter 8

Analysis

The summary of the systematic uncertainties for the reactor $\bar{\nu}_e$ detection is shown in Table 8.1. The sources of the uncertainties are classified into the detector and the expected number of events. The detector correlated uncertainties come from the event reconstruction and selection, and the efficiencies. The value is 5.4%^(I,II) and 5.5%^(III). The uncertainties from the expected number of events correspond to the reactor $\bar{\nu}_e$ flux, the number of target and the cross section of the inverse β -decay reaction. The value is 3.4%. The total systematic uncertainty is 6.4%^(I,II) and 6.5%^(III).

Parameter	Uncertainty (%)
- Efficiencies -	
Space correlation ($\Delta R \leq 200\text{cm}$)	1.6
Time correlation ($0.5 \leq \Delta T \leq 1000\mu\text{sec}$)	0.05
Trigger efficiency	-
Livetime calculation	0.06
- Event reconstruction and selection	
Analysis energy threshold	2.14 ^(I,II) , 2.33 ^(III)
Fiducial cut	4.71
Noise event cut	< 0.0002
Flasher event cut	< 0.01
- Reactor $\bar{\nu}_e$	
Distance	< 0.1
Thermal power	
Japanese reactors	2.0
Korean reactors	0.34
Other reactors	0.52
Chemical composition	< 1.0
$\bar{\nu}_e$ spectra	2.54
Time lag	0.01
Long-lived nuclei	0.02
- Number of target and cross section	
Number of target protons	< 0.1
Cross section	0.2
Total	6.42 ^(I,II) , 6.49 ^(III)

Table 8.1: Systematic uncertainties for $\bar{\nu}_e$ detection above 2.6 MeV prompt energy threshold. “(I,II)” means the analysis period I and II, “(III)” means the analysis period III.

In this chapter, the event ratio and significance of reactor $\bar{\nu}_e$ disappearance are described in Sec 8.1. In Sec 8.2, correlation between observed event rate and reactor $\bar{\nu}_e$ flux is shown. In Sec 8.3, two flavor neutrino oscillation analysis is described.

8.1 Event ratio and significance of reactor $\bar{\nu}_e$ disappearance

Numbers of expected events and observed events are listed in Table 8.2. 258 events are observed and in the absence of anti-neutrino disappearance, number of expected events is $365.2 \pm 23.7(\text{syst})$ $\bar{\nu}_e$ above 2.6MeV.

	Number of events
Expected events (no-oscillation)	$365.2 \pm 23.7(\text{syst})$
Background events	17.8 ± 7.3
Observed events	258

Table 8.2: Number of $\bar{\nu}_e$ events above $E_{\text{prompt}} = 2.6\text{MeV}$.

The average $\bar{\nu}_e$ survival probability is

$$\frac{N_{\text{obs}} - N_{\text{bg}}}{N_{\text{exp}}} = 0.658 \pm 0.044(\text{stat}) \pm 0.047(\text{syst}), \quad (8.1)$$

where the background error has been included in the systematic uncertainty as

$$\frac{N_{\text{obs}} - (N_{\text{bg}} \pm \Delta N_{\text{bg}})}{N_{\text{exp}}(1 \pm \sigma_{\text{sys}})}. \quad (8.2)$$

The statistical significance for reactor $\bar{\nu}_e$ disappearance is calculated as

$$P = \frac{1}{\sqrt{2\pi}\sigma} \int_0^\infty dx \exp\left(-\frac{(N_{\text{exp}} + N_{\text{bg}} - x)^2}{2\sigma^2}\right) \sum_{n=0}^{N_{\text{obs}}} P(n) \quad (8.3)$$

$$P(n) = \frac{x^n}{n!} e^{-x} \quad (8.4)$$

$$\sigma = \sqrt{(N_{\text{exp}} \cdot \sigma_{\text{syst}})^2 + \Delta N_{\text{bg}}^2} \quad (8.5)$$

where N_{obs} is the number of observed $\bar{\nu}_e$ events and N_{bg} is the number of expected background events and N_{exp} is the number of $\bar{\nu}_e$ events in the absence of oscillations. $P(n)$ is the Poisson distribution with the mean value x and σ is the total systematic uncertainty with the uncertainty for the $\bar{\nu}_e$ detection of σ_{syst} and the uncertainty of the background ΔN_{bg} . These results are confirming $\bar{\nu}_e$ disappearance at the 99.998% significance level. Assuming Gaussian statistics, a 4σ deviation would be needed to explain this deficit.

8.2 Correlation between observed event rate and reactor $\bar{\nu}_e$ flux

After September 2002, a number of Japanese nuclear reactors were off (7.5). The expected no-oscillation $\bar{\nu}_e$ flux decreased by more than a factor of two. So, the $\bar{\nu}_e$ flux dependence is studied in this section.

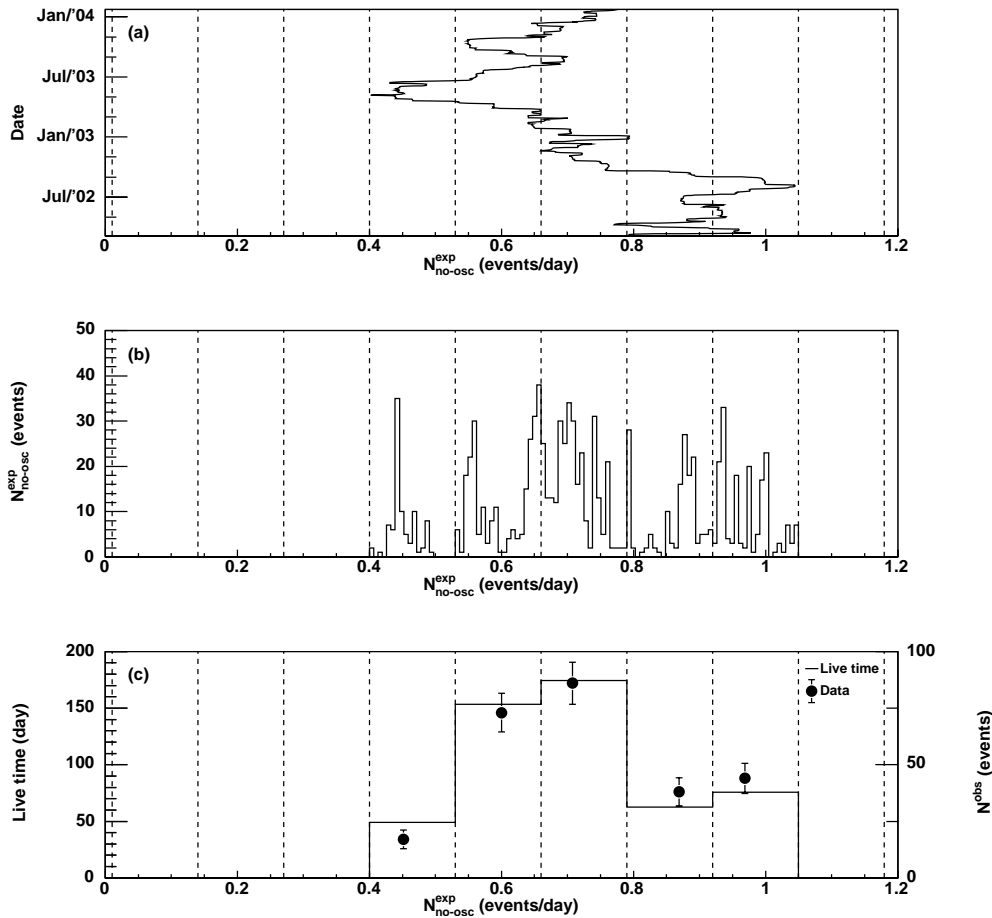


Figure 8.1: Reactor $\bar{\nu}_e$ flux dependence of the event rate. (a) Time variation of the expected $\bar{\nu}_e$ event rate assuming no anti-neutrino oscillation. (b) The event rate distribution for the no-oscillation expected $\bar{\nu}_e$ events in the KamLAND livetime. (c) Observed $\bar{\nu}_e$ events and livetimes in bins of equal expected event rate. Data point corresponds to an average no-oscillation $\bar{\nu}_e$ event rate in each bin.

8.2.1 Expected event rate bin case

Figure 8.1 shows reactor $\bar{\nu}_e$ flux dependence of the expected or observed event rate. Panel (a) shows the time variation of the no-oscillation expected event rate in the $\bar{\nu}_e$ event selection criteria. The event rate distributes from ~ 0.4 event/day to ~ 1.05 event/day. The number of expected events (shown in (b)) is corresponding to the total livetime in each bin (shown in (c)). The number of observed events is also shown in (c).

Figure 8.2 shows the signal counts plotted in bins of equal $\bar{\nu}_e$ flux corresponding to total reactor power. The slope can be interpreted as the $\bar{\nu}_e$ rate suppression factor and the intercept as the reactor independent constant background rate. Summary of the fitting parameters for three cases are listed in Table 8.3. The colored region in Figure 8.2 is the 90% C.L. region of the linear fit. The best fit parameter of intercept is 0.19event/day. This intercept is consistent with known backgrounds, but substantially larger backgrounds can not be excluded.

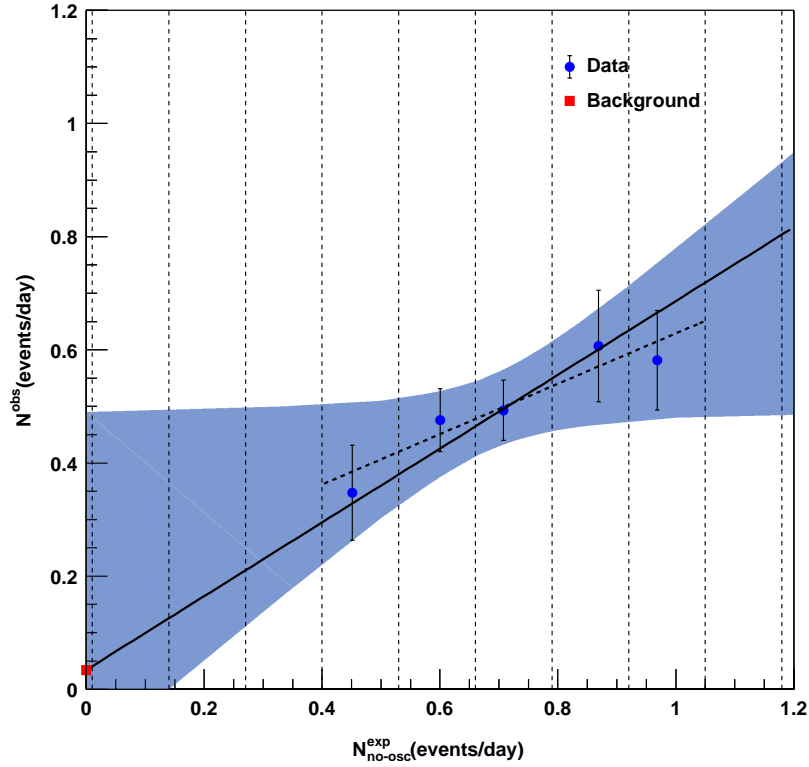


Figure 8.2: Observed $\bar{\nu}_e$ event rate versus no-oscillation $\bar{\nu}_e$ event rate. Data point corresponds to an average no-oscillation $\bar{\nu}_e$ event rate in each bin. The dashed line is a fit, the 90% C.L. is shown in gray. The solid line is a fit constrained to the expected background.

Fitting	Linear	Constrained to BG	Non-correlation
Slope	0.444	0.652	-
Intercept (events/day)	0.185	0.0342	0.490
χ^2/DOF	0.681/3	1.78/4	5.43/4

Table 8.3: Fit parameters for the $\bar{\nu}_e$ flux dependence in the event rate bin case.

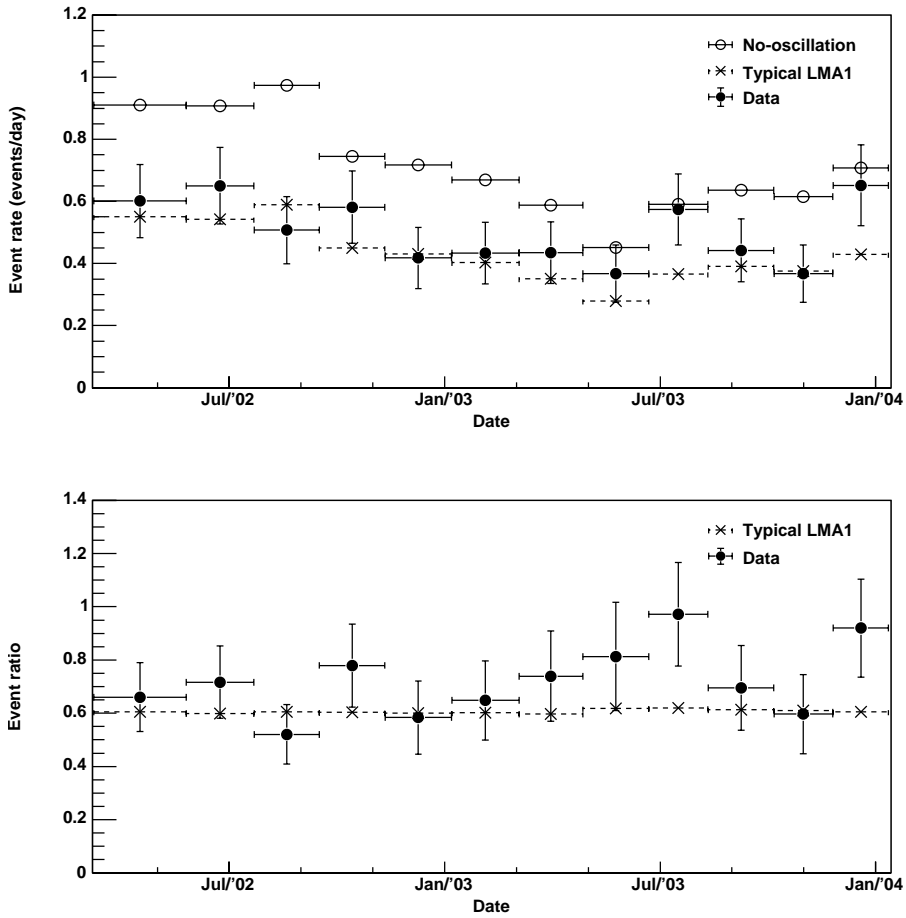


Figure 8.3: Time dependence of $\bar{\nu}_e$ events. Upper panel shows the time variation of the observed and expected $\bar{\nu}_e$ event rates. Data points correspond to intervals of equal livetime. The ratio of the number of $\bar{\nu}_e$ events to the number of no-oscillation $\bar{\nu}_e$ events is shown in Lower panel.

8.2.2 Livetime bin case

Figure 8.3 shows the event rate in bins of equal livetime of 42.9day. Upper panel shows the time variation of the $\bar{\nu}_e$ flux. Lower panel shows the time variation of the event ratio as $N_{\text{obs}}/N_{\text{exp}}$. The effective baseline varies with power output of the reactor sources. However, for the typical neutrino oscillation parameters and the known distributions of reactor output and distance, the expected oscillated $\bar{\nu}_e$ rate is well approximated by a straight line.

Figure 8.4 shows the correlation of the event rates in all bins. Summary of the fitting parameters are listed in Table 8.4. The colored region in Figure 8.4 is the 90% C.L. region of the linear fit. As similarly to the equal expected event rate bin case, substantially larger backgrounds can not be excluded. The best fit parameter of the intercept is 0.19event/day. This case is consistent with the event rate bin case.

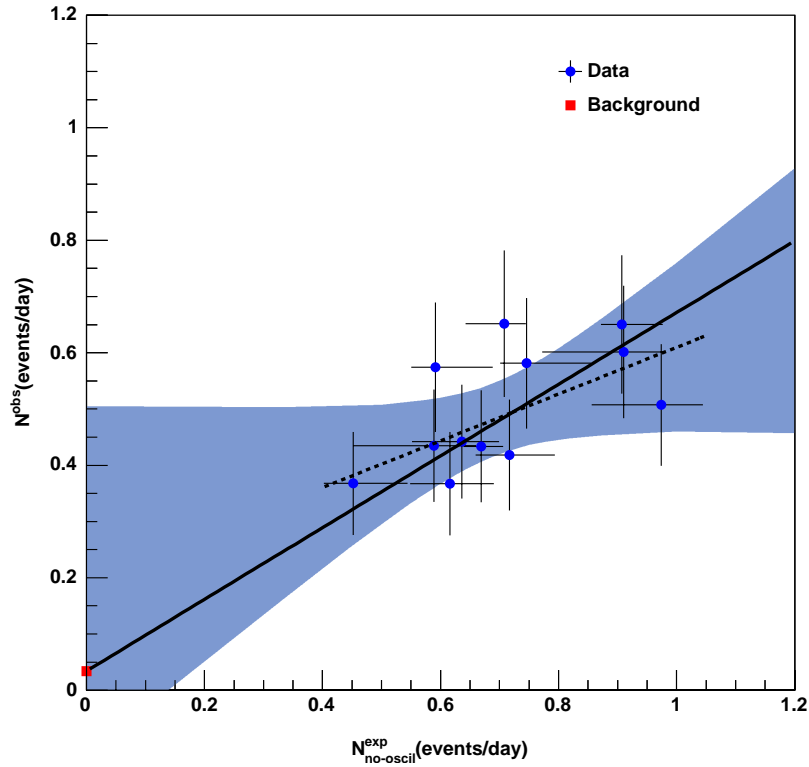


Figure 8.4: Observed $\bar{\nu}_e$ event rate versus no-oscillation $\bar{\nu}_e$ event rate. Data points correspond to intervals of equal livetime. The dashed line is a fit, the 90% C.L. is shown in gray. The solid line is a fit constrained to the expected background.

Fitting	Linear	Constrained to BG	Non-correlation
Slope	0.415	0.637	-
Intercept (events/day)	0.194	0.0342	0.481
χ^2/DOF	6.15/10	7.35/11	10.2/11

Table 8.4: Fit parameters for the $\bar{\nu}_e$ flux dependence in the livetime bin case.

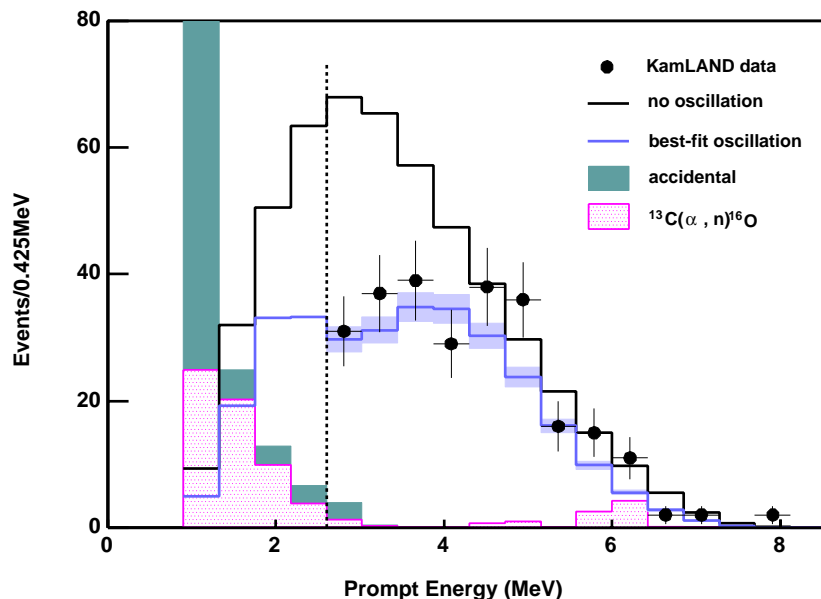


Figure 8.5: Prompt event energy spectrum of $\bar{\nu}_e$ candidate events with associated background spectra. The shaded band indicates the systematic error in the best-fit reactor spectrum above 2.6 MeV. The first bin in the accidentals histogram has ~ 113 events. The best-fit parameters are $\Delta m^2 = 7.9_{-0.5}^{+0.6} \times 10^{-5} \text{eV}^2$ and $\tan^2\theta = 0.46$.

8.3 Oscillation Analysis

8.3.1 Rate-and-shape analysis

The prompt event energy spectrum of $\bar{\nu}_e$ candidate events is shown in Figure 8.5. To obtain the best-fit oscillation parameters, the spectrum is analyzed with a maximum likelihood method with the following χ^2 definition,

$$\begin{aligned} \chi^2(\theta, \Delta m^2) &= \chi_{\text{rate}}^2(\theta, \Delta m^2) \\ &\quad - 2\log L_{\text{shape}}(\theta, \Delta m^2, \alpha_{1\sim 4}, \beta_{1\sim 3}) \\ &\quad + \chi_{\text{distortion}}^2(\alpha_{1\sim 4}) + \chi_{\text{BG}}^2(\beta_{1\sim 3}), \end{aligned} \quad (8.6)$$

$$\chi_{\text{rate}}^2(\theta, \Delta m^2) = \frac{(N_{\text{observed}} - N_{\text{expected}}(\theta, \Delta m^2) - N_{\text{BG}})^2}{\sigma_{\text{stat}}^2 + \sigma_{\text{syst}}^2} \quad (8.7)$$

where L_{shape} is the likelihood function of the spectrum including deformations from various parameters. $\alpha_{1\sim 4}$ are the parameters for the shape deformation coming from $\bar{\nu}_e$ spectrum uncertainty, energy scale uncertainty, finite energy resolution, and energy bias for fiducial volume. $\beta_{1\sim 3}$ are the estimated number of (α, n) backgrounds corresponding to the low energy (α, n) events, the high energy (α, n) events, and proton quenching effect. While the contributions around 2.6 MeV and 4.4 MeV are constrained to within 32 % of the estimated rate, the contribution around 6 MeV is allowed to float within 100% of the estimation because of uncertainty in the cross section, A 10% energy scale uncertainty for the 2.6 MeV contribution is assigned due to neutron quenching uncertainty. The best-fit for the rate-and-shape analysis is $\Delta m^2 = 7.9_{-0.5}^{+0.6} \times 10^{-5} \text{eV}^2$ and $\tan^2\theta = 0.46$, with a large uncertainty on $\tan^2\theta$.

To test the goodness-of-fit, the statistical techniques in Ref. [84] are performed. First, the data are fit to a hypothesis to find the best-fit parameters. Next, we bin the energy spectrum of the data into $n = 20$ equal-probability bins and calculate the Pearson χ^2 statistic (χ_p^2) for the data,

$$\chi_p^2 = \sum_{i=1}^n \frac{(N_i - N_{0i})^2}{N_{0i}} = 24.2, \quad (8.8)$$

where N_i and N_{0i} are the observed and expected event counts in bin i , respectively. Based on the particular hypothesis 10,000 spectra were generated using the parameters obtained from the data and χ_p^2 was determined for each spectrum. The confidence level of the data is the fraction of simulated spectra with a higher χ_p^2 . For the best-fit oscillation parameters and the a priori choice of 20 bins, the goodness-of-fit is 11.1% with $\chi_p^2/\text{DOF} = 24.2/17$. It is important to keep in mind that the χ_p^2 and goodness-of-fit results are sensitive to the choice of binning.

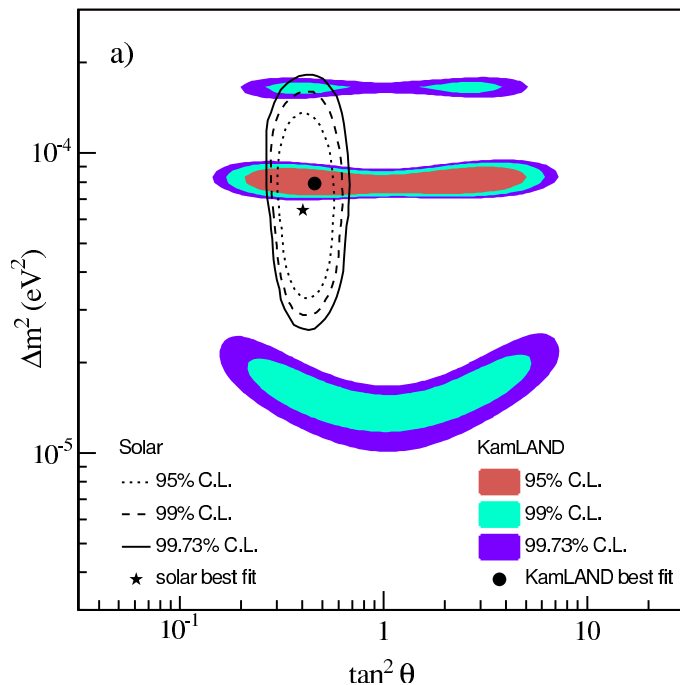


Figure 8.6: Allowed region of the neutrino oscillation parameter from KamLAND data (shaded regions). The best-fit parameters are $\Delta m^2 = 7.9_{-0.5}^{+0.6} \times 10^{-5} \text{eV}^2$ and $\tan^2\theta = 0.46$. The lines show solar neutrino experiments [57].

The allowed region contours in $\Delta m^2 - \tan^2\theta$ parameter space derived from the $\Delta\chi^2$ values are shown in Figure 8.6. The best-fit point is in the region commonly characterized as LMA I. Maximal mixing for values of Δm^2 consistent with LMA I is allowed at the 62.1% C.L. Due to distortions in the spectrum, the LMA II region (at $\Delta m^2 \sim 2 \times 10^{-4} \text{eV}^2$) is disfavored at the 98.0% C.L., as are larger values of Δm^2 previously allowed by KamLAND. The allowed region at lower Δm^2 is disfavored at the 97.5% C.L., but this region is not consistent with the LMA region determined from solar neutrino experiments assuming CPT invariance.

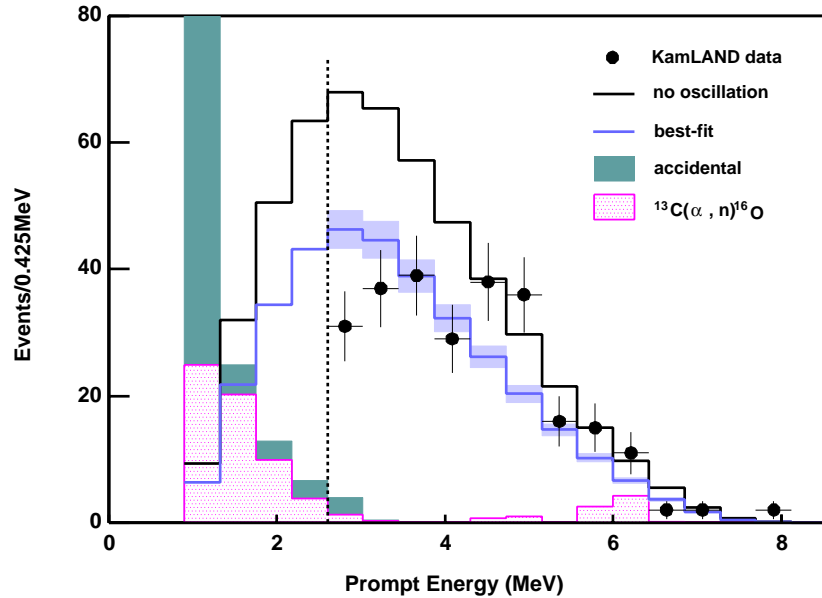


Figure 8.7: Best fit of the scaled no-oscillation spectrum. The unscaled no-oscillation reactor $\bar{\nu}_e$ spectrum is also shown.

8.3.2 Scaled no-oscillation spectrum

Figure 8.7 shows the best-fit of the scaled no-oscillation spectrum. The goodness-of-fit of the scaled no-oscillation spectrum where the normalization was fit to the data is 0.4% ($\chi^2_p/\text{DOF} = 37.3/18$) using the Pearson χ^2 . The observed energy spectrum disagrees with the expected spectral shape in the absence of neutrino oscillation at 99.6% significance.

The rate-and-shape analysis was performed with the following χ^2 definition,

$$\chi^2 = \chi^2_{\text{poisson}}(S_{\text{normalize}}, \alpha_{1\sim 4}, \beta_{1\sim 3}) + \chi^2_{\text{distortion}}(\alpha_{1\sim 4}) + \chi^2_{\text{BG}}(\beta_{1\sim 3}), \quad (8.9)$$

$$\chi^2_{\text{poisson}} = 2 \sum_{i=1}^{N_{\text{bin}}} \left(n_i \log \frac{n_i}{\mu_i S_{\text{normalize}}} + \mu_i S_{\text{normalize}} - n_i \right), \quad (8.10)$$

where $S_{\text{normalize}}$ is the normalization factor, n_i is the number of observed events in i -th bin, and μ_i is the number of expected events in i -th bin. The observed energy spectrum disagrees with the expected spectral shape in the absence of neutrino oscillation at 99.999995% confidence level.

8.3.3 L/E analysis

To illustrate oscillatory behavior of the data, Figure 8.8 is plotted. In this figure, The data and the best-fit spectra are divided by the expected no-oscillation spectrum. Two alternative hypotheses for neutrino disappearance, neutrino decay [87] and decoherence [88], give different

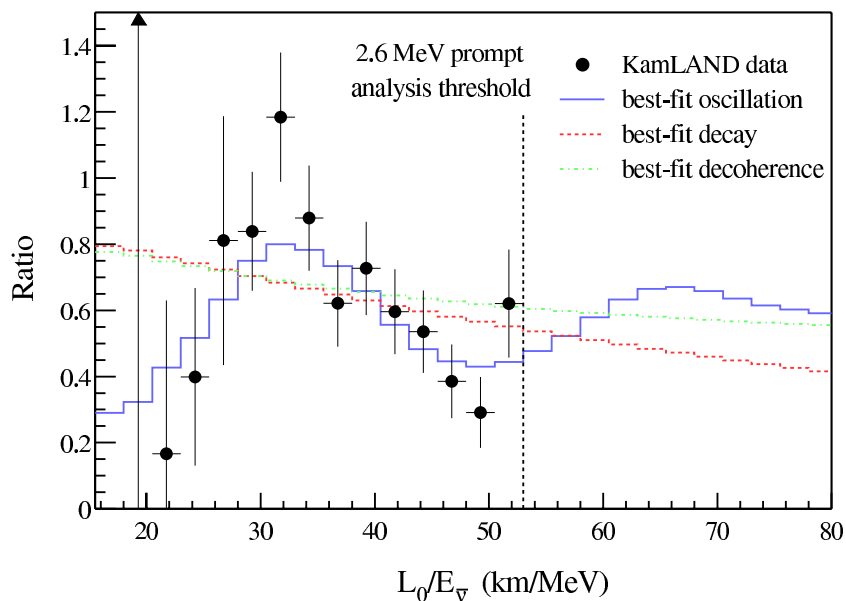


Figure 8.8: Ratio of the observed $\bar{\nu}_e$ spectrum to the expectation for no-oscillation versus L_0/E . The curves show the expectation for the best-fit oscillation, best-fit decay and best-fit decoherence models taking into account the individual time-dependent flux variations of all reactors and detector effects. The data points and models are plotted with $L_0 = 180\text{km}$, as if all anti-neutrinos detected in KamLAND were due to a single reactor at this distance.

L_0/E dependences as

$$P(\bar{\nu}_e \rightarrow \bar{\nu}_e) = \left(\cos^2\theta + \sin^2\theta \exp\left(-\frac{m_2 L}{2\tau_0 E}\right) \right)^2 : \text{Neutrino decay} \quad (8.11)$$

$$P(\bar{\nu}_e \rightarrow \bar{\nu}_e) = 1 - \frac{1}{2} \sin^2 2\theta \left(1 - \exp\left(-\gamma_0 \frac{L}{E}\right) \right) : \text{Neutrino decoherence.} \quad (8.12)$$

The best-fit points are $(\sin^2\theta, m/c\tau) = (1.0, 0.011\text{MeV/km})$ for decay and $(\sin^2 2\theta, \gamma^0) = (1.0, 0.030\text{MeV/km})$ for decoherence. Using the Pearson χ^2 , the decay has a goodness-of-fit of only 0.7% ($\chi_p^2/\text{DOF} = 35.8/17$), while decoherence has a goodness-of-fit of 1.8% ($\chi_p^2/\text{DOF} = 32.2/17$).

8.3.4 Combined analysis

A two-flavor analysis of the KamLAND data and the observed solar neutrino fluxes [85], with the assumption of CPT invariance, restricts the allowed $\Delta m^2 - \tan^2\theta$ parameters as shown in Figure 8.9. A fit to Δm^2 and $\tan^2\theta$ was performed by the global χ^2 written in the form

$$\chi_{\text{global}}^2 = \chi_{\text{solar}}^2 + \chi_{\text{KamLAND}}^2, \quad (8.13)$$

where χ_{solar}^2 is defined as

$$\chi_{\text{solar}}^2 = \chi_{\text{rate}}^2 + \chi_{\text{shape}}^2. \quad (8.14)$$

For this analysis, the event rate measured by Homestake, SAGE, GALLEX, GNO, SNO(CC and NC) and Super-Kamiokande, and the zenith angle spectra by Super-Kamiokande were used. The predicted solar neutrino fluxes are derived from the BP00 standard solar model.

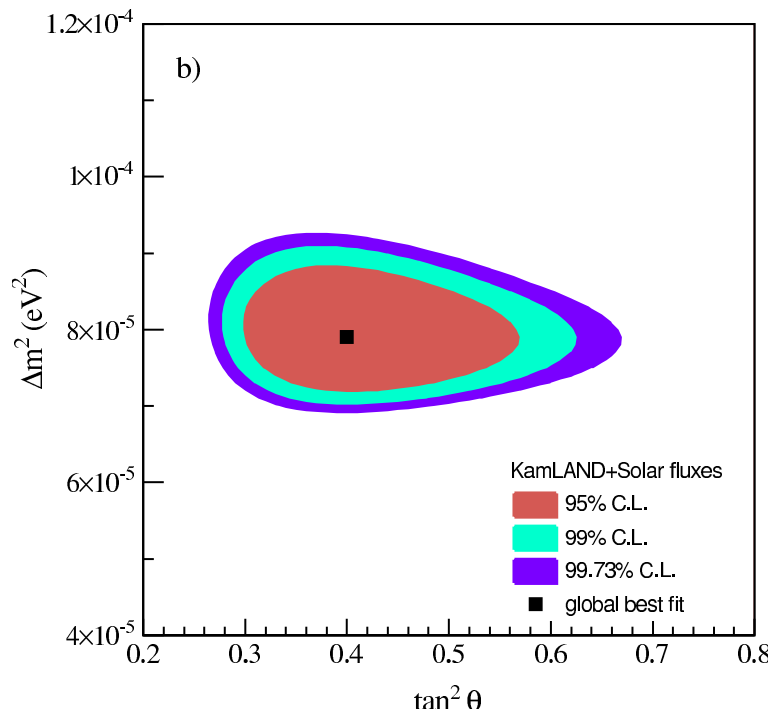


Figure 8.9: Combined two-neutrino oscillation analysis of KamLAND and observed solar neutrino fluxes under the assumption of CPT invariance. The fit gives $\Delta m^2 = 7.9_{-0.5}^{+0.6} \times 10^{-5} \text{ eV}^2$ and $\tan^2 \theta = 0.40_{-0.07}^{+0.10}$ including the allowed 1-sigma parameter range.

The sensitivity in Δm^2 is dominated by the observed distortion in the KamLAND spectrum, while solar neutrino data provide the best constraint on θ . The combined analysis gives $\Delta m^2 = 7.9_{-0.5}^{+0.6} \times 10^{-5} \text{eV}^2$ and $\tan^2\theta = 0.40_{-0.07}^{+0.10}$. These are the most precise determination to date.

Chapter 9

Conclusion

In a 766 ton-year exposure of KamLAND between March 9, 2002 and January 11, 2004, 258 $\bar{\nu}_e$ candidate events with $\bar{\nu}_e$ energies above 3.4 MeV are observed, which include 17.8 expected background events. To calculate expected time-dependent reactor $\bar{\nu}_e$ events at KamLAND, thermal output of all Japanese power reactors are traced. The systematic uncertainties from the fission rate calculation are reactor power (2.1%) and fuel composition (1.0%), which are smaller than the detector correlated uncertainties. The expected number of $\bar{\nu}_e$ events is 365.2 ± 23.7 (syst) with $\bar{\nu}_e$ energies above 3.4 MeV assuming no neutrino oscillation.

The ratio of the number of observed events to the expected number of events assuming no neutrino oscillation is 0.658 ± 0.044 (stat) ± 0.047 (syst). This deficit confirms $\bar{\nu}_e$ disappearance at 99.998% significance level. Studies of correlation between reactor $\bar{\nu}_e$ flux and observed event rate show that the background rate is consistent with estimation. The observed energy spectrum disagrees with the expected spectral shape in the absence of neutrino oscillation at 99.6% significance and prefers the distortion expected from $\bar{\nu}_e$ oscillation effects. A two-neutrino oscillation analysis of the KamLAND data gives a mass-squared difference $\Delta m^2 = 7.9_{-0.5}^{+0.6} \times 10^{-5} \text{eV}^2$ and a mixing angle $\tan^2 \theta = 0.46$. These values are in excellent agreement with the “Large Mixing Angle” solution to the solar neutrino problem. Assuming CPT invariance, a combined analysis of data from KamLAND and solar neutrino experiments yields $\Delta m^2 = 7.9_{-0.5}^{+0.6} \times 10^{-5} \text{eV}^2$ and $\tan^2 \theta = 0.40_{-0.07}^{+0.10}$, the most precise determination to date.

Appendix A

Japanese research reactors and world reactors

Institute	Name	Latitude	Longitude	Type	Power (kWth)	Dist. (km)
JNC	JOYO	36 16 04	140 33 14	Research Reactor	140000	290
JAERI	JMTR	36 16 10	140 32 52	Research Reactor	50000	290
JAERI	HTTR	36 15 58	140 32 50	Research Reactor	30000	290
JAERI	JRR-3	36 27 17	140 36 03	Research Reactor	20000	290
JAERI	JRR-4	36 27 14	140 36 02	Research Reactor	3500	290
JAERI	NSRR	36 27 38	140 36 23	Research Reactor	300	290
Kyoto University	KUR	34 22 59	135 21 00	Research Reactor	5000	280
Tokyo University	YAYOI	36 27 48	140 35 59	Research Reactor	2	240
Kinki University	UTR-KINKI	34 38 38	135 35 16	Research Reactor	0.001	250
JAERI	TCA	36 27 27	140 36 23	Critical Assembly	0.2	290
JAERI	FCA	36 27 25	140 36 25	Critical Assembly	2	290
JAERI	STACY	36 27 08	140 36 21	Critical Assembly	0.2	290
JAERI	TRACY	36 27 08	140 36 21	Critical Assembly	10	290
Toshiba Corporation	NCA	35 31 57	139 46 16	Critical Assembly	0.2	240
Kyoto University	KUCA	34 23 01	135 21 02	Critical Assembly	0.1	280

Table A.1: Japanese research reactors. JNC: Japan Nuclear Cycle Development Institute. JAERI: The Japan Atomic Energy Research Institute.

Each commercial reactor is identified in Taiwan, China, India, and Pakistan [69]. In other countries, the total electric output [70] is considered to be located at one point.

Country	Reactor	Longitude	Latitude	Power (MWe)	Dist. (km)	Flux (MWt/cm ²)
Taiwan	Chinshan-1	121.6	25.3	636	1929	4.0e-15
Taiwan	Chinshan-2	121.6	25.3	636	1929	4.0e-15
Taiwan	Kuosheng-1	121.7	25.2	985	1929	6.2e-15
Taiwan	Kuosheng-2	121.7	25.2	985	1929	6.2e-15
Taiwan	Maanshan-1	120.7	22	951	2253	4.4e-15
Taiwan	Maanshan-2	120.7	22	951	2253	4.4e-15
China	DayaBay-1	114.5	22.7	980	2649	3.3e-15
China	DayaBay-2	114.5	22.7	980	2649	3.3e-15
China	Qinshan1-1	120.9	30.4	300	1654	2.6e-15

Table A.2: World reactors.

Country	Reactor	Longitude	Latitude	Power (MWe)	Dist. (km)	Flux (MWt/cm ²)
China	Qinshan2-1	120.9	30.4	600	1654	5.1e-15
China	Lingao-1	112.2	21.8	900	2889	2.5e-15
India	Kakrapar-1	73	21.3	220	6105	1.4e-16
India	Kakrapar-2	73	21.3	220	6105	1.4e-16
India	Madras-1	80	12.6	170	6017	1.1e-16
India	Madras-2	80	12.6	170	6017	1.1e-16
India	Narora-1	78.3	28.1	220	5366	1.8e-16
India	Narora-2	78.3	28.1	220	5366	1.8e-16
India	Rajasthan-2	75.6	24.8	200	5731	1.4e-16
India	Rajasthan-3	75.6	24.8	220	5731	1.6e-16
India	Rajasthan-4	75.6	24.8	220	5731	1.6e-16
India	Tarapur-1	72.6	19.7	160	6216	9.7e-17
India	Tarapur-2	72.6	19.7	160	6216	9.7e-17
India	Kaiga-1	74.4	14.8	220	6331	1.3e-16
India	Kaiga-2	74.4	14.8	220	6331	1.3e-16
Pakistan	Kanupp	66.8	24.8	137	6416	7.8e-17
Pakistan	Chasnupp	71.5	32.5	325	5718	2.3e-16
- Total power in each country -						
US	-	-74	40.8	101171	9588	2.6e-14
France	-	2.5	49	62920	8661	2.0e-14
Germany	-	7	51.4	22365	8359	7.5e-15
Russia	-	37.6	55.8	21556	6893	1.1e-14
Canada	-	-79.6	42.7	10615	9321	2.9e-15
England	-	-0.2	51.2	13531	8591	4.3e-15
Ukraine	-	30.6	50.4	11818	7484	4.9e-15
Sweden	-	18.1	59.6	9822	7466	4.1e-15
Spain	-	-3.7	40.4	7798	9413	2.1e-15
Belgium	-	4.4	50.8	5995	8482	2.0e-15
Bulgaria	-	23.4	42.7	3760	8243	1.3e-15
Switzerland	-	7.4	46.9	3352	8638	1.1e-15
Lithuania	-	25.1	54.6	3000	7496	1.2e-15
Finland	-	25	60.3	2760	7183	1.3e-15
SouthAfrica	-	18.6	-34	1930	11580	3.4e-16
Hungary	-	19	47.5	1850	8159	6.5e-16
Czech	-	14.3	50.1	1760	8187	6.1e-16
Slovakia	-	18.2	47.9	2620	8168	9.2e-16
Mexico	-	-99.2	19.4	1364	9958	3.2e-16
Argentina	-	-58.5	-34.6	1005	12658	1.5e-16
Rumania	-	26.1	44.5	706	8015	2.6e-16
Slovenia	-	14.5	46.1	707	8426	2.3e-16
Brazil	-	-46.6	-23.5	657	12654	9.6e-17
Holland	-	4.8	52.9	481	8328	1.6e-16
Armenia	-	44.5	40.1	408	7251	1.8e-16

Table A.2: World reactors.

Appendix B

Operation data of Japanese reactors

In this table, monthly outputs of each Japanese power reactor are listed. Numbers in the first column correspond to the reactor number in Table 7.2. $P_J(\text{MWe})$ is the average electric output taken from Ref. [72].

#	Output	Top: January/2004, - , March/2003 to December/2003											
		1	2	3	4	5	6	7	8	9	10	11	12
0	P_J (MWe)	0.0	-	0.0	0.0	0.0	0.0	0.0	0.0	0.0	0.0	0.0	0.0
	P_J (MWe)	0.0	0.0	0.0	0.0	0.0	0.0	0.0	0.0	0.0	0.0	0.0	0.0
1	P_J (MWe)	829.5	-	0.0	0.0	0.0	0.0	0.0	0.0	0.0	0.0	0.0	228.9
	P_J (MWe)	680.3	840.0	840.0	840.0	839.7	839.0	835.4	833.3	832.7	836.5	839.3	815.0
2	P_J (MWe)	1119.9	-	1100.0	1100.0	1100.0	1100.0	1100.0	1100.0	1100.0	723.5	0.0	0.0
	P_J (MWe)	0.0	0.0	0.0	0.0	0.0	0.0	0.0	0.0	0.0	98.2	910.7	1112.2
3	P_J (MWe)	1145.5	-	1137.0	1137.0	1137.0	1136.9	1136.9	1136.9	116.2	0.0	0.0	0.0
	P_J (MWe)	0.0	0.0	0.0	0.0	0.0	0.0	0.0	746.6	1136.3	1137.0	1137.5	1145.1
4	P_J (MWe)	470.0	-	460.0	460.0	355.1	0.0	373.0	460.0	460.0	460.0	460.0	460.0
	P_J (MWe)	460.0	460.0	460.0	460.0	460.0	460.0	459.9	459.9	244.4	0.0	0.0	24.0
5	P_J (MWe)	825.6	-	820.0	820.0	820.0	820.0	819.9	817.2	819.3	820.0	820.0	820.0
	P_J (MWe)	820.0	819.9	819.9	379.5	0.0	0.0	0.0	786.2	818.2	820.0	822.3	826.8
6	P_J (MWe)	1073.3	-	1093.6	122.6	1098.7	1094.5	1091.9	1088.1	538.5	0.0	0.0	776.6
	P_J (MWe)	1103.5	1103.3	919.0	1103.6	1102.7	1103.1	1098.8	1098.7	1095.9	1100.6	1100.5	1102.1
7	P_J (MWe)	328.4	-	0.0	133.3	357.0	357.0	357.0	357.0	357.0	357.0	357.0	357.0
	P_J (MWe)	357.0	350.3	274.7	361.2	356.4	144.3	0.0	260.1	358.7	360.2	360.7	305.2
8	P_J (MWe)	1178.6	-	1159.9	1159.9	1159.9	371.9	801.2	1179.3	1185.4	1190.3	1192.9	717.8
	P_J (MWe)	1189.0	1190.0	1189.6	1191.6	1193.9	1192.9	1191.1	1187.0	148.8	52.8	1179.6	1179.9
9	P_J (MWe)	592.0	-	571.9	579.0	579.0	579.0	579.0	578.9	579.0	579.0	579.0	579.0
	P_J (MWe)	579.0	579.0	579.0	478.6	0.0	217.4	590.8	588.9	585.5	186.4	563.4	591.5
10	P_J (MWe)	596.0	-	579.0	579.0	579.0	579.0	579.0	579.0	579.0	579.0	579.0	165.1
	P_J (MWe)	11.7	573.1	593.4	593.1	593.5	594.0	594.0	591.0	193.2	0.0	190.6	595.3
11	P_J (MWe)	553.1	-	297.3	320.8	540.0	540.0	540.0	540.0	540.0	539.5	540.0	540.0
	P_J (MWe)	540.0	540.0	539.9	365.0	0.0	0.0	0.0	0.0	0.0	0.0	0.0	278.1
12	P_J (MWe)	0.0	-	0.0	38.3	0.0	134.0	164.3	157.0	111.6	164.5	24.4	124.3
	P_J (MWe)	165.0	165.0	150.4	0.0	0.0	0.0	0.0	0.0	0.0	0.0	0.0	0.0
13	P_J (MWe)	0.0	-	0.0	0.0	0.0	0.0	0.0	0.0	0.0	0.0	0.0	0.0
	P_J (MWe)	0.0	0.0	0.0	0.0	0.0	0.0	0.0	0.0	0.0	0.0	0.0	0.0
14	P_J (MWe)	145.3	-	339.7	339.7	339.7	338.9	333.1	326.8	0.0	0.0	92.3	351.5
	P_J (MWe)	352.5	352.4	352.7	352.3	350.2	347.2	343.6	339.9	341.4	347.4	348.7	350.5
15	P_J (MWe)	508.5	-	499.6	499.6	499.6	31.2	206.8	494.6	497.2	500.5	505.3	506.6
	P_J (MWe)	507.7	507.6	507.5	506.8	479.6	500.9	495.9	490.8	178.3	0.0	245.5	508.7
16	P_J (MWe)	862.1	-	455.4	825.9	825.9	825.9	825.9	825.9	825.9	825.9	405.2	825.4
	P_J (MWe)	825.9	825.9	825.9	825.9	183.1	283.2	848.4	836.6	836.8	844.6	851.3	860.4
17	P_J (MWe)	1188.3	-	692.5	1174.9	1174.9	1174.7	1170.2	1162.4	1169.4	1174.0	1174.9	1174.9
	P_J (MWe)	1174.9	1174.9	1174.9	502.5	0.0	1004.6	1180.3	1168.6	1167.7	1178.8	1185.5	660.0
18	P_J (MWe)	1203.1	-	1174.9	1174.9	1174.9	1174.9	1174.3	1169.8	1174.1	751.7	0.0	479.1
	P_J (MWe)	1209.3	1206.2	1210.8	1207.1	1201.4	1193.2	1182.6	1176.1	1174.4	1188.6	1194.7	1196.8
19	P_J (MWe)	1200.9	-	1179.9	1179.9	1179.9	1179.9	1179.9	1179.9	1179.9	1179.9	1179.9	1179.9
	P_J (MWe)	183.9	116.7	1198.2	1202.5	1202.5	1202.4	1200.4	1199.7	1197.9	1201.5	1202.5	1202.1
20	P_J (MWe)	1208.9	-	608.9	559.9	1200.9	1201.4	1201.1	1196.3	1198.7	1204.0	1206.5	1206.5
	P_J (MWe)	1207.5	1206.4	1207.8	1208.7	1208.3	477.0	0.4	1164.6	1199.1	1204.8	1206.1	1205.4
21	P_J (MWe)	863.9	-	825.9	825.9	825.9	825.9	825.9	825.9	825.9	825.9	519.7	0.0
	P_J (MWe)	0.0	373.2	866.6	867.0	866.4	864.2	861.3	856.3	855.8	861.5	863.8	864.9
22	P_J (MWe)	862.0	-	825.9	547.1	0.0	680.0	848.7	842.6	846.2	853.6	861.7	864.8
	P_J (MWe)	866.0	866.0	865.8	864.6	861.4	856.1	846.9	21.4	0.0	143.0	861.4	862.0
23	P_J (MWe)	0.0	-	869.9	869.9	869.9	869.7	869.7	869.7	604.2	0.0	722.0	905.6
	P_J (MWe)	906.1	907.4	907.7	907.0	905.4	902.0	902.7	899.7	900.5	903.5	907.1	494.8
24	P_J (MWe)	905.0	-	730.9	869.9	869.9	869.9	869.8	869.8	869.8	869.9	869.9	869.9
	P_J (MWe)	869.9	869.9	869.9	780.2	0.0	388.1	905.0	901.9	901.9	904.9	905.1	905.6
25	P_J (MWe)	575.1	-	564.2	573.5	572.9	163.1	0.0	260.9	567.7	570.0	572.7	573.2
	P_J (MWe)	572.5	573.3	573.7	573.1	571.9	570.9	568.6	567.8	558.4	0.0	0.0	116.6
26	P_J (MWe)	579.6	-	564.1	576.0	575.6	573.6	571.3	568.3	571.0	572.9	241.7	0.0
	P_J (MWe)	152.7	577.6	578.9	578.4	577.9	576.2	574.5	573.5	570.9	574.8	576.9	578.4
27	P_J (MWe)	1207.2	-	1179.8	1179.8	1179.8	1179.8	1179.8	1179.8	1179.8	1179.8	1179.7	681.4
	P_J (MWe)	0.0	274.8	1196.8	1203.8	1206.2	1205.1	1204.8	1204.2	1201.7	1205.2	1206.4	1206.5
28	P_J (MWe)	0.0	-	1179.8	1179.8	1179.9	1179.8	1179.8	860.8	0.0	196.4	1189.0	1191.7
	P_J (MWe)	1190.4	1188.2	1194.1	1195.3	1195.6	1195.1	1194.0	1193.9	1191.6	1195.8	1196.5	651.9
29	P_J (MWe)	899.8	-	857.3	899.2	897.4	896.2	897.1	895.5	895.5	897.0	899.7	899.1
	P_J (MWe)	900.1	900.6	900.8	567.3	0.0	313.0	894.7	894.0	893.0	897.8	898.9	899.8

Table B.1: Average output of Japanese power reactors

#	Output	Top: January/2004, - , March/2003 to December/2003											
		1	2	3	4	5	6	7	8	9	10	11	12
30	P_J (MWe)	907.0	-	889.9	353.4	0.0	493.8	898.0	897.5	898.3	900.4	903.2	903.5
	P_J (MWe)	904.0	903.9	903.9	903.7	902.3	899.0	900.0	84.3	2.7	831.8	907.3	907.3
31	P_J (MWe)	579.7	-	0.0	0.0	353.8	569.3	570.9	571.9	569.1	569.6	575.4	460.0
	P_J (MWe)	583.4	460.0	581.7	503.5	0.0	0.0	282.7	572.3	568.4	570.7	573.5	577.7
32	P_J (MWe)	580.7	-	565.9	567.7	577.6	573.3	573.1	571.1	569.2	570.5	576.4	581.0
	P_J (MWe)	487.9	0.0	0.0	522.2	580.8	575.7	572.2	573.6	569.3	584.6	574.5	578.4
33	P_J (MWe)	928.5	-	890.0	905.9	683.7	0.0	509.3	923.4	921.5	923.1	932.0	933.7
	P_J (MWe)	932.4	930.7	930.4	932.6	931.1	929.8	928.9	926.2	551.5	0.0	0.0	366.2
34	P_J (MWe)	526.7	-	524.0	524.0	524.0	524.0	523.9	523.9	121.3	0.0	0.0	0.0
	P_J (MWe)	0.0	0.0	0.0	0.0	0.0	0.0	39.4	526.9	526.8	527.3	527.2	527.3
35	P_J (MWe)	836.8	-	0.0	777.3	825.0	592.0	825.0	825.0	825.0	825.0	825.0	825.0
	P_J (MWe)	825.0	825.0	825.0	824.5	545.7	0.0	0.0	0.0	0.0	0.0	18.4	827.6
36	P_J (MWe)	854.9	-	824.9	825.0	825.0	825.0	825.0	825.0	825.0	824.8	825.0	824.9
	P_J (MWe)	824.5	673.5	0.0	274.4	755.1	850.0	852.5	851.6	852.1	854.1	854.6	854.7
37	P_J (MWe)	0.0	-	460.0	460.0	460.0	460.0	460.0	460.0	459.9	368.8	0.0	0.0
	P_J (MWe)	0.0	0.0	0.0	0.0	0.0	0.0	0.0	0.0	0.0	0.0	0.0	0.0
38	P_J (MWe)	0.0	-	218.1	784.0	784.0	784.0	783.8	783.8	784.0	784.0	784.0	784.0
	P_J (MWe)	784.0	784.0	754.3	0.0	0.0	0.0	0.0	0.0	0.0	0.0	0.0	0.0
39	P_J (MWe)	789.9	-	783.6	783.0	781.4	784.0	409.3	0.0	0.0	0.0	0.0	0.0
	P_J (MWe)	0.0	0.0	0.0	0.0	0.0	0.0	0.0	383.5	784.0	784.0	784.0	785.2
40	P_J (MWe)	0.0	-	784.0	783.8	784.0	784.0	783.8	782.3	387.1	0.0	0.0	0.0
	P_J (MWe)	0.0	0.0	0.0	0.0	0.0	0.0	0.0	0.0	0.0	0.0	0.0	0.0
41	P_J (MWe)	784.8	-	784.0	784.0	784.0	784.0	782.0	778.6	777.9	781.1	783.6	783.2
	P_J (MWe)	783.1	274.2	0.0	0.0	0.0	0.0	0.0	0.0	478.2	783.9	784.0	784.2
42	P_J (MWe)	0.0	-	1099.6	210.9	0.0	0.0	0.0	999.8	1100.0	1100.0	1100.0	1100.0
	P_J (MWe)	1100.0	1100.0	1100.0	505.1	0.0	0.0	637.9	1100.0	1054.8	0.0	0.0	0.0
43	P_J (MWe)	1110.4	-	1100.0	1100.0	1100.0	1100.0	1099.9	1098.9	1099.1	1099.7	1098.8	1095.6
	P_J (MWe)	206.5	0.0	0.0	0.0	0.0	0.0	0.0	4.4	1089.6	1107.0	1109.3	1110.5
44	P_J (MWe)	0.0	-	1099.2	1095.8	206.8	0.0	860.6	1104.1	71.9	0.0	0.0	0.0
	P_J (MWe)	0.0	0.0	0.0	0.0	0.0	0.0	0.0	0.0	0.0	0.0	0.0	0.0
45	P_J (MWe)	0.0	-	1100.0	1100.0	1101.0	1104.8	1105.7	1102.1	544.8	0.0	0.0	0.0
	P_J (MWe)	0.0	0.0	0.0	0.0	0.0	0.0	0.0	0.0	0.0	0.0	0.0	0.0
46	P_J (MWe)	0.0	-	1100.0	1100.0	1101.3	1109.1	1105.7	1104.5	1104.2	421.7	0.0	0.0
	P_J (MWe)	0.0	0.0	0.0	0.0	0.0	0.0	0.0	0.0	0.0	0.0	0.0	0.0
47	P_J (MWe)	0.0	-	734.2	1100.0	1100.0	1100.0	1100.0	1098.8	66.7	0.0	0.0	0.0
	P_J (MWe)	0.0	0.0	0.0	0.0	0.0	0.0	0.0	0.0	0.0	0.0	0.0	0.0
48	P_J (MWe)	0.0	-	986.1	31.1	1121.4	1125.2	1119.9	1114.2	729.1	0.0	0.0	0.0
	P_J (MWe)	0.0	0.0	0.0	0.0	0.0	0.0	0.0	0.0	0.0	0.0	0.0	0.0
49	P_J (MWe)	0.0	-	1100.0	1100.0	1084.2	1099.8	1098.1	313.0	0.0	0.0	0.0	0.0
	P_J (MWe)	0.0	0.0	0.0	0.0	0.0	0.0	0.0	0.0	0.0	0.0	0.0	0.0
50	P_J (MWe)	1118.2	-	1100.0	1100.0	1100.0	1100.0	1100.0	1099.7	1099.4	1098.9	1097.4	1092.6
	P_J (MWe)	194.1	0.0	0.0	0.0	0.0	0.0	204.3	1110.7	1110.5	1114.2	1116.4	1116.4
51	P_J (MWe)	0.0	-	1100.0	1100.0	1113.7	1111.5	1107.6	1102.8	1099.0	1110.6	1113.2	1113.7
	P_J (MWe)	1113.3	1103.2	0.0	0.0	0.0	0.0	0.0	0.0	0.0	0.0	0.0	0.0
52	P_J (MWe)	1408.2	-	1356.0	1356.0	1356.0	1356.0	1356.0	1356.0	1356.0	1356.0	1356.0	1355.3
	P_J (MWe)	1125.7	0.0	0.0	0.0	936.3	1356.0	1394.8	1390.9	1391.6	1399.9	1404.2	1406.4
53	P_J (MWe)	503.6	-	1305.4	309.9	0.0	0.0	122.8	1366.5	1382.6	1388.3	1394.6	1397.0
	P_J (MWe)	1398.2	1398.6	1253.4	0.0	0.0	408.9	1389.4	1382.3	1001.5	0.0	0.0	0.0

Table B.1: Average output of Japanese power reactors

Appendix C

Operation data of Korean reactors

In this table, monthly outputs of each Korean commercial reactor are listed. Numbers in the first column correspond to the reactor number in Table 7.6. $P(\text{MW})$ is the average electric output based on the operation data taken from Ref. [73].

#	Output	Top: January/2004, - , March/2003 to December/2003 Bottom: January/2003 to December/2004											
		1	2	3	4	5	6	7	8	9	10	11	12
54	P(MW)	1783.6	-	1774.9	1182.2	1044.4	1405.7	1403.6	1410.0	659.0	1658.3	1771.3	1772.5
	P(MW)	1590.2	9.5	1729.5	1777.6	1777.5	1772.7	1777.0	1772.9	1522.2	1780.3	1780.9	1782.6
55	P(MW)	1991.2	-	1980.1	1979.7	1982.6	1979.9	1978.5	1445.9	275.3	1984.1	1990.3	1990.9
	P(MW)	1990.6	1990.7	1992.1	1995.7	1603.8	1993.9	1994.3	1991.4	1603.4	695.0	813.2	1993.9
56	P(MW)	2909.4	-	2958.8	2956.6	2957.6	2957.4	2954.9	2622.2	42.3	2885.8	2962.4	2961.8
	P(MW)	2963.3	2964.5	2963.5	2962.9	2962.5	2962.2	2957.8	2945.6	2444.4	2955.3	2959.0	2961.7
57	P(MW)	2965.7	-	2966.2	2964.2	2963.5	2962.5	2960.1	2958.7	2954.8	2954.6	2963.7	2966.0
	P(MW)	2966.2	2966.5	2665.7	146.4	2745.2	2962.3	2959.0	2950.5	2466.7	2959.3	2963.6	2963.2
58	P(MW)	2903.3	-	2905.4	2910.8	2913.8	1165.9	421.5	2908.2	2903.1	1781.7	0.0	2255.4
	P(MW)	2911.7	2913.9	2913.4	1407.6	0.0	1936.7	2906.1	2900.2	2903.9	2903.9	2834.7	2891.7
59	P(MW)	2900.8	-	2914.1	2912.9	2909.7	2915.1	2914.3	2913.8	752.5	0.0	532.8	2907.9
	P(MW)	2912.6	2909.1	2907.9	2907.1	1359.6	108.3	2902.7	2894.6	2901.0	2907.7	2914.3	2908.3
60	P(MW)	3092.2	-	3090.1	3089.8	3090.1	3090.1	3090.1	3086.7	3082.2	3083.5	2168.0	12.3
	P(MW)	2953.5	3104.5	3105.1	3104.8	3104.8	3099.0	3100.7	3090.9	3088.3	3089.8	3092.3	3092.9
61	P(MW)	3084.2	-	3080.4	390.0	340.6	3086.8	3083.9	3032.8	3076.0	3075.1	3075.0	2800.6
	P(MW)	3051.2	3077.7	3079.8	3084.6	3080.9	3078.0	3079.1	2922.4	312.1	2908.9	3089.4	3086.6
62	P(MW)	2037.7	-	1201.7	2041.9	2045.8	2043.1	2038.4	2035.7	2002.8	2037.3	2042.3	2043.1
	P(MW)	2008.8	36.5	1051.0	2038.1	2039.9	2041.9	2040.0	2030.9	2012.5	2036.6	2038.8	2039.5
63	P(MW)	2158.4	-	2162.9	2164.7	2159.7	2155.8	1418.6	2135.1	2124.3	2142.3	2152.8	2158.1
	P(MW)	2162.7	2159.6	2160.9	2160.5	227.4	2139.7	2144.8	2125.7	1799.3	2141.0	2152.5	2155.6
64	P(MW)	2157.6	-	2147.8	2146.7	1627.3	570.8	2143.6	2136.9	2129.8	2144.7	2153.1	2154.1
	P(MW)	2155.8	2156.7	2159.5	2157.1	2156.9	2148.7	2147.1	1784.6	710.9	2143.0	2153.4	2154.0
65	P(MW)	2157.0	-	2057.2	0.0	1927.4	2151.1	2142.7	2136.8	2125.6	2142.2	2151.0	2158.0
	P(MW)	2157.2	2158.4	2158.9	2020.4	2157.6	824.1	2070.7	2126.4	2124.3	2140.7	2149.8	2153.8
66	P(MW)	2911.5	-	2635.6	2925.2	2934.6	2811.7	2900.2	2882.8	2889.4	2908.3	2910.5	2911.3
	P(MW)	2911.5	2060.2	2906.7	2502.4	816.4	1204.8	2882.7	2817.9	2865.5	2895.2	2907.1	2910.3
67	P(MW)	2881.5	-	2892.5	2891.7	2887.8	2874.1	2856.3	2840.3	2852.6	2875.8	2884.8	2885.4
	P(MW)	1426.0	786.8	2893.1	2888.5	2886.5	2876.3	2870.9	2851.6	2862.8	2889.8	2897.6	2898.2
68	P(MW)	3078.9	-	0.0	1424.6	3065.7	3057.9	3051.5	3038.2	3051.5	3062.3	3066.5	3067.7
	P(MW)	3068.3	3067.0	3067.5	3063.8	2370.8	296.6	3062.0	3053.4	3054.1	3067.6	2883.0	3076.7
69	P(MW)	3065.2	-	3072.5	3069.6	3066.1	3059.0	3047.2	3035.3	3034.8	1176.0	715.6	3086.8
	P(MW)	3042.1	2690.5	3088.2	3088.8	3086.9	3072.4	3069.4	3054.6	3041.2	3053.9	3062.2	3064.3
70	P(MW)	0.0	-	0.0	0.0	0.0	0.0	0.0	942.7	3079.3	3091.0	2785.1	3102.2
	P(MW)	3100.8	3099.2	1499.7	0.0	243.4	3095.6	3091.0	2739.9	3086.3	3092.9	3089.2	2594.6
71	P(MW)	0.0	-	0.0	0.0	0.0	0.0	0.0	0.0	0.0	0.0	0.0	550.9
	P(MW)	3112.2	3105.9	3104.5	3104.7	3100.3	3096.4	3093.3	3079.8	3080.9	3092.8	1770.5	0.0

Table C.1: Converted thermal output of Korean commercial reactors

Bibliography

- [1] A. Suzuki, Talk at the XVIII International Conference on Neutrino Physics and Astrophysics, Takayama, Japan, (1998), and its proceedings.
- [2] K. Eguchi *et al.*, Phys. Rev. Lett. **90**, 021802 (2003).
- [3] T. Araki *et al.*, [arXiv:hep-ex/0406035].
- [4] W. Pauli, Letter to L. Meitner and her colleagues (letter open to the participants of the conference in Tübingen) (1930).
- [5] F. Reines and C. L. Cowan, Nature **178**, 446 (1956).
- [6] B. Pontecorvo, Sov. Phys. JETP **6**, 429 (1958); Sov. Phys. JETP **7**, 172 (1958).
- [7] G. Danby *et al.*, Phys. Rev. Lett. **9**, 36 (1962).
- [8] Z. Maki, M. Nakagawa, S. Sakata, Progr. Theor. Phys. **28**, 870 (1962).
- [9] Y. Fukuda *et al.*, Phys. Rev. Lett. **81**, 1562 (1998).
- [10] Particle Data Group, DE Groom *et al.*, Eur. Phys. J. C **15** (2000) 1.
- [11] K. Kodama *et al.*, Phys. Lett. B **504**, 218 (2001).
- [12] Q. R. Ahmad *et al.*, Phys. Rev. Lett. **87**, 071301 (2001).
- [13] E. Kh. Akhmedov, hep-ph/0001264.
- [14] V. M. Lobashev *et al.*, Phys. Lett. B **460**, 227 (1999).
- [15] M. Apollonio *et al.*, Eur. Phys. J. C **27**, 331 (2003).
- [16] J. N. Bahcall, M. H. Pinsonneault, and S. Basu, Astrophys. J. **555**, 990 (2001).
- [17] K. Lande *et al.*, Astrophys. J. **496**, 505 (1998).
- [18] B. T. Cleveland *et al.*, Ap. J. **496**, 505 (1998).
- [19] J. N. Abdurashitov *et al.*, Phys. Rev. C **60**, 055801 (1999).
- [20] W. Hampel *et al.*, Phys. Lett. B **447**, 127 (1999).
- [21] P. Anselmann *et al.*, Phys. Lett. B **285**, 376 (1994).
- [22] J. N. Abdurashitov *et al.*, Phys. Lett. B **328**, 234 (1994).

- [23] Y. Fukuda *et al.*, Phys. Rev. Lett. **77**, 1683 (1996).
- [24] Y. Fukuda *et al.*, Phys. Rev. Lett. **81**, 1158 (1998).
- [25] K. S. Hirata *et al.*, Phys. Rev. Lett. **63**, 16 (1989).
- [26] Y. Fukuda *et al.*, Phys. Lett. B **539**, 179 (2002).
- [27] Y. Fukuda *et al.*, Phys. Rev. Lett. **77**, 1683 (1996).
- [28] J. Boger *et al.*, nucl-ex/9910016.
- [29] S. Eidelman *et al.*, Phys. Lett. B **592**, 1 (2004).
- [30] R. S. Raghavan, S. Schoenert, S. Enomoto, J. Shirai, F. Suekane and A. Suzuki, Phys. Rev. Lett. **80**, 635 (1998).
- [31] R. Becker-Szendy *et al.*, Phys. Rev. D **46**, 3720 (1992).
- [32] W. W. Allison *et al.*, Phys. Lett. B **449**, 137 (1999).
- [33] Y. Fukuda *et al.*, Phys. Lett. B **335**, 237 (1994).
- [34] Y. Fukuda *et al.*, Phys. Lett. B **436**, 33 (1998), Y. Fukuda *et al.*, Phys. Lett. B **433**, 9 (1998).
- [35] K. Hirata *et al.*, Phys. Rev. Lett. **58**, 1490.
- [36] A. Aguilar *et al.*, Phys. Rev. D **64**, 112007 (2001).
- [37] B. Armbruster *et al.*, Phys. Rev. D **65**, 112001 (2002).
- [38] A. O. Bazarko, Nucl. Phys. B Proc. Suppl. **117**, 33 (2003).
- [39] G. L. Fogli *et al.*, Phys. Rev. D **66**, 053010 (2002).
- [40] Lester H. Miller, PhD thesis, Stanford University, (2000)
- [41] T.R.England and B.F.Rider, Evaluation and Compiliation of Fission Product Yield, LA-UR-94-3106 (1993).
- [42] P. Vogel and J. F. Beacom, Phys. Rev. D **60**, 053003 (1999).
- [43] A. Kurylov *et al.*, Phys. Rev. C **67**, 035502 (2003).
- [44] Particle Data Group, D. E. Groom *et al.*, Eur. Phys. J. C **15**, 1 (2000).
- [45] ^{235}U : K. Schreckenbach *et al.*, Phys. Lett. B **160**, 325 (1985); $^{239,241}\text{Pu}$: A. A. Hahn *et al.*, Phys. Lett. B **218**, 365 (1989); ^{238}U : P. Vogel *et al.*, Phys. Rev. C **24**, 1543 (1981).
- [46] Y. Declais *et al.*, Phys. Lett. B **338**, 383 (1994).
- [47] B. Achkar *et al.*, Phys. Lett. B **374**, 243 (1996).
- [48] M. Apollonio *et al.*, Phys. Lett. B **466**, 415 (1999).
- [49] F. Boehm *et al.*, Phys. Rev. D **64**, 112001 (2001).

- [50] V. I. Kopeikin *et al.*, Physics of Atomic Nuclei, **64**, 849 (2001).
- [51] Technical Evaluation Committee Tohoku University, Technical Evaluation Report for the Liquid Scintillator Balloon, (2000).
- [52] T. Iwamoto, PhD thesis, Tohoku University, (2003).
- [53] O. Tajima, PhD thesis, Tohoku University, (2003).
- [54] H. Kume *et al.*, Nucl. Instr. and Meth. **205**, 443 (1986).
- [55] K. Tagashira, Master thesis, Tohoku University, (1999).
- [56] Q. R. Ahmad *et al.*, Phys. Rev. Lett. **89**, 011301 (2002).
- [57] S. N. Ahmed *et al.* (SNO Collaboration), Phys. Rev. Lett. **92**, 181301 (2004).
- [58] National Nuclear Data Center, <http://www.nndc.bnl.gov>.
- [59] R. B. Firestone *et al.*, Table of Isotopes (1995).
- [60] G. W. Kerr *et al.*, Nucl. Phys. A **110**, 637 (1968).
- [61] R. B. Walton *et al.*, Phys. Rev. **170**, 1065 (1957).
- [62] K. K. Sekharan *et al.*, Phys. Rev. **156**, 1187 (1967). An R-matrix evaluation from <http://www.nndc.tokai.jaeri.go.jp/ftpnd/jendl/jendl-an-2003.html> of this measured cross section was actually used.
- [63] G. Hirano, Talk at Atomic Energy Society of Japan, Sasebo, Japan, (2003).
- [64] K. Nakajima, Talk at the Physical Society of Japan, Miyazaki, Japan, (2003).
- [65] John R. Lamarsh and Anthony Baratta, "Introduction to Nuclear Engineering", Third Edition (Japanese language edition), Pearson Education Japan, Tokyo, (2003).
- [66] M. Edenius, K. Ekberg, B. H. Forssen, D. Knott, CASMO-4 - A Fuel Assembly Burnup Program - User's Manual. Studsvik Report. Studsvik of America (1993).
- [67] J. A. Umbarger, A. S. Digiovine, SIMULATE-3 - Advanced Three-Dimensional Two-Group Reactor Analysis Code - User's Manual. Studsvik Report. Studsvik of America (1992).
- [68] Federation of Electric Power Companies of Japan (FEPC), "Genshiryoku Zumenshu", (2003). Computer readable format at the web-page, (in Japanese) <http://www.fepc-atomic.jp/kyouiku/kyouzai/zumen/index.html>, was used.
- [69] International Nuclear Safety Center (INSC), Maps of nuclear power reactors at the web-page, <http://www.insc.anl.gov/pwrmaps/>.
- [70] Nuclear and Industry Safety Agency, Ministry of Economy, Trade and Industry, "Genshiryoku Shisetsu Unten Kanri Nenpou", 2003, Thermal and Nuclear Power Engineering Society, Tokyo (2004).
- [71] Civil Aviation bureau, Ministry of Land, Infrastructure and Transport, "Aeronautical information publication Japan", (2002).

- [72] Japan Atomic Industrial Forum, Inc. (JAIF), Operation records of Japanese nuclear power station at the web-page (in Japanese), <http://www.jaif.or.jp/ja/data/npp/index.html>.
- [73] Korea Hydro and Nuclear Power Co., Ltd. (KHNP), Operation records of Korean nuclear power station at the web-page (in Korean), http://www.khnp.co.kr/new_web/message/me2_01_01.jsp.
- [74] Atomic Energy Commission of Japan (AEC), White Paper on Nuclear Energy 1996, (1996). Computer readable format (in Japanese) is at the web-page, <http://aec.jst.go.jp/jicst/NC/about/hakusho/indexh.htm>.
- [75] Agency of Natural Resources and Energy, Ministry of International Trade and Industry, "Genshiryoku Hatsuden Binran", 1982, Denryoku Shimpo, Tokyo (1982).
- [76] Nuclear and Industry Safety Agency, Ministry of Economy, Trade and Industry, "Genshiryoku Shisetsu Unten Kanri Nenpou", Thermal and Nuclear Power Engineering Society, Tokyo.
- [77] H. Minakata *et al.*, Phys. Rev. D **68**, 033017 (2003).
- [78] M. Shiozawa, presented at the XXth Int. Conf. on Neutrino Physics and Astrophysics, Munich, May 2002.
- [79] T. Hagner *et al.*, Astroparticle Physics **14**, 33-47 (2000).
- [80] J. B. Birks, Proc. Phys. Soc. A **64**, 874 (1951).
- [81] T. Mitsui, Transparencies of the KamLAND internal meeting.
- [82] T. Mitsui, Internal note of KamLAND.
- [83] W. R. Leo, Techniques for Nuclear and Particle Physics Experiments. Springer Verlag.
- [84] A. Stuart *et al.*, "Kendall's Advanced Theory of Statistics", Vol. 2A, Oxford University Press, New York (1999).
- [85] J. N. Bahcall and C. Pena-Garay, New J. Phys. **6**, 63 (2004); M. Maltoni *et al.*, New J. Phys. **6**, 122 (2004).
- [86] Y. Ashie *et al.*, Phys. Rev. Lett. **93**, 101801 (2004).
- [87] V. D. Barger *et al.*, Phys. Rev. Lett. **82**, 2640 (1999).
- [88] E. Lisi *et al.*, Phys. Rev. Lett. **85**, 1166 (2000).